Exploiting sparse spectrum to accelerate spiral magnetic resonance spectroscopic imaging : method, simulation and applications to the functional exploration of skeletal muscle

Jabrane Karkouri

To cite this version:

Jabrane Karkouri. Exploiting sparse spectrum to accelerate spiral magnetic resonance spectroscopic imaging : method, simulation and applications to the functional exploration of skeletal muscle. Medical Imaging. Université de Lyon, 2019. English. NNT : 2019LYSE1295 . tel-02524504

HAL Id: tel-02524504
https://theses.hal.science/tel-02524504

THÈSE DE DOCTORAT DE L'UNIVERSITÉ DE LYON
opérée au sein de :
l'Université Claude Bernard Lyon 1

École Doctorale 205
École Doctorale Interdisciplinaire Science et Santé

Spécialité de doctorat : Innovation Technologique pour le Biomédical

Soutenu publiquement le 11/12/2019, par :
Jabrane Karkouri

Exploiting sparse spectrum to accelerate spiral magnetic resonance spectroscopic imaging:

method, simulation and applications to the functional exploration of skeletal muscle

---

Devant le jury composé de :

MEYERSPEER Martin Associate Professor, University of Vienna	**Rapporteur**
GAMBAROTA Giulio Professeur des universités, Université de Rennes	**Rapporteur**
BONNY Jean-Marie Directeur de Recherche, INRA, Clermont-Ferrand	**Rapporteur**
PIALAT Jean-Baptiste Professeur des Universités-Practicien Hospitalier, Université Lyon 1, Lyon	**Président**
BLANC-FERAUD Laure Directrice de Recherche, CNRS, Nice	**Examinatrice**
RATINEY Hélène Chargée de Recherche, CNRS, Lyon	**Co-encadrante de thèse**
VIALLON Magalie Physicienne médicale HDR, CHU de Saint-Etienne	**Directrice de thèse**
MILLIOZ Fabien Maitre de Conférence, Université Lyon 1, Lyon	**Invité**
LE PETIT-COIFFE Matthieu Responsable partenariat scientifique et clinique, Siemens Healthineers	**Invité**

Composition de la FST

UNIVERSITÉ CLAUDE BERNARD - LYON 1

Président de l'Université	**M. le Professeur Frédéric FLEURY**
Président du Conseil Académique	M. le Professeur Hamda BEN HADID
Vice-président du Conseil d'Administration	M. le Professeur Didier REVEL
Vice-président du Conseil Formation et Vie Universitaire	M. le Professeur Philippe CHEVALIER
Vice-président de la Commission Recherche	M. Frabrice VALLÉE
Directrice Générale des Services	Mme Dominique MARCHAND

COMPOSANTE SANTÉ

Faculté de Médecine Lyon Est - Claude Bernard	Directeur: M. le Professeur G.RODE
Faculté de Médecine et de Maieutique Lyon Sud - Charles Mérieux	Directeur: Mme la Professeure C.BURILLON
Faculté d'Odontologie	Directeur: M. le Professeur D.BOURGEOIS
Institut des Sciences Pharmaceutiques et Biologiques	Directeur: Mme la Professeure C. VINCIGUERRA
Institut des Sciences et Techniques de la Réadaptation	Directeur: M. X. PERROT
Département de formation et Centre de Recherche en Biologie Humaine	Directeur: Mme la Professeure A-M. SCHOTT

COMPOSANTES ET DEPARTEMENTS DE SCIENCES ET TECHNOLOGIE

Faculté des Sciences et Technologies	Directeur: M. F. DE MARCHI
Département Biologie	Directeur: M. le Professeur F. THEVENARD
Département Chimie Biochimie	Directrice: Mme C. FELIX
Département GEP	Directeur: M. Hassan HAMMOURI
Département Informatique	Directeur: M. le Professeur S. AKKOUCHE
Département Mathématiques	Directeur: M. le Professeur G. TOMANOV
Département Mécanique	Directeur: M. le Professeur H. BEN HADID
Département Physique	Directeur: M. le Professeur J-C PLENET
UFR Sciences et Techniques des Activités Physiques et Sportives	Directeur: M. Y.VANPOULLE
Observatoire des Sciences de l'Université de Lyon	Directeur: M. B. GUIDERDONI
Polytech Lyon	Directeur: M. le Professeur E.PERRIN
Ecole Supérieure de Chimie Physique Electronique	Directeur: M. G. PIGNAULT
Institut Universitaire de Technologie de Lyon 1	Directeur: M. le Professeur C. VITON
Ecole Supérieure du Professorat et de l'Education	Directeur: M. le Professeur A. MOUGNIOTTE
Institut de Science Financière et d'Assurances	Directeur: M. N. LEBOISNE

Acknowledgement

This document presented here is the result of three years of work at CREATIS, Lyon, Siemens Healthcare and CHU St-Etienne. I would like to thank all the people that contributed to this project, were helping me and supporting me all the way during these three years.

I first would like to thank Magalie Viallon, who was actually the person who recruited me. I would like to thank her for supervising me and for giving me the opportunity to use the clinical MR scanner in the CHU St-Etienne. I am also grateful for her involvement in this project, especially on clinical applications and clinical protocols developments, for her support, her advices, her corrections and remarks, that kept me going on this PhD thesis without being stuck for a too long time. I also thank her for giving me the opportunity to work in good conditions, and for always being here when the situation needed it.

I am really grateful to Hélène Ratiney for supervising me, and for her major contributions. She was of huge help and I thank her a lot for sharing with me her knowledge and experience on signal processing, physics and spectroscopy. I thank her as well for her kindness, her patience, and her involvement in the project, her corrections, remarks and advices on my documents, articles, reports that were of great help. I am also very grateful of her help on some post-processing developments in this work. She is a talented and serious researcher that I am more than happy to have worked with.

I thank Fabien Millioz for supervising me on the signal processing side of this thesis. I am also grateful of his advices, comments and remarks, especially on the article that we have been writing during this thesis. I thank him also for the nice and interesting intellectual discussions that we had throughout our numerous meetings, and for his patience, positivity and kindness.

I thank Rémy Prost also for supervising me on the signal processing side. I thank him very much for sharing with me his knowledge of many years of research on signal processing. His advices and remarks were of high interest and his rigorous attitude helped me a lot to improve my clarity and for the writing of the first paper.

I am grateful to Pierre Croisille also for giving me the opportunity to work at the CHU St-Etienne. I thank him for his advices, remarks that were pertinent and for his help and involvement on the clinical projects and clinical protocols developments.

I would like to thank Jill Slade for sharing her knowledge and experience on physiology and physiology of energetic metabolism. I also thank her for her advices and corrections that helped me understand more about how the chemical processes occur inside the skeletal muscle. I thank her for her involvement and her help on the clinical protocol development and the clinical project. I also thank Anne Tonson for introducing me to skeletal muscle physiology and orienting me towards the right things to read for basic learning.

I thank Arthur Coste for his help during the project, even if he did not have much time, for the nice discussions and moments we had, and for his involvement. I wish him the best for the rest of his studies. I thank Samuel Guerin for his help on the demonstration of the theorem of the invariant trace by circular shift. He is a very talented and smart person and I am very happy to have shared intellectual conversations with him. I also thank him for being around during these three years, and wish him the best for the end of his PhD.

I am grateful to Siemens Healthcare, for having me as an employee during these three years, and for supporting me all along as well, financially and scientifically as well. I thank Thomas Troalen, for supporting me on the sequence development side, and on scan operations. I also thank Matthieu Le Petit-Coiffe for his support in Siemens, and for accepting to attend my defense.

I also thank William Romero, for being an awesome colleague during these years, for volunteering many times for my tests, and for all the time we have spent together, at work or outside of work. I wish him the best and hope that the end of his PhD will go well.

I thank Hamza Raki, my neighbour desk, for his support, and for all the shared experiences, moments, laughs that were very nice during these years. I thank him also for his kindness, positivity and solidarity. I wish him the best as well for the end of his PhD.

I would like to thank as well the whole CREATIS laboratory for welcoming me, accepting me, and supporting me. I thank Charly Caredda, Angéline Nemeth, Pilar Sango, Mathilde Bigot, Eloise Mougel, Clement Daviller, Laure Alston, Pauline Lefèvre, Isabelle Saniour, Purushothaman Nangalan, Majunathan Nanjappa for all the moments we have shared at work or outside of work. I hope you all the best to you too and hope to see you soon again. I also thank Kevin Tse Ve Koon, Eric Van Reeth, Olivier Beuf, Sophie Gaillard, Marion Lissac, Simon Lambert for their advices and comments.

I thank Sylvain Grange and Rémy Grange for their involvement on the clinical project, the development of the clinical protocol and for volunteering when they could.

I would like to thank the reviewers, for accepting to read and evaluate my work, Martin Meyerspeer, Giulio Gambarotta and Jean-Marie Bonny. I also thank Laure Blanc-Féraud and Jean-Baptiste Pialat for accepting to attend my defense.

I thank the Société Francaise de Résonance Magnétique en Médecine et Biologie (SFRMBM), the International Society for Magnetic Resonance in Medicine (ISMRM), France Life Imaging (FLI) for their financial support allowing me to attend interesting national and international conferences. I also thank the LabeX PRIMES for welcoming me during my MasterâĂŹs internship that lead to this PhD thesis, and for their financial support as well allowing me to attend stimulating international conferences.

I thank all my friends for always supporting me, and helping me morally to get away from the PhD environment and have some fun during these three years, Samuel Guerin, Louis Rapet, Vincent Jaillot, Michel Barthelemy, Romain David, Loic Dejong, Valentin Machado, Angélique Garnier, Nais Roy, Sami Salam, Nicolas Berkouk, Loic Teikiteetini-Vaysse, Jeanne Bernet, Sylvain Rigaud, Maixent Rigaud, Chloe Bioley, Alexandre Changenet and many others. Thanks a lot and I hope you all the best.

Finally, I would like to thank hugely my family for their continuous moral support, nice moments, escapes, nice meals. I thank my parents Zahra and Abdelllatif, and my sister Boutaina, my brother Adham for always supporting and believing in me. I thank my aunt Souad for her kindness and support in Lyon during these three years. I am also grateful to my grandmother Fatima, my aunt Fatima, my aunts Kaltoum and Nezha, my uncles Mohammed and Mustapha, my aunt Fatima, my uncles Mohammed, Hamid, Abdesslam and my cousins Sakina, Anass, Imad, Aissam, Wacil, Najib, Nissrine, Hamza, Yassine, Omar, Asma, Said and Ismail.

Résumé

La quantification du métabolisme musculaire énergétique et de la capacité mitochondriale est cruciale pour étudier les troubles musculaires, les maladies métaboliques ou cardiovasculaires comme la myopathie mitochondriale, le diabète ou les maladies artérielles périphériques. La spectroscopie ^{31}P est un moyen non invasif de monitorer le métabolisme énergétique et les concentrations dynamiques de métabolites phosphorylés pendant ou après un exercice et fournit des informations sur la capacité mitochondriale et oxydative du muscle squelettique.

L'évaluation du métabolisme énergétique par spectroscopie ^{31}P peut se faire par spectroscopie non localisée, spectroscopie monovoxel et imagerie spectroscopique par résonance magnétique (ISRM). Dans la pratique clinique, la spectroscopie ^{31}P non localisée est généralement réalisée, ce qui empêche de mesurer les informations métaboliques de différents muscles individuellement, et une information moyenne résultant du muscle entier est collectée en une seule fois par la bobine de surface utilisée pour l'expérience. L'utilisation de la spectroscopie ^{31}P localisée permettrait d'accéder à des informations spatialement résolues et de motiver le développement de nouvelles séquences intégrant les développements techniques les plus avancés. L'imagerie spectroscopique par résonance magnétique disponible dans les systèmes cliniques a un temps d'acquisition très long qui limite son utilisation clinique à l'acquisition statique, alors que ce qui est d'intérêt est essentiellement la capacité à mesurer dynamiquement les variations de concentration des métabolites phosphorylés au cours d'un protocole d'exercice.

Les développements méthodologiques sur l'ISRM réalisés dans le cadre de cette thèse, se sont attaqués précisément à réduire le temps d'acquisition, en vue d' applications cliniques. Une méthode d'acquisition ISRM rapide a donc été développée, impliquant un échantillonnage non cartésien dans l'espace k (échantillonnage en spirale), couplé à un sous-échantillonnage intelligent de la dimension temporelle, ou sous-échantillonnage du signal de résonance magnétique - le spectre RMN correspondant à la transformée de fourier de ce signal - , exploitant la connaissance a priori de la parcimonie du support spectral et une estimation par moindres carrés pour la reconstruction du signal. Cette méthode a été validée à l'aide de simulations et mise en oeuvre dans un système IRM, optimisée puis testée in vivo sur le muscle du mollet pour des applications ISRM ^{1}H et ^{31}P. Des applications dynamiques ^{31}P ont également été réalisées à 3T et l'utilisation de la séquence sous-échantillonnée d'ISRM spiral développée a montré qu'elle était capable de révéler les changements dynamiques attendus dans le PCr. La quantification du signal nous a permis en outre d'accéder à la capacité mitochondriale, avec une résolution temporelle dynamique deux fois supérieure à celle du cas ISRM spiral avec échantillonnage régulier, et une résolution temporelle similaire à celle de l'ISRM non localisée utilisée conventionnellement. Ces développements sont d'un intérêt crucial pour une évaluation spatialement résolue de la capacité mitochondriale au sein de différents muscles ; c'est-à-dire pour mettre en évidence des altérations musculaires individuelles liées à des dommages spécifiques ou des différences de consommation d'énergie entre les différents chefs musculaires pendant l'exercice.

Des améliorations de séquence sur la spectroscopie ^{31}P localisée 1D ont également été intégrées dans un protocole clinique en cours, afin, à terme, d'appliquer les développements de séquence réalisés pendant cette thèse à un contexte clinique. D'abord testé sur des volontaires sains pour la reproductibilité, le protocole implique des patients qui souffrent d'artériopathie de la jambe inférieure. L'objectif était d'évaluer la capacité mitochondriale de ces patients avant et après une revascularisation de l'artère endommagée. Les résultats ont montré une amélioration significative de la capacité mitochondriale après revascularisation.

Mots-clés: spectroscopie ^{31}P, spectroscopie par résonance magnétique, Imagerie Spectroscopique, sous-échantillonnage, échantillonnage non cartésien, échantillonnage spiralé, reconstruction des moindres carrés, Capacité mitochondriale

Abstract

Quantifying energetic muscular metabolism and mitochondrial capacity are of crucial interest to reveal muscular disorders, metabolic diseases or cardiovascular diseases like mitochondrial myopathy, diabetes or peripheral arthery diseases. ^{31}P spectroscopy is a non invasive way to monitor energetic metabolism and dynamic concentrations of ^{31}P during exercise or after during recovery, and provides information on mitochondrial and oxidative capacity.

The assessment of energetic metabolism via ^{31}P spectroscopy can be done with non-localized spectroscopy, single voxel selection spectroscopy and Magnetic Resonance Spectroscopic Imaging (MRSI). In clinical practice, mostly non localized ^{31}P spectroscopy is done, preventing metabolic information from different individual muscles to be measured, but an average information resulting from the whole muscle and collected at once by the surface coil used for the experiment. The use of localized ^{31}P spectroscopy would enable to access spatially resolved information and motivate the development of new home made sequences integrating the most advanced technical developments. Magnetic resonance Chemical shift Spectroscopic Imaging (CSI) available in clinical systems have very long acquisition time that limits their clinical use to static acquisition, while this is essentially the capacity to measure ^{31}P dynamically during an exercise protocol that is of interest.

The methodological developments on MRSI realized in the context of this thesis were aimed precisely to reduce the acquisition time and in view of some clinical applications. A fast MRSI acquisition method has thus been developed involving a non-cartesian k-space sampling (spiral sampling), coupled to a smart under-sampling along the temporal dimension, corresponding to the acquired magnetic resonance signal - the spectrum being obtained after the Fourier transform of this signal - exploiting a priori known spectral support and a least-squares estimation for signal reconstruction. This method has been validated using simulations, and implemented in a MR scanner, optimized and then tested in vivo on the calf muscle for ^{1}H and ^{31}P MRSI applications. Dynamic ^{31}P applications were also performed at 3T and the use of the under-sampled CSI spiral MRSI developed sequence has been shown to adequately reveal the expected dynamic changes in PCr. Quantification of the signal further enable us to access mitochondrial capacity, with a twice higher dynamic temporal resolution compared to the fully sampled CSI spiral MRSI case, and similar temporal resolution as the non-localized classically used MRS sequence. Those developments are of crucial interest for a spatially resolved assessment of mitochondrial capacity within different muscles, i.e. to point out individual muscle alterations related to specific damages or differences between muscle energy consumption during the exercise.

Sequence improvements on 1D localized ^{31}P spectroscopy were also integrated in the clinical sequence and used in an on-going clinical protocol; in order, in the long term, to apply the sequence developments carried out during this thesis to a clinical context. First tested on healthy volunteers for reproducibility, the protocol involves patients that suffers from lower leg arteriopathy. The objective was to assess mitochondrial capacity of those patients before and after a revascularization of the damaged artery. Results showed significant improvement in mitochondrial capacity after revascularization.

Keywords: ^{31}P **spectroscopy, Magnetic Resonance Spectroscopic Imaging, undersampling, spiral sampling, least square reconstruction, a priori known support, dynamic** ^{31}P **application, Mitochondrial capacity**

Contents

Introduction

1

Summary

1.1 General Introduction

The study of energetic metabolism in the skeletal muscle enables the diagnostic of metabolic diseases and muscular disorders. In order to produce energy in the form of Adenosine Triphosphate (ATP), to perform exercises and contractions, many cellular and chemical processes in the muscle are occurring, starting from the ingestion of nutriments to the ATP release within all living cells and the muscles. The process of ATP production occurs in the mitochondrial matrix and mitochondrial capacity can be assessed with ^{31}P magnetic resonance spectroscopy (MRS).

In nuclear magnetic resonance (NMR), the proton ^{1}H is mostly used to study the anatomy of the body in the case of imaging, and the metabolism in the case of spectroscopy. Indeed, ^{1}H NMR spectroscopy gives access for example to intra and extra myocellular lipids information, proton metabolite concentrations such as carnosine, creatine, etc... The use of ^{31}P spectroscopy allows studying energetic metabolism and the mechanism of ATP production. ^{31}P spectroscopy can be done dynamically during exercise and recovery, which gives access to the oxidative capacity within the muscle.

Several ways of performing NMR spectroscopy exam exist. Non-localized spectroscopy is the simplest technique, especially and widely used in the phosphorus case, and gives a spectral distribution of biochemical compounds involved in different metabolic pathways inside the body. 1D localized spectroscopy enables both the spatial and spectral metabolite distribution but only within one voxel of interest. Magnetic resonance spectroscopic imaging (MRSI) will give a spatial and spectral distribution within multiple voxels of interests. Single voxel localized spectroscopy and magnetic resonance spectroscopic imaging suffers from poor signal to noise ratio (SNR), and particularly in the case of MRSI, from a long acquisition time. That is why MRSI use in clinical practice is limited. Several conventional techniques have been proposed to reduce MRSI acquisition time such as EPSI, spiral MRSI, radial, etc... but at the expense of SNR. Recent advances with the Compressed Sensing (CS) theory made possible the reconstruction of NMR signals from fewer measurements than the Nyquist-Shannon criterion, by exploiting the sparsity of the data to acquire.

In the context of this thesis, a new fast acquisition method has been developed for MRSI applications in the muscle. This fast acquisition method relies on a non-cartesian spiral k-space sampling, coupled with a novel temporal under-sampling technique exploiting the sparsity of MR spectra with a least square signal reconstruction based on *a priori* known spectrum support. The proposed method shares many characteristics with the recently introduced compressed sensing concept. In our method, the parsimony of the data is expressed through the prior knowledge of the support of the data in a given domain. Given a known signal support in a domain, a l_2-norm can be used for signal reconstruction from undersampled data. In a noisy scenario, the signal reconstruction error depends on the choice of the samples to acquire. In our method, the algorithm called Sequential Backward Selection (SBS) proposed by Gao and Reeves is used in order to minimize the error magnification. This thesis work established his entire acquisition strategy on these charateristics (Sequential backward Selection of the data samples and l_2-norm reconstruction) and sought to take advantage of the under-sampling process to save acquisition time in the case of spiral spectroscopic imaging.

The proposed strategy has been implemented on Siemens' integrated development environment for applications software (IDEA).

In vivo experiments were done in ^{1}H and ^{31}P MRSI and on dynamic ^{31}P MRSI. In this thesis, ^{1}H MRSI has been applied on the calf muscle at 3T for fat-water and ^{1}H metabolites quantification in the muscle and ^{31}P MRSI has been applied at rest for phosphorus metabolites quantification, intra-cellular pH assessment and during exercise to assess mitochondrial capacity within different muscles such as the gastrocnemius and the soleus muscles.

Parallel to those developments, a clinical protocol has been developed for patients with a lower leg artheriopathy; in the view of being able to quickly integrate in a clinical context the methodological developments carried out during this thesis work. This MR protocol, named SPECTROAMI, is performed before and after revascularization of the patients and includes a dynamic localized ^{31}P spectroscopic exercise protocol. The aim is to assess oxidative capacity before and after the surgery and results on four patients are presented.

1.2 Thesis Overview

The thesis project was done partly at Creatis, Lyon laboratory and partly at University Hospital Saint-Etienne (CHUSE), in the radiology department headed by the professor Pierre Croisille. There human studies were conducted on a 3T MRI scanner. A 1.5T MRI scanner was used at the research facility "Centre d'Etude et de Recherche Multimodal Et Pluridisciplinaire" (CERMEP) for sequence testing on phantoms. Clinical protocols were conducted at St-Etienne on ^{31}P and ^{1}H MRS and MRSI. This project was done in partnership with Siemens, Saint-Denis, France, according to a "Conventions Industrielles de Formation par la REcherche" (CIFRE grant). It consisted mainly in methodological developments for the exploration of the skeletal muscle with spectroscopic imaging and in view of some clinical applications.

The present manuscript is divided into 4 chapters:

The second chapter provides basis on several aspects of the project. Human physiology is first introduced, followed by NMR basics and finishing with an introduction to sparse signal reconstruction and compressed sensing. The NMR basics section includes the fundamental concepts of NMR, a description of pulse sequences and clinical applications of MRSI.

The third chapter details, from the signal processing point of view, the proposed fast MRSI methods based on spiral k-space sampling and temporal undersampling. The theory of the method is presented, including the signal acquisition strategy and reconstruction. It provides at the end theoretical results on simulated data.

The fourth chapter focuses on the implementation of MRS sequences that was designed during the thesis project. A first MRS sequence was developed for signal spatial localization, adapted for ^{31}P applications. This step was necessary from the point of view of project management to handle the programming environment of

Siemens. The second and innovative contribution of this part was the implementation of a fast spiral MRSI sequence based on spiral k-space sampling and temporal under-sampling, in accordance with the acquisition strategy described in the second chapter. In vivo ^{1}H and ^{31}P results are shown at the end.

The fifth chapter is oriented towards clinical applications and details the clinical protocol that has been implemented during the thesis project. An exercise protocol to study energetic metabolism has been developed to study a cohort of patients with lower leg artheriopathy. The end of the chapter presents how the implemented MRSI sequences could fit into this protocol.

The manuscript concludes with a synthetic and critical review of the work accomplished and proposes perspectives.

Context and theory basis

2

Summary

In this chapter, we will introduce some basis first on nutrition and on muscle physiology, then on nuclear magnetic resonance (NMR) and finally on signal processing and under-sampling. We will explain how the digestive process leads to energy production under several forms, how we can explore molecules, anatomy and metabolism in the body by means of NMR and magnetic resonance imaging (MRI) and magnetic resonance spectroscopic imaging (MRSI). Finally, we will show how an under-sampled signal can be reconstructed assuming the parsimony of the spectrum to be reconstructed.

2.1 Physiology and phosphoylated compounds

2.1.1 Human nutrition

The products that we eat are composed of chemical components called "nutriments": carbohydrates, lipids and proteins. Each of these nutriments can be decomposed in several families [Méd09].

Simple glucids are called dares. Monosaccharides, disaccharides and polysaccharides form the glucids' family. Monosaccharides have one molecule of dare, such as glucose or fructose, disaccharides two molecules of dare, such as saccharose or lactose and polysaccharides more than two molecules of dare, such as glycogen for example, which is a long carbonate chain and stored in muscles and the liver.

Lipids are composed of fatty acids, which can be divided in three families as well-saturated fatty acids, mono-unsaturated fatty acids and polyunsaturated fatty acids-, triglycerides, which are stored in adipocytes, and complex lipids.

Proteins are composed of amino acids and can have multiple combinations.

All of these nutriments, once eaten, go through the digestive tract which is composed of several organs. They are going to be subject to several metabolic reactions and hydrolysis. The process of digestion will transform the large molecules into many smaller ones. For example, polysaccharides are hydrolyzed into disaccharides which are then splitted into glucose and fructose, proteins are hydrolyzed into amino acids and triglycerides into monoglycerides, fatty acids and glycerol. After the digestive process, the small molecules will be absorbed by the small intestine, mainly.

The secretion of enzymes by the different digestive organs will indeed promote the hydrolysis and catalysis of macronutriments. To regulate blood sugar levels, hormones, such as insulin and glucagon, play a key role. They have opposite effect, insulin will have as an impact to decrease blood glucose, while glucagon will intend to increase blood glucose. Insulin will stimulate the penetration of glucose into muscles and adipocytes. Therefore, it plays an important role in energetic muscle metabolism. Glucagon will stimulate the glycogenolysis, which is a reaction mainly happening in the liver and frees the glucose which was stored under glycogen. It plays an important role in the case of a diet or fast.

The mechanism of energetic production, needed by nearly all the cells in the body, will happen from all the transformed components after the digestive process in the mitochondria. This production will convert the energy contained in carbon-hydrogen bonds in the form of Adenosine Triphosphate (ATP).

2.1.2 Muscle energetic metabolism

The energetic metabolism in skeletal muscles is summarized in figure 2.1.

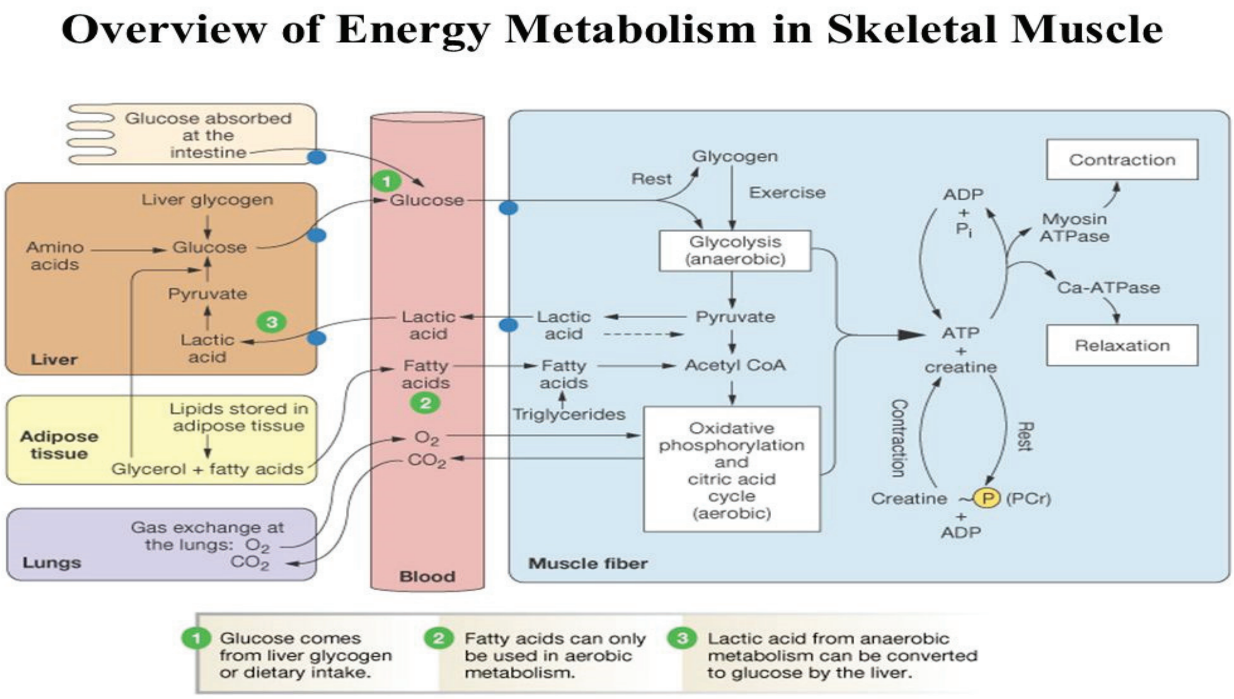

Figure 2.1.: Overview of the energetic metabolism in the muscle [Åđa09]

ATP production is performed in all cells in the mitochondrion. A mitochdrion is a double membrane bound organelle found in the cytoplasm of nearly all living cells . It has a small size of 0.5 to 10 μm [WL16], and their number vary depending on the type of cell. They are numerous in liver and muscle cells (with hundreds or thousands of mitochondria) whereas no mitochondrion can be found in red blood cells for example [Kai+07].

The inner membrane of mitochondria contains the mitochondrial matrix, which holds in the mitochondrial deoxyribonucleic acid DNA, and many enzymes and substrates necessary for ATP production.
[Méd09].

Figure 2.2 shows the structure of the mitochondrion with the inner and outer membranes.

Several mechanisms in the mitochondria matrix are happening to produce energy, and they are all components of the citric acid cycle.
^{31}P Magnetic Resonance Spectroscopy (MRS) enables to detect and quantify phosphorylated metabolites that gives information about ATP turnover, pH and mitochon-

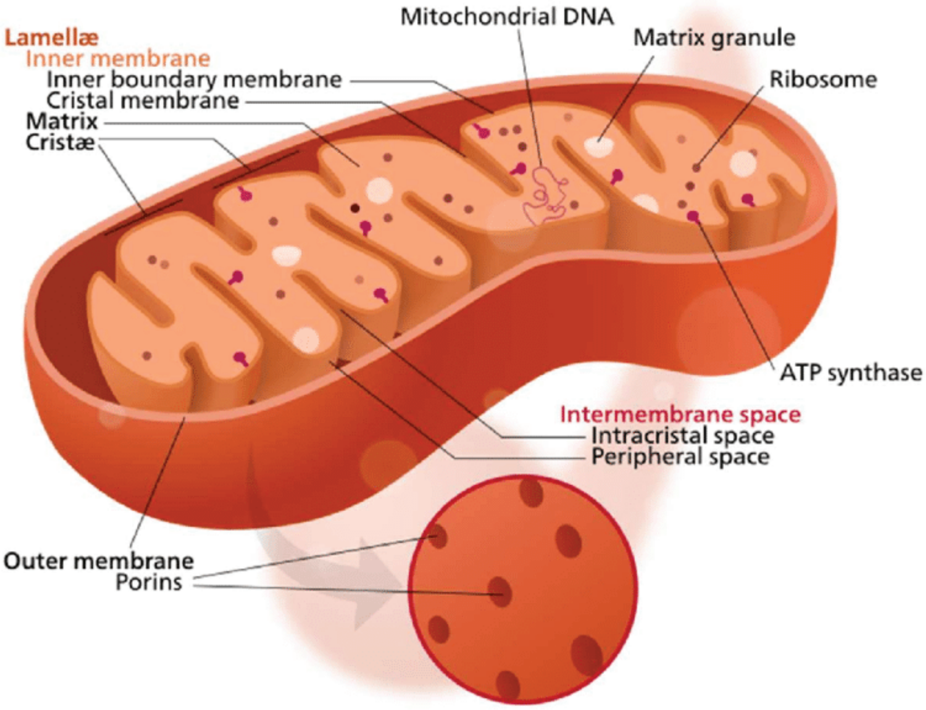

Figure 2.2.: Structure of a mitocondrion [Bod17]. The inner membrane contains enzymes responsible for ATP production. Citric acid cycle and oxidative phosphorylation both are processes happening in the inner membrane.

drial capacity [Iot+93].

It is assumed that the ATP supply equals the ATP demand. When we need to do an exercise, there is an ATP demand and ATP is used by the sarcolemmal Na+/K+-ATPase, the sarcoplasmic Ca2+-ATPase and by the force-generating myosin ATPase in order to produce energy. The ATPase, ATP contractile cost, or hydrolysis rate, depends on the fiber types within the muscle and is an average from all the fibers. It also depends on the nature of exercise that is done and its intensity [Kem+14]. For an isometric contraction, ATP cost rises linearly with the time of the exercise, but for an intense isotonic exercise, the ATP cost depends on the force or intensity and the duration of the contraction. For all types of exercise, isometric, isotonic, aerobic and anaerobic, the ATP production is done simultaneously by several processes which are glycolysis, PCr hydrolysis and oxidative phoshorylation. ATP can be produced as well by the oxidation of fatty acids and amino acids.

ATP synthesis through Glycolysis

The glycolysis is used by all cells in the body for energy generation. It is a series of reactions that first lead to pyruvate and ATP production [Cro+02a; Cro+02b]. Pyruvate will then enter in the citric acid cycle to produce more energy. In anaerobic condition, pyruvate does not enter in the citric acid cycle and turns into lactic acid [MW06]. The anaerobic glycolysis reaction from glycogen-stored glucose to lactate can be written as:

$$(\mathrm{glucose})_{\mathrm{n}} + 3\mathrm{ADP} + 3\mathrm{P_i} \rightarrow (\mathrm{glucose})_{\mathrm{n}-1} + 3\mathrm{ATP} + 2\ \mathrm{lactic\ acid} \tag{2.1}$$

This reaction produces lactic acid and is the main reason of acidosis during an exercise. This process is fast but produces little energy (3 ATP) and acid. Intense exercises lead to further more acid production.

ATP synthesis by phosphates

ATP and PCr stored in skeletal muscles enable to produce energy via 2 main reactions. The production of ATP by ADP and PCr is a reaction catalyzed by the creatine kinase (CK):

$$\mathrm{PCr} + \mathrm{ADP} \leftrightarrow \mathrm{ATP} + \mathrm{Cr} \tag{2.2}$$

ADP can directly be phosphorylated to ATP with adenylate kinase as follows:

$$\mathrm{ADP} + \mathrm{ADP} \leftrightarrow \mathrm{ATP} + \mathrm{AMP} \tag{2.3}$$

ATP free energy over time may remain constant for metabolic purposes. Indeed, we should not spend more energy than we have or than we can produce [MW06].

Glycolysis and PCr hydrolysis play a linked role in ATP free energy buffering. One will prevent the decrease of ATP free energy caused by the other. Moreover, when the ATP demand is too high, the CK reaction will avoid a massive ATP depletion, such that ATP demand will allways match ATP supply. The ATP concentration in the muscle will therefore not change, on the contrary to the concentration of PCr.

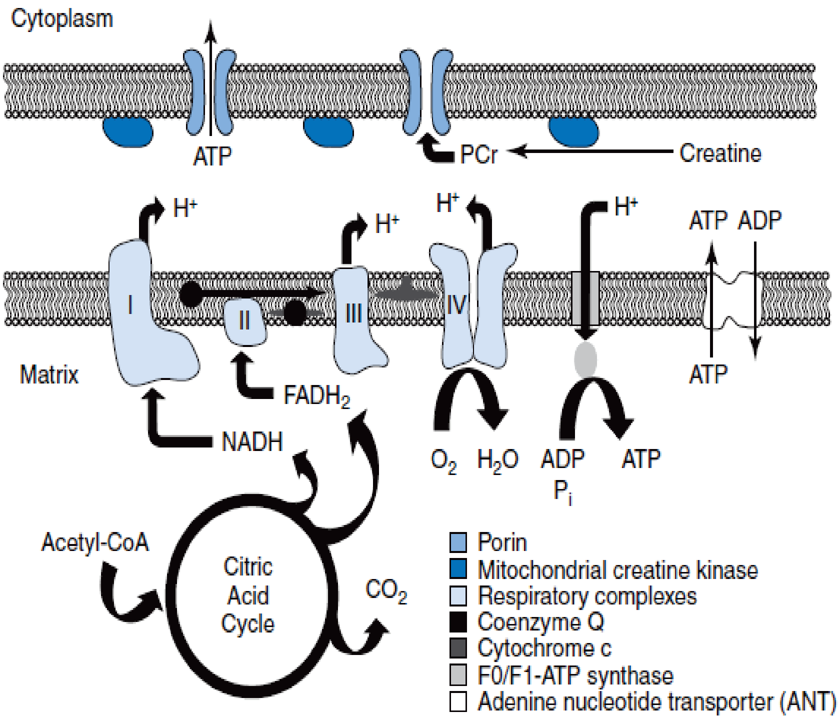

Figure 2.3.: Illustration of the respiratory components in the oxidative phosphorylation and the citric cycle [MW06].

ATP hydrolisis reaction can be written as

$$\mathrm{ATP} \leftrightarrow \mathrm{ADP} + \mathrm{Pi} \tag{2.4}$$

ATP production via the creatine kinase reaction is thus accompanied with PCr depletion and Pi rise.

Changes in PCr concentration is accompanied with opposite changes in Creatine and Pi. The sum of PCr + Pi and of PCr + Cr remain thus is assumed to remain constant during an exercise.

Cellular pH

Via ^{31}P MRS data, it is possible to measure the intra-cellular pH. Glycolytic ATP synthesis produces lactic acid and H^+. This H^+ will then lower the pH. PCr hydrolysis will consume H^+ at a lower rate to finally produce Cr and Pi. The pH is also buffered by many other processes so that it does not decrease too much. Therefore, a decrease in pH would be detected for an intense exercise.

Oxidative phosphorylation and Citric acid cycle

Oxidative phosphorylation is an ATP production process that has the capacity to support prolonged aerobic exercise. It occurs at the same time as glycolysis and PCr hydrolysis, and is less efficient for ATP production in the first seconds, but during a prolonged exercise, while the other processes will not produce a lot of ATP over time, this process will be of main importance. Note that this is a process that needs oxygen, nicotinamide adenine dinucleotide (NAD) and flavin adenine dinucleotide (FAD). All three are part of the transport chain were energy is delivered in the form of ATP.
The citric acid cycle is a wheel (Figure 2.3) where one molecule of acetyl CoA will take part of several chemical reactions to produce ATP, and electrons that contains energy and will therefore go into the transport chain, forming the oxidative phosphorylation [MW06].

ATP demand is thus the sum of ATP synthesis occurring with oxidative phosphorylation, glycolysis and PCr hydrolysis. If U is the ATP demand, L the glycolitic ATP synthesis and Q the oxidative ATP synthesis, we can write

$$U = L + Q - \frac{\delta \mathrm{PCr}}{\delta t} \tag{2.5}$$

For an aerobic exercise, the ATP synthesis is mainly oxidative, so $Q >> L$. To buffer ATP concentration so that it remains always the same, the CK reaction will transform ATP to resynthesized PCr. Therefore, it can also be assumed that $U \approx 0$. We then have

$$Q \approx \frac{\delta \mathrm{PCr}}{\delta t} \tag{2.6}$$

Fatty acids oxydation

Fatty acids are catabolized via a process called beta oxidation where they will produce at the end a molecule of acetyl CoA which will then join the citric acid cycle.

Energy stock, glycogenolysis

Carbohydrates are stocked in the form of glycogen, in muscles and liver. The glycogen stored in the liver represents energy for the whole body whereas the glycogen stored in muscles is only used by muscles for contractions. Glycogen is synthetized by glycogenosis and glycogenoneogenosis. The neoglucogenosis synthesizes glucose from glycogen. In the case of a diet, the neoglucogenosis have a major role for carbohydrates synthesis.

Lipids are synthesized after several chemical reactions, starting with one including a molecule of acetyl CoA. They are stocked in the form of triglycerides in the adipose tissues.

^{31}P MRS studies

Many ^{31}P MRS studies have been done on human skeletal muscle, mainly on the quadriceps and the calf muscle to study the energetic metabolism. Indeed ^{31}P MRS is one of the first application of MR spectroscopy in vivo. It can be done with a resting muscle, for example to evaluate the pH and have metabolic measurement from a perfused muscle at rest [Par+13a]. At rest, phosphomonoesters (PME) and phosphodiesters (PDE) components concentrations within muscle are biological markers of muscular dystrophies [Kem+93]. Moreover, exchange flux, between PCr and ATP, or Pi-ATP, can be measured with magnetization transfer methods at rest [Par+13d; Nab+10].

Many studies have been conducted with exercised muscles [AB09; Sch+12] at different magnetic fields, from 3 T to 7 T [Par+13b; Mey+11]. During the exercise, PCr breakdown can be detected and quantified to estimate the contractile cost of the exercise [Jen; Kem+94]. The pH can be detected and evaluated during the exercise. At the steady state exercise, there is a linear relationship between oxidative ATP synthesis and PCr concentration. During recovery, PCr concentration increase rate is related to the rate of oxidative ATP synthesis and mitochondrial capacity [Tho+95]. In this thesis, we are interested in localized ^{31}P MRS at 3 T that allow studying the metabolism and extract the mitochondrial capacity of different muscles in the body.

2.2 NMR basis

2.2.1 Introduction and Boltzmann distribution

Nuclear Magnetic Resonance (NMR) spectroscopy and imaging enable the detection of metabolites inside the body. This allows to study the metabolism, physiology and anatomy of living tissues in a non-invasive way.
An NMR experiment can be divided into three main steps. First, an excitation of the environment of interest with radiofrequency pulses manages and manipulates the magnetization, and prepare the NMR information. The NMR signal will then be detected in a second step. The NMR signal comes from the induced signal in a receiver coil. The use of magnetic gradients acts on the phase of the transverse magnetization and manages the spatial encoding of the NMR signal. The NMR signal can thus be spatially localized. The acquisition and detection scheme are part of what is called a magnetic resonance sequence. The parameters of the sequence will shape the further detected NMR signal given what are our objectives and constraints: what we want to detect, what resolution we want, Signal to Noise Ratio, what contrast we want on our images, constraints on exam time, etc... The third and last step consists in the signal processing, including reconstruction of mineable images and parameter extraction. Given a certain model of physical phenomenon, it is then possible to extract quantitative information: in the case of magnetic resonance spectroscopy and magnetic resonance spectroscopic imaging, the access to *in vivo* biochemical composition of the studied tissue or part of the body is made possible. We will give some details about the physical concepts of NMR in the following and the next sections.

In Nuclear Magnetic Resonance (NMR) [Bro+14], the objective is to excite the spins with a radiofrequency (RF) wave at the Larmor Frequency ν_0 and then detect the electromagnetic wave resulting from excited spins returning to their original energy state. In practice, a radiofrequency wave perpendicular to the direction of the static magnetic field $\overrightarrow{B}_0$ is applied. The relationship between the Larmor frequency ν_0 and the static magnetic field is

$$\nu_0 = \frac{\gamma}{2\pi} B_0 \tag{2.7}$$

where γ is the gyromagnetic ratio of the studied nucleus. In this thesis, two nuclei are being studied, ^{1}H and ^{31}P. Some gyromagnetic ratios of nuclei used in *in vivo*

Isotope	Spin	Natural abundance (%)	$\gamma/2\pi$ (MHz/T)	NMR frequency (MHz) at 3 T
^{1}H	1/2	99.985	42.58	127.728
^{2}H	1	0.015	6.54	19.608
^{7}Li	3/2	92.580	16.55	49.638
^{13}C	1/2	1.108	10.703	32.112
^{19}F	1/2	100	40.05	120.156
^{23}N	3/2	100	11.26	33.786
^{31}P	1/2	100	17.24	51.705
^{39}K	3/2	93.10	1.99	5.964
^{129}Xe	1/2	26.44	11.78	35.331

Table 2.1.: NMR properties and gyromagnetic ratios of nuclei used in *in vivo* NMR.

NMR are given in table 2.1.

In practice, we will face macroscopic samples which have a large number of spins. The macroscopic magnetization of spins of $I = 1/2$ is related to the Boltzmann probability distribution. The two possible quantum states $\pm 1/2$ can be referred as α and β spin states. If $\bar{N_\alpha}$ and $\bar{N_\beta}$ are the mean spin population in the α and β states, under thermal equilibrium condition, and in interaction with a static field B_0, we have

$$\bar{N_\alpha}, \bar{N_\beta} = \frac{\exp(\frac{\pm\gamma\hbar B_0}{2k_BT})}{\exp(\frac{-\gamma\hbar B_0}{2k_BT}) + \exp(\frac{\gamma\hbar B_0}{2k_BT})} \tag{2.8}$$

where T is the temperature, k_B is the Boltzmann constant and $\hbar$ is Planck's constant. If we assume that k_BT is much larger than $\gamma\hbar B_0$, the population ratio becomes approximately

$$\bar{N_\alpha}, \bar{N_\beta} \approx 1 + \frac{\gamma\hbar B_0}{2k_BT} \tag{2.9}$$

The magnetic field B_0 increases the difference between populations. ^{1}H nucleus is naturally abundant in the body and is therefore easy to detect compared to other nuclei such as ^{31}P or ^{13}C, which have moreover a lower gyromagnetic ratio (table 2.1).

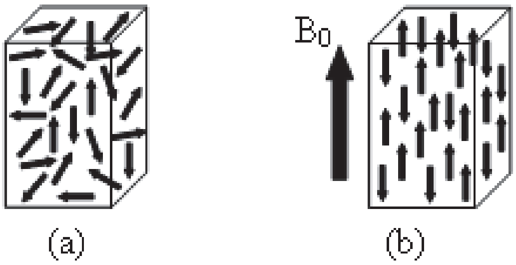

Figure 2.4.: Without magnetic field, the spins are randomly oriented (a) and in the presence of a magnetic field B_0, spins align with its direction (b) (z direction). An x-y direction compound remains, spins are indeed precessing, but the z direction parallel to the magnetic field B_0 is preferred [Tac09].

2.2.2 Macroscopic magnetization

In the absence of an external magnetic field $\overrightarrow{B}_0$, the spins are randomly oriented and directed. There macroscopic magnetic moment $\overrightarrow{M}$ is zero. In the presence of a magnetic field $\overrightarrow{B}_0$, the spins will be directed along the $\overrightarrow{B}_0$ axis and will precess around its axis at the Larmor frequency. The longitudinal component of the macroscopic magnetic moment M_0 is expressed as

$$M_0 = \sum \mu_z = \frac{\gamma\hbar}{2}(\bar{N}_\alpha - \bar{N}_\beta) \tag{2.10}$$

with N the total spin population. M_0 can be derived as

$$M_0 = \frac{N\gamma^2\hbar^2}{2k_B T} B_0. \tag{2.11}$$

The magnitude of the macroscopic magnetization is highly depending on the external magnetic field and the gyromagnetic ratio. For some applications with a low gyromagnetic ratio, it becomes quite tricky to access enough Signal to Noise Ratio (SNR).

2.2.3 Bloch equations - Magnetic field gradients

The nuclear magnetic resonance phenomenon was discovered in 1946 through the works of Felix Bloch and Edward Purcell [Blo46; Pur+46].

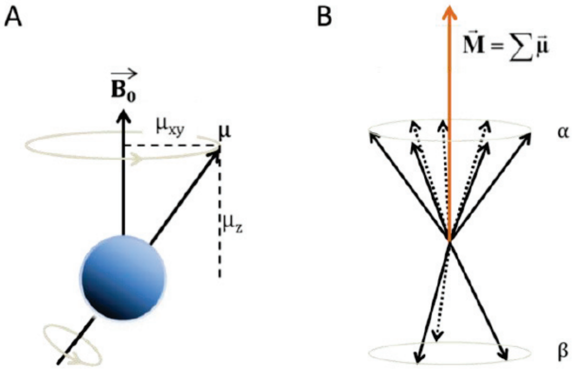

In order to generate an electrical signal, or electromotive force (emf) via Faraday's law, a precessing magnetic field needs to be generated. In a static magnetic field $\overrightarrow{B}_0$, no precession from the macroscopic magnetization can be noticed.

The evolution of the macroscopic magnetization under the magnetic field $\overrightarrow{B}_0$ is governed by

$$\frac{\partial \overrightarrow{M}}{\partial t} = \overrightarrow{M} \wedge \gamma \overrightarrow{B}_0 \tag{2.12}$$

If a gradient $\overrightarrow{G}$ is applied at the same time as $\overrightarrow{B}_0$, the magnetic field varies with the position $\overrightarrow{r}$ as

$$B(\overrightarrow{r}) = B_0 + \overrightarrow{G}.\overrightarrow{r} \tag{2.13}$$

The precession frequency at position $\overrightarrow{r}$ is then

$$\nu(\overrightarrow{r}) = \frac{\gamma}{2\pi}(B_0 + \overrightarrow{G}.\overrightarrow{r}) \tag{2.14}$$

This precession is of high interest for spatial localization of the NMR signal. The precession frequency identifies the position along the gradient. The spatial localization will be further explained in a next section.

In order to excite the spins and flip the magnetization, an additional transverse magnetic field $\overrightarrow{B}_1$ is applied which will rotate the spins in the transverse plane. $\overrightarrow{B}_1$ is rotating around $\overrightarrow{B}_0$ with a frequency equal to the Larmor frequency in order to be "seen" by the spins. This corresponds to the resonance phenomenon. During the application of this B_1 field, which corresponds to a radiofrequency pulse, the magnetization is subjected to interaction with B_0 plus this radiofrequency field. At the end of the excitation, the excited spins, with coherent phases will result in transverse magnetization which will also precess around $\overrightarrow{B}_0$ at the Larmor frequency, creating an electromotive force which induces an electric current, or NMR signal, detected by a receiver coil. In practice, the RF excitation $\overrightarrow{B}_1$ is very short and its duration and amplitude sets the flip angle of the transverse magnetization (for amplitude modulated pulses). The transverse magnetization is maximum when the flip angle is $90°$. In the rotating frame at the Larmor frequency, a magnetic field $\overrightarrow{B}_1$ rotating at the same frequency would be static. This is why the rotated frame (x',y',z') is often introduced in NMR. Here, we will take the laboratory frame (x,y,z) which is the frame where the magnetic field $\overrightarrow{B}_0$ is always static. The evolution of the macroscopic transverse magnetization in this frame under the effect of both $\overrightarrow{B}_0$ and $\overrightarrow{B}_1$ is

$$\frac{\partial \overrightarrow{M}}{\partial t} = \overrightarrow{M} \wedge \gamma(\overrightarrow{B}_0 + \overrightarrow{B}_1) \tag{2.15}$$

The projection in each axes leads to the Bloch equations and is written as follow:

$$\frac{\partial M_x}{\partial t} = \gamma(M_y(t)B_0 - M_z(t)B_{1y}) - \frac{M_x(t)}{T_2} \tag{2.16}$$

$$\frac{\partial M_y}{\partial t} = \gamma(M_z(t)B_{1x} + M_x(t)B_0) - \frac{M_y(t)}{T_2} \tag{2.17}$$

$$\frac{\partial M_z}{\partial t} = \gamma(M_x(t)B_{1y} + M_y(t)B_{1x}) - \frac{M_z(t) - M_0}{T_1} \tag{2.18}$$

The time constants T_1 and T_2 are relaxation times related to the return of the magnetization to its thermodynamic equilibrium state after the RF pulse. T_1 describes the longitudinal recovery of M_z to M_0 and T_2 the transverse decay of M_{xy} (Figure 2.5).

2.2.4 Radiofrequency pulses

Radiofrequency (RF) pulses allow to manipulate the magnetization [Ber+04] (excitation, inversion, refocusing). Spins within the frequency bandwidth of the radiofrequency pulse will be excited. Applied in the presence of a gradient field, it allows

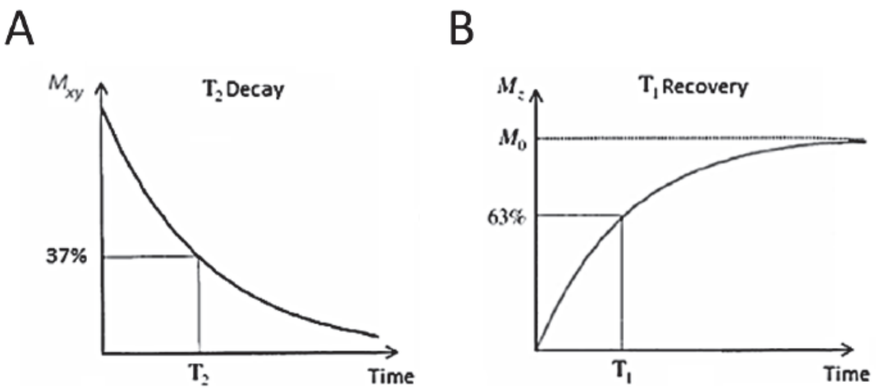

Figure 2.5.: Illustration of the effect of T_1 and T_2 relaxation times on the longitudinal and transverse magnetization. In A, the T_2 decay describes the exponentially decrease of the transverse magnetization with time, corresponding to spin dephasing. t=T_2 corresponds to the time where the transverse magnetization is reduced to 37% of its initial value. In B, the T_1 relaxation time describes the longitudinal magnetization exponential increase. At t=T_1, the longitudinal magnetization reaches 63% of its initial value [LK15].

a spatial localization of the signal. The bandwidth, the frequency profile and the dependence of the B_1 field of the radiofrequency pulse are parameters to take into account to evaluate the pulse.
In this section, we will take the rotating frame as reference. In this frame, $\overrightarrow{B}_1$ is static, and the macroscopic transverse magnetization can be rewritten as:

$$\frac{\partial \overrightarrow{M}}{\partial t} = \overrightarrow{M} \wedge \gamma \overrightarrow{B}_{\text{eff}} \tag{2.19}$$

where $\overrightarrow{B}_{\text{eff}} = \overrightarrow{B_0} + \overrightarrow{B_1} - \frac{\Delta\omega}{\gamma}$ is the effective magnetic field and $\Delta\omega = \omega_0 - \omega$, ω being the precession frequency of the studied magnetization.

On resonance, when $\omega = \omega_0$, the magnetization rotates around $\overrightarrow{B}_1$, and otherwise, spins will rotate around $\overrightarrow{B}_{\text{eff}}$ with a frequency $\frac{\omega}{2\pi}$.

When applying a radiofrequency pulse during a time T_p, the flip angle of the whole magnetization α is

$$\alpha = \gamma B_{\text{eff}} T_p \tag{2.20}$$

On resonance, we have $\alpha = \gamma B_1 T_p$. The flip angle varies with the duration of the radiofrequeny pulse and its intensity. In practice, the intensity of a radiofrequency

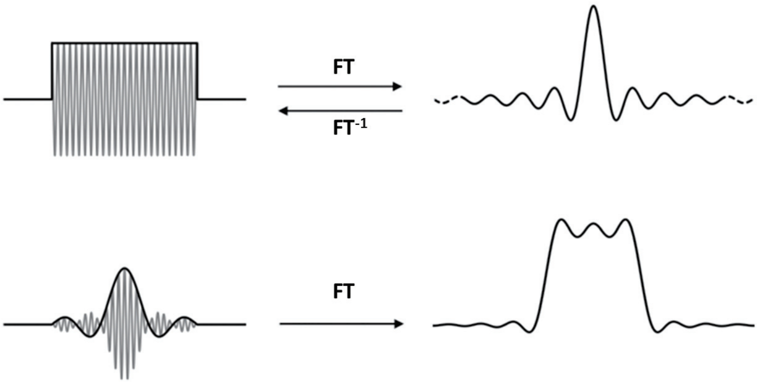

Figure 2.6.: RF pulse design illustration. A square pulse gives a sinc excitation profile while a sinc pulse gives square frequency profile. This is how sinc pulses achieve frequency selective excitation profiles [DG19].

pulse is limited by hardware constraints while the duration of the pulse will be limited by the energy deposition. This kind of pulses is amplitude modulated RF pulses. The Time Bandwidth product, TBP, is constant for a given RF pulse and is $\mathrm{TBP} = T \cdot \varDelta w$, where $\varDelta w$ is the bandwidth of the pulse.

To measure the pulse bandwidth, it is possible to do a Fourier Transform of the pulse to have its frequency profile, and then calculate the Full Width at Half Maximum (FWHM). One can then calculate the duration of the pulse needed to reached a desired bandwidth.

Conventional pulses are modulated in amplitude. The flip angle varies with time during the pulse application.

Square pulses

Using square pulses is the easiest way to excite the magnetization. It consists in the application of a constant magnetic field B_1 during a time T_p at the larmor frequency. The flip angle will be depending on the pulse duration and the intensity of the RF pulse. The use of surface coils with these types of pulses is not efficient as the transmitting B_1 is inhomogeneous and these pulses are amplitude modulated. Moreover, these pulses are non-slice selective. Indeed, their frequency profile is a cardinal sinus and present side lobes that does not allow good localization. In order to increase the spectral bandwidth, it is therefore better to use short pulse duration, but it requires a higher intensity of the RF pulse for the same flip angle.

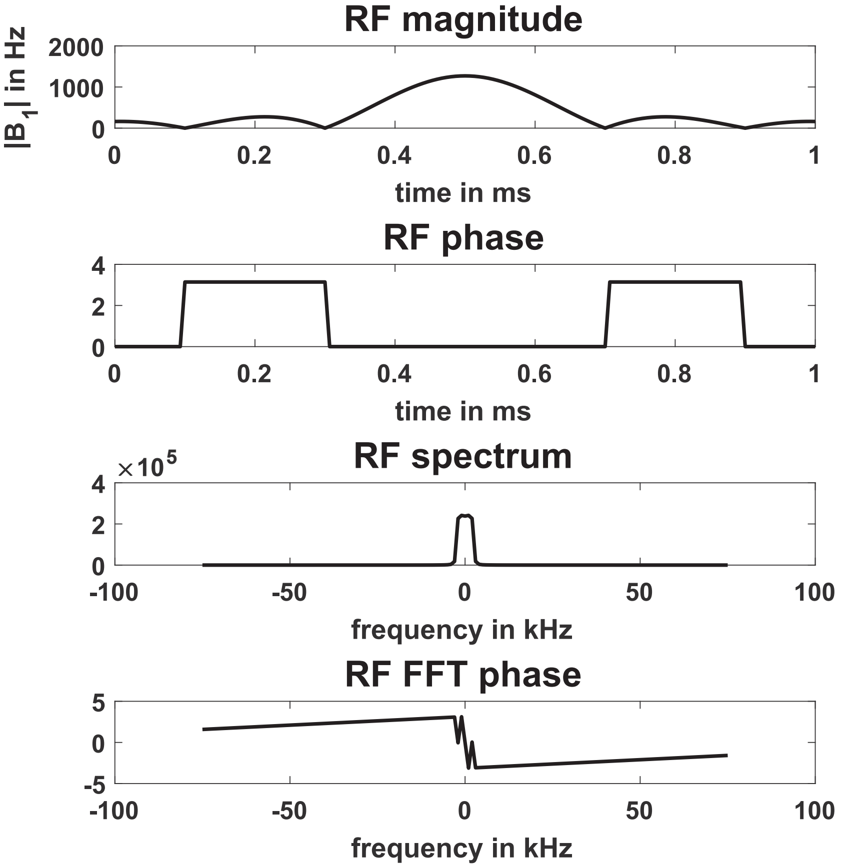

Figure 2.7.: Cardinal sinus pulse magnitude, phase, spectrum and fft phase.

Sinus cardinal pulses

The most used RF pulse that is slice selective and allows a good spatial localization is the cardinal sinus (sinc) RF pulse. On the contrary to the square pulse, its frequency profile is quite uniform and does not contain significant side lobes (Figure 2.6), as for square pulses. Still, this kind of pulse remains amplitude-modulated and is *a priori* not perfectly appropriate to the use of surface coil with inhomogeneous B_1 field. This pulse is used in the majority of sequences in the clinical environment. Many different types of cardinal sinus RF pulse waves exist that have different frequency behaviors. For example the number of lobes defines a type of sinc pulse.

Adiabatic Radiofrequency pulses

These types of pulses, which are frequency and amplitude modulated, are particularly useful in the case of a strong B_1 field inhomogeneity and the use of surface coils [TG97]. Indeed, in the case of surface coils, the B_1 field is not constant spatially in respect to the distance from the surface coil. It becomes quite tricky to study deep structures.

Their specificity is that the flip angle is less sensitive to the RF pulse intensity or B_1 amplitude. In the adiabatic regime, the flip angle does not depend on the RF pulse intensity and is moreover the same wherever in space. The adiabatic regime is achieved after a certain B_1 amplitude threshold.

In the case of adiabatic pulses, $\varDelta\omega(t)$ depends on time. The effective magnetic field thus varies with time as well. When complying to the adiabatic condition,

$$\frac{d\alpha}{dt} \ll \gamma B_{\text{eff}}(t) \tag{2.21}$$

and thus

$$\alpha = \arctan(\frac{\varDelta\omega(t)}{\gamma B_1}). \tag{2.22}$$

Satisfying the adiabatic condition will ensure that the magnetization that was parallel to the effective magnetic field $\overrightarrow{B}_{\text{eff}}(t)$ will remain that way and the magnetization that was perpendicular will remain perpendicular and rotate around $\overrightarrow{B}_{\text{eff}}(t)$. To calibrate an adiabatic pulse, it is possible to keep a constant pulse length and increase the RF pulse intensity. When the signal intensity remains constant, it means that the adiabatic regime has been reached.

Examples of adiabatic pulses are hyperbolic secant pulses, tangent hyperbolic pulses. Adiabatic pulses are most commonly used for inversion or refocusing. Adiabatic Full passage (AFP) pulses of $180°$ and Adiabatic Half Passage (AHP) pulses of $90°$ commonly used are hyperbolic secant pulses:

$$B_1(t) = B_{1\text{max}}\text{sech}(\beta(\frac{2t}{T_p} - 1)) \tag{2.23}$$

The modulation in frequence is given by

$$\varDelta\omega(t) = -\mu\beta\tanh(\beta(\frac{2t}{T_p} - 1)) \tag{2.24}$$

T_p is the pulse duration. β and μ are parameters defining the truncation factor (β is defined as $sech(\beta) = 0.01$). The hyperbolic secant pulse characterization are shown in figure 2.8.

A general class has been introduced by [TG97; TG+96] of adiabatic pulses that satisfies the adiabatic condition for all the frequencies within a given bandwidth. They are called Offset-Independent Adiabaticity pulses (OIA). The most used pulses of this class are the HSn family functions described as

$$B_1(t) = B_{1\mathrm{max}}\mathrm{sech}(\beta(\frac{2t}{T_p} - 1)^n) \tag{2.25}$$

$$\varDelta\omega(t) = -\int \mathrm{sech}^2(\beta(\frac{2t}{T_p} - 1)^n) \tag{2.26}$$

These types of pulses enable to reduce the energy deposition and lower down the required peak power by reducing the $B_{1\mathrm{max}}$. AFP pulses will be used for inversion and refocusing. The longitudinal magnetization is rotated from M_z to $-M_z$ in the case of an inversion and from $M_x + iM_y$ to $M_x - iM_y$ in the case of a refocusing. Applying one AFP pulse to rotate the magnetization and perform an inversion when starting at M_z enables an insensitive to B_1 inhomogeneity and frequency selective inversion. Applying the AFP in other directions x or **y** to perform a refocusing leads to signal dephasing. It is necessary to use an other AFP pulse after a delay τ_{PCr} to have a cleaner refocusing and without signal loss. The application of a second AFP pulse allows rewinding the phase acquired during the first AFP pulse [Con+89; Con+91]. It cancels the phase accumulated by the first pulse and the transverse magnetization remains constant regarding frequency offset and RF amplitude. This method of refocusing is used in the LASER sequence.

In order to perform a plane rotation of $90°$, Adiabatic Half Passage (AHP) pulses are used. B_1-Insensitive Rotation with 4 segments (BIR-4) pulses are AHP and achieve a suitable non-slice selective rotation but with high insensitivity to B_1 inhomogeneity

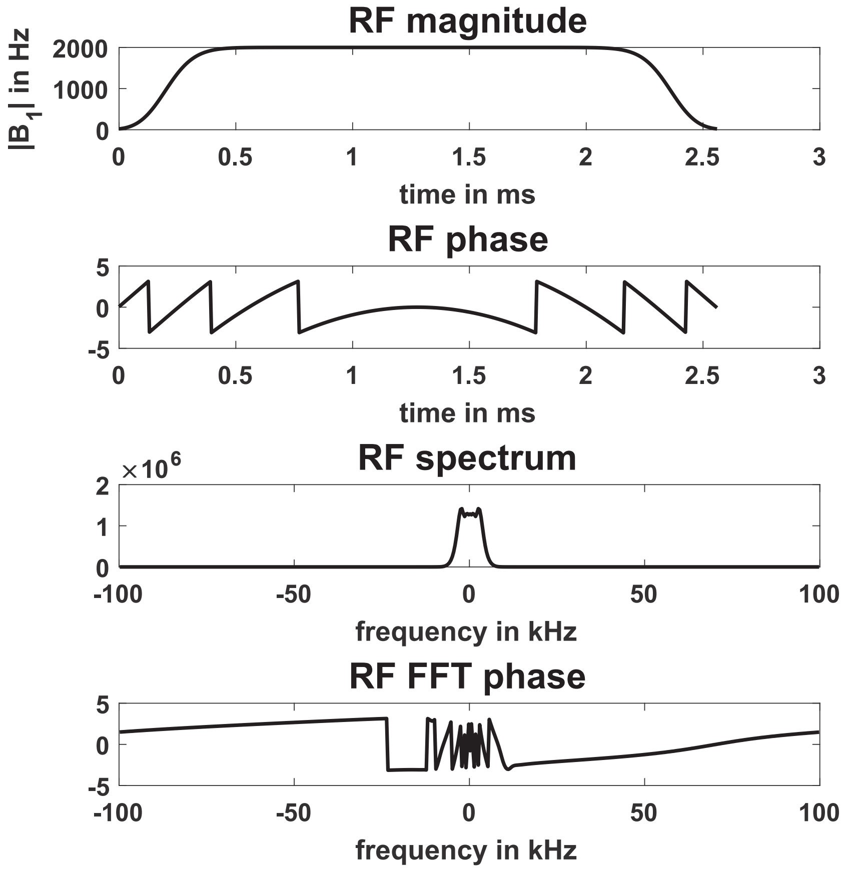

Figure 2.8.: Hyperbolic secant HS8 pulse magnetization, phase, spectrum and fft phase.

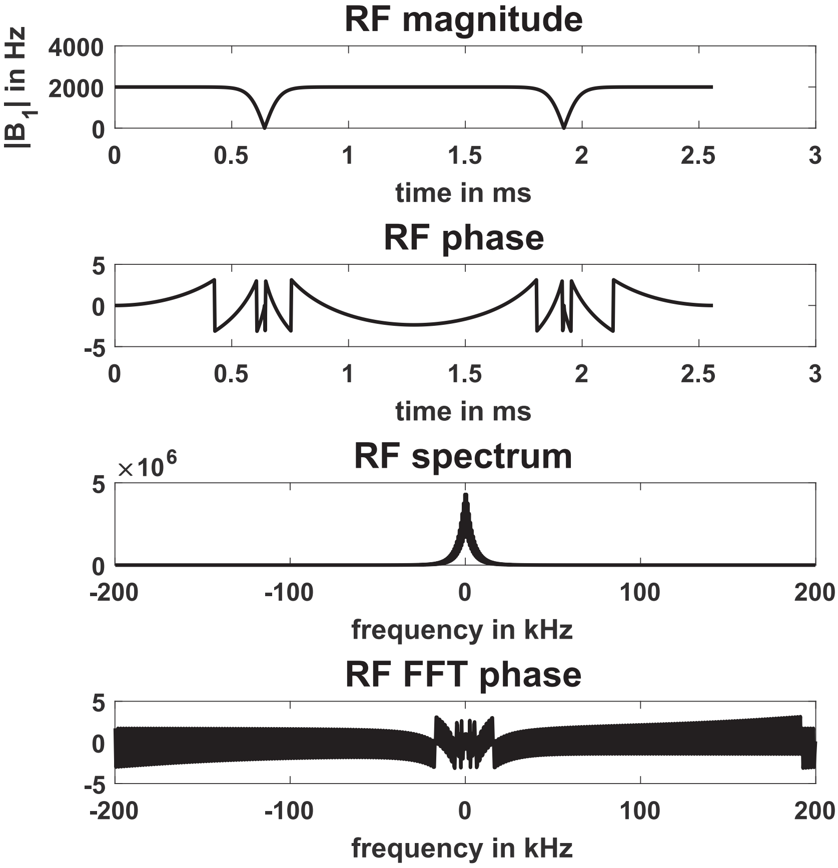

Figure 2.9.: BIR4 pulse magnetization, phase, spectrum and fft phase.

and resonance offsets. It is efficient for 3D applications for example, as in 3D Multi-echo imaging. The Specific Absorption rate (SAR) (energy absorbed by the studied region in the body) of this pulse is quite high and requires the use of long repetition times. It is employing hyperbolic tangent and tangent modulation functions with 4 segments as shown in figure 2.9.

2.2.5 Relaxation times T_1, T_2 and T_2^*

Longitudinal relaxation time

T_1 relaxation characterizes the speed at which the longitudinal magnetization M_z returns to its thermal equilibrium state M_0. It is induced by the energetic transition of the spins after the RF excitation. The spins will transit from their unstable equilibrium state to their stable equilibrium state $m = -1/2$ to $m = 1/2$. The total energy will be dissipated to the environment as thermal energy. The energy disspated will be equal to the energy received to excite the spins. The evolution of the longitudinal magnetization over time is

$$\frac{\partial M_z(t)}{\partial t} = \frac{M_0 - M_z(t)}{T_1} \tag{2.27}$$

which becomes after solving:

$$M_z(t) = M_0 + (M_z(0) - M_0)\exp(-t/T_1) \tag{2.28}$$

where $M_z(0)$ is the initial value of the longitudinal magnetization.

In practice, M_z never completely recover to its original state M_0. Indeed, *in vivo* a repetition time TR is used to sequentially repeat the NMR experiment. TR is often too small compared to the time necessary for M_z to completely return to its equilibrium state. After a few repetitions, a steady-state is nevertheless achieved; This steady state ensures that the signal received will be of same intensity and order one experiment after the other. The optimal excitation angle, in terms of resulting SNR, can be calculated knowing the TR and T_1. This angle is known as Ernst angle and is given by

$$\alpha_{Ernst} = \arccos(\exp(-TR/T1)) \tag{2.29}$$

The use of Ernst angle is particularly useful for short TRs in which the longitudinal magnetization cannot recover completely.

Tranverse relaxation time

After the excitation, spins are all in phase and the transverse magnetization makes its apparition. Transverse T_2 relaxation induces the decrease of the magnitude of the transverse magnetization. What happens is that spins will dephase because of dipolar interactions between spins under the influence of the local magnetic field. They will all have individually different phases and not be coherent one with another. This entropy will affect the transverse magnetization, decreases its magnitude because of the loss of phase coherent which will therefore decrease the received NMR signal as well. The entropy increase is irreversible and the decrease of the signal cannot be

Isotope		T_1 (ms)	T_2 (ms)	gyromagnetic ratio $\gamma/2\pi$ (MHz/T)
^{31}P	PCr	6400	330	17.24
	Pi	5200	150	
	γ-ATP	4500	78	
	α-ATP	2600	55	
	β-ATP	3500	55	

Table 2.2.: NMR properties ^{31}P and associated relaxation times of its metabolites in the muscle at 3 T. PCr stands for Phosphocreatine, Pi for inorganic phosphate and ATP for Adenosine Triphosphate [Mey+03; Bog+09].

avoided.

The presence of magnetic field $\overrightarrow{B}_0$ inhomogeneities has an effet on transverse relaxation. This induces an increase in the coherence loss over time. In fact, the transverse magnetization decreases with a characteristic time T_2^* shorter than T_2. In practice, it is possible to reduce the effect due to magnetic field heterogeneities, for example by shimming or using a spin echo sequence [Koc+06]. The transverse magnetization decreases exponentially as

$$M_{xy}(t) = M_{xy}(0)\exp(-t/T_2^*) \tag{2.30}$$

where $M_{xy}(0)$ is the initial value of the transverse magnetiazation.

T_2^* is related to T_2 and magnetic field heterogeneities by the relation

$$\frac{1}{T_2^*} = \frac{1}{T_2} + \gamma \Delta B_0 \tag{2.31}$$

The term $\gamma \Delta B_0$ is the relaxation rate related to field inhomogeneities across the voxel of interest.

Table 2.2 gives the tranverse and longitudinal approximate relaxation time values of ^{31}P metabolism in the muscle at 3 T.

2.2.6 NMR signal and spectrum

The detected signal is proportional to the macroscopic transverse magnetization. Indeed, the transverse, precessing magnetization induces an electromotive force and thus an electrical signal detected by receiver coils. This signal decreases mono exponentially with time and the constant time T_2^*. The received signal is also called free induction decay (FID) and oscillates, before demodulation, at a very high frequency, close to the larmor frequency. For example, at 3 T, for the proton, it oscillates at around 125 MHz. This signal is demodulated and then sampled by an analog to digital converter. An electronic device is used to demodulate the signal at the carrier frequency.

$$M_{xy}(t) = M_{xy}(0)\exp(-t/T_2^*) \tag{2.32}$$

The signal has a real and imaginary part. The NMR spectrum is obtained after applying a Fourier transform on the time-domain complex signal (Figure 2.10). The spectrum, as a first approximation, consists in Lorentzian absorption and dispersion peaks. The NMR spectrum is analyzed by measuring, for each peak at a given resonance frequency, the intensity of the peak, the area of the peak and full width at half maximum (FWHM). For the case of exponentially damped sinusoids in the time domain, FWHM will be equal to $\frac{1}{\pi T_2^*}$.

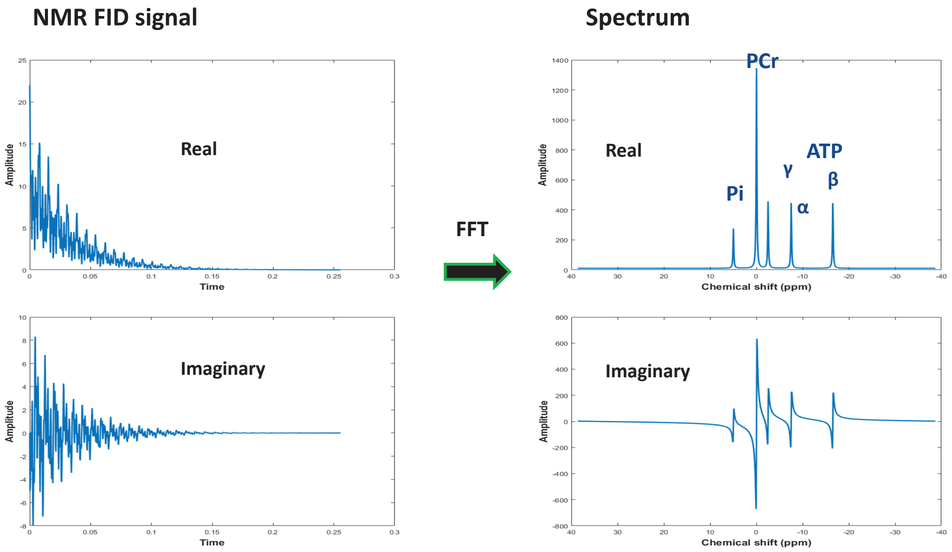

Figure 2.10.: Illustration of the NMR signal and its spectrum in the phosphorus case.

2.2.7 Chemical shift

Spin precession frequency is mostly subject to the external magnetic field $\overrightarrow{B}_0$. However, as nuclei belong to molecules, their a chemical environments vary and thus their own precession frequencies vary. Indeed, due to this chemical environment, they are surrounded by local magnetic fields, that give an effective field smaller or higher than B_0 [Gov+00; DG19]. It results that a spin will be subject to an effective magnetive field $\overrightarrow{B}_e$ which is proportional to $\overrightarrow{B}_0$:

$$\overrightarrow{B}_e = (1 - \sigma)\overrightarrow{B}_0 \tag{2.33}$$

where σ is constant that characterizes the chemical environment of the spin, $|\sigma| << 1$. The resonant frequency is not exactly equal to the Larmor Frequency but is then

$$\nu_e = (1 - \sigma)\nu_0 = \frac{\gamma}{2\pi}(B_0 - \sigma) \tag{2.34}$$

σ may vary with the chemical environment, or changes in the chemical environment such as pH and temperature. This means that spins from a same atom but surrounded by a different chemical environments can have different resonant frequencies. The difference between this frequency and the reference resonant frequency is called chemical shift. It is expressed in parts per million and its definition is

$$\delta = \frac{\nu - \nu_{ref}}{\nu_{ref}} 10^{-6} \tag{2.35}$$

where ν_{ref} is the spin reference frequency. δ is dimensionless and independant of the magnetic field. The reference frequency is calibrated with Tetra-methyl-silane (TMS) for 1^H and phenyl-phosphonic acid (PPA) or hexa-methyl-phosphorous-triamide (HMPT) for 31^P.

2.2.8 J-coupling

J-coupling is mediated through chemical bonds between two spins [Gov+00]. Spins interact indirectly through their shared electron within a molecule.

In the case of two bounded atoms A and X, the orientation of spins and the magnetic field B_0 will affect the magnetic field "felt" by each spin. Each atom induces a local magnetic field that will be added to the static magnetic field B_0 or removed from the static magnetic field. Whether this local field is added or removed depends on the orientation of spins in the atom. This total magnetic field felt by the atom will therefore have multiple resonating frequencies separated by the constant J. This constant does not depend on the static magnetic field, but depends on the number, the nature and the geometry of the bounds between coupled atoms. The more there are bounds between coupled atoms, the less the coupling will be and the smaller the J constant will be. The smaller the J constant is, the harder it is to detect it in vivo. The coupling can also be of more than two bounds. It can be coupling of three, four bounds (triplets, quadruplets,...). For example, the ^{31}P spectrum is mainly composed of a peak of phosphocreatine (PCr), a peak of Inorganic Phosphate (Pi) and a molecule of ATP which is composed of three phosphates groups. Those three phosphates can be distinguished in the spectrum with one doublet corresponding to γ-ATP at -2.7 ppm, another doublet corresponding to α-ATP at 7.8 ppm and one triplet β-ATP at -16.3 ppm (Figure 2.11).

Chemical shifts and J-coupling are the two phenomena responsible behind the spectral signature of a given molecule NMR Spectrum.

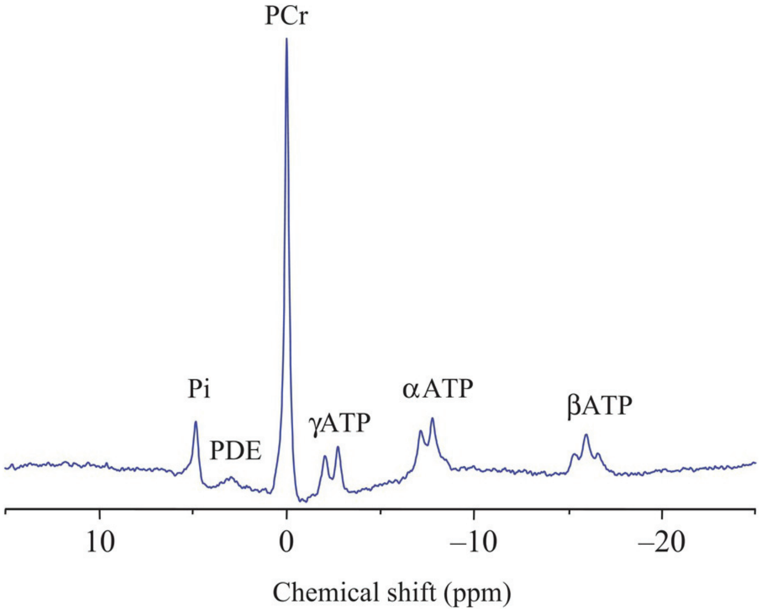

Figure 2.11.: Phosphorus spectrum with its metabolites resonating at different chemical shifts: ATP spectral signature shows multiplets which are due to J-coupling.

2.2.9 Spin Echo

Transverse magnetization decreases, after the excitation RF pulse, with a characteristic transversal relaxation time T_2^* as described in subsection 2.2.5. T_2^* results from the effect of the relaxation time constant T_2 and the static magnetic field inhomogeneities. After a $90°$ excitation pulse, spins dephase under the effect of T_2^*. To compensate the phase accumulated by the spins, one can apply a second pulse of $180°$, also called refocussing pulse, that will create a spin-echo with an echo top located at a time T_E after the RF pulse [Hah50]. $T_\mathrm{E}/2$ corresponds to the delay between the excitation pulse and the refocusing pulse. The phase accumulated by the spins at time $T_\mathrm{E}/2$ will be compensated at time T_E, creating an echo. The refocusing pulse is played on the xy-plane, on the contrary to the excitation pulse which is played on the z-plane. The spin echo effect can be used to estimate T_2 relaxation times. There are many spin echo sequences and some of them are listed in a next section. Adiabatic refocusing selective pulses of $180°$ are numerous and can be used to face B_1 inhomogeneities, in the case of surface coils for example, on the contrary to adiabatic slice selective excitation pulses (of $90°$). Indeed, adiabatic excitation pulses are numerous but, currently, adiabatic slice selective excitation pulses do not exist.

2.2.10 Magnetic Resonance spectroscopy (MRS) signal localization

The spatial localization of the NMR signal is of high interest in *in vivo* NMR spectroscopy. Proper spatial localization will lead to good quality spectra, and enables to access the metabolites of interest inside the selected Volume of Interest (VOI) avoiding unwanted signal from outside the region [DG19]. It is often combined with other techniques of signal suppression, mainly water in ^{1}H spectroscopy. Water is indeed very abundant inside the body and its contribution is much larger than other metabolites that are in smaller concentration in the body. B_0 field inhomogeneities spread the peaks at all resonances. B_0 inhomogeneities can be reduces by shimming (i.e procedure to adjust the homogeneity of the static magnetic field) inside the region of interest. Other adjustments can be made to enhance the NMR signal coming for the selected region: by calibrating the RF pulse excitation or homogenizing the B_1 field.

Several spatial localization techniques exist to do Single Volume Spectroscopy (SVS). We will present some of them.

Outer Volume Suppression (OVS)

An OVS module [SG93] saturates the magnetization coming from other regions than the selected one. This technique is less efficient in the case of a use of a surface coil and non-adiabatic RF pulses such as sinc pulses, because of B_1 inhomogeneities [Ber+04]. It is necessary to have a good suppression to avoid any pollution by the outside volume. This technique is used as a module placed before the sequence which creates the signal of interest. For example, with a non-localized FID sequence, the module will be placed before the rectangular RF pulse (Figure 2.12) in order to saturate the magnetization before exciting the magnetization left non saturated, and thus will enable to acquire the FID signal remaining from the selected region. To reduce the sensitivity to B_1 field inhomogeneities, particularly in the case of surface coils, small angles can be set for the OVS module pulses if the pulses that are used are amplitude-modulated, conventional, pulses. Another way to reduce its sensitivity is to apply adiabatic RF pulses (cf chapter 4) that are insensitive to B_1 field inhomogeneities, but the RF is of higher power and the SAR becomes significant.

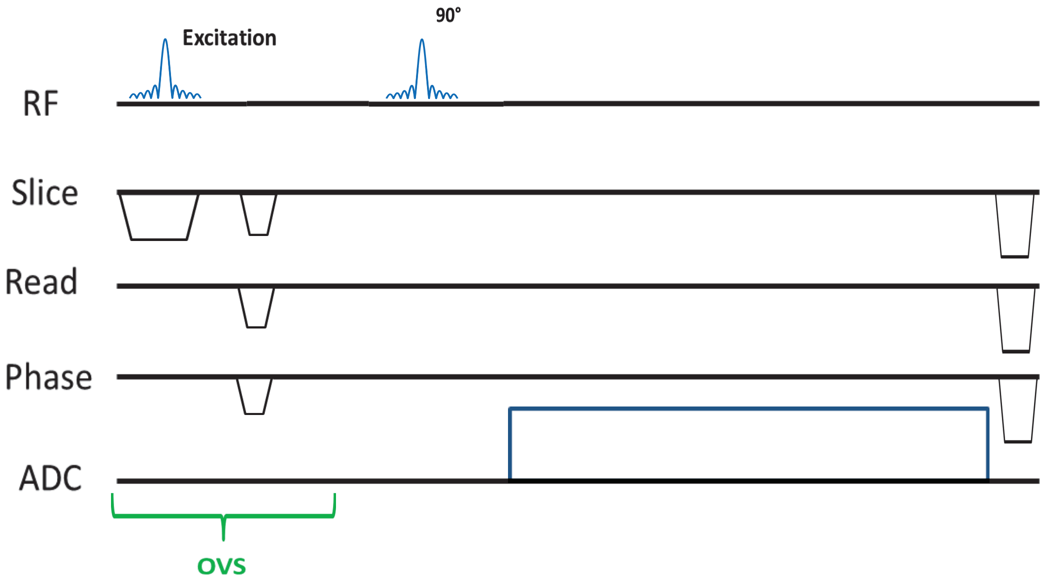

Figure 2.12.: Sequence chronogram of an SVS localization with an OVS module. The OVS module may be repeated several times prior the 90° pulse excitation to saturate the signal in several directions. It is placed before the excitation and before acquiring the signal of interest.

Point Resolved Spectroscopy (PRESS)

The PRESS module [Bot87] is one of the most commonly used methods for signal localization. The PRESS module is represented on figure 2.13. It consists in one slice selective pulse excitation and 2 slice selective refocusing pulses. This is a double spin-echo method. The slice selective refocusing pulses are applied in the two orthogonal directions than the first excited plane. Doing so will ensure that outside regions will either not be excited or not refocused. The first refocusing pulse creates a spin echo at time T_{E1}, and the second creates a spin echo at time $T_{\mathrm{E1}} + T_{\mathrm{E2}}$, where T_{E1} is the delay between the excitation pulse and the first echo, and T_{E2} is the delay between the first refocusing pulse and the second echo. Spoiler gradients are placed between RF pulses in order to dephase volume magnetization and any undesirable coherences. The coherent signal will thus only correspond to the selected region. In clinical practice, the minimum T_{E} that can be accessed with a PRESS module is about 30 ms.

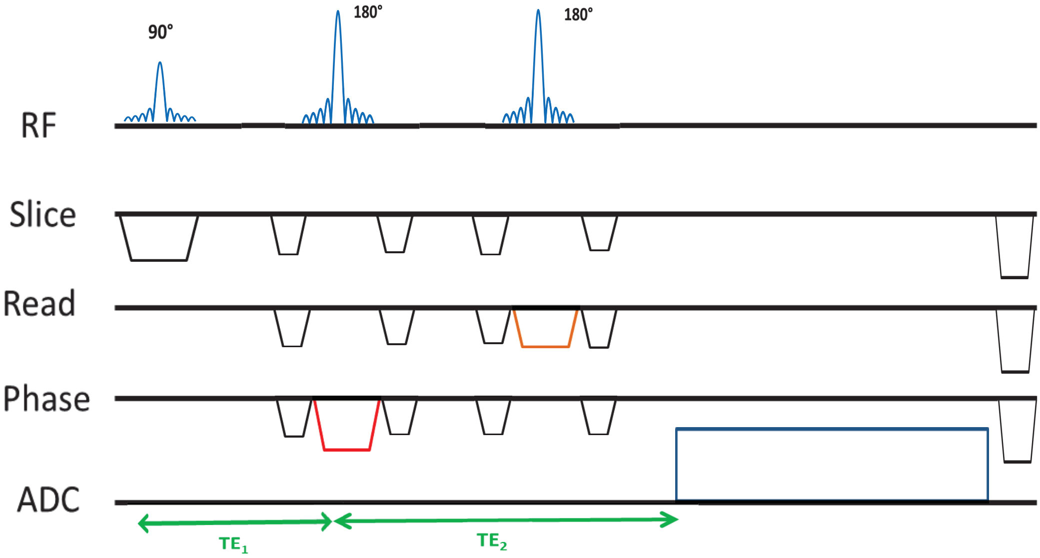

Figure 2.13.: Sequence chronogram of an SVS localization with the PRESS technique.

Stimulated Echo Acquisition Mode (STEAM)

The STEAM module [Fra+87] is the other most commonly used methods for SVS (Figure 2.14). It consists of 3 slice selective excitation pulses. The succession of the 3 excitation pulses generates 5 echoes and 3 FID signals. The first two pulses are delayed by $T_{\mathrm{E}}/2$ and the second and third by a time called mixing time or T_{M}. The stimulated echo appears a $T_{\mathrm{E}} + T_{\mathrm{M}}$ and is the one of interest because it corresponds to the signal in the selected VOI. The application of spoiler gradients during the mixing time allows to eliminate the spin echoes. Due to its robustness, STEAM is very used in clinical practice, and it allows to acces echo times smaller than the ones we could acces with PRESS (about 20 ms). Using excitation pulses instead of refocusing pulses is easier to implement, they have a shorter duration and a better profile.

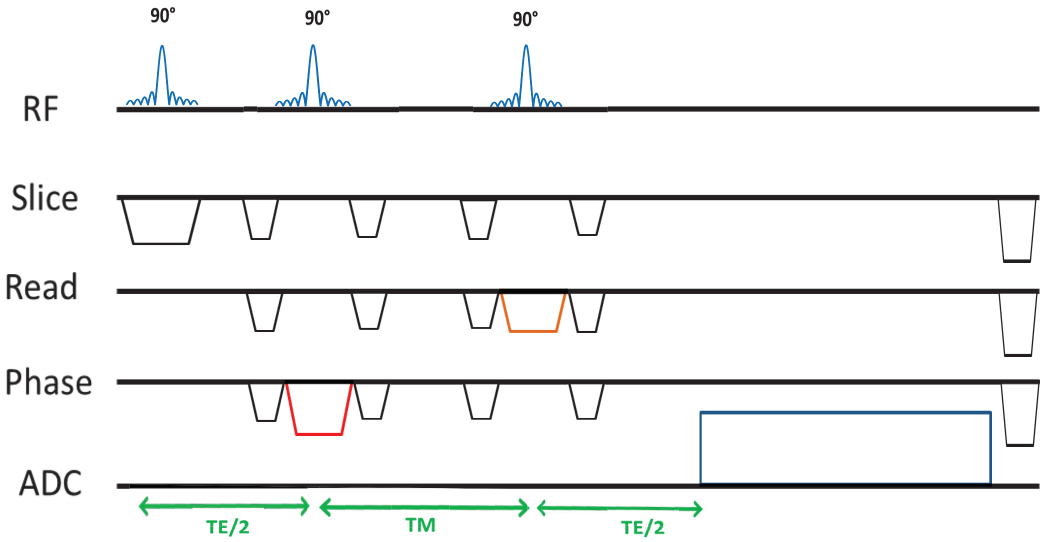

Figure 2.14.: Sequence chronogram of SVS localization with the STEAM technique.

Localized Adiabatic Selective Refocusing (LASER)

The LASER sequence [GD01] is an efficient sequence for SVS in the case of the presence of B_1 field heterogeneities. The use of adiabatic pulses that are insensitive to B_1 field heterogeneities enables to overcome flip angle problems. As already seen, with B_1 field inhomogeneities and conventional pulses, the flip angle may vary from one position to an other. The LASER sequence can be seen as the adiabatic version of the PRESS sequence. It consists in an adiabatic half passage (AHP) excitation pulse of $90°$, followed by three pairs of slice selective refocusing Adiabatic Full Passage (AFP) $180°$ pulses. Each pair is associated with one spatial direction. Gradient spoilers are placed around each AFP pulse to destroy the magnetization outside the VOI. The TE that can be achieved is longer compared to PRESS and STEAM sequences. In the case of the semi-LASER sequence, the VOI is selected with a conventional selective non adiabatic RF pulse in one spatial direction and is followed by 2 pairs of adiabatic refocusing pulses in the 2 other directions. These 2 types of sequences LASER and semi-LASER are robust in front of B_1 inhomogeneities and small errors due to chemical shift artifacts are achieved with these sequences. Nevertheless, the energy deposition is high due to the use of many adiabatic pulses and compared to the PRESS and STEAM sequences, and the minimum echo time achieved by this sequence is longer (about 70 ms).

Chemical shift artifacts and outer volume suppression

Given the application of a magnetic field gradient, the spin frequency becomes dependent on the position r:

$$\omega(r) = \omega_0 + \frac{\gamma}{2\pi} rG \tag{2.36}$$

If Δw is the RF pulse bandwidth, i.e the RF pulse will excite spins within the frequency bandwidth $\omega_0/2\pi \pm \Delta\omega/2\pi$, the corresponding slice thickness is

$$\Delta r = \frac{\Delta w}{\gamma G} \tag{2.37}$$

The chemical shift displacement artifact is due to the fact of exciting different spins populations at different spatial positions and at different resonant frequencies. The chemical shift displacement is given by

$$\Delta x = \frac{\omega - \omega_s}{\Delta w} \Delta r \tag{2.38}$$

where ω corresponds to the carrier frequency and ω_s to the resonating frequency of an other spin population.

The chemical shift displacement artefact is a function of the RF pulse bandwidth, covering the chemical shift of given molecules. To reduce chemical shift displacement artefacts, one can increase the RF pulse bandwidth, by increasing the gradient strength, or reducing the RF pulse duration, which means, for an equivalent flip angle, increasing the RF pulse amplitude. However, the RF pulse amplitude is in practice limited by hardware constraints and the maximum $B_{1\max}$ achievable.
The chemical shift artifact increases with the magnetic field strength. The consequences of this artifact are an error on the voxel composition evaluations, because the voxel may not be where it is supposed to be. Also, it is sensitive to B_0 inhomogeneities. Indeed, B_0 may be homogenized for water signal but not for other

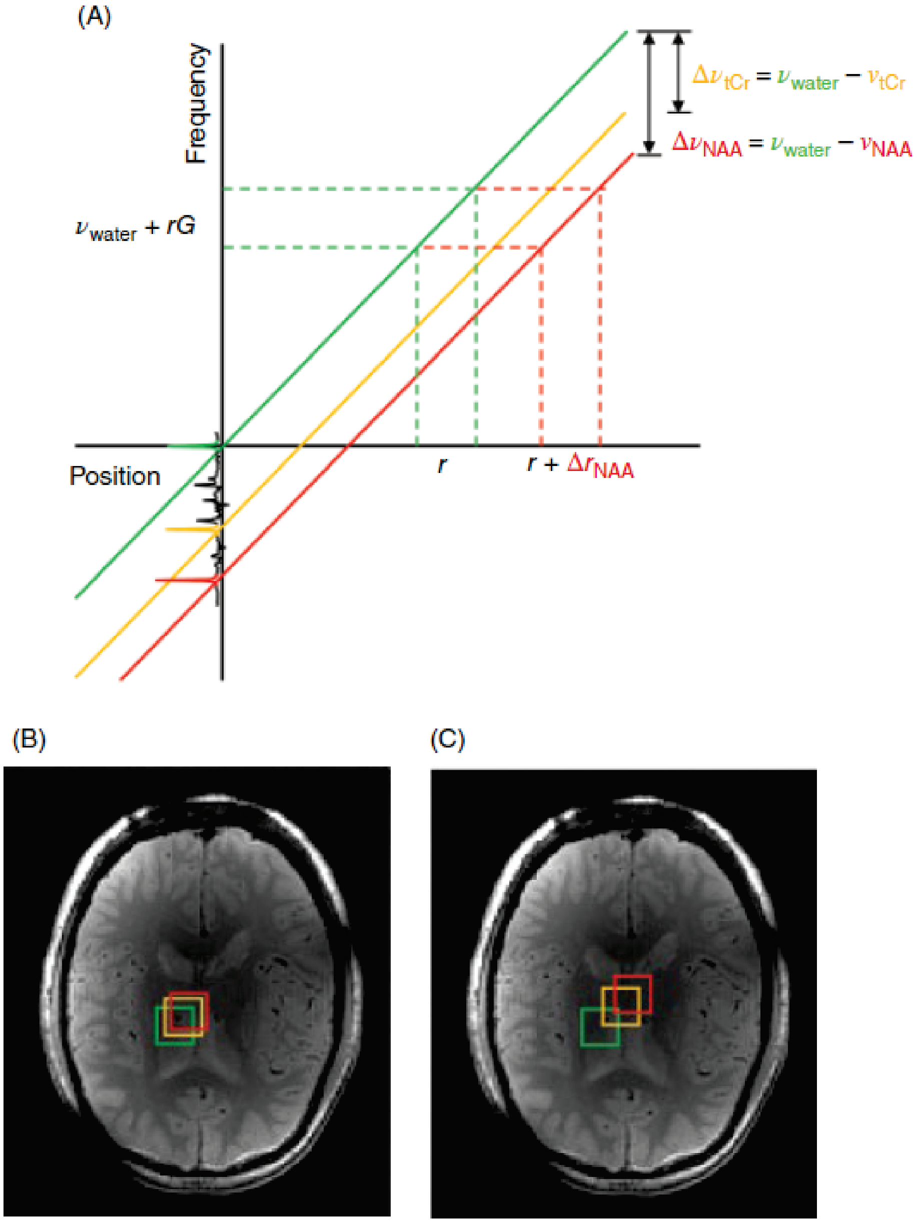

Figure 2.15.: Illustration of the chemical shift displacement artifact [DG19]. The colored boxes correspond to water selected voxel in green, Creatine selected voxel in yellow and NAA selected voxel in red. An RF pulse, centered on water resonance and that has a bandwidth exciting water, Creatine and NAA will create 3 VOIs centered at different spatial positions due to the frequency differences between water and NAA and Creatine. In C, the localization pulse sequence is the same as in B, but the magnetic field strength and thus spectral dispersion increase from 3 T to 7 T. A higher error due to chemical shift displacement can be seen.

resonances such as lipids, which can lead to other resonant frequencies contamination, for example in the brain applications. Indeed, if a voxel is selected in an area, based on water frequency, a contamination from extra cranial lipids may occur as the voxels corresponding the lipids frequencies may be spatially different (Figure 2.15). That is why SVS techniques are often combined with OVS techniques to saturate the signal outside of the wanted VOI in order to avoid any contamination.

To reduce chemical shift artifact when using a selective pulse, a larger pulse bandwidth has to be set. Pulses that have a high Time Bandwidth product (TBP) are to be preferred to reduce the chemical shift artefacts. However, the energy deposition with these types of pulses is high. Other types of pulses called Frequency Offset Corrected Inversion (FOCI) [Ord+96] have been developed in order to achieve high gradient strength with lower RF intensity. Thus, they increase the RF pulse bandwidth through magnetic field gradient modulation.

2.2.11 Magnetic Resonance Spectroscopic Imaging

In MRI and MRSI, we are interested in spatial distribution of metabolites, and their concentration in the case of MRSI, inside the body. The spatial encoding of the NMR signal is key to have a spatial distribution. In the next section, we will thus introduce the notion of k-space.

NMR signal spatial encoding and k-space

The application of a magnetic field gradient linearly varies the magnetic field with the position in space $\overrightarrow{r}$:

$$B(\overrightarrow{r}) = B_0 + \overrightarrow{G}.\overrightarrow{r} \tag{2.39}$$

The corresponding phase acquired at the position $\overrightarrow{r}$ is then

$$\phi(\overrightarrow{r}, t) = \gamma \overrightarrow{r} \int_0^t \overrightarrow{G}(t')dt'. \tag{2.40}$$

In the case of a constant magnetic field gradient along the x direction, we have

$$\phi(\overrightarrow{r}, t) = \gamma \times G \times t \times x. \tag{2.41}$$

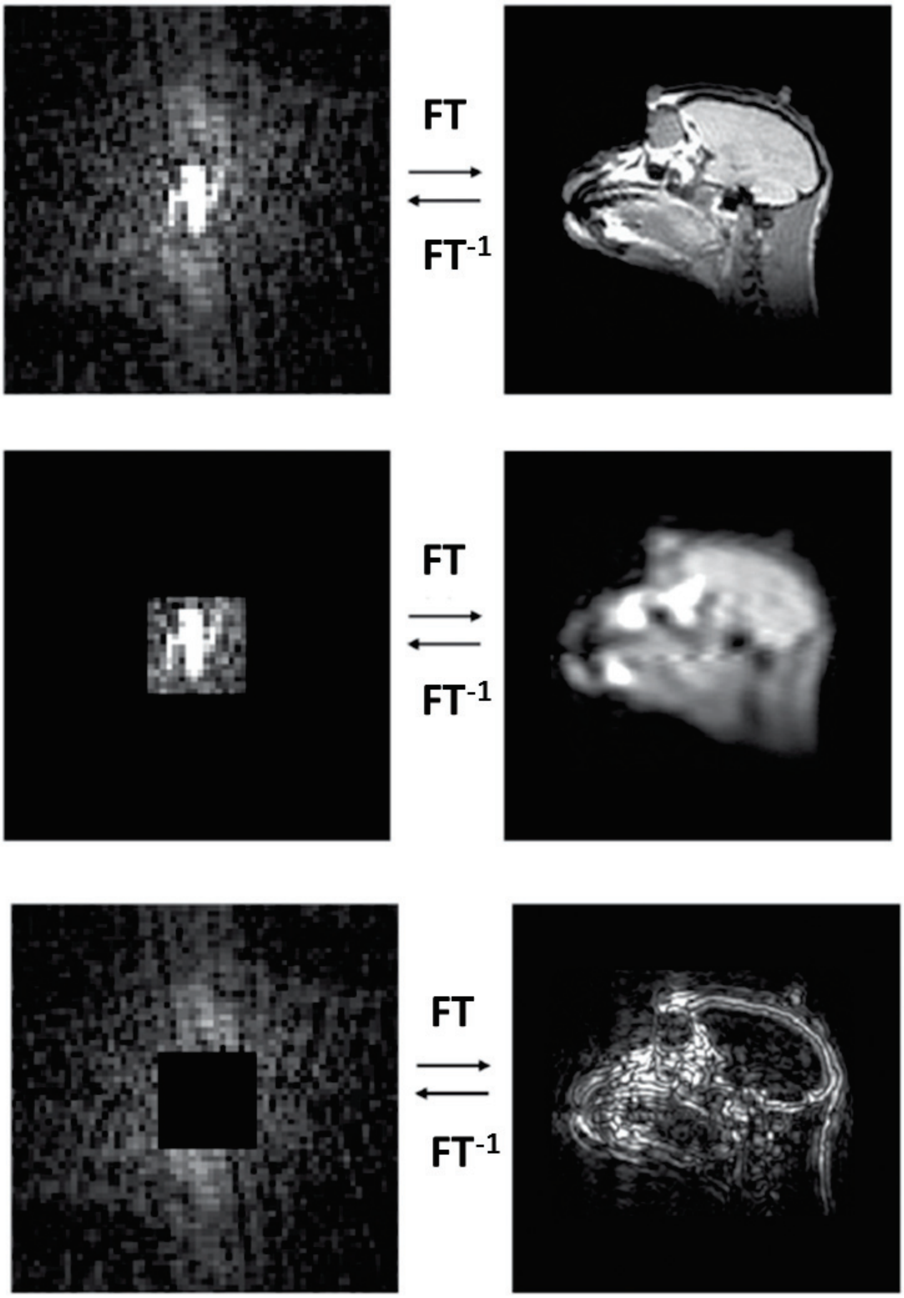

Figure 2.16.: Relationship between the k-space and the image [DG19]. Illustration of the influence of the k-space spatial frequency sampling and the corresponding shoulder image. Sampling only the center of the k-space gives a blurry image and sampling only the edges or higher spatial frequencies gives a detailed image but with low SNR and poor contrast.

In order to introduce the k-space, we can rewrite equation 2.40 as

$$\phi(\overrightarrow{r},t) = 2\pi\frac{\gamma}{2\pi}\overrightarrow{r}\int_0^t \overrightarrow{G}(t')dt' = 2\pi\overrightarrow{r}\overrightarrow{k}(t) \tag{2.42}$$

where $\overrightarrow{k}(t)$ is

$$\overrightarrow{k}(t) = \frac{\gamma}{2\pi}\int_0^t \overrightarrow{G}(t')dt'. \tag{2.43}$$

The unit of $\overrightarrow{k}(t)$ is m^{-1} and defines the k-space. The total signal coming from the whole excited volume can be written as

$$S(\overrightarrow{k}) = \int \rho(\overrightarrow{r}) \exp(2\pi \overrightarrow{r}\overrightarrow{k}) d\overrightarrow{r}. \tag{2.44}$$

Clearly, $S(\overrightarrow{k})$ is the Fourier transform of the spatially distributed magnetization density $\rho(\overrightarrow{r})$. The sampling frequency of the NMR signal follows in most cases the Nyquist-Shannon theorem and is twice bigger than the maximum frequency of the signal. In the k-space domain, we have a band limited spectrum that must contain all the resonant frequencies of the signal in order to avoid folding artefacts. As the signal is sampled and discretized, we do not have a continuous integral in equation 2.44 but sums for each spatial direction. We are operating a Fast Fourier Transform (FFT) in 2D or 3D according to the application.

The edges of the k-space correspond to the high frequencies of the signal, and the center corresponds to the low frequencies. Most of the energy is concentrated in the center of the k-space in practice (see figure 2.16). As we can see in equation 2.43, the trajectory in the k-space depends on the gradients waveforms, their amplitude and duration.

Conventional MRI sequences include the Rapid Imaging with refocused echoes (RARE) [Hen+86] technique, Fast Low Angle shot imaging (FLASH) [Haa+86], echo planar imaging [Man77].

Chemical Shift Imaging

In Chemical Shift Imaging, or CSI also called magnetic resonance spectroscopic imaging (MRSI), we are dealing with a k-t space. It combines a spatial information given by an image and a spectroscopic information given by a spectrum on each voxel. To do this, it is necessary 1) to sample, for each k-space position, sufficiently finely the NMR signal along time to get the spectroscopic information, and 2) use gradients to encode the spatial information through k-space. Some CSI sequences combine the SVS localization techniques with spatial encoding schemes. Generally, CSI sequences use phase encoding steps to preserve the spectroscopic information. In that case, the acquired phase at each phase encoding step is as equation 2.41.

Several types of CSI sequences exists and are listed in a next section.

Point Spread Function (PSF)

The nominal voxel δv size in CSI is given by

$$\delta v = \frac{\mathrm{FOV}}{\mathrm{NE}}, \tag{2.45}$$

where NE is the number of phase encoding increments.
Due to inherent characteristics of the Fourier Transform [Bro+87], the actual nominal voxel size may be different from this theoretical value. Indeed, after Fourier Transform, signal from neighbouring voxels is contaminating the actual voxel of interest, leading to partial volume effects and a decrease of the spatial resolution. The Point Spread Function is a way to see the signal contamination in the image domain due to the sampling scheme performed in the k-space. In conventional MRSI, a double phase encoding method is used to sample the k-t space and the corresponding PSF along one direction is

$$\mathrm{PSF} = \Delta k_x \frac{\sin(\pi NE \Delta k_x x)}{\pi \mathrm{NE} \Delta k_x x} \tag{2.46}$$

where k_x is the position in the k-space, **x** is the position in the image domain. Note that $\mathrm{FOV} = 1/k_x$. The resulting PSF for a regular sampling scheme is a cardinal sinus function (Figure 2.17). The partial volume effects are quite important in that case. The PSF may be improved with apodization methods for example by using a weighted sampling scheme, during the acquisition or after. Apodization functions need to be applied in the frequency domain, k-space, and they also need to be symmetrical compared to the origin (Figure 2.17). A quite efficient and commonly used apodization function is the hamming filter

$$W(k) = \alpha + \beta \cos\left(\frac{\pi k}{k_{\mathrm{max}}}\right) \quad \text{with} - k_{\mathrm{max}} \leq k \leq k_{\mathrm{max}} \tag{2.47}$$

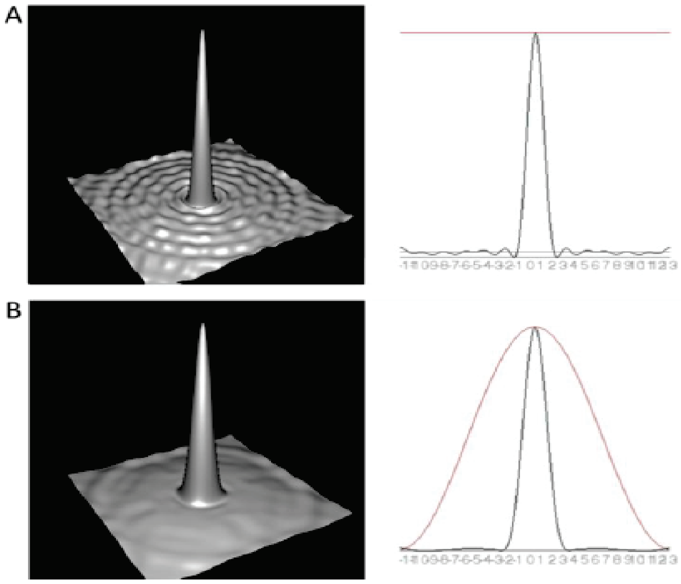

Figure 2.17.: Illustration of a PSF and the effect of an apodization function. On the first row, the corresponding PSF in 3D and 2D is given for a conventional phase encoding sampling scheme. On the second row, we can see the effect of a Hamming filter on the PSF. It has smoothed and significantly reduced the side lobes of the PSF [LK15].

Conventional MRSI sequences

The CSI-FID The CSI-FID sequence (figure 2.18) is the most conventional sequence for MRSI. It consists in the acquisition of one point of the k-space and its whole temporal dimension after one excitation. The sequence scheme contains only one slice selective excitation, directly by the acquisition of the signal. The advantage of this sequence is that it can achieve very short echo times as we acquire the signal directly after the excitation, and has a high SNR. It is useful for applications with metabolites that have a very short T_2 relaxation, for example the detection of collagen in the case of ^{1}H applications, or for the detection of ATP metabolites in ^{31}P applications. However, it results in a very long acquisition time limiting its application in practice.

The CSI-Spin echo This sequence as shown in figure 2.19 has the same sampling strategy as the CSI-FID. The sequence differs by the additional slice selective refocusing pulse placed after the excitation pulse to rephase the spins in the selected slice. This sequence permits to reduce T_2^* effects due to B_0 field heterogeneity and

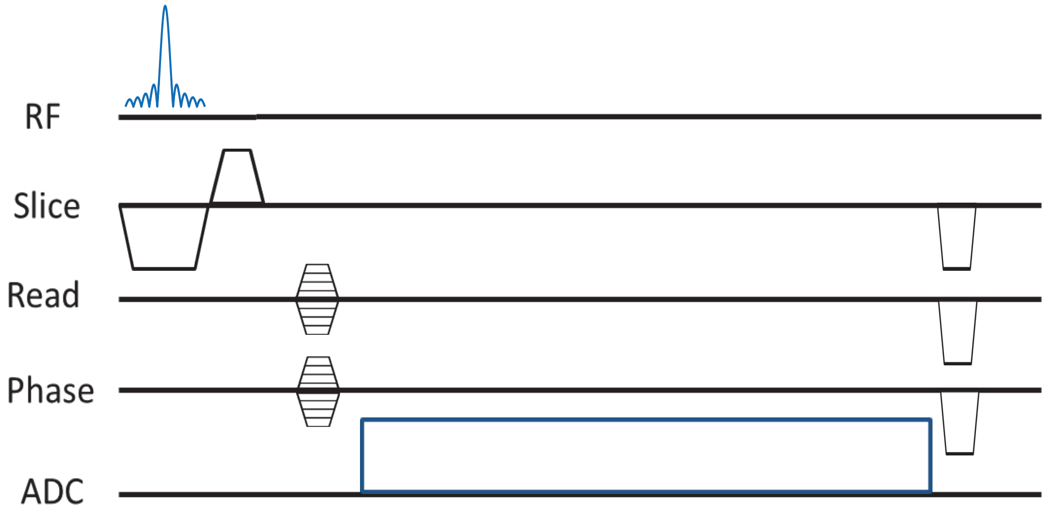

Figure 2.18.: Sequence chronogram of a CSI-FID sequence, based on the phase encoding method for k-space sampling.

magnetic susceptibility, and thus access cleaner signal for different echo times.

The CSI-PRESS This sequence combines the PRESS localization technique with spectroscopic imaging (Figure 2.20). It is a double spin-echo spectroscopic imaging technique containing one slice selective excitation pulse followed by two slice selective refocusing pulses. The VOI selected will be larger than the ones we select in a monovoxel acquisition. Afterwards, the signal is acquired by the same phase encoding method as in the CSI-FID and CSI-SE sequence. Compared to a simple CSI-Spin Echo technique, the CSI-PRESS will have a signal of beter quality (better SNR) inside the selected than outside. The VOI is smaller than the total Field Of View (FOV). It is a sequence of interest for brain applications where the signal is often contaminated by subcutaneous lipids. Thus, it is often combined with Outer Volume Suppression modules to avoid any contamination by outside subcutaneous lipids.

Fast MRSI sequences

In MRSI, the TRs used are usually long, about 1 or 2 s, to reduce T_1 weighting, and to increase SNR. Moreover, sampling only one point of the k-t space after each excitation leads to long acquisition times. For example, for a matrix size of 32×32,

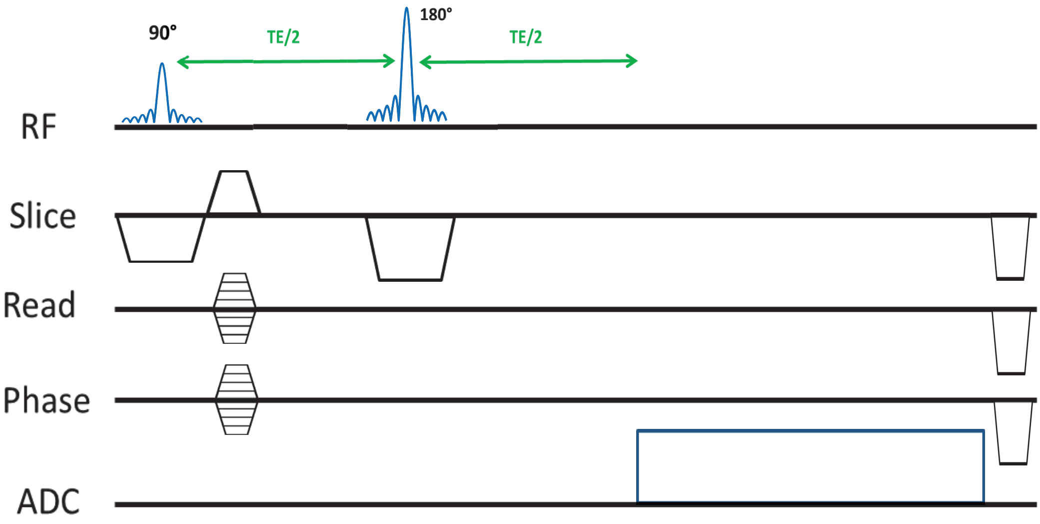

Figure 2.19.: Sequence chronogram of a CSI-SE sequence, based on the phase encoding method for k-space sampling.

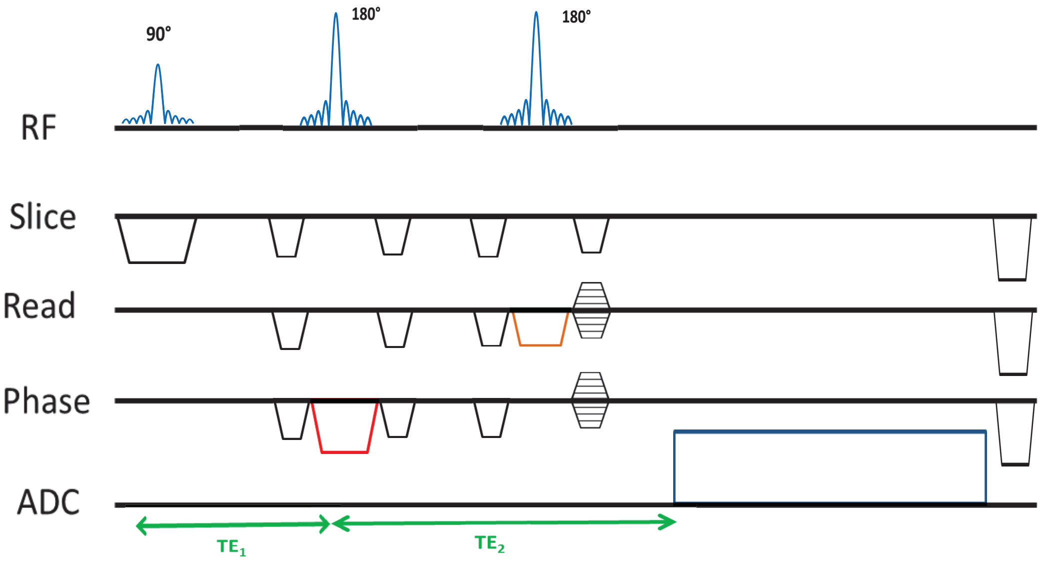

Figure 2.20.: Sequence chronogram of CSI sequence combined with the PRESS technique based on the phase encoding for k-space sampling.

one slice and a TR of 2 s, the acquisition time is about 35 min. In order to reduce the acquisition time, several techniques have been developed and proposed [Poh+97]. The SNR resulting from acquisitions with the phase encoding method is high. Reducing the acquisition time will reduce the SNR and is also generally accompanied by greater complexity in post-acquisition data processing and implementation of the sequence. Magnetic gradients can be pushed to their limit and the signal can be

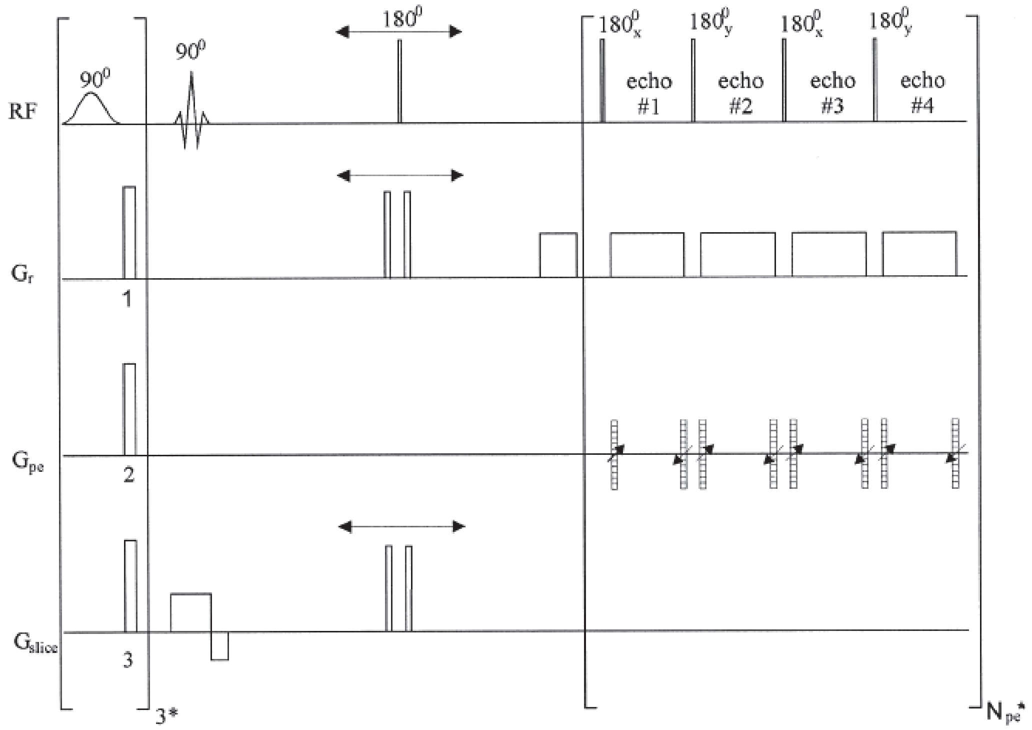

Figure 2.21.: Sequence chronogram of the spectroscopic RARE sequence [DL02].

more complex if we sample the spectral and spatial dimension at the same time.

Many fast MRSI sequences are based on fast MRI sequences.

The spectroscopic Rapid Acquisition with Refocused Echo (RARE) [DL02] is based on the RARE technique used in MRI and consists in refocusing pulses surrounded by phase encoding gradients. The number of refocusing pulses is a multiple of 4 and allows a phase cycling in 4 steps. The RARE module (Figure 2.21) is placed after a slice selective excitation pulse and a slice selective refocusing pulse. The k-space is encoded one line after an other and after each excitation, delaying the application of the RARE module allows to encode the spectroscopic information. This is a robust technique that is comparable with conventional phase encoding methods but energy deposition remains elevated.

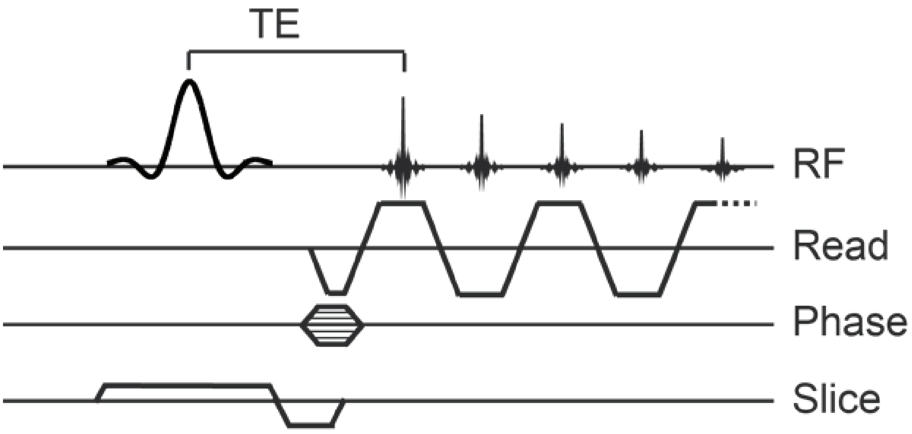

Figure 2.22.: Sequence chronogram of the EPSI sequence [Wei12].

The Echo Planar Spectroscopic Imaging (EPSI) EPSI [Pos+13] which chronogram sequence is shown on figure 2.22 is a sequence based on Echo Planar Imaging used in MRI. It is a technique that simultaneously encodes the spatial and spectral information. Readout trapezoidal gradients vary from negative values to positive values. After each excitation, one spatial dimension and one spectral dimension are acquired. This technique considerably reduces the acquisition time compared to conventional methods but the reconstruction process is more complex. The performance of the gradient system is important as well for this technique as they have to rapidly change from a negative value to a positive value and etc. For example, for a matrix size of 32×32, one slice and a TR of 2 s, the minimum acquisition time would be 64 s.

Multi echo sequences Multi echo sequences such as Turbo spin echo or Multi gradient echo can be a way to reduce the acquisition time and access the spectroscopic information as well (Figure 2.23) [DM93]. To do that, it is necessary to use a short echo delay time, short enough to reconstruct the spectroscopic information of interest. One line of the k-space and one spectral dimension would be acquired after the excitation which reduces the acquisition time considerably. However, the echo delay time is limited because of the time needed to form the echo, either by a spin echo with a slice selective refocusing pulse or a gradient echo.

Reducing the spatial sampling of the k-space Reducing the spatial sampling of the k-space [Mau+94; PT94] leads to fewer acquisitions to sample the whole k-t space and thus reduce the total acquisition time. Indeed, the main information is concentrated in the center of the k-space, corresponding to the low frequencies.

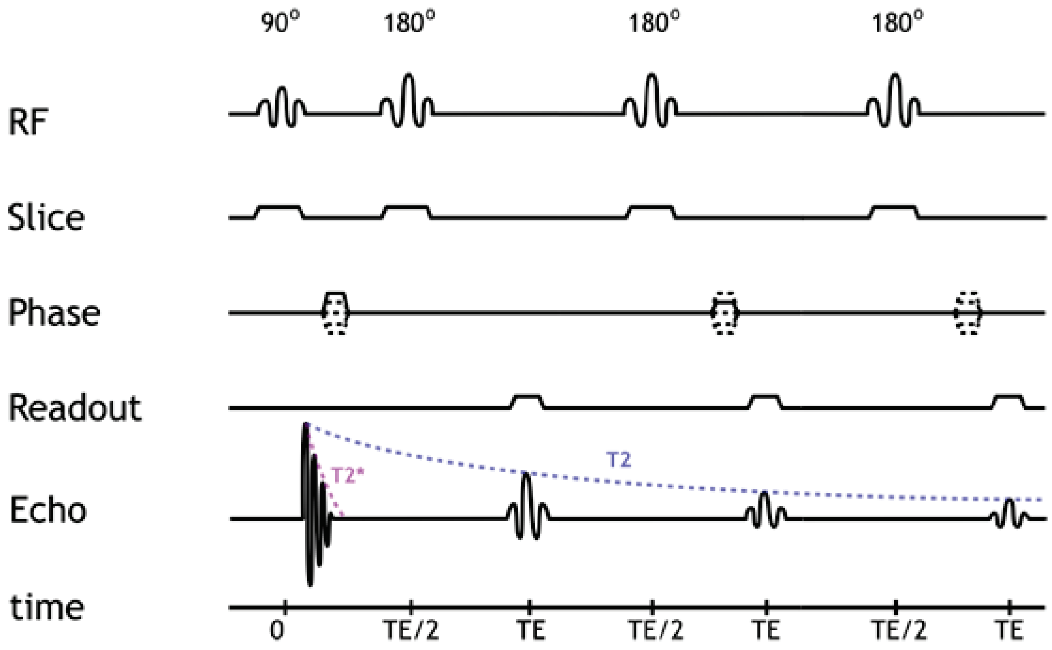

Figure 2.23.: Sequence chronogram of a Turbo spin echo sequence with 3 echoes [Ham].

Sampling only 50 % of the k-space in the center reduces the acquisition time by 2 [Mau+94]. The use of compressed sensing can also be of interest to reconstruct the k-space with a random sampling and few samples [Lus+08].

Non-cartesian k-space sampling Non-cartesian k-space sampling can be used to sample the k-space, not line by line as reached in the cartesian sampling by the application of trapezoidal gradients, but with non-cartesian trajectories such as spirals, radial or circle lines [Chi+18]. This sampling technique also allows us to sample simultaneously the spatial and spectral dimensions. These types of trajectories are realized by applying time varying gradients during signal acquisition. Data reconstruction of the spatial dimension has to be done with non-cartesian reconstruction techniques such as Gridding or Non-uniform Fast Fourier Transform (NUFFT) [Sar+01; FS03]. Because of technical constraints, it is not possible to sample the whole k-t space after one excitation, it is necessary to interleave spatially and temporally the acquisition to sample the whole spatio-temporal domain. We will detail this in chapter 3 in the particular case of spiral trajectories. The minimum acquisition time that can be accessed is smaller than other fast techniques such as EPSI or spectroscopic RARE but highly depends on the gradient system and the nucleus we are studying. The shorter the γ constant is, the longer the acquisition time will be, which can be a limitation for example in $^{31}\mathrm{P}$ or $^{11}\mathrm{Na}$ applications.

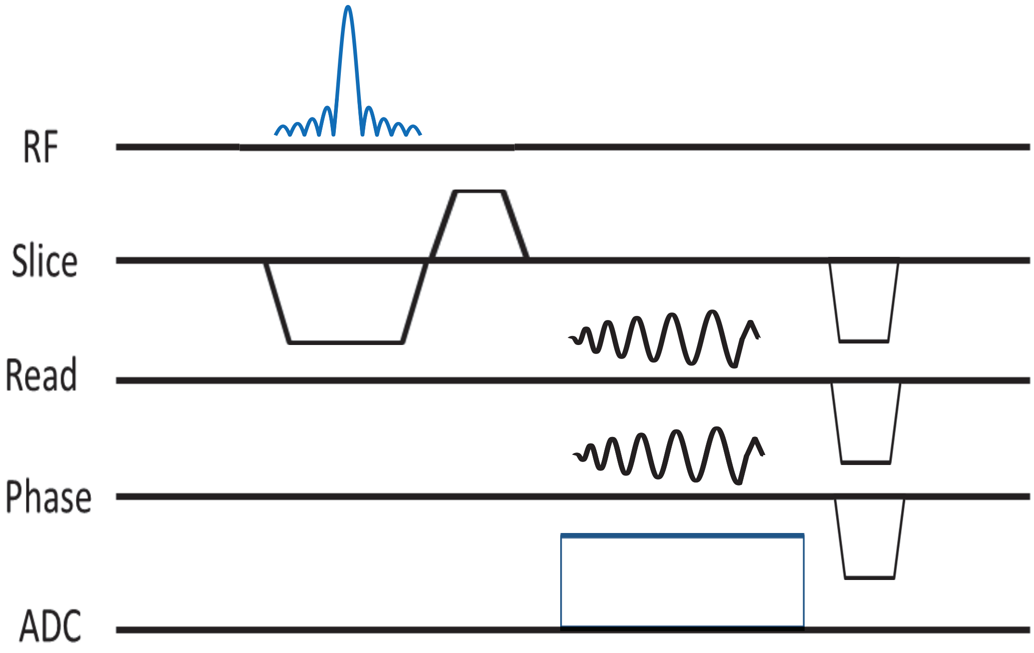

Figure 2.24.: Sequence chronogram of a spiral MRI sequence, based on a spiral k-space sampling. Short echo times can be accessed with this type of sequence.

Spiral spectroscopic imaging Spiral spectroscopic imaging is also an MRSI sequence based on an MRI sequence with a spiral k-space sampling. In MRI, k-space trajectories can be performed with sinusoidal gradients waveforms with a rising amplitude in the readout and phase directions played during the acquisition window, or while the Analog-to-Digital-Converter is played out. Traditional spiral MRI is composed of one excitation pulse followed by oscillating gradients waves in x and y directions during the acquisition as shown in figure 2.24 and is the basic building block for spiral MRSI. Spiral k-space detection can be used with a spin echo excitation, and can also be combined with modules placed before the excitation, such as OVS or water saturation, or other modules to encode diffusion for example. As we see in figure 2.24, one k-space is sampled at a specific time after the excitation. The length of the spiral can be reduced by using spatial interleaves, which implies acquiring multiple time the FID signal with different partitions of the k-space at each repetition time T_R (see figure 2.25).

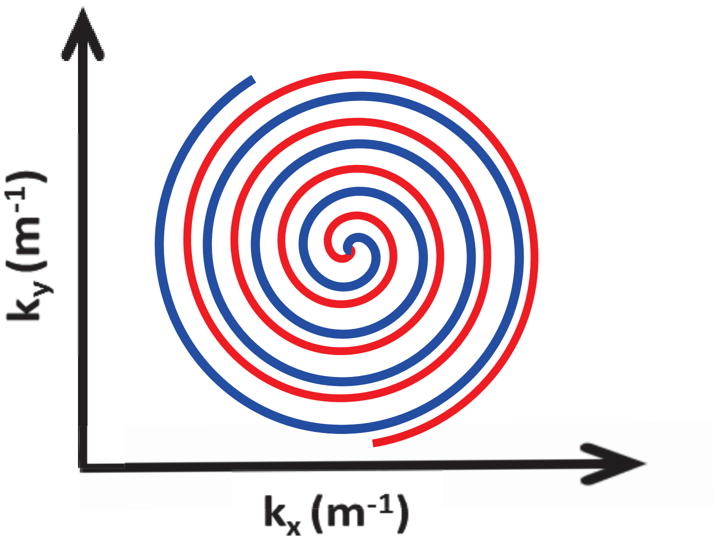

Figure 2.25.: Illustration of spatial interleaves for spiral MRI and MRSI for 2 spatial interleaves. One excitation is needed per spatial interleave.

In spiral spectroscopic imaging, we want to sample the evolution of k-spaces over time as shown in figure 2.26, an evolution which is modulated by the spectroscopic information. The FID signal is thus sampled with a train of spirals rather than one unique spiral and a spectroscopic information can be assessed after Fourier transform of the acquired signal. The time points - at the time a spiral is acquired - fixes the spectral bandwidth. As the spiral duration can be longer than the desired sampling time (or correspondingly the desired spectral bandwidth), temporal interleaves (see figure 2.27) are often needed (which means acquiring several spiral trains, each of them being delayed according to a time delay proportional to the wanted FID sampling time T_{res}). This approach will be more detailed in chapter 3 and 4.

All these techniques can also be combined, if possible, with parallel imaging techniques such as Sensitivity Encoding (SENSE) [Pru+99] or GeneRalized Autocalibrating Partial Parallel Acquisition (GRAPPA) [Gri+02] to reduce even more the acquisition time. However, these approaches make the reconstruction process even more complex.

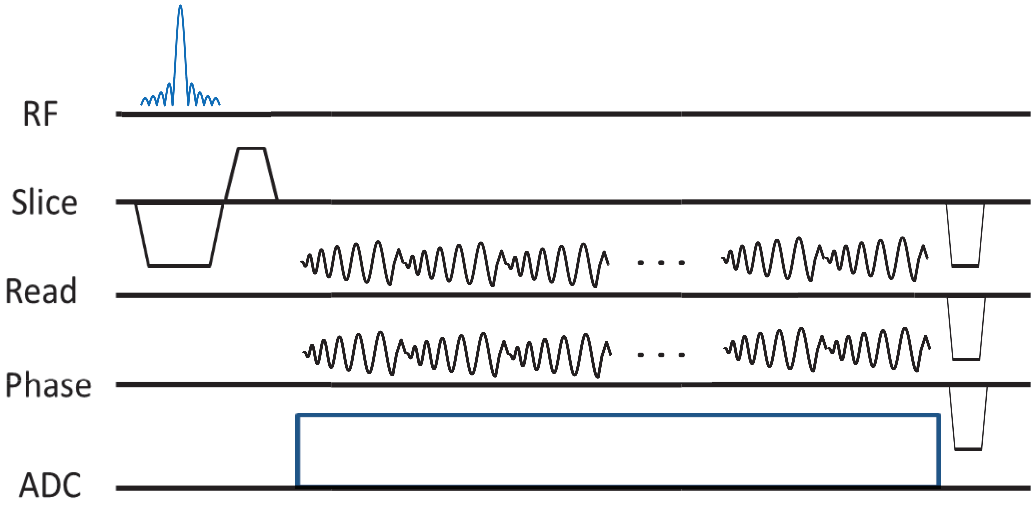

Figure 2.26.: Sequence chronogram of a CSI-spiral sequence, based on a spiral k-space sampling. Short echo times can be accessed with this type of sequence. It can also be combined with the PRESS technique, water suppression or OVS.

Clinical applications of MRSI

MRSI has various applications in the clinical environment in the brain, liver, muscle. Its advantage compared to other imaging techniques is that it is non-invasive and allows to study the metabolism of tissues inside the body, with spatially distributed information. It has interesting application in cancer, epilepsy, multiple sclerosis, schizophrenia and muscle metabolism assessment. In practice, single voxel spectroscopy is more commonly used than spectroscopic imaging because it is faster, easier to process. In spectroscopic imaging, the B_0 field homogenization, or shim, is of great importance for clean NMR signals.

The most used SVS sequences are PRESS and STEAM, which are made available by most of the MR system constructors. A SVS-STEAM is particularly useful to reach small echo times. An SVS based on LASER technique is also sometimes used to overcome B_1 heterogeneities.

In spectroscopic imaging, used sequences in the clinical environment are mainly based on the phase encoding method, with the CSI-FID sequence, or CSI-SE sequence. The Echo Planar Spectroscopic Imaging (EPSI) technique tends to be more and more used but it is still not common at all as it is not provided, by default, by the constructors.

In the muscle, several applications have been made on proton spectroscopy for fat-water quantification, or metabolite quantification such as creatine, lipids and

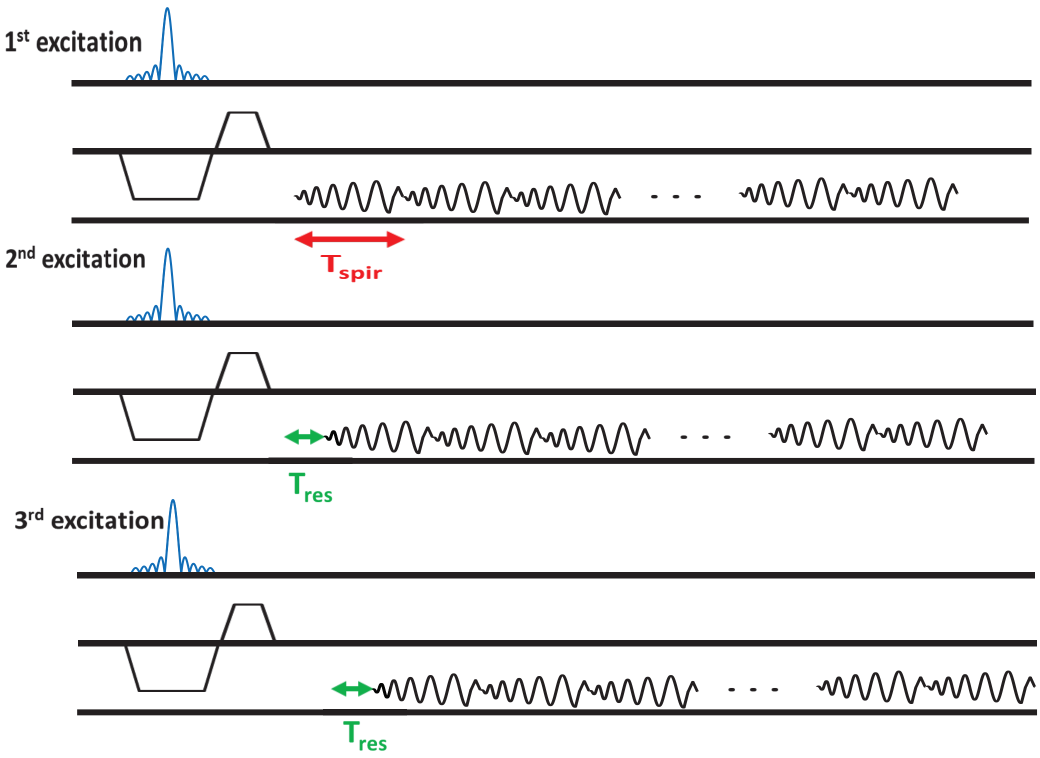

Figure 2.27.: Illustration of termporal interleaves for spiral MRSI in the case of 3 temporal interleaves. The spiral length T_{spir} is too long compared too the wanted spectral bandwidth. It is therefore nedded to do more acquisitions and excitations. After each excitation a delay is applied, proportionnaly to FID time sampling T_{res}.

Trimethylamonium (TMA) [Chi+18; Han+18; Bog+12]. Other interesting work include the assessment of intra and extra myocellular lipids [Ver+04; Boe+97; Ver+12]. These works are mainly based on conventional sequences such as CSI-FID or SVS, but some work has been done on spiral spectroscopic imaging as well [Ma+17; Cha+15; Ada+98]. In order to study the energetic metabolism, many studies have been done on phosphorus spectroscopy, during an exercise or not, to follow the energetic metabolism response after an exercise or an intense effort for example [Val+17; Nie+18; Ma+17; Fie+15]. These types of studies are in majority done with a classic FID non localized sequence. Some work is done as well on phosphorus imaging [Par+13c; Par+13a; Par+13b]. More recently, studies involving spiral spectroscopic imaging showed that it was possible to do spiral ^{31}P CSI during an exercise [SD+19; Val+16; Ma+17].

2.3 Signal processing and under-sampling

2.3.1 Compressed sensing theory

The Nyquist-Shannon theory stipulates that the sampling of a signal is imposed by its spectral bandwidth [Sha34]. This theory is a base for signal acquisitions protocol and analog/digital converters. As a reminder, the Nyquist-Shannon theorem is:

Theorem: Given a signal with a spectral content that has a maximum frequency $f_{\max}$, the sampling frequency f_e must be at least twice this maximum frequency in the signal in order to reconstruct properly, without folding, the signal after applying a low-pass filter:

$$f_e = 2 \times f_{\max} \tag{2.48}$$

The compressed sensing theory appeared recently and enables to lower down the sampling frequency f_e [Can+06; Don06a]. Indeed, Nyquist-Shannon theory enables to reconstruct the every signal, but it is not a necessary condition when the signal is sparse in a given domain. Compressed sensing allows the reconstruction of under-sampled signals with a sampling frequency lower than the sampling frequency given by the Nyquist-Shannon theorem when the signal is sparse in an appropriate basis.

Sampling with CS theory allows transforming acquired analog data into their compressed numeric representations. This enables to get reconstructed signal from fewer measurements than the measurements imposed by the Nyquist-Shannon Theorem. The two fundamental principles of CS are sparsity and incoherence of the measurement compared to the base where the signal will be reconstructed.

Sparsity means that the signal has finite number of non-zeros. In practice, in a temporal signal, it expresses that the useful information of its spectrum does not cover the whole spectral bandwidth. Note that in this work, we will consider ^{31}P MRS spectra as sparse in the spectral domain.

In this section, we will detail the mathematical principles of CS and some applications.

2.3.2 Under-sampled data acquisitions and reconstruction

The mechanism of data acquisition is classically defined as

$$\mathbf{y} = A\mathbf{x} \tag{2.49}$$

with $\mathbf{y}$ the measured vector of size m, $\mathbf{x}$ the desired signal we want to acquire of size n and A the matrix of size $m \times n$ which is the encoding matrix to go from $\mathbf{x}$ to $\mathbf{y}$.

With the CS theory, we are in the case where $m < n$, the number of measurements are lower that the dimension of the signal $\mathbf{x}$. We have an inverse problem to solve with under-determined matrix system. Finding the exact solution $\mathbf{x}$ from the measurement $\mathbf{y}$ is not possible, but if $\mathbf{x}$ is sparse it becomes possible to reconstruct the signal.

There are 3 main optimization problems used in the case of CS to reconstruct the signal. The first one uses a least square optimization under the constraint of equation (2.49) (defined as $|||x||_{l_0} := |i, x_i \neq 0|)$. The second uses the l_0 (defined as $|||x||_{l_0} := |i, x_i \neq 0|)$ norm under the constraint of equation (2.49). In that case, the most sparse solution will be chosen. Sparsity of the signals is not always the case, but it can be assumed that it is sparse in some other space, which is the case for signals in practice. If we note Φ the base of the domain where the signal $\mathbf{x}$ may not be sparse and Ψ the base of the domain where $\mathbf{x}$ may be sparse, we have

$$A = R\Phi\Psi \tag{2.50}$$

where R is the new matrix of size $m \times n$ in the new base. The complexity of the problem with a l_0 norm is high and grows exponentially with N.

The third optimization problem uses the l_1 under the constraint of equation (2.49) (defined as $|||x||_{l_1} := \sum_{i=1}^{n} |x_i|)$. It has been demonstrated by Candès and Tao that it is the optimization problem that finds the most sparse solution, under restricted conditions.

To evaluate the robustness of CS reconstruction algorithms, a property called Restricted Isometric Property (RIP) is used [CT04; CT05; Can08]. This property enables to see if the reconstruction algorithm, generally based on the matrix A is efficient to reconstruct the signal from fewer measurements or not. The unicity of a solution may not be the case, but the existence of a solution is key for a robust and efficient reconstruction algorithm.

l_2, l_1, l_0 minimization

In order to avoid the solving of a NP-hard problem with the use of the l_0 for signal reconstruction, the idea is to use the l_1 norm instead, which actually give the same solution in most cases [Don06b]. Minimizations from l_1 and l_2 norms give very different results. The l_2 norm has been proven not to be efficient in most cases. The l_1 is the best trade off between the hard complexity of a minimization by a l_0 norm and the inefficiency of a reconstruction with a l_2 norm.

Compressed sensing reconstruction algorithms include for example Orthogonal Matching Pursuit (OMP), Least Absolute Shrinkage and Selection Operator (LASSO), total-variation, Iterated thresholding for example [Boy+14; Wan+12; BD09; Kra+17]. Most of them are iterative and are looking for the sparse support where the signal may be reconstructed given a smaller number of measurements. For example, the OMP algorithm is an iterative algorithm based on the l_2 norm. It will iterate until the support is found and then perform a final l_2 minimization to reconstruct the signal. The LASSO method relies on a l_2 minimization with a l_1 regularization. Regularizing with l_1 favours the sparsity.

2.3.3 Applications of CS

Compressed Sensing has various applications in Magnetic Resonance Imaging, single pixel camera [Dua+08a], digital holography [Riv+10; Mar+11], radar imaging [HS09] or schlieren deflectometry [Sud+13; Sud+15].

Single pixel camera is an image acquisition based on a single photodiode. The observed object is focused through a lens on a digital micro-mirror (DMD). This will reflect the image through the photodiode. The DMD device consists in an array of small mirrors which orientation can be switched in order to reflect the light from the object or not. It receives a small portion of the object and then reflects it. Switching on and off every mirror that take a small fraction of the object enable finally to reconstruct the total image. The acquisition time is related to the number of samples

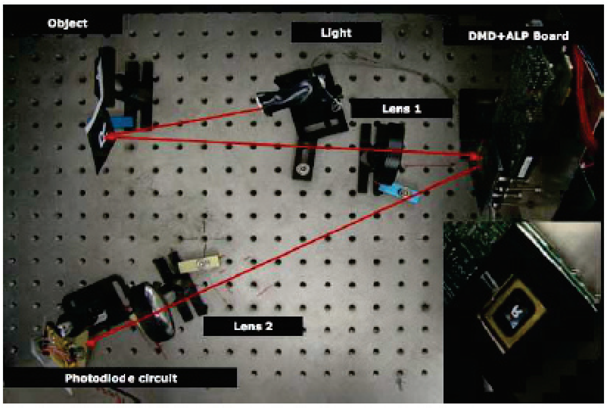

Figure 2.28.: Illustration of the single pixel camera proposed by (Takhar, Duarte)

of the image we need to reconstruct the full image. Lowering down the number of measurement samples enables to use CS and it has been demonstrated that the number of measurements can be significantly reduced and still be able to accurately reconstruct the signal [Dua+08a].

Radar imaging is a technology that creates 2 dimensional images from radio waves emission and reception by the radar. The radar emits radio waves which are then reflected and received back by the radar. Radar images are compressible using parametric models of physical scattering. It can be compressed as well using transform coding.

CS in MRI [Lus+08] enables to considerably reduce the scan acquisition time. It consists, in most cases, to randomly under-sample the k-space. Under-sampling the k-space leads to less excitation needed and thus a gain in terms of acquisition time [Blo+07]. It has also other applications in dynamic MRI [Gam+08; Lin+11], parallel imaging [Kno+12; Jin+16] and functional MRI [Zah+12]. It can be combined with data learning as it is done in [RB10].

Most of the under-sampling is done randomly but can be done as well with *a priori* known knowledge. For example, we know that most of the energy is concentrated in the center of the k-space. Other under-sampling have been developed based on *a priori* knowledge of the spatial support [Lia+12].

CS is nowadays mainly used for imaging but can also be used for spectroscopic imaging.

Applications of compressed sensing for non-proton MRSI are not numerous. It is mainly applied by under-sampling the spatial dimension on sodium MRSI [Mag+15], phosphorus MRSI [SD+19; Hat+17; Ask+12], and on fluorine MRSI [Kam+10]. Under-sampling the temporal dimension as well can be done to reduce the acquisition time, and this has been indeed performed on hyperpolarized $^{1}3C$ studies [Lus+06; Lar+11].

Other techniques have been developed based on a *a priori* information knowledge of the spatial support in [GR00],- leading to an irregular under-sampling and a least-square estimation, but which cannot be classified as a compressed sensing method (as it is not a random under-sampling) -, or on a *a priori* information knowledge of the frequency resonances as in [Wie+12]. In [Wie+12], only images at specific frequency resonances are reconstructed, with a least reconstruction as well, and with a strong *a priori* knowledge of the frequency peak resonances. The technique that is used is called iterative decomposition of water and fat with echo asymmetric and least-squares estimation (IDEAL) spiral CSI and has been applied on hyperpolarized ^{13}C pyruvate.

In [GR00], the choice of the samples to acquire in the k-space is done, given a limited known spatial support, with an algorithm called Sequential Backwards Selection (SBS). The acquisition sequence relies on a k-space acquisition with two phase encoding gradients. The selection of k-space samples is therefore not random, but still leads to an irregular sample acquisition. The image reconstruction is done with a least-square estimation, and the choice of the samples via the SBS algorithm enables to minimise the noise magnification due to the least square reconstruction. The SBS algorithm and a new fast MRSI strategy are proposed in chapter 4.

The work in this thesis aims to accelerate magnetic resonance spectroscopic imaging for application on phosphorus on the skeletal muscle. The proposed method, which will be detailed in the next chapters, is based on a temporal under-sampling of the FID signal given an a priori known spectrum support, and on spiral k-space sampling.

3

Time undersampled acquisition for multidimensional sparse signals with application to magnetic resonance spectroscopic imaging

Summary

3.1 Introduction

Methodological developments were done in this thesis on Magnetic Resonance Spectroscopic Imaging (MRSI) in order to accelerate acquisitions. The method is based on signal processing, irregular under-sampling, an *a priori* known spectrum support, a least square signal reconstruction and an algorithm called Sequential Backwards Selection (SBS) introduced by Stanley J. Reeves in 1995 [RH95a]. Previous work has been done using this algorithm and a least square reconstruction in the laboratory CREATIS in [Mer+14] for 2D NMR spectroscopy with an *a priori* known support. During this thesis, the goal was to extend this method to MRSI using a spiral k-space sampling. A multidimensional acquisition method has thus been developed for sparse signals which we detail in the following article submitted to the journal "IEEE Transactions on Signal Processing": Time undersampled acquisition for multidimensional sparse signals with application to magnetic resonance spectroscopic imaging.

3.2 Article Manuscript

3.2.1 Abstract

This paper deals with acceleration of multidimensional signal acquisition. The signal is assumed to have multiple discrete spatial dimensions where each point is time varying. The one-dimensional Fourier transform of the time evolution of each point is assumed to have an *a priori* known bounded support. The Fourier transform of the spatial domain is divided into several partitions, each of which can be sequentially acquired over time. We propose a method for undersampling the time dimension that enables interleaving of the samples to speed up signal acquisition. This method is applied to realistic simulated magnetic resonance spectroscopic imaging data, which leads to a reduction in the acquisition time by a factor of three.

3.2.2 Introduction

Compressed Sensing (CS) [Can+06; Don06a] introduced a new way to sample, with a lowered sampling rate compared to the Nyquist-Shannon criterion. The signal to be sampled has to be sparse in a given space so that CS can be applied. CS has already been used for several applications in medical imaging [Lus+08], digital imaging [Dua+08b] and radar imaging [HS09]. It is based on the three main tasks of are sparse representation, measurement encoding, and sparse signal reconstruction [CW08].

Given a known sparse spectrum support, it is possible to accelerate and simplify the reconstruction process. In [GR00; Mer+14] the l_2 norm was used to reconstruct the signal with a known sparse spectrum support using the least square (LS) overdetermined solution. Compared with the orthogonal matching pursuit algorithm (OMP)[Wan+12], the LS solution corresponds to the last step of this algorithm when all of the samples of the support are found [TG07]. Note that these methods fall into the group of single measurement vector (SMV) methods. In a noisy scenario, the reconstruction error depends on the choice of the acquired time samples. The use of the sequential backwards selection (SBS) algorithm [GR00] enables selection of the samples to acquire to minimize the noise magnification due to the LS signal reconstruction. In addition, the irregular sampling favors the invertibility of the matrix of the system. SBS has been proposed previously to accelerate signal acquisition [GR00]. This was used in a case where the acquisition time was directly related to the sampling rate. For a time-domain signal sampled with N samples and period T_s ending at time NT_s, irregular sampling with $P < N$ samples (selected using SBS) also ends at time NT_s and no acquisition time is saved. However as soon as the N samples need to be acquired in several scans, the duration of the acquisition can be reduced using SBS, which is the goal of this paper.

In the present study, we tackle the problem of the design of a fast sampling strategy for multidimensional signal acquisition, with its application to simulated magnetic resonance spectroscopic imaging (MRSI) data [GR00]. Here we use the SBS algorithm in a different way, and we push further the method to design a new sampling strategy. The first results from this study were presented at the [Kar+17].

Magnetic resonance spectroscopic imaging signals consist of several spatially distributed one-dimensional spectra. As for magnetic resonance imaging, the acquisition is performed in a spatial two-dimensional spectrum domain called the k-space, for which (k_x,k_y) represents the wave numbers in each dimension. In MRSI, this k-space evolves in time according to an oscillatory function with an exponential decay. The oscillation frequencies are characteristic of the molecular content under analysis. A two-dimensional Fourier transform of the k-space is then necessary to spatially localize the biochemical information, and a one-dimensional Fourier transform along the time direction is needed to obtain the magnetic resonance spectra. The time domain and the k-space domain are separable. At each (k_x,k_y) point, the associated spectrum is band limited. In *in vivo* magnetic resonance spectroscopy, *a priori* known molecular resonance frequencies in living tissues [Gov+00; DG19] and the expected 'full width at half maximum' of the resonating peaks are usually used as the starting values and the prior knowledge for magnetic resonance signal quantification [Rat+05]; here, these are used to define *a priori* this limited band; *i.e*, the spectrum support.

In this study we deal with a spatio-temporal signal model $y(U, n)$, where U is a multidimensional space and n is the number of discrete time dimension points. For MRSI, U is the k-space; and it can be divided into several partitions. Due to physical constraints, it is not possible to scan the whole joint spatio-temporal signal all at once. Indeed, at each scan, the data points are sequentially acquired. Given that the signal is transient, several scans are required to obtain the full U over time. As a result, the full and dense sampling of this signal is time consuming. This approach is similar to multiple measurement vectors (MMV) [Cot+05; CH06] methods, which represent an extension of the single measurement vector methods, with the difference that the acquisitions are sequential and the spectral support is known.

Several fast k-space scanning or CS methods have been proposed [Pos+13; DG19]. The undersampling of the temporal dimension is rarely used and only in a CS scenario [Hu+08]. In the special case of sparse spectra, we show in the present study that subsampling the temporal dimension allows us to interleave the acquisitions of partitions of U of the signal $y(U, n)$ and to decrease the number of scans, and thus to speed up the acquisition of the signal. We propose an algorithm that specifies the signal acquisition scheme.
This paper is organized as follows. In section 3.2.3 we propose the signal acquisition strategy based on SBS. Here, we present the SBS algorithm and derive two essential theorems that lead to the proposed acquisition algorithm. The MRSI application is presented in section 3.2.4, which is followed by a discussion in section 3.2.5 and the conclusions.

3.2.3 SBS-based acquisition strategy for a multidimensional signal

3.2.3.1. Spectrum estimation from subsampled signals

Given an N-samples time-domain signal y, the associated spectrum x is assumed to have a known M-samples sparse support S. The sampling period is T_s, and consequently, the discrete time is $t = nT_s$, $n = 0 \dots N-1$. The discrete frequency is $f = k/NT_s$, with $k = 0 \dots N-1$. The time signal y is related to its spectrum x by

$$y = F^{-1}x, \tag{3.1}$$

where F is the unitary discrete Fourier matrix of size $N \times N$,with $F_{n,k} = \exp(-i2\pi nk/N)/\sqrt{N}$. The objective is to find the M nonzero values of the spectrum x from the P-samples signal y_p, obtained by irregular subsampling the signal y, with $P < N$. Let x_m be the restriction of x to its M nonzero values (its support S), then Equation (3.1) becomes

$$y_p = Ax_m, \tag{3.2}$$

where A is a $P \times M$ matrix that is obtained by selecting from F^{-1} the rows that correspond to the P acquired elements from y and the columns that correspond to the M elements of x in S.

To solve Equation (3.2), more time samples are required than spectrum samples; *i.e*, $M \leq P$. If $M < P$, the matrix system is overdetermined. If A^*A is invertible, then the spectrum can be evaluated from y_p by the LS estimate of x_m,

$$x_m = (A^*A)^{-1}A^*y_p, \tag{3.3}$$

where * denotes the conjugate and the transpose. Note that if N is a prime, A is full rank, from Lemma 1.3 of [Tao05], and the recovery of x_m is exact. When the data are noisy with the hypothesis of a Gaussian zero mean noise identically distributed with variance σ^2, this results in an error with the mean square error given by,

$$E||x - x_m||^2 = \sigma^2 tr[(A^*A)^{-1}]. \tag{3.4}$$

As F is unitary the lowest error is obtained for $P = N$, and subsampling of the signal results in noise magnification [RH95b]. The next section presents the SBS iterative method to select the set of indices $\{p\}$ of the samples of y_p while limiting the value of the trace in Equation (3.4).

3.2.3.2. The SBS algorithm

We previously saw that subsampling signal y and constructing an overdetermined matrix system leads to a noise amplification. The P time samples to acquire can be chosen such that the noise amplification remains small. This is the role of the SBS algorithm [RH95b].

The SBS algorithm sequentially eliminates one row at a time of the matrix A from Equation (3.2), from the N candidates, until P rows remain. At each iteration, the SBS algorithm sequentially selects a single row of A, and for each row it computes the $\mathrm{tr}(A) = \mathrm{tr}[(A_{-}{}^{*}A_{-})^{-1}]$, where A_{-} is the matrix A with the selected row removed. The row that leads to the lowest value is selected for the iteration and A is updated to the corresponding A_{-}. The trace in Equation (3.4) increases monotonically with the removed rows [RH95b].

At a new iteration, the trace $tr(A)$ can be computed by either direct inversion or by the faster Shermann-Morrison-Woodbury formula [RH95b]. However, due to the instability of Shermann-Morrison-Woodbury formula [Yip86], each iteration increases the inversion error. In this study, the Shermann-Morrison-Woodbury is used to select the row to eliminate, but a direct inversion is used to update the matrix $(A_{-}{}^{*}A_{-})^{-1}$ to preserve the stability.

The trace of the matrix $(A^{*}A)^{-1}$ is key, and it has some interesting properties for our application. These are presented by the two theorems in the next section.

3.2.3.3. Properties of the matrix A

Some of the properties of the matrix A from Equation (3.2) are derived in this section, which will be useful for our acquisition method described in a next section "SBS-based multi set acquisition".

Theorem 1.
Let A be the $P \times M$, $M \leq P \leq N$ matrix constructed from the discrete Fourier transform matrix F^{-1} of size $N \times N$, where $N - M$ columns and $N - P$ rows have been deleted. The entries of A are $e^{2\pi i n_s k_s/N}$, where k_s and n_s are the kept rows and columns of the matrix A, respectively. Consider a circular shift d of the rows of the matrix A: if $A^{*}A$ is nonsingular, then $tr[(A^{*}A)^{-1}]$ is invariant to the circular shift.
Proof.
Write $(A^{d})_{n,k} = (A)_{n+d,k} = e^{2\pi i(n+d)k/N}$ (left shift for $d > 0$)
Then $(A^{d})_{n,k} = e^{2\pi idk/N}(A)_{n,k}$
It follows that
$A^{d} = AD^{d}$, where $D^{d} = \mathrm{diag}(e^{2\pi idk/N}), k = 0, 1, \ldots, M-1$.
Note that $D^{d*}D^{d} = I_M$, where I_M is the $M \times M$ identity matrix.
The inverse matrix $(A^{d*}A^{d})^{-1}$ can be expressed as
$(A^{d*}A^{d})^{-1} = (D^{d*}A^{*}AD^{d})^{-1} = (D^{d})^{-1}(A^{*}A)^{-1}(D^{d*})^{-1}$.
Finally,

$\mathrm{tr}[(A^{d*}A^{d})^{-1}] = \mathrm{tr}[(D^{d})^{-1}(A^{*}A)^{-1}(D^{d})^{-1*}]$
$= \mathrm{tr}[((D^{d*})^{-1}(D^{d})^{-1})(A^{*}A)^{-1}] = \mathrm{tr}[(A^{*}A)^{-1}].$ □

*Involvement of **Theorem 1***
For noisy data with the same hypothesis as in section 3.2.3.1, the selected time samples to acquire can be circularly shifted without increasing the resulting trace of the square matrix $(A^{*}A)^{-1}$, and therefore without increasing the noise amplification (Equation(3.4)). This enables more flexibility in the choice of time samples used to solve Equation (3.3) during the signal acquisition and this is a key point for our method based on the interleaved acquisition described in 3.2.3.5.

Theorem 2.
Given the matrix A defined in **Theorem 1**, consider a circular shift d of the selected columns of the matrix A: if $A^{*}A$ is nonsingular, then $A^{*}A$ is invariant from the circular shift, and therefore $tr[(A^{*}A)^{-1}]$.

Proof.
Write $(A^{d})_{n,k} = (A)_{n,k+d} = e^{2\pi in(k+d)/N}$ (left shift for $d > 0$)
Then $(A^{d})_{n,k} = e^{2\pi idn/N}(A)_{n,k}$
It follows that
$A^{d} = D^{d}A$, where $D^{d} = diag(e^{2\pi idn/N}), n = 0, 1, \ldots, P - 1.$
Note that $D^{d*}D^{d} = I_P$, where I_P is the $P \times P$ identity matrix.
Then $A^{d*}A^{d} = A^{*}D^{d*}D^{d}A = A^{*}A$ □

*Involvement of **Theorem 2***
$tr[(A^{*}A)^{-1}]$ is invariant from any circular shift of the spectrum's support, which does not require a new computation of the SBS algorithm. In practice, and for our MRSI application, this property is not as advantageous as the first Theorem. However, one can choose a sparser support, and shift the support if necessary, to center it properly on the frequency peaks.

3.2.3.4. SBS characterization

The selection of the rows of A from the SBS algorithm is related to the given spectrum support of size M. The more time samples that are eliminated by the algorithm (*i.e.*, the lower the P), the more the trace increases, which will therefore increase the noise amplification. However, the lower the P, the faster the signal acquisition may be. Consequently, it is necessary to select an appropriate trade-off between noise amplification and acquisition acceleration.

To select an appropriate number of sampled points P, the evolution of the trace *versus* the spectrum support (size and type) is studied in the following.

The SBS algorithm has been applied to three types of support, as compact, block, and random, each of which has two sizes, $M = 128$ and $M = 256$, with $N = 1024$. A compact support is defined as M consecutive nonzero frequency locations. A block support is defined as eight different compact supports of size $M/8$ that are randomly distributed. A random support is defined as M randomly selected nonzero frequency locations.

Figure 3.1 shows the trace evolution that is averaged on 1000 random realizations of each support, *versus* the number $N - P$ of eliminated rows with $N = 1024$. The trace strongly increases for block and random supports with respect to the eliminated rows.

Sparser spectral support leads to a lower trace, and the trace is also lower when the support is more compact.

These results show that the trace is support dependent and thus application dependent. This trace can be computed prior to any signal acquisition given a known sparse spectrum, and thus this allows the selection of an appropriate trade-off between noise amplification and P, the number of samples to acquire.

3.2.3.5. SBS-based multiset acquisition

In this section, a model for the proposed MRSI application is presented, with a multidimensional discrete temporal signal $y(U, n)$. This signal must be acquired both over U, the spatial k-space and n, the temporal dimension. The objective is to sample this signal as fast as possible. We call the acquisition of samples in U over time the **'time-scan'**. A previous work has been done on this in [Kar+17] given in annexe 1. This paper details how an under-sampling of the time domain can be done with the SBS algorithm for application on phosphorus MRSI. Here, we aim to optimize the temporal sample selection by taking advantage of the circular shift theorem, **additionnally to the use of SBS only**.

The model and the novel proposed interleaved acquisition is presented in the following subsections.

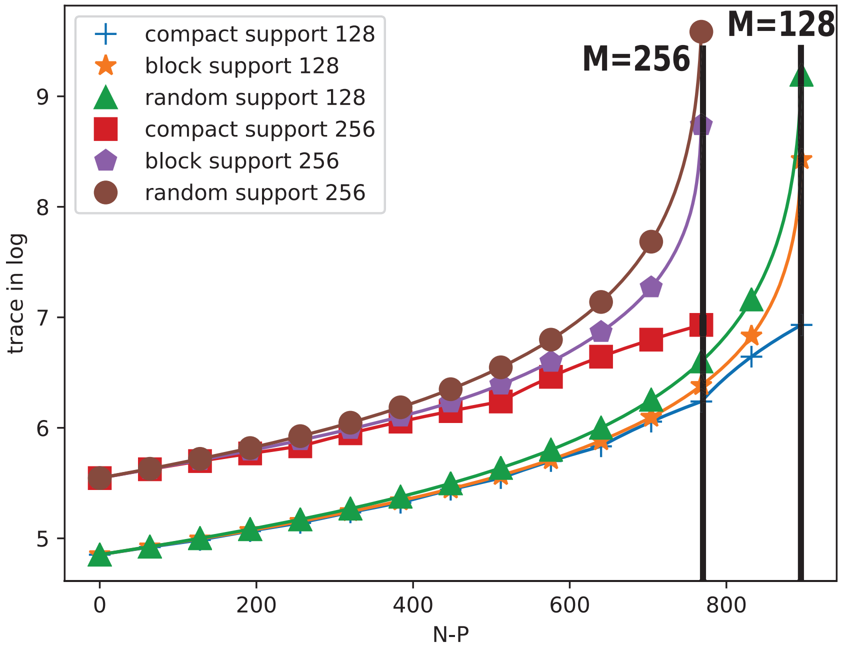

Figure 3.1.: Trace evolution (in log-scale) *versus* the number of eliminated rows $N-P$ of the matrix A for different support sizes and for three support types: compact, random, and block. The signal is made of $N = 1024$ time samples. Vertical lines correspond to the minimal value $P = M$.

3.2.3.5.1. Model of the temporal signal $y(U, n)$ In $y(U, n)$, it is assumed that U can be divided into N_u partitions,

$$y(U, n) = \cup_{u=0}^{N_u-1} y_u(n) \qquad \forall n \in [0, N-1]. \tag{3.5}$$

At each n, it is assumed that only one partition $y_u(n)$ can be acquired. Consequently, N_u time-scans of the signal $y(U, n)$ are required to collect all of the N_u partitions, and thus the full signal $y(U, n)$. For a uniformly sampled temporal dimension, the acquisition duration is

$$T_{\text{acq}}^{\text{full}} = T_{\text{scan}} N_{\text{acq}}^{\text{full}}, \tag{3.6}$$

where $T_{\text{scan}} = NT_s$ is the duration of one time-scan, T_s is the sampling time period of the signal $y_u(n)$ and $N_{\text{acq}}^{\text{full}} = N_u$ the total number of time-scans.
To reduce the acquisition time, we subsample $y_u(n)$, to reduce the number of scans along the temporal dimension. Each signal $y_u(n)$ is assumed to have an identical

known sparse spectrum support S. Thus, the signals $y_u(n)$ can be sub-sampled as described in section 3.2.3.1. Let $\{p\}$ be the set of all the selected time samples by SBS with $\mathrm{Card}(\{p\}) = P < N$, $P \geq M$.

As each $y_u(n)$ has the same spectrum support S, it follows that the selected samples $\{p\}$ are also identical for each $y_u(n)$. At each time sample p, N_u partitions have to be acquired simultaneously and thus N_u time-scans are still required. To reduce the acquisition time the idea is to take advantage of the empty time zones, for the time indices $n \notin \{p\}$ to acquire other partitions of U. From *Theorem 1*, these empty time zones can be filled by a circular shift of $\{p\}$.

The ideal scenario would be to fill the N_uP samples to be acquired without any empty time zones during the N-points time-scan. This results in N_uP/N time-scans compared to N_u time-scans in the full sampled acquisition. The best acceleration factor is thus N/P. In practice, this is very unlikely to happen.

3.2.3.5.2. Interleaving the acquisition in the time domain The objective is to minimize the total number of time-scans N_{full} to acquire $y(U, n)$. This objective requires that the maximum number of partitions to acquire at any n should be minimal.

Let $\{p\}_u$ be the set of selected time samples for the signal of the partition u, $y_u(n)$. Let $I_u(n)$ be an index vector of length N that indicates the P-samples to acquire in partition u, $I_u(n) = 1$ if $n \in \{p\}_u$, 0 otherwise. The total number of time-scans is then $N_{\text{full}} = \max_n(\sum_{u'=1}^{N_u} I_{u'}(n))$.

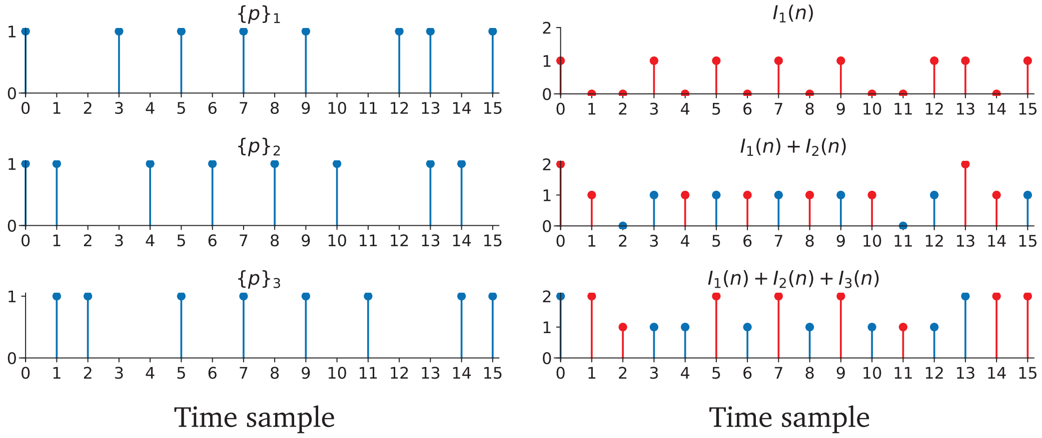

Figure 3.2.: Illustration of the proposed algorithm for $N = 16$, $M = 7$, and $P = 8$. At each iteration, $\{p\}_u$ is a circular shift of $\{p\}_1$ (in this case, 1-shift for $\{p\}_2$ and 2-shift for $\{p\}_3$) which minimizes the maximum value of $\sum_1^u I_u(n)$, where $I_u(n) = 1$ if $n \in \{p\}_u$, 0 otherwise. The maximum corresponds to the number of time-scans needed to sample all of the partitions. In red are represented all the new index vectors, that correspond to the new set of acquisition $\{p\}_u$ ($\{p\}_2$ or $\{p\}_3$ here)

The proposed algorithm minimizes the maximum number of partitions to acquire at any n. It searches at each iteration j for a set $\{p\}_j$ that minimizes the number of acquisitions considering only the first j partitions,

$$N_{\text{full}}^{j} = \max_{n}\Big(\sum_{u'=1}^{j} I_{u'}(n)\Big), \tag{3.7}$$

where j is from 1 to N_u.

The algorithm selects the best circular shift of $\{p\}$ that minimizes N_{full}^{j}, to determine $\{p\}_j$. In the case of multiple solutions, the smaller shift is selected. The first iteration sets $\{p\}_1 = \{p\}$, and the final iteration $j = N_u$ gives the final number of acquisitions $N_{\text{full}} = N_{\text{full}}^{N_u}$, and all the sets $\{p\}_u$ gives the time samples to acquire for each partition. Let us define $I_1(n-d \mod N)$ the d circular shift of $I_1(n)$.

The proposed algorithm follows:

```
- Run SBS algorithm to get $\{p\}$
- Set $\{p\}_1 = \{p\}$ and derive $I_1(n)$
for $j = 2$ to $N_u$ do
    - Search $d_j$ such that $\min_{d_j}(\max_{n}(\sum_{u'=1}^{j} I_{u'}(n)))$,
        with $I_j(n) = I_1(n - d_j \text{ mod } N)$
    - Set $\{p\}_j = \{p$, circularly shifted by $d_j\}$, derive $I_j(n)$
end for
- $N_{\text{full}} = N_{\text{full}}^{N_u} = \max_{n}(\sum_{u'=1}^{N_u} I_{u'}(n))$
```

The new acquisition time of $y(U,n)$ is then

$$T_{\text{full}} = T_{\text{scan}} N_{\text{acq}}. \tag{3.8}$$

Compared to the Equation (3.6), the time acceleration factor is $N_{\text{acq}}^{\text{full}}/N_{\text{acq}} = N_u/N_{\text{acq}} \geq 1$.

3.2.3.5.3. Illustration of the proposed algorithm An illustrative example of the proposed algorithm is used here, as a signal of size $N = 16$ with a spectrum block support size $M = 7$. The number of partitions is set to $N_u = 3$. The SBS algorithm is run with $P = 8$ time samples.

Figure 3.2 shows the iterative steps of the algorithm and the sets $\{p\}_u$ and $I_u(n)$

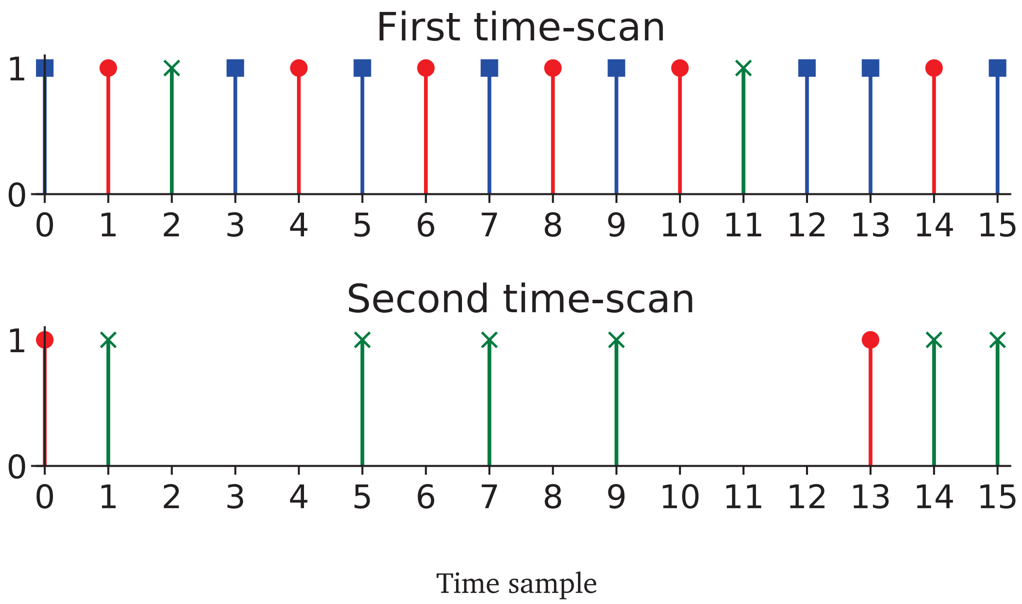

Figure 3.3.: Each row corresponds to a time-scan of the algorithm illustrated in Figure 3.2. The first partition is in blue with a square symbol, the second is in red with a circle symbol, the third is in green with a cross symbol. Two time-scans are enough to sample all of the time samples of all of the partitions.

generated at each step. In this example, the final number of acquisitions N_{acq} is 2, to give a time acceleration factor of $3/2$. For each iteration, the new time samples are represented in red in Figure 3.2. In the first step, $\{p\}_1 = \{p\}$ and $I_1(n) = 1$ if $n \in \{p\}_1$, 0 otherwise. In the second step, there is no circular shift of $\{p\}_1$, such that the maximum of $I_1(n) + I_2(n)$ is 1. In the third step, the algorithm finds a solution such that the maximum of $I_1(n) + I_2(n) + I_3(n)$ leads to two time-scans.
Figure 3.3 illustrates how the partitions are acquired at each time-scan.

3.2.3.5.4. Study of the time acceleration factor To evaluate the time acceleration factor reached by the algorithm proposed in the previous section, the algorithm is run to test different spectrum supports.

The signal size is set to $N = 1024$; the spectrum has M nonzero values, with $M \in \{64, 128, 256\}$; the support type of the spectrum is *compact*, *block* or *random* (cf section 3.2.3.4); the number of partitions is $N_u \in \{2, 4, 8, 16\}$.

The SBS algorithm is run with $P = M$ time points, which is the largest feasible subsampling with a given sparse spectrum.

For each set of parameters, the algorithm is run on 100 realizations of the randomly chosen support. For each run, the following are computed: the highest number of acquisitions required $N_{\text{acq}}^{\text{full}} = N_u$; the ideal lowest number of acquisitions $N_{\text{acq}}^{\text{full}} M/N$ (rounded up); and the number N_{acq} of acquisition given by the proposed algorithm. The results are averaged over the 100 realizations, as in Table 3.1.

We can see that the acquisition speed-up, which is defined as $N_{\text{acq}}^{\text{full}}/N_{\text{acq}}$, increases with the number of partitions and decreases with the number of samples in the spectrum support.

M		64				128				256			
N_u ($= N_{\text{full}}^{\text{full}}$)		2	4	8	16	2	4	8	16	2	4	8	16
N_{full}	random support	1	1.47	2.01	3.27	1.62	2	3.33	7.67	2	3.95	7.95	15.95
	block support	1	1	1.38	2.24	1.01	1.46	2.42	4.65	1.55	2.42	5.08	11.15
	compact support	1	1	1	1	1	1	1	2	1	1	2	4
best $N_{\text{full}} = \lfloor N_u M/N \rfloor$		1	1	1	1	1	1	1	2	1	1	2	4

Table 3.1.: Given N_u, M and different support types, the highest number of acquisitions $N_{\text{full}}^{\text{full}}$ ($= N_u$), the lowest $N_{\text{full}}^{\text{full}} M/N$ (rounded up) and the computed N_{full} by the proposed algorithm are given, averaged over 100 realisations of the randomly chosen support. SBS was computed with $P = M$ and $N = 1024$.

As expected, the sparser the spectrum, *i.e.*, the lower the M, the lower the number of acquisitions. In comparison, the number of partitions N_u has less influence. The support type has strong influence: the more "compact" it is, the better acquisition gain it gives. Interestingly, for a sparse spectrum of M contiguous frequency samples, the algorithm always gives the lowest possible number of acquisitions.

3.2.3.5.5. Optimality and complexity of the algorithm The algorithm proposed in section 3.2.3.5.2 searches sequentially in $N_u \times N$ circular shifts, for the combination of shifts that leads to the lowest number of time-scans, over a total of N_u^N possible combinations. Given the results in the previous section, this algorithm is optimal with a compact support. For the two other cases, an extensive search in the N_u^N possibilies is run over 100 iterations of both the block and compact supports, with a signal size $N = 128$, $N_u = 4$ partitions and spectra of M nonzero values, $M \in \{8, 16, 32, 64\}$. When the spectrum is very sparse, $M = 8$, many combinations lead to the best possible N_{acq}, and the proposed algorithm always finds this. On the other hand, when half the spectrum points are used, $M = 64$, the extensive search gets a better result than our algorithm, as all the time for a random support, and 44 times for a block support. For $M = 16$ and $M = 32$, the extensive search gets a better N_{acq} in 3% of the runs for a block support, and in 27.5% of the runs for a random support.

The proposed algorithm first runs the SBS algorithm, then performs circular shifts as detailed in section 3.2.3.5.2. The SBS algorithm has a complexity of $O((N^2 - P^2)M^2)$

[RZ99]. As $N \gg P$, the complexity can be reduced to $O((NM)^2)$, with $M \ll N$. The proposed algorithm in section 3.2.3.5.2 has a complexity of $O(NN_u)+O(NP)$, which thus has a global complexity of $O((NM)^2)$. The LS reconstruction has a complexity of $O(M^2P)$. The total complexity of the proposed method is then $O((NM)^2)$. The main contribution to the whole complexity of the proposed approach comes from the selection of the temporal samples to acquire (SBS).

3.2.4 Application

3.2.4.1. Magnetic resonance spectroscopic imaging (MRSI)

Nuclear magnetic resonance consists in a physical phenomenon that induces a perturbation of the macroscopic magnetization of an ensemble of nuclear spins that interact with a surrounding static magnetic field. This perturbation is caused by radiofrequency pulses, which are more commonly called excitation pulses and leads to an electromagnetic signal response with frequencies related to the atoms considered and their chemical environment [DG19]. This signal is called the free induction decay and it is encoded in the k-space with the help of field gradients. It is complex, of the form $y(k_x, k_y, n)$, and it depends on the time and the spatial two-dimensional excited environment. In magnetic resonance imaging, the signal $y(k_x, k_y, n)$ is acquired in the Fourier domain, which is called the k-space excitation, at a given t. To obtain the corresponding anatomic image, an inverse Fourier transform is performed. In MRSI, we are interested in the acquisition of the temporal evolution of the FID signal multiples time, which is why it is acquired for $t \in [0, (N-1)T_s]$. For each (k_x, k_y), the signal is modeled by

$$y_{k_x,k_y}(n) = \sum_j a_j(k_x, k_y) \exp(i2\pi f_j n T_s - nT_s/T_2^*), \tag{3.9}$$

where the time constant T_2^* is the transverse relaxation that accounts for the spin-spin relaxation and the field inhomogeneity. Due to the term $\exp(-nT_s/T_2^*)$, its spectrum is not band limited because each spectral line becomes Lorentzian shaped; however, it can be approximatively considered as sparse [Mer+14]. The coefficient $a_j(k_x, k_y)$ is complex and is the Fourier transform of the metabolic image characterized by the frequency f_j.

Each excitation results in the same free induction decay signal. Excitations can be repeated as many times as necessary to get the joint spatial spectral information. At the end of the scan, a delay can be added to ensure that the macroscopic magnetization returns to its original state. The time between two excitations is called the repetition time, $T_\mathrm{R} \geq NT_s$.

In clinical routine, the sequences that are commonly used acquire the k-t space (k_x, k_y)-point by (k_x, k_y)-point with the phase encoding method [Pos+13]. A single point of the k-space and the whole temporal dimension is acquired at each excitation. This results in a long acquisition time $T_\mathrm{acq}^\mathrm{full}$ from Equation (3.6), because N_u, as the number of partitions of the k-space, is very large. For example, for a 32×32 matrix, the number of (k_x, k_y) points is $N_u = 32 \times 32 = 1024$. To speed up the acquisition, it is possible to group the k-space points into partitions, that have to be acquired in the k-space after each excitation, which leads to the model of Equation (3.5). However, due to technical constraints (MRI gradients), the acquisition of one partition, i.e travelling through k-space, is not instantaneous. The larger the partition is, the longer the acquisition is. There is an issue if the partition acquisition duration is longer than the sampling time period T_s, because this means that the next time sample is to be acquired while the previous one is still in the process of being acquired. Let T_{part} be the acquisition time of each partition. The acquisition of each partition lasts for $N_p = \lfloor \frac{T_{part}}{T_s} \rfloor$ time sampling periods and forbids the acquisition of the next $N_p - 1$ time sample. $N_p - 1$ additional excitations are required to acquire the full signal. This is called temporal interleaving. Moreover, as the repetition time T_R is longer than NT_s, the total time acquisition can be rewritten as

$$T_\mathrm{acq}^{\mathrm{full}'} = T_R N_u N_p. \tag{3.10}$$

Acquiring the whole signal requires $N_u \times N_p$ excitations. Choosing small partitions, which are faster to sample, decreases N_p but increases the number of partitions N_u, and *vice versa*.

3.2.4.2. Time interleaved application to MRSI acquisition

The additional constraint of the noninstantaneous acquisition of a partition requires an update of the proposed algorithm in section 3.2.3.5.2. In the previously proposed algorithm, the assumption of instantaneous acquisition of a partition is equivalent to $N_p = 1$. $I_u(n)$ is the index vector that indicates whether the time sample n of the partition u is to be acquired, consequently forbidding any other acquisition at time index n. With the constraint of the duration of one partition, a time sample at position n forbids the $N_p - 1$ following sample to be acquired. As an example for $N_p = 2$, if there are two consecutive points to acquire, the acquisition of the first

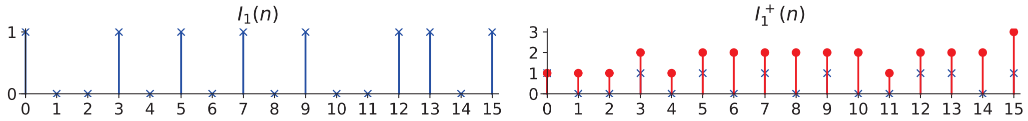

Figure 3.4.: Illustration of the difference between $I_1(n)$ and $I_1^+(n) = \sum_{d=0}^{Np-1} I_1(n-d)$ with $N_p = 4$. The same parameters as in Figure 3.2 are used here. $I_1(n)$ is shown with a cross symbol on these two panels, and $I_1^+(n)$ with a circle symbol in the right panel. $I_1^+(n)$ shows the number of excitations required for each n.

one blocks out the acquisition of the second. This leads to at least two excitations to obtain the two points. By setting

$$I_u^+(n) = \sum_{d=0}^{N_p-1} I_u(n-d) \tag{3.11}$$

,the number of excitations to acquire the partition u is $\max(I_u^+(n))$, as illustrated in Figure 3.4.
It follows then that the algorithm in section 3.2.3.5.2 requires the replacement of $I_u(n)$ by $I_u^+(n)$. To promote the scan of the beginning of the free induction decay where the signal magnitude is maximal, the $\{p\}_u$ are circularly left shifted, if necessary, thanks to *Theorem 1*.

In the case of a non instantaneous acquisition of a partition, the use of the circular shift theorem is not necessary to speed up acquisition time. Indeed, not using the proposed algorithm leads to the acquisition of the same temporal samples $\{p\}_u$ for all the partitions. Note that this still leads to a gain in terms of acquisition time, as detailed in [Kar+17]. Indeed, SBS leads to an irregular sub-sampling that enable to reduce the number of excitation (i.e the acquisition scan) compared to full and regular sampling, in the case where time entanglement is required to achieve a desired spectral bandwidth. The acquisition scheme for both techniques are the same, but using the proposed algorithm leads indeed to a higher speed up gain.

The steps to fully reconstruct the spectroscopic image $y(x, y, f)$ are the following:

- determine the time samples $\{p\}_u$ for each partition, through the algorithm in section 3.2.3.5.2 with $I_u^+(n)$ instead of $I_u(n)$;
- acquire each partition $y_u(n)$ for $n \in \{p\}_u$ of the k-space;
- apply LS reconstruction on each partition to obtain $y_u(f)$ (Equation (3.3));

- merge all partitions to get the whole k-f space:
  $y(k_x, k_y, f) = \cup_{u=0}^{N_u-1} y_u(f)$;
- apply a two-dimensional nonuniform discrete Fourier transform [Fes; FS03] to reconstruct the spectroscopic image $y(x, y, f)$.

This is indeed different from the reconstruction process that is done in [Kar+17], where the spatial domain is reconstructed before the spectral one. Indeed, as all the partition in [Kar+17] are being sampled at the same temporal points given by the SBS algorithm, it is possible to directly merge all partitions after the acquisition to get the full k-t space. Then, the I-t space is generated with a Non uniform Fourier transform followed by a LS reconstruction on each pixel to reconstruct the I-f space.

Note that reproduction of the experiments of section 3.2.3.5.4 with the additional parameter N_p shows that N_p has similar influence to N_u on the speed-up gain.

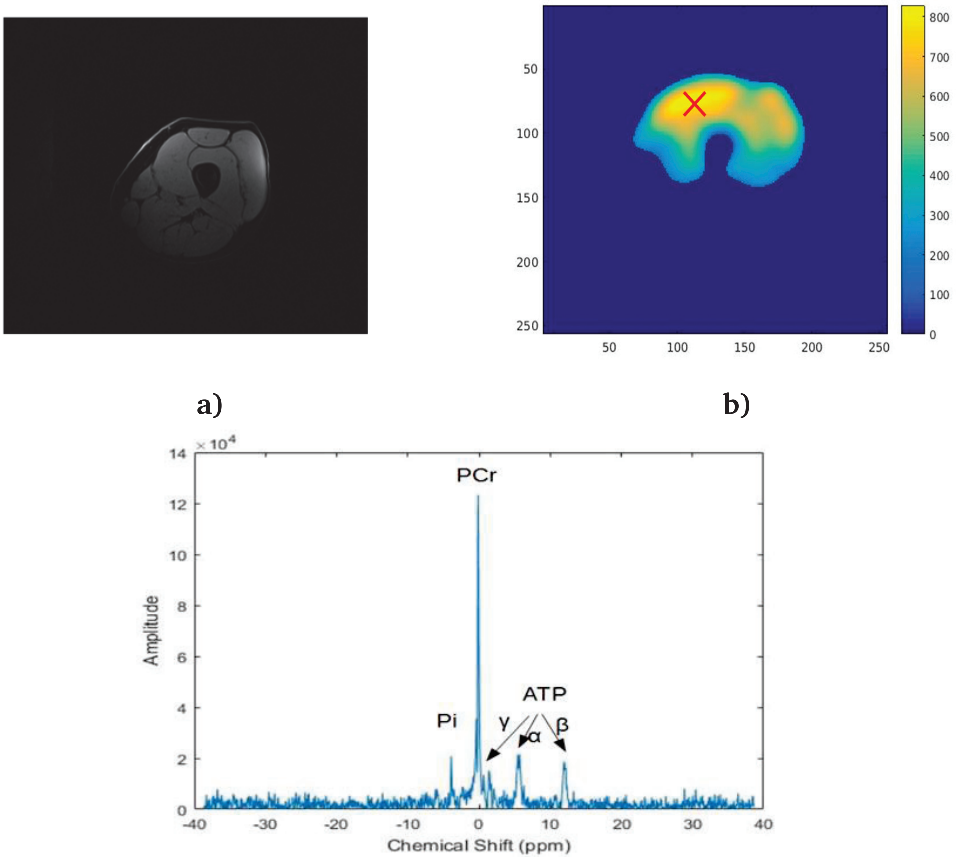

a)

b)

c)

Figure 3.5.: a) Anatomic image from a dixon sequence acquisition (FA $9°$, T_{R} 4.1 ms, T_{E} 1.4 ms, matrix size 118×192, FOV 169×206 mm^2), b) ^{31}P image acquired from a standard CSI acquisition (FA $90°$, $T_{\mathrm{R}} = 1$ s, 5 averages, matrix size 16 x 16, FOV 200 mm square, total acquisition time 32 min). In c), a spectrum from the CSI acquisition is shown for the pixel highlighted by the red cross on the CSI image.

3.2.4.3. Simulation and Results

To compare the fully sampled method with the proposed interleaved time undersampling method, we use ^{31}P MRSI data, for sparse spectra. A numerical phantom with three compartments as defined in Figure 3.6-a and with different metabolite ratios for each compartment are used. ATP concentration was set to a constant in the whole numerical phantom, but Pi and PCr concentrations vary depending on the compartment. The phantom was based on an vivo acquisition of the quadriceps muscle of a healthy man laying down prone, with a surface coil ^{1}H/^{31}P Tx/Rx placed under its quadriceps muscle. Indeed, phosphorus CSI was acquired with a FA $90°$, $T_{\mathrm{R}} = 1$ s, 5 averages, 4 dummy scans, matrix size 16 x 16, FOV 200 mm

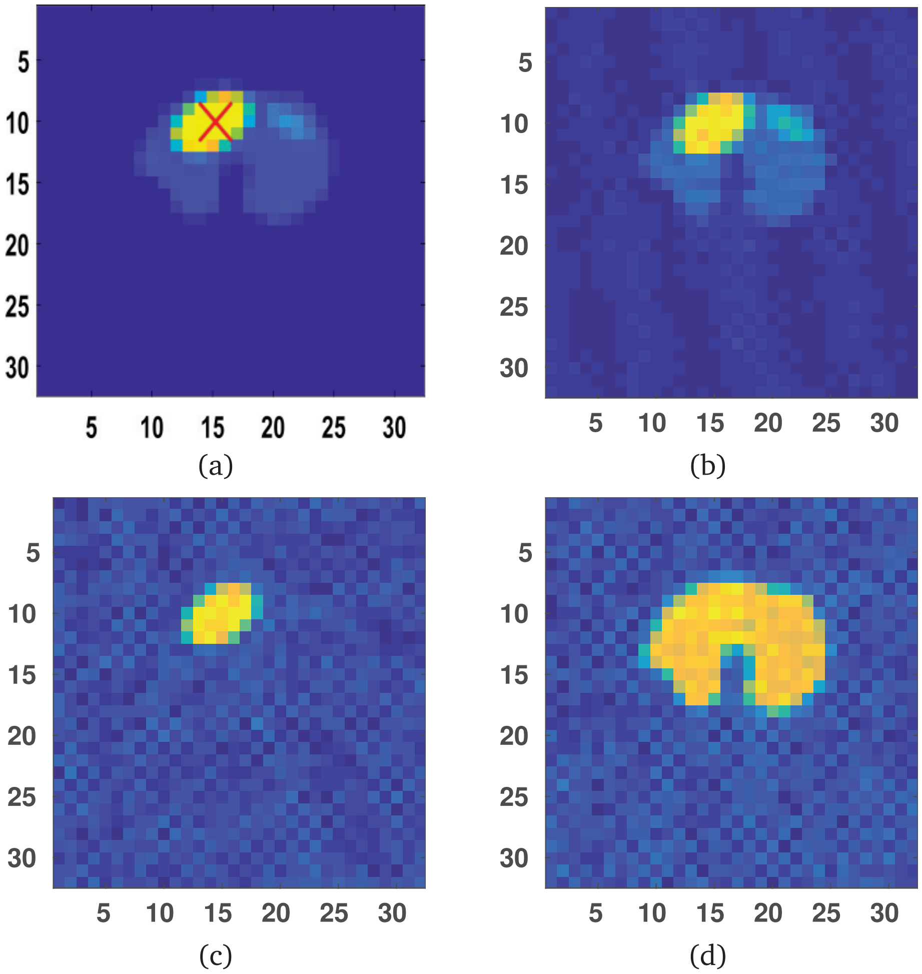

(a) (b) (c) (d)

Figure 3.6.: a) Referenced phantom at t=0 (based on ^{31}P *in vivo* image). ATP amplitude was set to 7 in the whole phantom, PCr and Pi amplitudes to 20 and 7 in the left ellipse, PCr amplitude to 17 in the right ellipse and 8 elsewhere. Spectral images for phosphocreatine (b) (frequency = 0 Hz), inorganic phosphate (c) (f = 258 Hz), and adenosine triphosphate (d) (f = -129 Hz, -387 Hz, -853 Hz). The red cross is used in Figure 3.8.

square for an acquisition time of 21 min and 20 s. In figure 3.5, the anatomic image, phosphorus CSI image (on which the phantom is based) and a reconstructed spectrum in a pixel in the quadriceps.

The acquisition is simulated with a field of view of 25 cm, and an image matrix size of 32×32. The k-space is partitioned in both methods with four spirals, as illustrated in Figure 3.7. The simulation parameters are $N_u = 4$ partitions, time sampling period $T_s = 0.25$ ms, $N = 1024$ time samples, repetition time $T_R = 2$ s, and spiral of $N_p = 10$ discrete time samples which corresponds to a duration of $T_{\text{part}} = 2.5$ ms. Each partition is a discrete spiral of 2048 points, which leads to 8192 points to sample the whole k-space. The support of the phosphorus spectrum comprises two blocks, of total size $M = 217$ samples. Here, the support is chosen

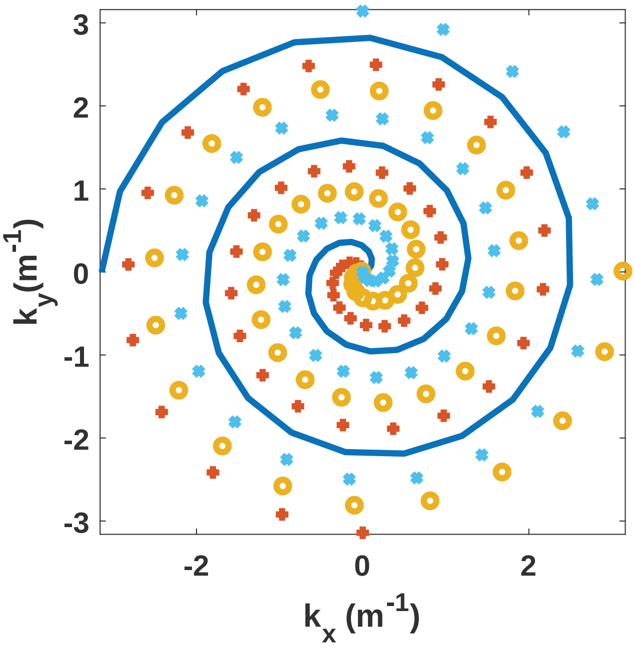

Figure 3.7.: Partition of the k-space with $N_u = 4$ spirals

such that the truncation of the spectral peaks is less than 1 % of the total peak energy. In practice, the resonance frequency of the molecule is always the same and the full width at half maximum depends on the static magnetic field homogeneity which is rather reproducible, so a support can be determined a priori on a simulated realistic spectrum. For the proposed interleaved method, an objective of a best acceleration factor of 4 is used by setting $P = 256$. As the spiral is not instantaneous in practice, every sample of the spiral is phase-corrected according to the Fourier shift theorem.

For the fully sampled spiral method, the acquisition time is $T_{\text{acq}}^{\text{full}'} = 80$ s. When applying the algorithm of section 3.2.4.2, this results in an acquisition time $T_{\text{acq}} = 26$ s. The gain in terms of the acquisition time is a factor of 3.08.

The two methods are also compared in terms of the signal-to-reconstruction error ratio (SRER) in decibels (dB)

$$\text{SRER} = 20 \cdot \log \frac{||x||_{l_2}}{||x - x_m||_{l_2}}, \tag{3.12}$$

where x is the original spectrum and x_m is the reconstructed spectrum according to Equation (3.3), with both restricted to the spectral support.

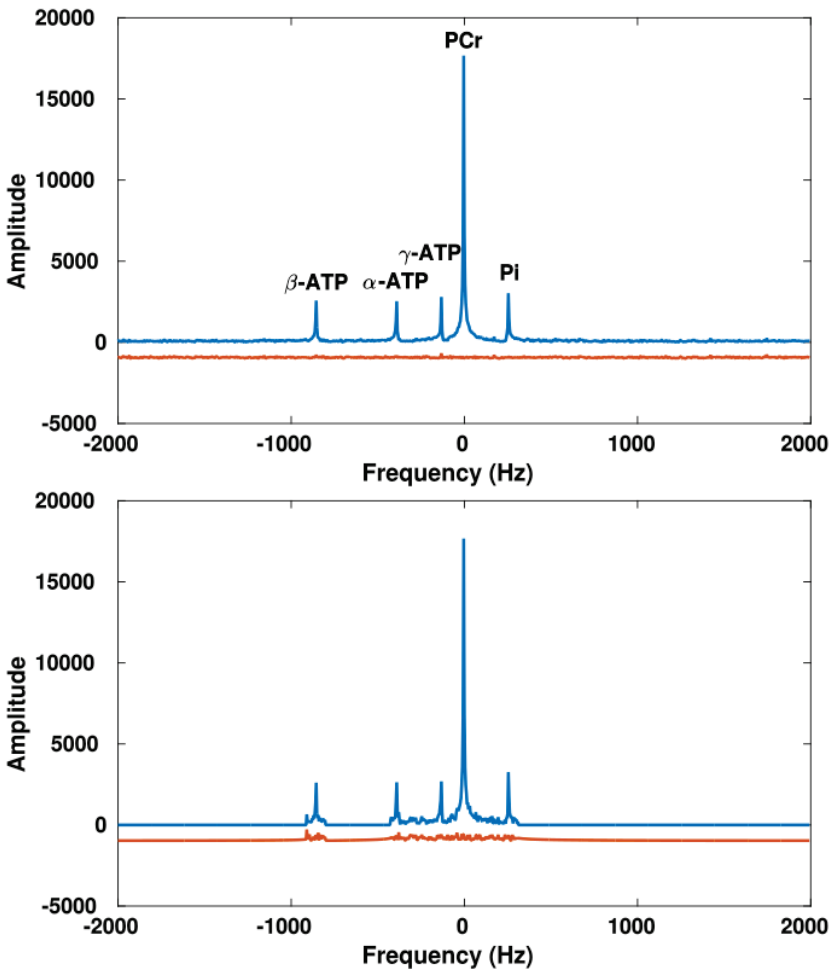

Figure 3.8.: Noisy reconstructed modulus spectrum from a voxel in the left ellipse (red cross in Figure 3.6-b) for the fully sampled spiral method (left) and for the new proposed approach (right). The reconstruction error (shifted by -500) is given at the bottom.

SRER performance for a realistic signal

The results for a realistic simulated numerical phantom are shown in Figures 3.6 and 3.8. Figure 3.6 shows the reconstructed phantom with the use of spiral spatial sampling, for each molecule (*i.e.*, phosphocreatine, inorganic phosphate, adenosine triphosphate). Figure 3.8 shows the reconstructed spectra with the noisy acquisition given, with their respective errors. The T_2^* used for the exponential decay of the free induction decay signal is 100 ms. In a noise-free acquisition, the SRER compared to the original spectrum used for the simulation is 31.6 dB for the fully sampled spiral method and 29.7 dB for the proposed method (averaged on the mask containing all of the pixels of the left ellipse of the phantom). The 1.9 dB SRER loss is due to the truncation of the spectrum. For a noisy acquisition (*i.e.*, complex Gaussian noise with a standard deviation such that signal-to-noise-ratio varies between 12dB and

22dB in the left ellipse), the SRER, averaged for 10 different generations of Gaussian noise and for all of the pixels in the left ellipse, is of 24.6 dB for the fully sampled spiral method and 19.3 dB for the proposed method.

Reconstruction of the proposed method with the LASSO method

The proposed LS solution is exact for an exactly bounded (known) support. In MRSI, the spectrum is not exactly band limited because each spectral line is Lorentzian (see section 3.2.4.1 for details). In addition, we use a larger support than that known by nuclear magnetic resonance theory, to take into account both spectral line widening and experimental error. Thus, we compare our LS approach with the LS-L_1 regularized method known as the least absolute shrinkage and selection operator (LASSO) [Boy+14]. We search x with

$$\min_x ||y - Ax||_{L_2} + \gamma \cdot ||x||_{L_1}. \tag{3.13}$$

The L_1-norm has been used in various applications to promote sparse solutions. In our approach, this heuristic promotes a sparser solution than that given by the implicit support defined by the columns of matrix A, and regularizes the solution for a not precisely bounded support. We used the cvx code [GB14]. The value for the hyper parameter γ, given by the optimal trade-off curve between $||y - Ax||_{L_2}$ and $||x||_{L_1}$ is 0.01.

For the spectrum in Figure 3.9, the noise-free SRER is 18.7 dB for the LS reconstruction and 19.6 dB for the regularized reconstruction.

In the noisy case, given a 20 dB signal-to-noise-ratio (SNR) in the free induction decay, calculated as

$$\mathrm{SNR} = 20 \times \log(\frac{\sqrt{||x||_{l_2}}}{\sigma}) \tag{3.14}$$

with x the simulated spectrum, and σ the standard deviation of noise, this results in an SNR of 27.8 dB on the spectrum support. The SRER of the LS reconstruction with 100 realizations of noise is 16.6 dB, giving a loss of 2.1 dB. The SRER of the regularized solution is 18.04 dB. In conclusion the L_1 regularization increases the SRER of 1 dB in the noise-free by recovering some lost energy and tends to decrease the noise, in the noisy case with an increase of 1.7 dB of the SRER over L_2 reconstruction.

The proposed acquisition method significantly reduces the acquisition time compared to a temporal fully sampled case. The reconstruction performed by L_2 minimization might, however, be improved by adding a L_1 regularization term in the minimization.

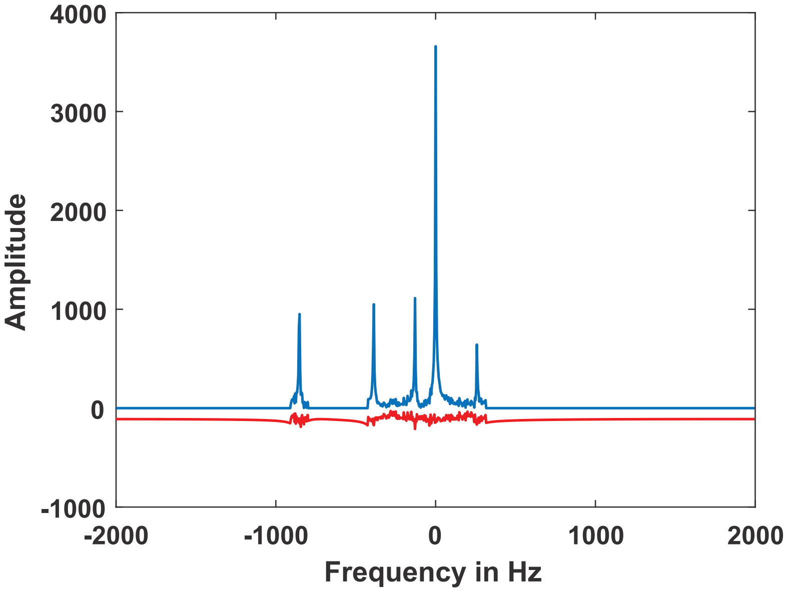

Figure 3.9.: Reconstructed spectrum with the LASSO method. The reconstruction error (shifted by -100) is given at the bottom.

Also, other reconstruction algorithms that require knowledge of the support have been proposed and become interesting in terms of reconstruction performance compared to the L_2 reconstruction when the SNR deteriorates. We mention in particular the approximate message passing for multiple measurement vector [ZS12] or the modified CS-based method for problems with partially known support proposed in [VL10] that we successfully applied on the magnetic resonance spectroscopic data (results not shown).

3.2.5 Discussion

Recent studies have focused on both jointly sparse signal recovery and underdetermined systems, because of many real-world scenarios where multiple sensors acquire signals simultaneously such as Distributed Network [WV14], and wireless communication [May+16]. These studies are MMV problems where the measurement matrix is identical for each acquisition, and in that sense they share similarities with our application. MMV-based reconstruction algorithms include mixed norm minimization methods [Cot+05], greedy pursuit methods [WV14], Bayesian-based MMV reconstructions [ZS12].

The proposed method cannot be classified as one of these CS-based methods. Our approach is specific to *a priori* known supports and overdetermined systems. The reconstruction process of our method consists of a LS minimization. One of the main difference between CS and the proposed method is the choice of the samples. We choose the samples with the SBS algorithm, and these are irregularly spaced. This selection of samples is carried out only once before the signal acquisition. The acquisition of an other signal with the same spectral support does not require another run of the proposed algorithm. Any other acquisitions result in low computational cost. In contrast, the complexity of CS-based reconstruction algorithm is related to the signal reconstruction process, especially due to the spectral support search for greedy algorithms, or due to the regularization implementation. The samples are randomly selected and this does not contribute to the overall complexity.

Randomly choosing the samples would not change the proposed acquisition architecture, but we do not control the trace amplification (or the noise magnification) in this case. With randomly selected samples, the SRER decreases [Mer+14].

The method has been applied on phosphorus MRSI with a home made numerical phantom miming real phosphorus CSI data in the calf muscle. MR acquisition parameters have a major importance on data quality and noise. Indeed, spatial resolution, spiral duration, spectral bandwidth, the number of partition and the repetition time but also and this is often the case relaxation T_2^* time of each metabolite, have a major importance on the data quality. In practice, it is also necessary to average the spectra to get enough Signal to Noise ratio (SNR), i.e do the same acquisition multiple times which in practice implies that the subject does not move, that the carrier frequency does not move, etc... which is a strong hypothesis. The relaxation time T_1 not discussed here has also its importance and, for phosphorus metabolites, T_1 can be quite long, and implies to favor long repetition time T_R. The T_2 of phosphorus metabolites is quite short, especially for ATP resonances, which is a limitation in practice, because it is necessary to sample the signal as much as we can directly after the excitation pulse. Finally, the spectral bandwidth (defined as $1/T_s$) is related to acquisition time, the smaller the spectral bandwidth is, the shorter the acquisition time will be. Therefore, it is better to use a small bandwidth, but on the other hand, this makes the spectrum less sparse. Because of low SNR, and particularly for phosphorus applications, the spatial resolution cannot be very high (matrices of 8×8 or 16×16 with a FOV of 20 cm are preferably used), which reduces the number of partitions. All these parameters, which are key in a real implementation, are being studied more deeply in the next chapter.

3.2.6 Conclusion & Perspectives

A new method of acquisition of interleaving time samples in undersampled signals is proposed here to speed up acquisition times. For multidimensional spatial signals, assuming that each spatial point has a known sparse spectral support, the SBS-based undersampling can be chosen such that the noise amplification is minimized with LS reconstruction. The spatial domain is divided into several partitions. We show that a circular shift of the selected samples does not change the reconstruction error. The proposed algorithm searches for the best circular shift of the undersampling of each partition to reduce the total acquisition time by interleaving the partition samples in the time domain. The proposed algorithm is applied here to MRSI and takes into account real implementation constraints. The time acquisition is reduced by a factor of 3.08 but the signal error increases by 5 dB in a realistic noisy acquisition.

Magneto-encephalography can also be considered here, as an inverse problem used for brain imaging [Phi+97; Gor+95]. Magneto-encephalography signals come from activated regions in the brain. Taking several signals over time enables the magnetic response of the brain to be followed over time. The activated regions could be *a priori* known thanks to the knowledge of brain functional structure, and our method can be applied.

A future goal will be to apply this method to exercise dynamics ^{31}P applications, accurate fat/water quantification, and^{1}H MRSI or hyperpolarized ^{13}C studies.

Under-sampled spiral spectroscopic imaging sequence has been implemented and tested on a real MR system, what is described in the next chapter. Note that the algorithm, that has been detailed in this chapter, is not used in the implementation in the following chapter. In the following, the under-sampling is done only by using the SBS algorithm, without optimising the sampling pattern by circular shifting all the partition" that is to say that every partition has the same under-sampling pattern - or again, the choice of the temporal samples will be the same for all partitions.

3.3 Acknowledgements

This study was partly supported by the LABEX PRIMES (ANR-11-LABX-0063), program "Investissements d'Avenir" (ANR-11-IDEX-0007) and Siemens Healthineers.

4

Sequence implementations and optimisations

Summary

4.1 Introduction

The thesis project is about muscle energetic metabolism exploration by the mean of ^{31}P MRS and MRSI. Parallel to theoretical developments detailed on chapter 3, sequence developments were performed for immediate clinical applications in the context for example of the protocol SPECTROAOMI detailed in chapter 5, on localized spectroscopy. An other objective was to implement the MRSI method developed and explained in chapter 3 on a clinical scanner. This chapter is divided into two sections. The first one details the sequence developments done for localized ^{31}P MRS, followed by the implementation of the fast spiral undersampled MRSI sequence.

Considering the chronological sequence of the work carried out during this thesis, the implementation of the different MR sequences were done in parallel to methodoligical development detailed in the previous chapter. For this reason, the method in [Kar+17] has been implemented here, relying on an under-sampling of the temporal dimension of the FID, with the same under-sampling and choice of samples for all partitions, given by the SBS algorithm. The SBS algorithm has therefore been implemented, but not the algorithm proposed in chapter 3. Thus, the reconstruction process differs in the fact that, in the case of an under-sampling, the spatial dimension is reconstructed before the spectral dimension. Due to practical constraints, a challenge while implementing and testing the sequence was the low SNR, low sensitivity, particularly in the case of phosphorus application. Even with an uniform and conventional spiral MRSI, the choice of parameters such as T_{R}, slice thickness, spatial resolution has to be properly done in order to have data of enough quality. In the theoratical point of view, detailed in the previous chapter, no detail has been given such as how to choose the acquisition parameters, but more details on the sequence implementation, and on the choice of acquisition parameters, will be given here.

4.2 Sequence development for localized spectroscopy of $^{31}\mathrm{P}$

4.2.1 Constraints in $^{31}\mathrm{P}$ MR spectroscopy

Localization in 1D spectroscopy is an issue and especially in $^{31}\mathrm{P}$ applications because of the short T_2 of the phosphorus metabolites, especially the ATP compounds, which are about 50ms at 3 T and their low concentrations conducting to very low SNR. Moreover, the slice selective inversion or refocusing pulses that are used in sequences such as PRESS and STEAM are not adiabatic and subject to B_1 inhomogeneities (cf subsection 2.2.4), in the case of the use of a surface coil for signal transmission and reception for $^{31}\mathrm{P}$ studies.
The use of a semi-LASER sequence is a way to face B_1 inhomogeneities and do localized $^{31}\mathrm{P}$ MRS [Fie+15]. Other localized MRS sequences that enable no echo times (zero T_{E})exist like Image-Selected In vivo Spectroscopy (ISIS) [Ord+86], Depth-resolved surface-coil spectroscopy (DRESS) [Val+14; Bot+84].

Saturation bands can also be used to confine the signal in regions of interest. The saturation has to be done with adiabatic pulses that are robust to B_1 inhomogeneities. In this thesis, The B_1 Insensitive Train pulses to Obliterate signal (BISTRO) module which has revealed to be efficient for phosphorus applications [Luo+01] has been implemented.

4.2.2 1D localized sequence development based on OVS

4.2.2.1. B_1 Insensitive Train pulses to Obliterate signal outside of region of interest

The BISTRO module consists in the application of a train of increased amplitude of adiabatic full passage (AFP) hyperbolic secant pulses, with an increase following a hyperbolic secant function, and placed before the excitation.

With n the total number of pulses and $i = [1 : n]$ the pulse number, the *i*th pulse can be written as

$$B_{1i}(t) = B_{1\max} \times \operatorname{sech}[\beta(1 - \frac{2t}{T_p})] \times \operatorname{sech}[\beta(1 - \frac{i-1}{n-1})]. \tag{4.1}$$

where T_p is the duration of the pulse and β a truncation factor chosen such that $\operatorname{sech}(\beta) = 0.01$.

4.2.2.2. BISTRO characterization

Using Bloch equation propagation, simulations of the pulse behaviour regarding its B_0 , B_1-inhomogeneity, and pulse amplitude were done. The hyperbolic secant pulse used was the HS8-R20. Its phase, spectrum, longitudinal magnetization and transverse magnetization are shown in figure 4.1. Transversal and longitudinal magnetization obtained for the application of 2 different bandwidth are shown in figure 4.2.

These simulations show that the pulse is frequency selective and robust within its defined bandwidth. The excited bandwidth is quite uniform and is therefore what interests us for our applications and experiments. Indeed, we will not reach the adiabatic condition for these pulses (too power demanding) but we will use these properties to excite and saturate uniformly the defined bandwidth. The bandwidth is dependent on the pulse duration, because the time samples of the pulse are fixed. Morever, this pulse results in an uncoherent phase magnetization, which improves its saturation efficiency.

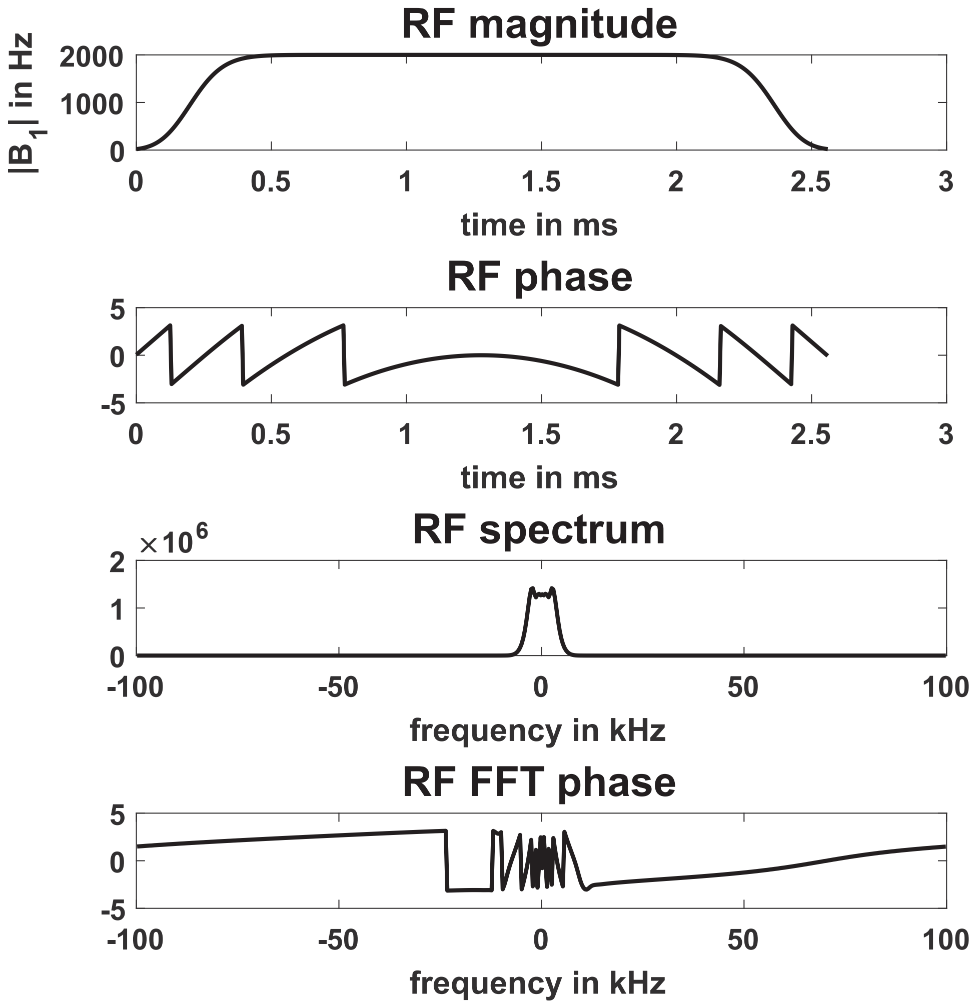

Figure 4.1.: Hyperbolic secant HS8 pulse magnetization, phase, spectrum and fft phase.

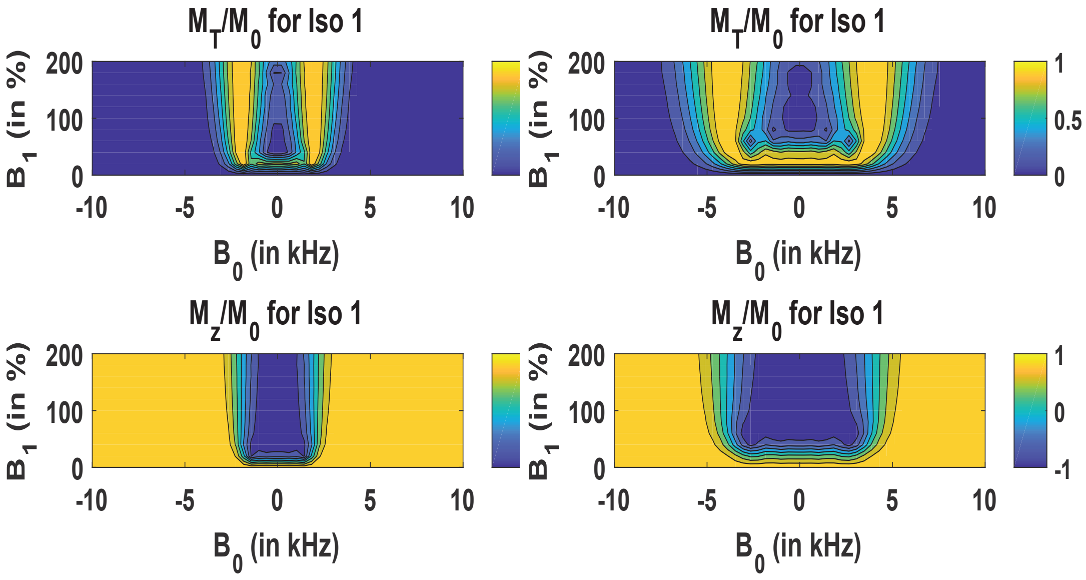

(a) (b)

Figure 4.2.: Transverse magnetization MT/M0 and longitudinal magnetization Mz/Mo profiles for a bandwidth of 4083 Hz for a) 8166 Hz for b)

4.2.2.3. Material and methods

A Siemens water phantom has been used for the proton application. A standard CSI sequence was used with a Flip angle of 90°, T_R of 1.5 s, 2 averages, a matrix size of 16 x 16 and a FOV of 30 cm, with a head surface coil. The BISTRO OVS module was composed of 6 RF hyperbolic secant pulses of 7.86 ms durations, corresponding to a 2722 Hz pulse bandwidths. The 6 RF hyperbolic pulses were of rising amplitudes. The last pulse of the module, the sixth, has a maximum flip angle of 90°. It has been compared with a standard OVS module composed of one cardinal sinus RF excitation pulse with a 90° Angle and a 12 kHz bandwidth.

4.2.2.4. Experimental results on phantom

The results on proton spectroscopic imaging of the effect of the saturation bands are shown in figure 4.3. The same scales were used in the illustration, to visually see the effect of the saturation of the 2 OVS modules, OVS cardinal sinus based module and BISTRO module. The reconstructed spectra by the inner Siemens platform are shown for a pixel of the CSI-grid. A saturation efficiency of 60 % is reached with the cardinal sinus based OVS, and of 95 % with the BISTRO OVS.

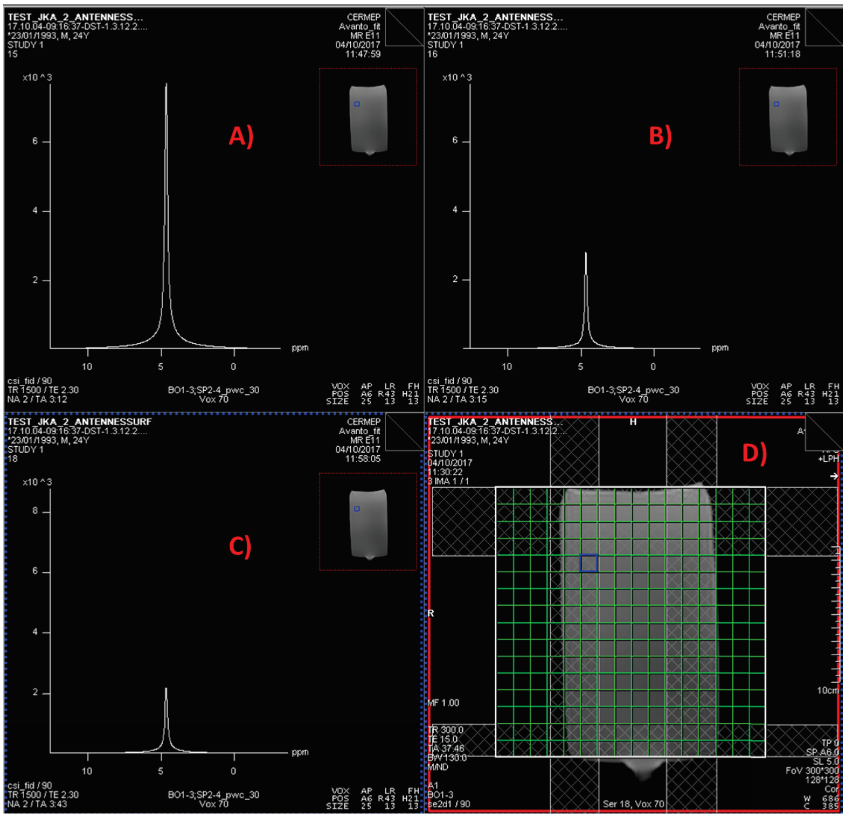

Figure 4.3.: A) Unsaturated spectrum from the highlighted pixel in the CSI-grid shown in D). In B), the saturated spectrum with an OVS module composed of a cardinal sinus pulse is shown and in C) the saturated spectrum with an BISTRO OVS module. The placement of the saturation bands on the phantom are shown in D).

4.2.2.5. Discussion

The BISTRO module has been implemented on the Siemens plateform for OVS saturation and compared with a more commonly used cardinal sinus based OVS. It proved to be more efficient when being tested on a standard CSI sequence, with a better saturation efficiency than a standard OVS module. The implemented BISTRO module has thus been used in the ^{31}P MRS clinical protocol SPECTROAOMI detailed in chapter 5. For this purpose, the module has been added to a spatially non-localized FID sequence.

4.3 Fast spiral MRSI sequence development

4.3.1 Principles of a spiral trajectory

Conventional spectroscopic imaging relies on a phase encoding scheme in which the k-space is sampled following a cartesian grid. During the acquisition, no gradient is played in order to acquire the spectroscopic information of the FID signal. Data is thus reconstructed with a Fourier transform of each sampled k-space over time. This method results in a very long acquisition times which limits its application in clinical practice. In spectroscopy, repetition times are often long, so if for example we have a T_R of 2 s, acquiring a 32×32 CSI image would lead to an acquisition time of around 34 min for a single slice. In terms of SNR, this method is very efficient but the PSF for this type of scheme presents side lobes (cf chapter 2) that have to be kept in mind, because the voxels of the resulting spectroscopic image will be contaminated by nearby voxels. This problem becomes of more and more importance as the spatial resolution becomes lower.

Spiral spectroscopic imaging allows the simultaneous encoding of the spatial and spectral dimension of the k-t space. During the acquisition, several k-spaces or partitions of k-spaces are acquired over time. It results in a much lower acquisition time and a lower SNR than conventional encoding. Depending on the applications, it is sometimes necessary to average the acquired signal over several acquisitions to obtain sufficient SNR. For the same example of a T_R of 2 s and a grid of 32×32, the minimum acquisition time would be of 20 s (for a slew rate of 150 mT/m/ms) for one average and one slice. For proton applications, the SNR is often high enough to do only one average (for water-fat applications), but for x-nuclei applications such as ^{31}P for example it is necessary to accumulate several times (around 10 times to see all phosphorus metabolites). However, for spectroscopic ^{1}H applications, averaging could lead to a high spatially resolved proton metabolite quantification.

Several works have been done on spiral trajectories and many types of spiral trajectories exist. It is possible either to begin the spiral from the k-space center or from the k-space edges (in-out spiral and out-in spiral). The shape of the spiral can either be uniform or with a variable density [Glo99; Kim+03]. Using variable density spirals can be useful for example to oversample the center of the k-space and sample less the edges, which can be of interest for applications with short T_2 values for example. It can also be used to oversample the edges of the k-space, which will affects the high frequencies of the image and increase the details. Note that in the case of MRSI, several k-spaces are acquired over time, so it is necessary to return to the k-space center before launching the next spiral. Gradient rewinders are therefore required. For our application, we have implemented spirals with uniform density variations [Glo99] on Siemens Prisma 3 T Scanner.

4.3.2 Constraints of spiral trajectories

Spiral trajectory designs are limited by hardware constraints such as the gradients slew rate and maximum amplitudes. Other physical constraints complicate the CSI reconstruction like B_0 inhomogeneities, eddy currents, delay times between the ordering of the launch of the spiral or the acquisition and the actual launch of the spiral or the acquisition. A robust reconstruction process should take all these constraints into account. A way to reduce their effects is to use short spirals for example.

The reconstruction process includes an interpolation from the acquired k-space points to a cartesian grid, density compensation, filtering.

4.3.3 Spiral trajectory design

Spirals with uniform density were implemented following the Glover algorithm [Glo99], based on archimedian spirals.

The Archimedian spiral trajectory is defined as:

$$k(\tau) = \lambda \tau e^{i\omega\tau} \tag{4.2}$$

where $k(\tau) = k_x(\tau) + ik_y(\tau)$ corresponds the complex location in the k-space.

The gradient waveform is given by:

$$g(t) = \frac{2\pi}{\gamma}\frac{dk(t)}{dt} = \frac{2\pi}{\gamma}\lambda\frac{d\tau}{dt}(1 + i\omega\tau)e^{i\omega\tau} \tag{4.3}$$

where γ is the gyromagnetic ratio.

The slew rate is the derivate of the gradient waveform and is therefore equal to:

$$s(t) = \frac{dg(t)}{dt} = \frac{2\pi}{\gamma}\lambda[\frac{d^2\tau}{dt^2} - \omega^2\tau(\frac{d\tau}{dt})^2 + i\omega(\tau\frac{d^2\tau}{dt^2} + 2(\frac{d\tau}{dt})^2)]e^{i\omega\tau} \tag{4.4}$$

There are two cases in this algorithm. As an increasing spiral which begins from the center of the k-space to the edges is wanted, the gradient waveforms amplitudes have to be increasing. The first case corresponds to the time when the maximum gradient amplitude has not been exceeded, and we are only using the maximum slew rate to sample the k-space as fast as possible. In this case, we have:

$$g(t) = i\frac{4\pi}{3\gamma}\lambda(\frac{9\beta}{4\sqrt{\omega}})^{2/3}t^{1/3}e^{i\omega(\frac{9\beta}{4\omega^2})^{1/3}t^{2/3}} \tag{4.5}$$

with $\beta = \frac{\gamma}{2\pi\lambda}S_0$ and S_0 the maximum gradients slew rate [Glo99].

If the maximum gradient amplitude G_0 is exceeded before the end the spiral trajectory design, we move to the other case, the gradient amplitude limited case. We have:

$$g(t) = G_0(\frac{1}{\omega\tau_2(t)} + i)e^{i\omega\tau_2(t)} \tag{4.6}$$

with $\tau_2(t)$ equal to:

$$\tau_2(t) = \sqrt{\frac{\gamma G_0}{\pi\lambda\omega}(t - T_g) + \tau_s^2} \tag{4.7}$$

and T_g the time corresponding to the moment the maximum gradient amplitude has been reached.

The use of spatial interleaves is possible and enables to improve SNR as the spiral length will become shorter. In the case of spatial interleaves, the k-space is sampled with several spirals as shown in Figure 4.4, rotated one with another, by the formula

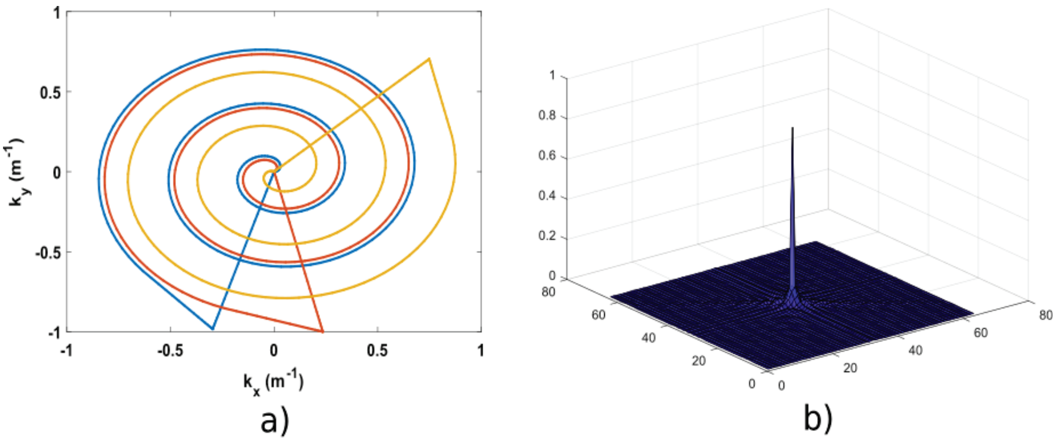

Figure 4.4.: Illustration of the designed spiral trajectory with spatial interleaves for a matrix size of 64×64 and 12 spatial interleaves; only the first, second and sixth is shown here. The PSF is also given in b)

$$g_{xi}(t) = g_{x1}\cos(\frac{2\pi}{N_{spat}}(i-1)) - g_{y1}\sin(\frac{2\pi}{N_{spat}}(i-1)) \tag{4.8}$$

$$g_{xi}(t) = g_{x1}\sin(\frac{2\pi}{N_{spat}}(i-1)) - g_{y1}\cos(\frac{2\pi}{N_{spat}}(i-1)) \tag{4.9}$$

where N_{spat} is the total number of spatial interleaves and $i = [1, N_{spat}]$.

Gradient rewinders are played out after the end of the spiral in order to return to the k-space center. In MRSI, we would have sinusoidal gradient waveforms one after an other in order to sample the (k_x, k_y, t) space.

Figure 4.4 shows the spiral trajectory in the k-space for the first, second and sixth interleave, in the case of a matrix of size 64×64, a FOV of 20 cm, a max slew rate of 150 mT/m/ms and 12 spatial interleaves. The corresponding PSF is also shown.

4.3.4 Spiral under-sampled magnetic resonance spectroscopic imaging

In MRSI, k-space domain, and time domain need to be sampled. More precisely, several k-spaces over time need to be sampled. This enables to encode the spectroscopic dimension. The spectroscopic bandwidth has to be defined such that all the wanted metabolite resonant frequencies can be detected. Typical spectroscopic bandwidth for proton spectroscopy at 3 T is 2000 Hz. As a spiral is not instantaneous, and the temporal spectroscopic resolution can be smaller than the length of the spiral, temporal interleaves are often needed. This implies applying a delay before the acquisition of the spiral train, proportionally to the temporal resolution.

If we call T_{res} the temporal resolution of the FID signal sampling, it is related to the bandwidth as $T_{\text{res}} = 1/\text{BW}$. Let N_{temp} be the number of temporal interleaves, then we have:

$$N_{\text{temp}} = \lfloor \frac{T_{spir}}{T_{\text{res}}} \rfloor \tag{4.10}$$

The number of signal acquisition N_{acq} that has to be done depends on the number of temporal interleaves and spatial interleaves:

$$N_{\text{acq}} = N_{\text{spat}} \times N_{\text{temp}} \tag{4.11}$$

Figure 4.5 illustrates the spiral MRSI acquisition scheme, with all the parameters of interest T_{res} the FID time sampling and T_{spir} the spiral duration. A delay is applied after a new excitation to sample other time points of the FID signal: this is called temporal interleaves. One k-space, or partition of k-space, is acquired by one spiral.

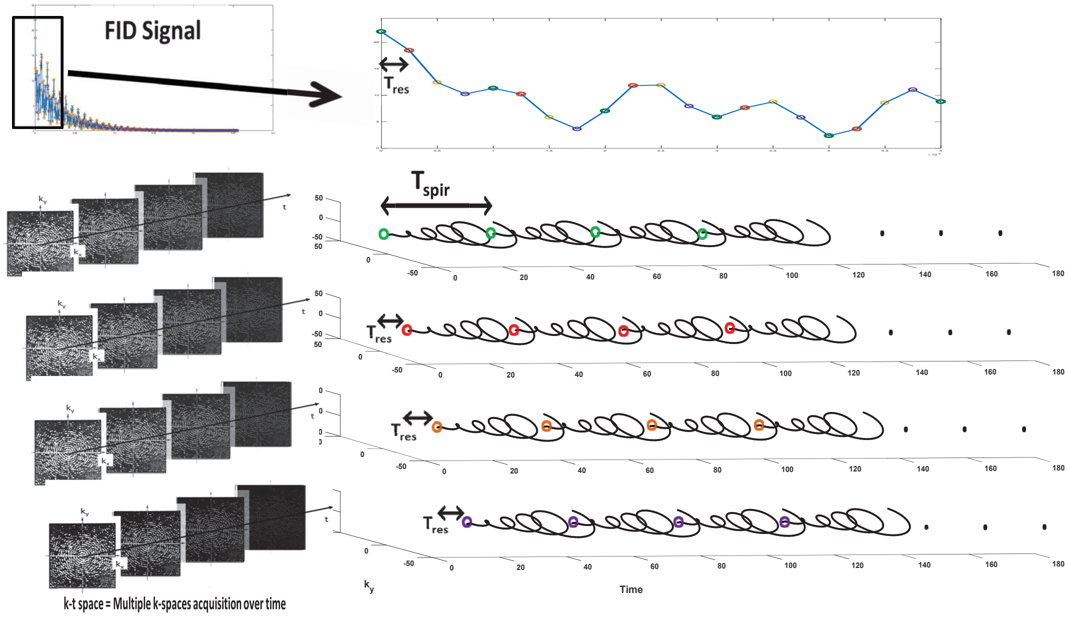

Figure 4.5.: Illustration of the spiral MRSI acquisition scheme with temporal interleaves. The duration T_{spir} is sassumed to be too long to reach the desired spectroscopic bandwidth.

Table 4.1 illustrates the relationship between all the spiral MRSI parameters with the number of acquisition. Note that the smaller the temporal resolution is, the smaller

M_s	16			64			128		
BW (Hz)	3333	2000	1000	3333	2000	1000	3333	2000	1000
$T_{\text{res}}(= 1/\text{BW})$ (μs)	300	500	1000	300	500	1000	300	500	1000
N_{spat}	1	1	2	1	12	12	12	26	26
T_{spir} (μs)	3039	3039	1760	21440	2560	2560	5919	3360	3360
N_{temp}	11	7	2	72	6	3	20	7	2
N_{pts}	512	1024	1024	512	1024	256	1024	256	512
Acq window (ms)	153,6	512	1024	153.6	512	256	307.2	128	512
N_{acq}	11	7	4	72	72	36	240	182	52

Table 4.1.: Impact of the spiral MRSI parameters on the total acquisition time for a FOV of 200 mm and a slew rate of 150 mT/m/ms

the acquisition window is as well, and this leads to a higher Signal to Noise ratio.

In the case of under-sampling the time dimension, less temporal interleaves would be required and thus the acquisition time would be reduced.
In order to estimate the number of temporal interleaves and thus the gain in terms of acquisition time with the use of an under-sampling and SBS, the following algorithm has been developed [Kar+17]:

Pseudo code for finding N_{acqsbs}
Input and variables: p previouly calculated SBS irregular positions are stored in the vector P, recall that $p < n$, and the acquired sample number p_t at the current discrete time index t are stored in the vector P_t. The index t_{prev} is used to select two time samples ensuring a spacing greater than the spiral length.
Initialisation:
$P_t = [],\ p_t = 0,\ N_{\text{exsbs}} = 0$
Procedure:

```
while $p_t < p$ do
    $N_{\text{acqsbs}} = N_{\text{acqsbs}} + 1$
    $t_{\text{prev}} = -T_{\text{spir}}/T_{\text{res}}$
    for $t = 0$ to $T_{\text{sig}}/T_{\text{res}}$ do
        if $t \in P$ & $(t - t_{\text{prev}}) > T_s/T_{\text{res}}$ then
            $t_{\text{prev}} = t$, $p_t = p_t + 1$, $\{P_t\}_{p_t} = t$
        end if
    end for
end while
```

We then have $N_{\text{acqsbs}} \leq N_{\text{acq}}$.

As seen in chapted 3, the reduction factor cannot be higher than N/P. The higher the reduction factor is, the lower the Signal to Noise Ratio is likely to be.

4.3.5 Non-cartesian image reconstruction

Non-cartesian sampling schemes are known to be less sensitive to motion (for example for radial or spiral sampling), and to sample more efficiently the k-space, to access very short echo times, and therefore detect metabolites with a very short T_2^*. Their nature requires dedicated image reconstruction algorithm, as a standard inverse Fourier transform cannot reconstruct the MR data. Several non-cartesian reconstruction methods exist. Gridding methods consist of a projection of the acquired data points in the k-space into a cartesian grid. Then an inverse Fourier Transform is applied to reconstruct the image domain. Most gridding methods use a Kaiser-bessel kernel [Jac+91] which is a convolution kernel going through the k-space trajectory and assign a weight to grid points according to their distance to the sampled points. This is also the convolution kernel used in image reconstruction in this Thesis.

An other reconstruction method that has been used in this thesis, particularly in the part detailed in the previous chapter, was the Non-Uniform Fast Fourier Transform method (NUFFT). This method takes into account the irregular distribution and the sparsity of the trajectory in k-space. In [FS03], NUFFT has been improved. Pr. Jeff Fessler developed an algorithm available online called image reconstruction toolkit ([Fes]) and that is what we use in this thesis. The principle of NUFFT extends the regular Discrete Fourier Transform (DFT) expression as

$$X_k = \sum_{t=1}^{N} x(s_t) \exp(-2i\pi kn/N) \tag{4.12}$$

where X_k is the non uniform fourier transform of x evaluated at samples s_t. The spacing between samples s_t is not uniform. The NUFFT algorithm has been compared with the Kaiser-Bessel gridding method [Sar+01] and it has been found that they were two similar techniques, as the NUFFT algorithm is actually the same as a Gaussian kernel gridding method [Sar+01].

These image reconstruction methods are often combined with density compensation functions, in order to weight each sample of the trajectory before gridding [JP09].

Several density compensations can be used such as a linear one, or a Voronoi diagram [Vor08; Mal+05]. The Voronoi diagram based density compensation function computes a partition of a spatial domain given the samples points and their distribution over space. This results in many regions called "cells" which area decreases as the number of neighbouring samples increases. The weight will thus be higher for samples close to the edges than samples in the center. In this thesis, the voronoi diagram has been used for density compensation (figure 4.6).

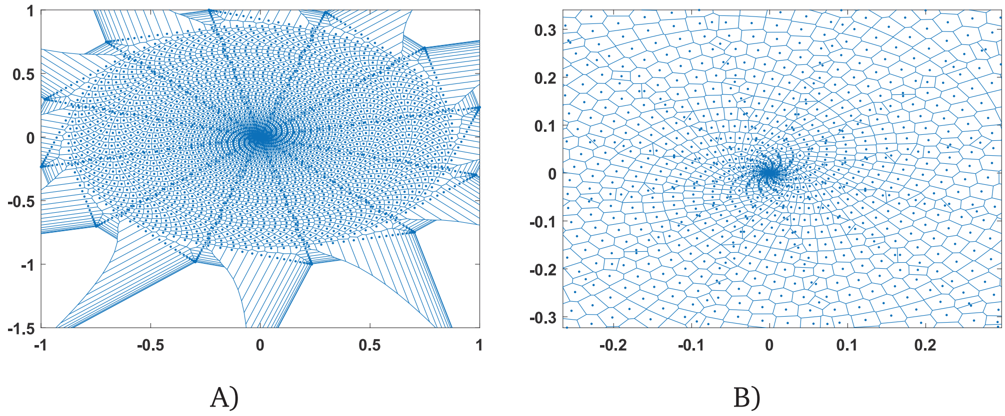

A) B)

Figure 4.6.: A) Illustration of a 2D computer diagram for the designed spiral trajectory with a matrix size of 64×64 and 12 spatial interleaves. A zoom in the center is shown in B). The size of the cells decreases when the number of samples in a region is highly concentrated.

4.3.6 Sequence design, specificities and hardware

4.3.6.1. Implementation steps

Sequence implementation of the final spiral under-sampled MRSI sequence has been done in several steps.

1) First, the objective was to do spiral imaging with a slice selective sinus cardinal excitation pulse followed by sinusoidal gradient waveforms (in the readout and phase directions) sampling one k-space with a spiral, or multiple ones in the case of the use of spatial interleaves.

2) Then, a train of gradient waveforms sampling several k-spaces over time, with a temporal resolution equal to the length of one spiral, has been implemented to get MRSI acquisitions with low spectral resolution.

3) To increase the spectral resolution, temporal interleaves were then implemented to finally reach the final goal of implementing the spiral under-sampled MRSI se-

quence with a temporal selection of samples with the SBS algorithm.

At each step of the implementation, tests were done on a water phantom and validations had to be made to go to the next step. The first objective was to be able to properly reconstruct an image, and then reconstruct a spectrum when a train of spirals has been used. Details about sequence implementation and problems encountered are given in next sub-sections.

4.3.6.2. Under-sampled spiral MRSI sequence development on IDEA

The sequence has been developed under Siemens' Integrated Development Environment for Applications (IDEA) software. A sinus cardinal pulse combined with the slice selective gradient, followed by a refocusing gradient are used before the spiral train is played. The sequence was tested on a Prisma 3 T scanner (max slew rate = 200 T/m/sec and Max Gradient amplitude G_{max} = 80 mT/m). Gradient rewinders were used at the end of each spiral to return to the k-space center. Spoilers in each axes were added at the end of the spiral train. The spectral bandwidth BW sets the spectroscopic temporal resolution T_{res}. The matrix size M_s and the number of spatial interleaves N_{spat} set the duration of one spiral T_{spir}.

The number of temporal interleaves N_{temp} can then be calculated as well as the total acquisition time T_{acq} which depends on the Repetition Time (T_{R}):

$$T_{\mathrm{acq}} = T_{\mathrm{R}} \times N_{\mathrm{spat}} \times N_{\mathrm{temp}} \tag{4.13}$$

The impact of the different spiral MRSI parameters on the acquisition time are illustrated in table 3.1.

The SBS algorithm (see section 3.2.3.2) was embed in the IDEA code and takes as inputs the frequency support, the vector size N_{pts} and the reduction factor for under-sampling which can be set by the user in a Special Card. It outputs then the temporal samples to acquire.
The frequency support depends on the applications and can be properly chosen from a global spectrum obtained from a spatially non-selective FID sequence.


Nb of Interleaves 1

Type of excitation pulse Sinc pu...

Sinc Pulse duration 1280

Spin-echo Spin-echo ☐

Temporal spectrsocopic resolution (in us) 500

B1 MAP B1 MAP ☐

First angle (in degrees) 30

B0 MAP B0 MAP ☐

First echo (in us) 25

Grad X off Grad X off ☐

Figure 4.7.: Illustration of the 'Special Card' which is the window interface where the user can manage and modify parameters such as the number of spatial interleaves, the maximum gradients slew rate, whether we want to use an under-sampling or not...

The user can manage many parameters and they are all stored in a user interface called Special Card (figure 4.7). The user can choose the number of spatial interleaves, the Analog to Digital Converter (ADC) 'dwell time' in μs (it is actually the sampling time of a spiral sampling, different from the sampling time of the FID signal), the gradients maximum slew rate in mT/m/ms, the type of excitation pulse (between a sinus cardinal slice selective pulse and rectangular non slice selective pulse), the pulse duration in the case of a sinc pulse, the temporal spectroscopic resolution (or FID signal time sampling), which is the inverse of the spectroscopic bandwidth, the frequency support of interest (with a maximum of 3 blocks), the reduction factor for the under-sampling.

Figure 4.8 illustrates the difference between the spiral sampling 'dwell time', the spiral duration T_{spir}, and the FID time sampling T_{res}.

Switches also enables to use the sequence as a spin-echo sequence, to do B_1 and B_0 maps or to turn off one or two gradients, for example for k-space trajectory estimation. Indeed, k-space trajectory calculation can be made by switching on and off the readout and phase gradients, within one or two slice as in [Duy+98; TM09] or within 4 different slices, for a more accurate trajectory estimation as in [Zha+98].

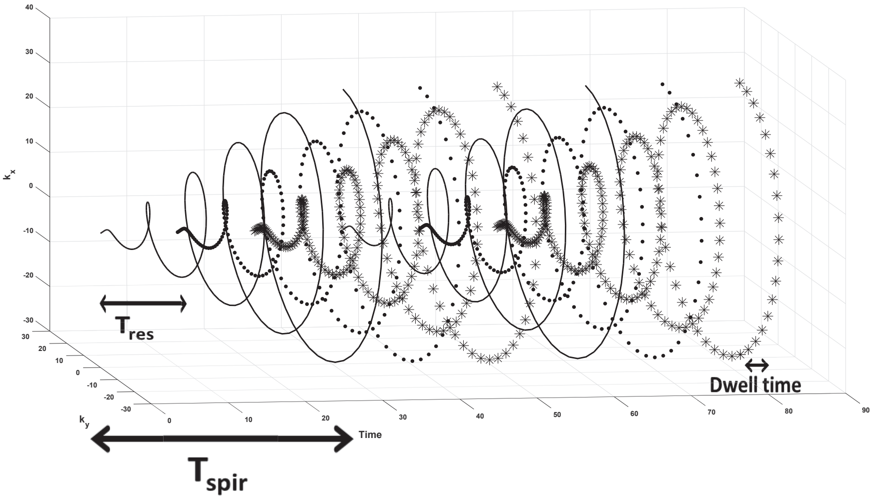

Figure 4.8.: The different timings used in the developed spiral spectroscopic sequence. T_{spir} corresponds to the spiral duration, T_{res} to the FID time sampling and the 'dwell time' is the spiral sampling time.

To conclude, two sequences were implemented and compared:

1) A spiral MRSI sequence with a uniform and full temporal sampling of the FID signal, which we will call afterwards "Conventional spiral MRSI" (see figure 4.9)
2) A spiral MRSI sequence with an irregular SBS-based under-sampling of the FID signal, which we will call afterwards "Under-sampled spiral MRSI" (see figure 4.10)

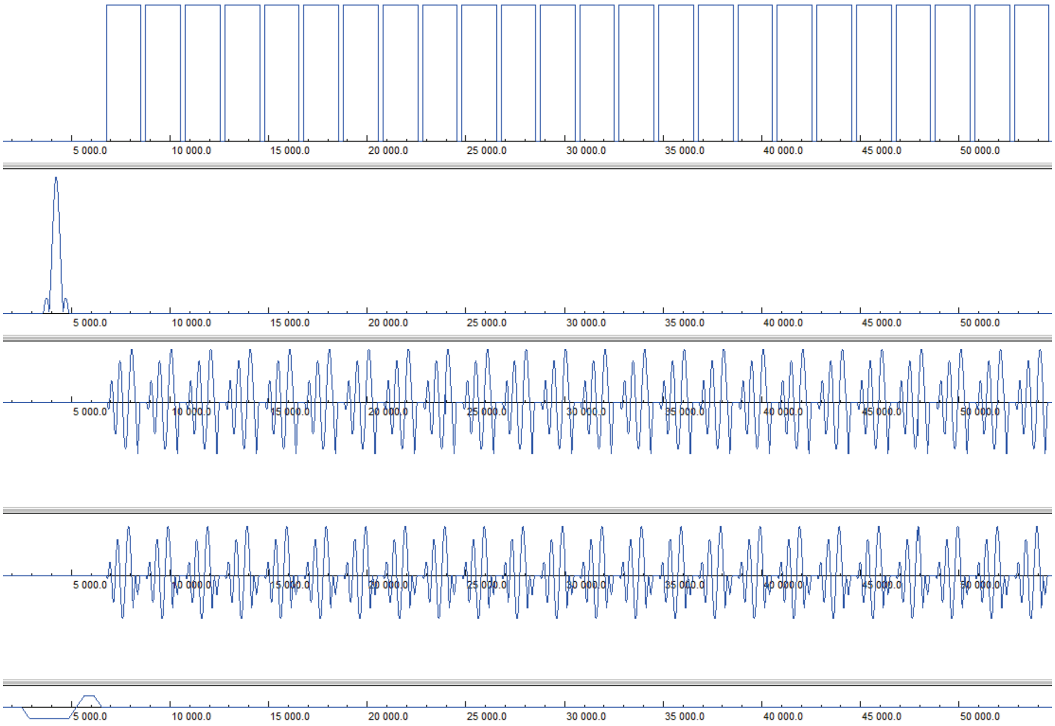

Figure 4.9.: Sequence diagram of the spiral MRSI sequence taken from Siemens' IDEA simulator environment. The first line is for the ADC, second line is for the pulse excitation, third line for the readout gradient, fourth for the phase gradient and fifth for the slice selective gradient.

4.3.6.3. Technical constraints

In order to reduce technical problem during the preparation and the launch of the sequence on a MR system, some specific implementation had to be done.

A small delay is applied before the launch of the spiral train, to be sure that the ADC does not launch while the refocusing gradient is still running and being acquired. In the case of the use of spatial interleaves, the same scheme is repeated, with a rotation of the gradient waveforms proportionally to the number of spatial interleaves. If temporal interleaves are needed, the scheme is also repeated with an additional delay on the application of gradients, proportionnally to the temporal spectroscopic resolution chosen in the 'Special Card'.

The goal is to sample a number of temporal points, with spirals sampling a k-space, or a partition of it in case of spatial interleaves. The vector size is chosen in the user interface window and with a defined spectroscopic temporal resolution.

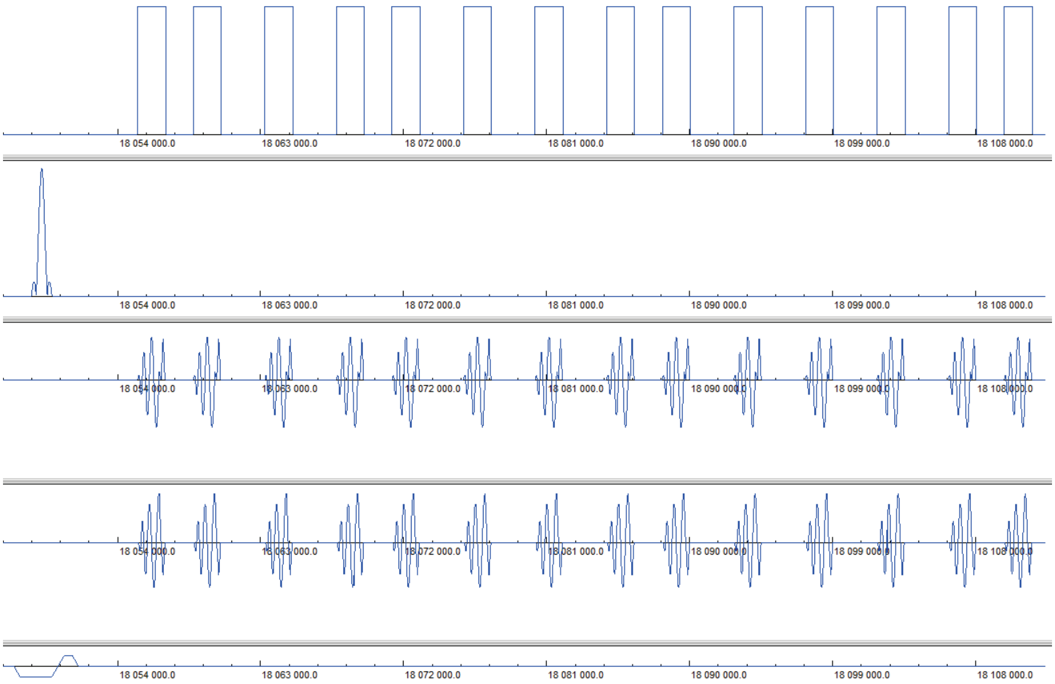

Figure 4.10.: Sequence diagram of the spiral under-sampled MRSI sequence taken from Siemens' IDEA simulator environment. The first line is for the ADC, second line is for the pulse excitation, third line for the readout gradient, fourth for the phase gradient and fifth for the slice selective gradient. Some dead times are present due to the under-sampling of the temporal dimension.

The delay between one ADC and another has to be proportional to this temporal resolution. One ADC per spiral is used. The maximum ADC length seems to be of 16384 sample points (in IDEA), that is why we opted for one ADC per spiral because we have a lot more than 16384 points to sample (with all the spirals). An "ADCSet" (for clock synchronization) is played at the beginning of each ADC.

Two modes are available: The full sampling mode and the under-sampling mode. A dead time is necessary and is added in the case of an under-sampling between ADCs. This dead time is proportional to the spectroscopic resolution and will therefore enable to sample irregularly and temporally k-spaces given the prior selection with the SBS algorithm (see figure 4.10). In the case of a full sampling, no additional dead time between ADCs is required as we sample every time points at a given spectroscopic resolution. However, an additional delay is played after each ADC, so that we are sure that every time points we sample will be proportional to the chosen temporal spectroscopic resolution. The timing is incremented each time an ADC is run.

To calculate the T_R fill we remove from the wanted T_R the length of each ADC, the length of the slice selective gradients and the refocalization gradient, and of all the introduced dead times. The ADC header is filled with all relevant information.

In the run loop (loop that executes the scanning in the MR scanner), a loop for averages including one for spatial interleaves and one for temporal interleaves are used. Each of the relevant numbers are stored in the Measurement Data Header (MdH): spatial interleaves, averages, temporal interleaves and ADC number. In the case, of spatial interleaves, the gradients are rotated according to the number of spatial interleaves at each step of the spatial interleaves loop.

4.3.7 ^{1}H *In vivo* experiments

4.3.7.1. Material and methods

For^{1}H experiments, a surface coil ^{1}H/^{31}P Tx/Rx placed under the calf muscle of the volunteer placed in supine position was used for the experiments. The MR system was a 3 T Siemens Prisma. ^{1}H acquisitions were done with a T_R of 1 s, a bandwidth of 2000 Hz or 3300 Hz for reconstruction of spectra (containing water and all lipid resonance frequencies). Matrices were set to 128 x 128, with a Field Of Vew (FOV) of 20 cm, a slice thickness of 2.5 cm or 4 cm and 4 dummy scans. No averages were done. A reduction factor of 3 has been used for the under-sampled spiral CSI. The spectral support has been chosen such that it included the main lipid frequency peak and the water peak.

4.3.7.2. Reconstruction method

The reconstruction pipeline is given in figure 4.11. After reading the raw data, a gridding algorithm is performed to reconstruct the 2D spatial dimension. Afterwards, a 1D FFT is done to reconstruct the spectrum for each pixel in the case of a uniform sampled MRSI acquisition and a LS reconstruction in the under-sampled case. Finally, a quantification is done using a mono-exponential fit on a home made MATLAB routine to extract metabolite and T_2^* maps.

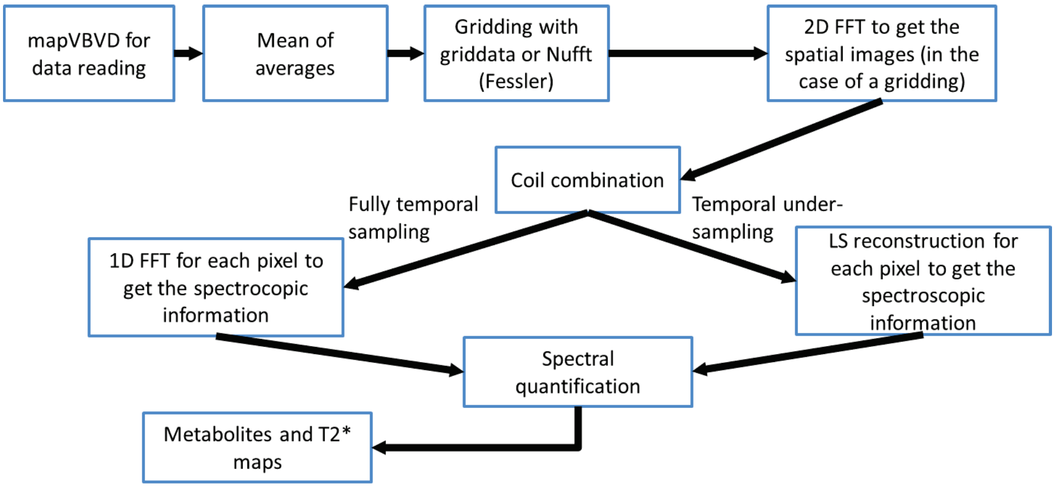

Figure 4.11.: Reconstruction pipeline from raw data reading to final spectral reconstruction, and metabolite and T_2^* maps generation.

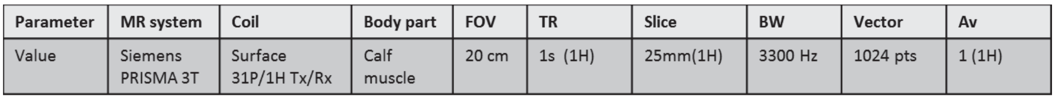

Parameter	MR system	Coil	Body part	FOV	TR	Slice	BW	Vector	Av
Value	Siemens PRISMA 3T	Surface 31P/1H Tx/Rx	Calf muscle	20 cm	1s (1H)	25mm(1H)	3300 Hz	1024 pts	1 (1H)

Figure 4.12.: Acquisition parameters for the results shown with spectroscopic artefacts in ^{1}H MRSI.

4.3.8 Conventional spiral MRSI ^1H *In vivo* results: spectroscopic artefacts

In this part, no under-sampling is being considered. Indeed, 2 methods are compared, the conventional and non-undersampled spiral MRSI sequence. Note that an SBS-based undersampled spiral MRSI sequence will be shown and discussed in a further section. At one point of the implentation, problems were encountered with the use of the implemented spiral MRSI sequence that we still have, at the end of the thesis project, for ^{1}H experiments. In order to understand and reduce the artefacts that we see on our experiments, many tests were done. Here, we present results showing the actual state of the problem.

Results shown in figure 4.13 and 4.14 were obtained in experiments on the calf of a healthy man of 37 years. Detailed parameters of the acquisitions are given on Figure 4.12. In this experiment the number of temporal interleaves was 13 and the number of spatial interleaves was 26. This corresponds to 13 delays applied at each train of gradient waveforms to sample the whole 1024 time points wanted. On one spiral train we will then have around $1024/13$ spiral sampling $1024/13$ k-spaces at specific time points.

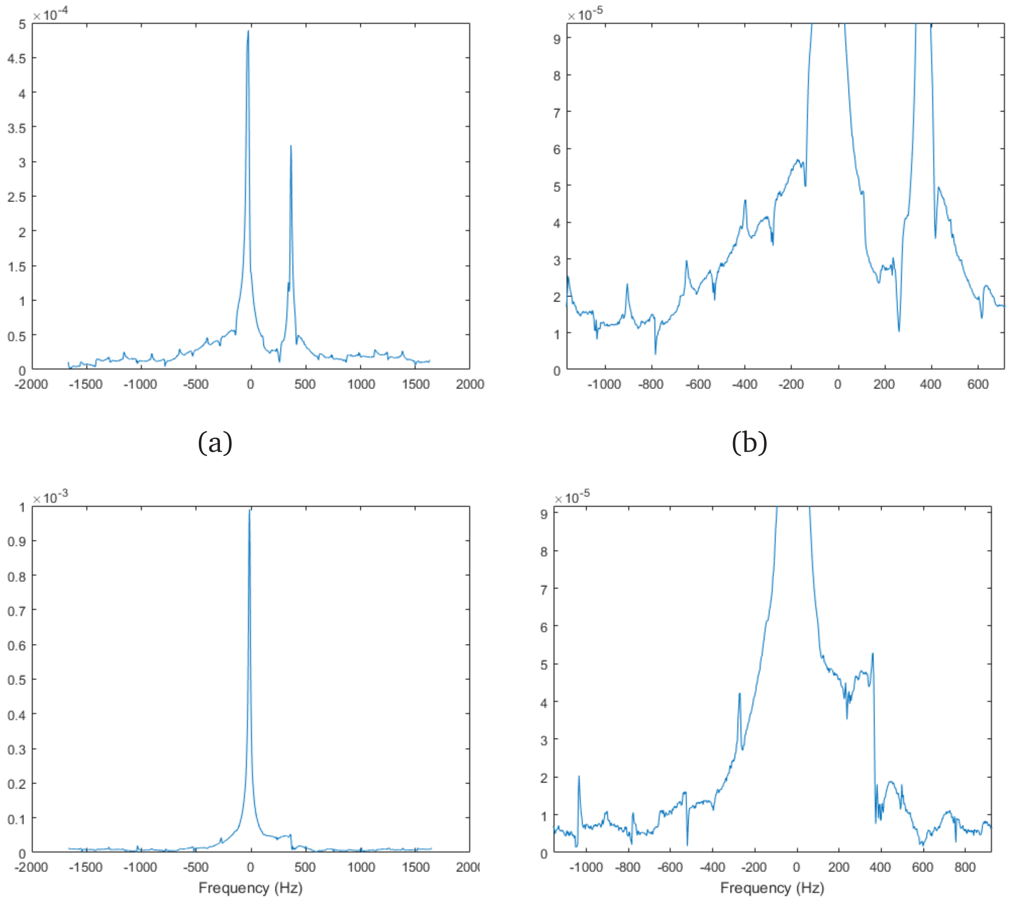

(a) (b)

(c) (d)

Figure 4.13.: Reconstructed spectra in the muscle and fat, (a)Magnitude spectrum in a voxel containing fat, (b) Zoom on the spectrum in a voxel containing fat, showing artefacts encountered (c) Magnitude spectrum in a voxel located in the muscle, (d) Zoom on the 1H spectrum acquired in the muscle showing the artefacts encountered

4.3.8.1. *In vivo* results: observations

In figure 4.13, the reconstructed spectra for pixels in the muscle and a voxel containing fat are shown. We can see the spectroscopic artefacts: Unwanted peak replications are in the spectra.

4.3.8.2. Study and modeling of artefacts

In order to understand why these peak artefacts occur, we studied the module, phase of the signal corresponding to this artifact signal through an approach to model the artefacts. Figure 4.14 shows, for one pixel, the magnitude, spectrum of the whole

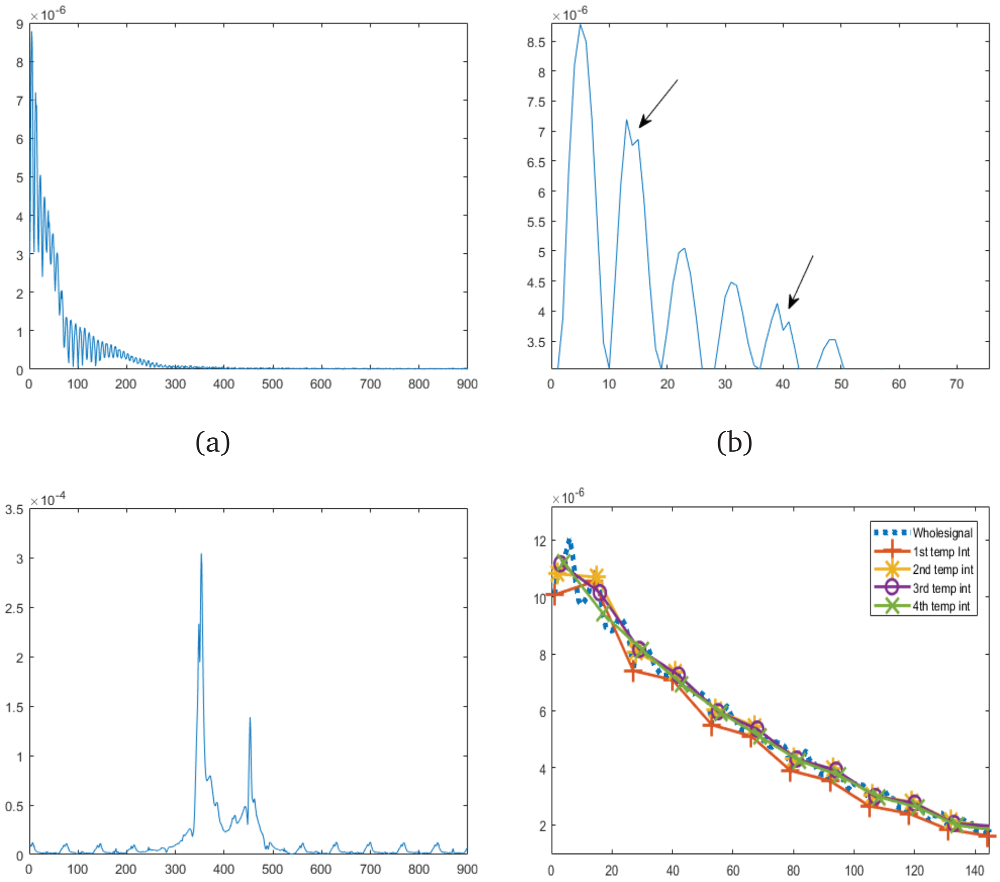

(a) (b)

(c) (d)

Figure 4.14.: (a) Absolute time domain signal, (c) its associated spectrum in modulus and (b) zoom on the fifty first time point signal (d) decomposition corresponding to the first 4 temporal interleaves. First temporal interleave in red, second in yellow, third in pink and fourth in green. Note that The first temporal interleave is abnormally shifted downwards

signal, and the signal from the first four spiral trains, or temporal interleaves.

When we represent the signal magnitude (Figure 4.14), the phase or spectra of each temporal interleave, we do not detect any issue or artefact (i.e within one spiral train). The signal seems coherent. However, the signal is not coherent for one interleave with an other. We can see a magnitude issue from one to an other, as well as a phase issue. They don't seem to have the same zero and first order phase. The first temporal interleave appears to have the most significant difference with the other ones, in amplitude and phase.

In order to model the artefacts, we used the HLSVD algorithm (available on the jMRUI software, java Magnetic Resonance User Interface, version 5.0) applied on the whole signal. With the help of the HLSVD decomposition, we were able to extract the signal only coming from the artefacts (Figure 4.15). Then, we were able to look at each temporal interleave in this signal by plotting only the signal every 13 points, 13 being the number of temporal interleaves. As already seen, we observed that the first temporal interleave had the most significant impact on the artefact, the other temporal interleaves were impacting it less. We can look at the modelled signal and the corrected signal by applying the original one minus the modelled artefact signal on figure 4.15.

The zero order phases of the signals from each spiral train are different, especially the zero order phase of the first spiral train, with respect to the others. By correcting the zero order phase of all the temporal interleaves, we were able to reduce even more the artefacts. To find the optimal zero order phase to apply, we implemented an algorithm that searches for the zero order phases that minimize the artefacts based on a simulated annealing algorithm optimization looking for these phases, with MATLAB.

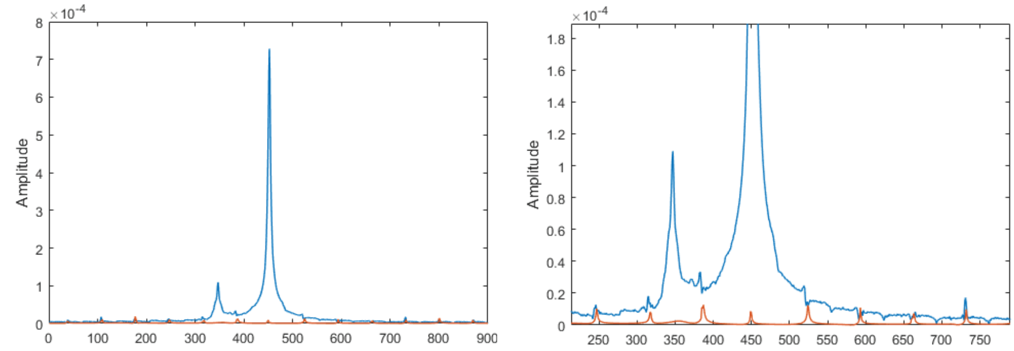

(a) Spectrum in the muscle

(b) Zoom

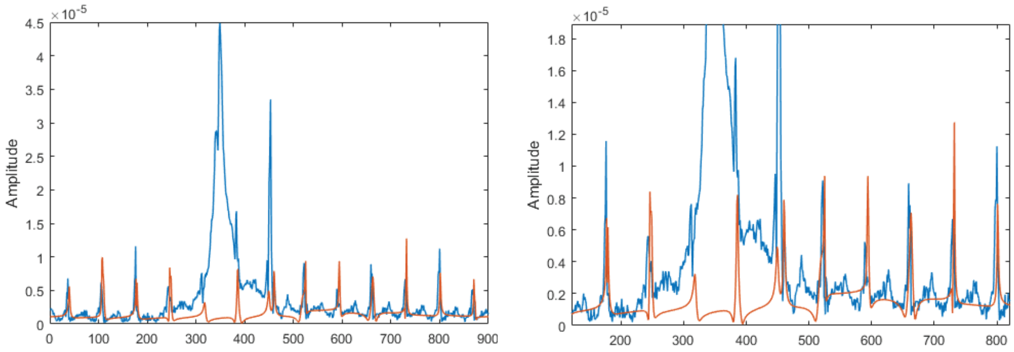

(c) Spectrum in the fat

(d) Zoom

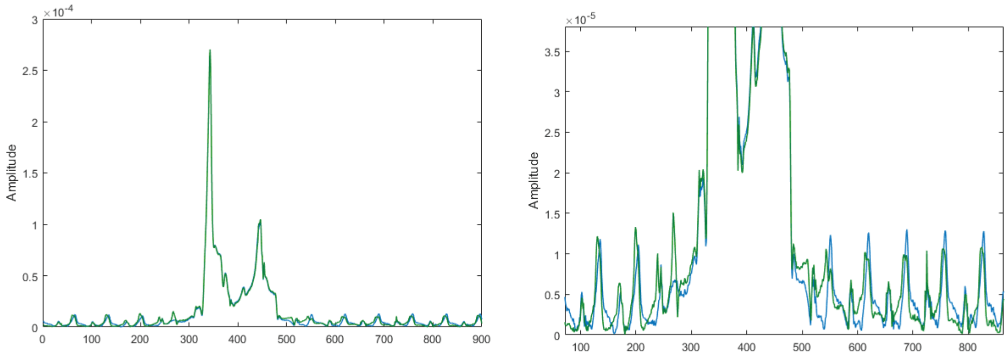

(e) Original signal(blue) and Corrected signal (green)

(f) Zoom

Figure 4.15.: Reconstructed spectra after correction of the spectra from a modeling with the HLSVD algorithm (a), b), c), d)). In blue the original signal, in red the modelised spectra resulting from the HLSVD algorithm, and in green the corrected signal (original signal minus the modelised signal with artefacts) (e), f))

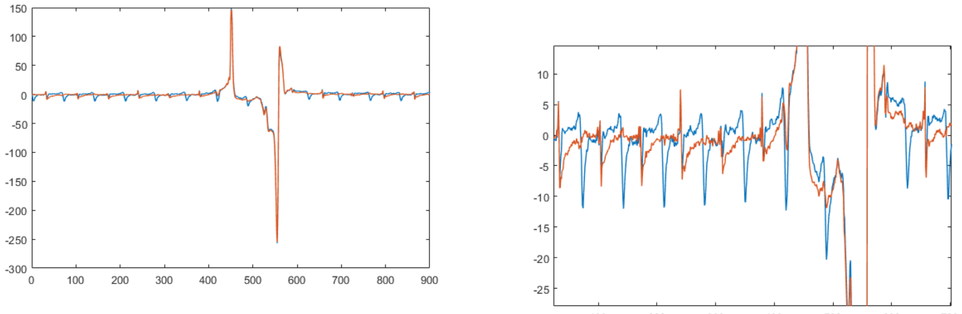

(b) Original signal(blue) and Corrected signal(red)

(b) Zoom

Figure 4.16.: Impact of an order 0 phase correction for all temporal interleaves on the final reconstructed spectra. The original spectra is in blue and the corrected one in red.

4.3.8.3. Discussion and Comments on observed artefacts

When no gradient is played out, we see the same issue, so this is not a k-space trajectory problem. The higher the number of interleaves, the higher the number of artefacts, thus the artefacts are linked to temporal interleaves

When the SNR decreases the signal of interest is of the same order of magnitude as the artefacts. Artifact peak magnitude is not related to the number of temporal interleaves. In fact, magnitude and phase jumps between each temporal interleaves.

Our hypothesis to the cause of this problem are

- first the ADC numeric filter, that can affect our received signal.
- Maybe as well, there is an ADC opening delay. Each ADC may not open at the proper time, the dead time may vary from one ADC to the other.
- The ADC phases is maybe not well managed in the code. The fact that no ADCNeg is played could be a mistake.
- This is surprising that the first temporal interleave is the most different from the other (in terms of order 0 phase, signal amplitude). It seems really different from the others. We have been thinking of some kind of steady state effect, but before all our acquisitions, we do 4 dummy scans.

- Further tests will include changing the ADC dwell time, to see if the digital filter has an impact on the reconstruction. K-space trajectory measurements are going to be done as well in order to be sure that the center of the k-space is sampled at each spiral's start.

- As the spiral spectroscopic imaging readout is demanding in terms of gradients and scanner hardware, slow frequency drifts over times are induced and are a problem if RF excitation pulses are used [Bog+14b]. Maybe it is necessary to use interleaved navigators to correct those frequency drifts [Bog+14a].

4.3.9 ^1H *In vivo* for fat-water and proton metabolite quantification

Previously seen artefacts were reduced by increasing the SNR and increasing the slice thickness. Inside the muscle, the SNR is higher than in the periphery, so the artefacts are less significant. It was therefore possible to analyze ^{1}H MRSI data. Both sequences, conventional and under-sampled spiral MRSI, were tested with a spectral bandwidth of 2000 Hz and a slice thickness of 4 cm. The acquisition times were of 3 min and 32 s for the conventional spiral MRSI and 1 min and 48 s for a matrix size of 128×128, 26 spatial interleaves, which results in a gain in terms of acquisition time of around 2.

Additional tests were done, with a lower spatial resolution (matrix size of 64×64, 12 spatial interleaves) and more accumulations (5 averages), in order to possibly assess small proton metabolite concentrations. This has been done only in a conventional spiral MRSI acquisition and resulted in a total acquisition time of 6 min and 4 s.

4.3.9.1. Results

Figure 4.17 shows images of water, fat and T_2^* maps of water and fat both in the conventional and the under-sampled case. The average T_2^* values were around 20 ms in the muscle and 30 ms in the sub-cutaneous regions for the T_2^* of water, for both the conventional and under sampled spiral MRSI sequences.

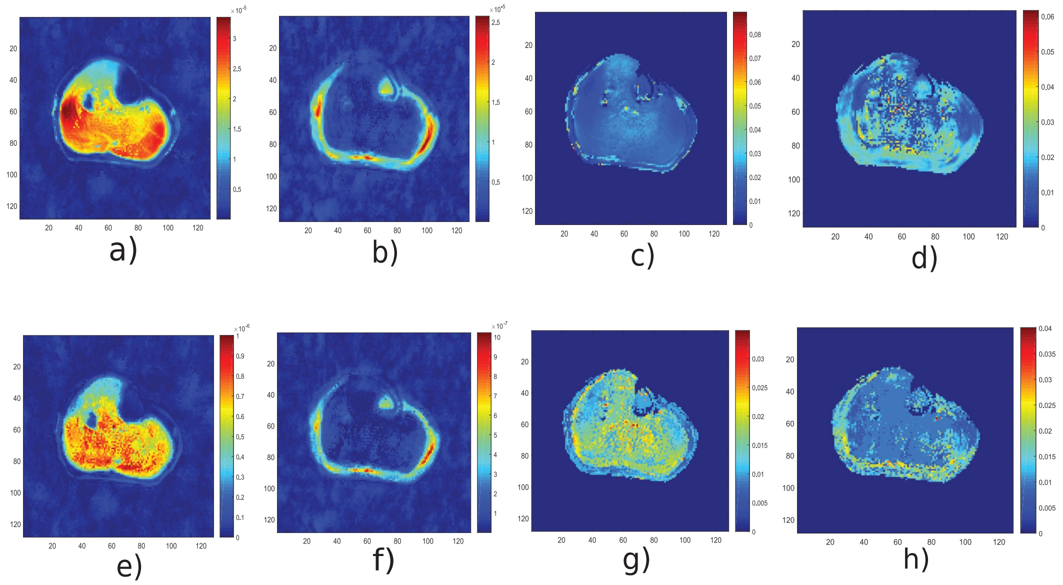

a) b) c) d)

e) f) g) h)

Figure 4.17.: Images of water (a)), fat (b)), T_2^* of water (c)) and T_2^* of fat (d)) for the conventional spiral MRSI and for the under-sampled spiral MRSI (e),f),g),h))

In figure 4.18, the raw spectra and the estimated one, on water and fat only, for one pixel of the calf muscle can be seen and for both full and under-sampled methods. The estimated parameters (for the estimated spectrum from the red cross shown in figure 4.18) were, for the full case, 4.66 ppm for the frequency of water, 1.54 ppm for fat, 2.78×10^{-5} for the water amplitude, 6.03×10^{-6} for the fat amplitude, which corresponds to a fraction (water over fat) of 4.63. Estimated dampings were of 49.3 Hz for water and 44.3 Hz for fat. For the under-sampled case, the estimated frequencies were 4.64 ppm for water, 1.51 ppm for fat, the estimated amplitudes of 7.17×10^{-7} for water and 1.54×10^{-7} for fat, which corresponds to a ratio of 4.66. Finally, estimated dampings were 54.8 Hz for water and 43.9 Hz for fat.

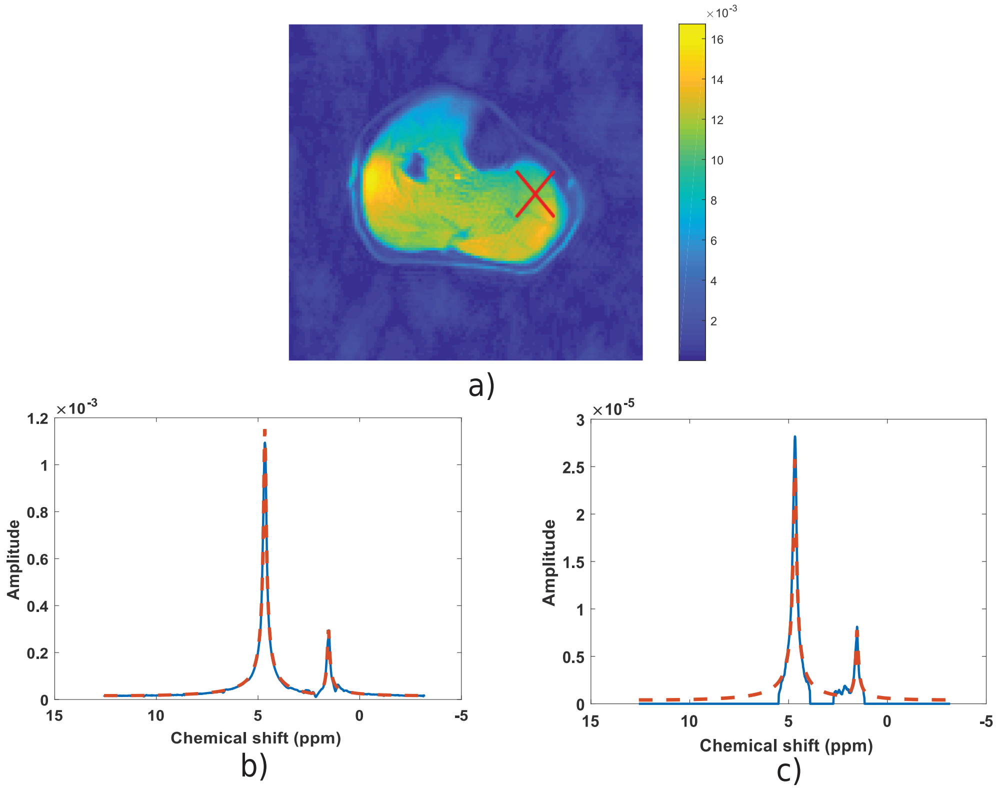

Figure 4.18.: Raw spectra in blue and fitted spectra in dotted red for the highlighted pixel shown on the reconstructed water image (a)) for the conventional spiral MRSI case (b)) and the under-sampled case (c)).

A more spectrally resolved and accumulated spectrum is shown in figure 4.19. Intra- and extra-myocellular lipids can be seen for the spectra in this pixel.

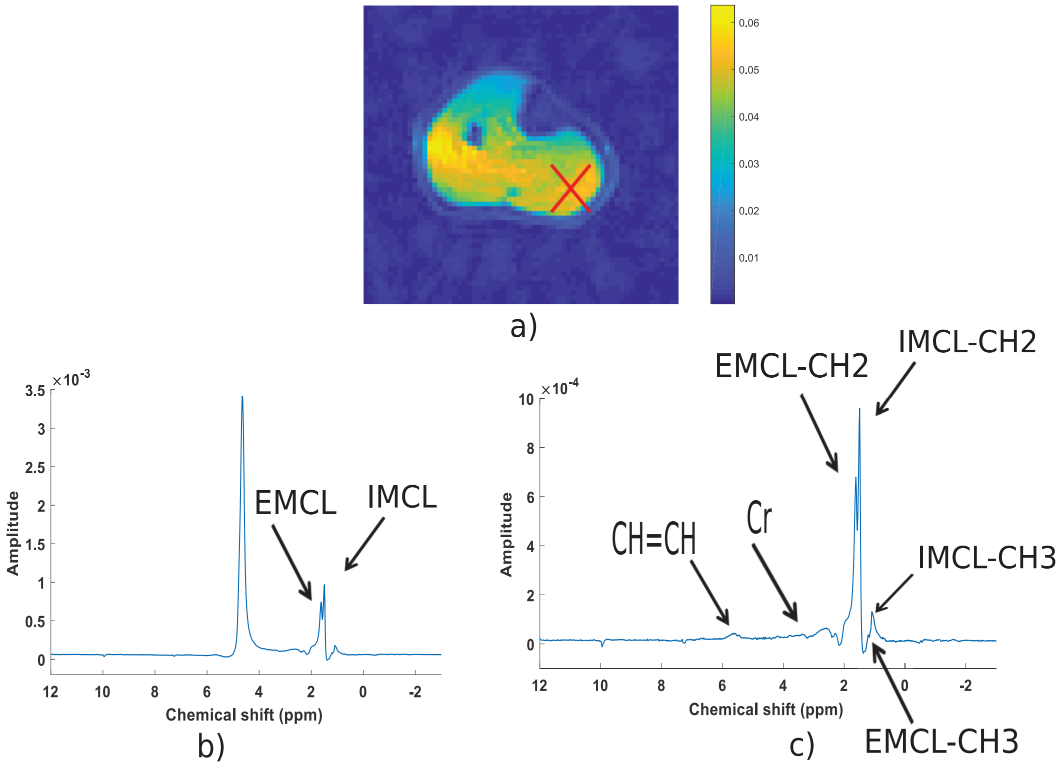

Figure 4.19.: Reconstructed spectrum from the highlighted pixel without (a)) and with (b)) water suppression performed, in a postprocessing step, with the HLSVD algorithm which decomposes the signal in a sum of lorentzian lines and removes thoses corresponding to the water peak. Proton metabolites and lipid compounds that can be detected are shown.

4.3.10 Discussion of ^{1}H experiments

In the context of this thesis, ^{1}H experiments were first done because the SNR is higher than x-nucleus applications which ease sequence development. Many problems have been encountered and the still unresolved issues are the peak replications artefacts (in the case of a conventional spiral MRSI). These artefacts prevented us to do high, clean spectrally and spatially resolved ^{1}H MRSI to quantify proton metabolites of small concentration as seen in figure 4.19 because the artefacts are of the same amplitude (or higher) as of the small concentration ^{1}H metabolites such as creatine or TMA. The under-sampled spiral MRSI sequence would not suit for this type of application because the spectral support of interest would become too large if we want to look at all proton metabolites' resonances.

As explained in a previous section, the lower the bandwidth is, the lower the number of temporal interleaves are going to be, but the less sparse the spectra will be as well with respect to the spectral bandwidth used for spectral representation. For our developed fast under-sampled spiral MRSI method, which assumes a sparse

spectrum, this is a limitation that prevents its application in the case of a spectrum support length equivalent to the full bandwidth length.
However, this under-sampled spiral MRSI sequence proved to be interesting in the case of fat-water applications, when the spectral support will contain only the main water and lipid peak resonance frequencies: it has the advantage, compared to IDEAL/mDIXOn sequences, of providing T_2^* measurements of the lipid peak.

4.3.11 $^{31}\mathrm{P}$ *In vivo* experiments

4.3.11.1. Introduction and constraints due to phosphorus applications

The first goal of the development of the prosposed under-sampled spiral MRSI sequence was to apply it on phosphorus CSI. Phosphorus applications suffers from low SNR and low sensitivity. It implies to use a spatial resolution much lower than for proton applications, a longer repetition time, and fewer partitions or spatial interleaves. Morever, the gyromagnetic factor of the phosphorus nucleus is smaller than proton nucleus, and therefore, the gradients waveforms designing the spiral k-space sampling change. They become longer as well as the spiral duration. In other words, for the same spatial resolution, and the same gradients amplitude and slew rate, the time to sample one k-space will be longer in the case of a phosphorus application. Therefore, more temporal interleaves would be needed for the same spectral bandwidth, and longer the acquisition time would be as well.

The spectral bandwidth was chosen here such that it contains all phosphorus resonances, from inorganite phosphate to beta-ATP, which corresponds to a spectral bandwidth of 2000 Hz at 3 T. The spectral support was chosen such that it contains Pi, PCr and gamma-ATP resonances, and composed of 2 blocks, one centered on the Pi resonance, large enough to take into account the Pi resonance frequency variations due to pH variations during an exercise, and another block containing PCr and gamma-ATP resonances. It was chosen manually during the acquisition (in the user special card) and its size was around 260 frequency points (for a total of 1024 frequency points in the spectral bandwidth). A reduction factor of 3 was therefore chosen for the under-sampled acquisitions ($N/P \approx 3.9$).

4.3.11.2. Material and methods

A surface coil ^{1}H/^{31}P Tx/Rx placed under the calf muscle has been used for the experiments. For dynamic ^{31}P measurements, isometric plantar flexions of the calf muscle were periodically operated using an MR compatible ergometer (Trispect, Ergospect, Innsbruck, Austria). This system allows us to trigger the acquisition at the resting period between exercise, to control and monitor the intensity of the exercise. The protocol consisted in 40 s of rest, 2 min exercise (one push every 2 s) and 4 min rest. Both conventional and under-sampled spiral CSI sequences were run one after an other.

A volunteer positioned supine, with the coil placed under the calf muscle, underwent a protocol including, previous to ^{31}P experiments, a dixon sequence acquisition to refine the localisation for proper localization (Flip angle $9°$, T_{R} 4.1 ms, T_{E} 1.4 ms, matrix size 118×192, FOV $169 \times 206\ \mathrm{mm}^2$).

Careful shimming was previously achieved for all spectroscopy acquisitions with a box containing the calf muscle of interest, avoiding sub-cutaneous lipids.

4.3.11.3. ^{31}P protocol: ^{31}P-Spiral CSI conventional and under-sampled

First, ^{31}P experiments at rest were made using a non-localized ^{31}P-MRS sequence with a T_{R} of 4 s, and with matrices size of 8 x 8, as well as with a ^{31}P-CSI double phase encoding sequence. For the latter, the FOV was set to 20 cm, and the slice thickness to 6 cm (table 4.2). 10 accumulations have been done and 4 dummy scans were used prior to scanning for a final acquisition time of 4 min 32 s. Finally, a ^{31}P-CSI spiral sequence and an under-sampled ^{31}P-CSI spiral sequence with the same acquisititon parameters were performed at rest. The resulting acquisition times were 2 min 56 s for the conventional spiral CSI sequence and 1 min 36 s in the under-sampled case, which results in a gain in the terms of acquisition time of a factor of 1.8.

Dynamic ^{31}P experiments were done with an isometric flexion movement. No pedal activation was possible by the volunteer in order to prevent movements during the acquisition. The pedal of the ergometer was blocked by imposing a manual and maximal pression of 5 bars in order to reduce volunteer motion amplitude and residual motion outside the exercice periods. The T_{R} used for dynamic experiments was 4 s for the FID non selective standard exercise, and 2 s for the conventional

Parameter	FOV (cm)	T_{R}	BW	M_s	Slice thickness (cm)
Value	20	4 (static) or 2 (dynamic)	2000	8×8	6

Table 4.2.: Acquisition parameters used for ^{31}P experiments

spiral CSI and under-sampled for the under-sampled spiral CSI. The bandwidth for proper ^{31}P spectra reconstruction has been set to 2000 Hz. The number of temporal interleaves was 4 for the conventional spiral CSI and 2 for the under-sampled spiral CSI, which lead to a resolution between full spectra of 8 s in the conventional case and 4 s in the under-sampled case. Matrix size was of 8 x 8, with a 20 cm FOV and 6 cm slice thickness.

4.3.11.4. Data processing and analysis

The whole reconstruction process is done on MATLAB (The MathWorks) and JMRUI (java Magnetic Resonance User Interface, version 5.0). After data reading, as a spiral is not instantaneous in practice, every sample of the spiral is phase-corrected according to the Fourier shift theorem. Thus, a gridding is done for each sampled k-space. The spatial domain is thus reconstructed. Each image is interpolated into a 16×16 grid by zero filling the k-space. Voxels from the same muscle are then averaged to increase SNR. Along the temporal dynamic dimension, a denoising procedure is done using a Singular Value Decomposition (SVD). The denoising procedure is done on spectra along the temporal dynamic dimension [Zhu+03].

In the conventional spiral CSI case, a 1D FFT is done to reconstruct the spectra for each pixel. In the under-sampled spiral CSI case, a Least Square reconstruction is done to reconstruct the spectra (as proposed in chapter 3). A zero order phase and a time shift had to be processed on the signal from each pixel for proper quantification. Each spectrum was further analyzed and quantified using the jMRUI software with the AMARES (advanced method for accurate, robust, and efficient spectral fitting) fitting routine. PCr and Pi amplitudes and frequencies were quantified in order to extract the PCr constant recovery time and the pH evolution over time.

pH is related to PCr and Pi frequency difference as follow:

$$\mathrm{pH} = \mathrm{p}_{\mathrm{Ka1}} + \frac{\log(((\mathrm{Freq}_{\mathrm{Pi}} - \mathrm{Freq}_{\mathrm{PCr}}) - \mathrm{p}_{\mathrm{Kam}}).}{\mathrm{p}_{\mathrm{KaM}} - (\mathrm{Freq}_{\mathrm{Pi}} - \mathrm{Freq}_{\mathrm{PCr}})} \tag{4.14}$$

with $\mathrm{p}_{\mathrm{Ka1}} = 6.75$, $\mathrm{p}_{\mathrm{Kam}} = 3.27$, $\mathrm{p}_{\mathrm{KaM}} = 5.69$ and $\mathrm{Freq}_{\mathrm{PCr}}$ and $\mathrm{Freq}_{\mathrm{Pi}}$ the resonant frequencies of PCr and Pi.

The PCr recovery was fitted using a mono-exponential function (on a MATLAB routine) on the PCr amplitude curve normalized by the sum of PCr and Pi, giving access to the PCr recovery constant τ_{PCr} directly related to the mitochondrial capacity in the muscle (section 2.1).

Figure 4.20 details the data processing and analysis.

For both conventional spiral MRSI and under-sampled spiral MRSI methods, the oxidative metabolism, via the calculation of recovery constant τ_{PCr}, of the gastrocnemius and the soleus muscles are compared.

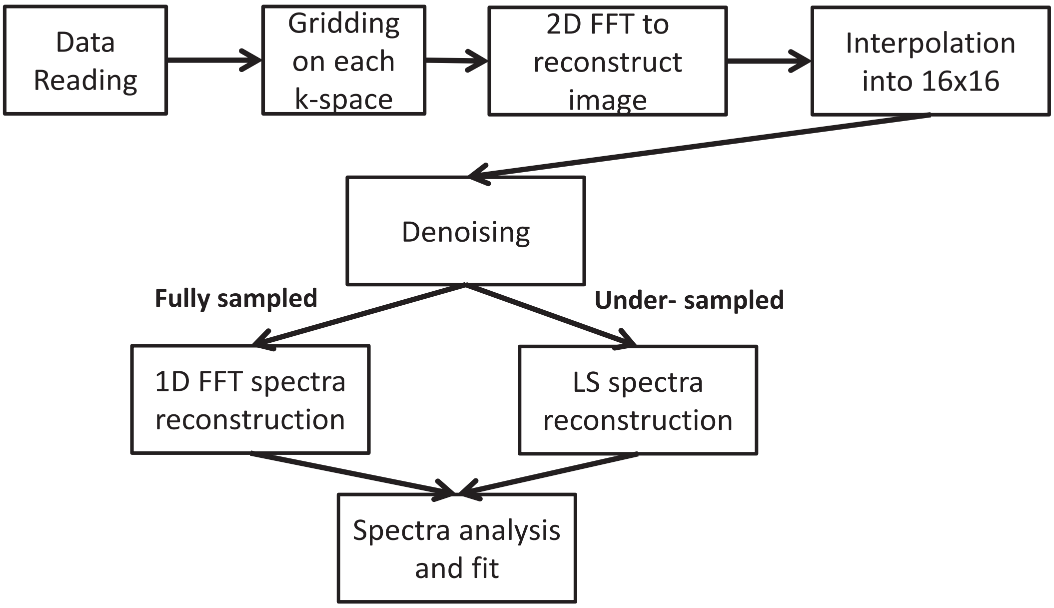

Figure 4.20.: Reconstruction steps for ^{31}P data analysis

The Signal to Reconstruction Error Ratio (SRER) is calculated in the spectral support from the least square difference between the spectrum from a conventional spiral CSI acquisition and a spectrum from an under-sampled spiral CSI acquisition as follows:

$$\mathrm{SRER} = 20 \times \log \frac{||x_F||_{L_2}}{||x_F - x_U||_{L_2}}, \tag{4.15}$$

where x_F is the reconstructed spectrum from the a conventional acquisition and x_U from an under-sampled acquisition.

4.3.12 $^{31}\mathrm{P}$ *In vivo* results

4.3.12.1. $^{31}\mathrm{P}$ static experiments

Figure 4.21 shows PCr and Pi maps acquired at rest with the two methods conventional spiral CSI and under-sampled spiral CSI. Reconstructed spectra are shown as well for a voxel of the image. The SRER in the highlighted voxel is $19,01$ dB, which corresponds to an energy of the reconstruction error 9 times smaller than the energy of the signal. The SRER has also been averaged within all the voxels containing soleus and gastrocnemius muscle and its value is $17,31$ dB.

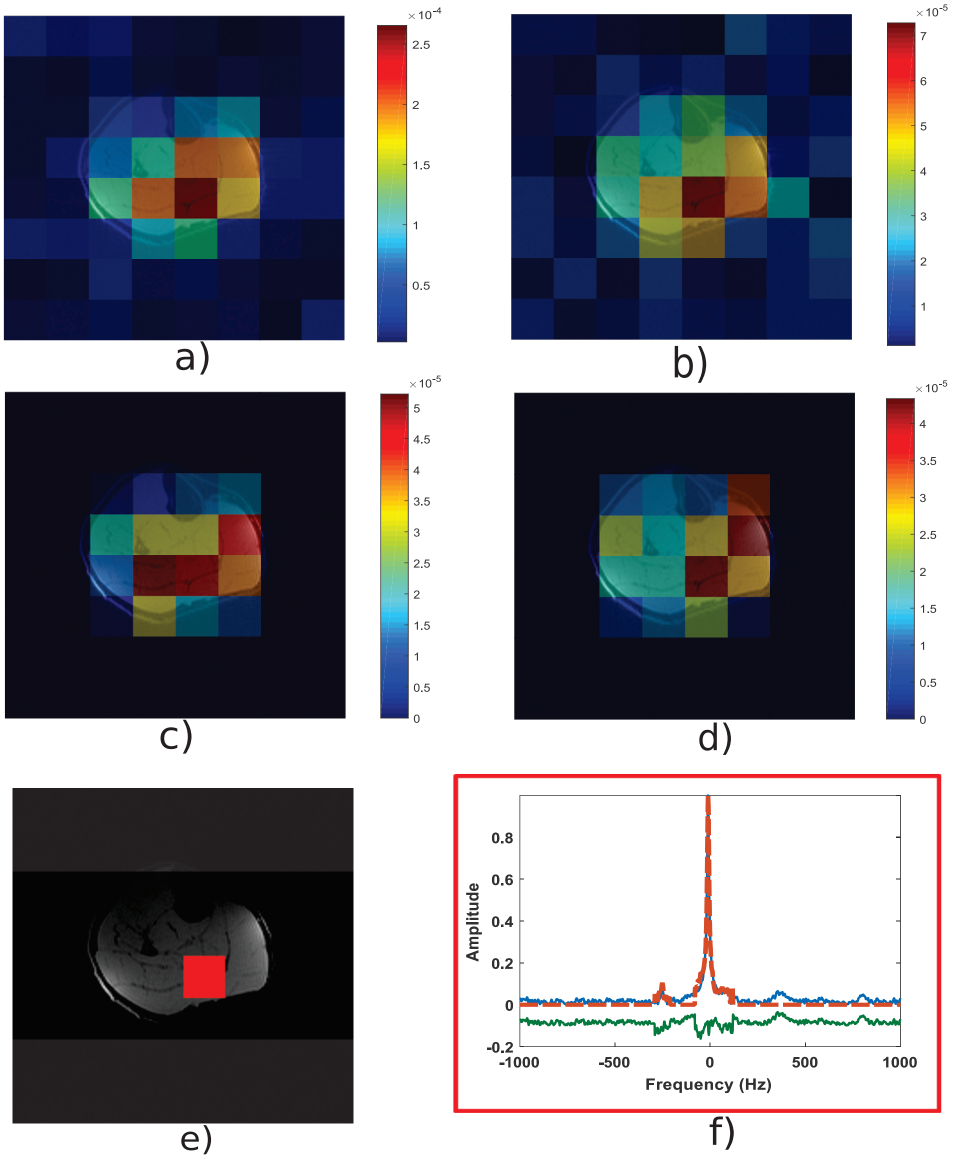

Figure 4.21.: Reconstructed PCr and Pi maps acquired at rest with 10 averages and matrix size of 8 x 8, overlayed with the anatomic transversale image acquired with a dixon sequence. The PCr maps are shown in a) for the conventional spiral CSI acquisition, and in b) for the under-sampled spiral CSI acquisition. The Pi maps are shown in c) for the conventional spiral CSI acquisition, and in d) for the under-sampled spiral CSI acquisition. The anatomic image is given in e), overlayed with the voxel localization where the spectra in f) were reconstructed. In blue, the reconstructed spectrum for the conventional case and in dotted red for the undersampled case, normalized by the amplitude of PCr. The shifted error spectrum is given in the bottom in green. As we can see, the spectrum corresponding to the under-sampled acquisition in dotted red is equal to zero outside of the chosen spectrum support. Only PCr, Pi and γ-ATP frequency resonances are reconstructed.

Table		Volunteer
Soleus Muscle	Conventional case	45.4
	Under-sampled case	44.2
gastrocnemius Muscle	Conventional case	34.7
	Under-sampled case	39.3

Table 4.3.: PCr recovery constant times for the volunteer in both conventional and under-sampled spiral CSI cases

4.3.12.2. $^{31}\mathrm{P}$ dynamic experiments

^{31}P spectra at the beginning and end of exercise in the soleus and the gastrocnemius muscles for both methods are shown in figure 4.22. PCr depletion was 47 % in the soleus muscle and 34 % in the gastrocnemius muscle for the conventional spiral CSI case and 38 % in the soleus muscle and 31 % in the gastrocnemius muscle for the under-sampled spiral CSI case.

Normalized PCr by PCr + Pi evolution over time is shown in figure 4.23 for both methods in the soleus and the gastrocnemius muscles. The sum of PCr and Pi is also given. PCr recovery quantification are summarized in table 4.3 for the volunteer.

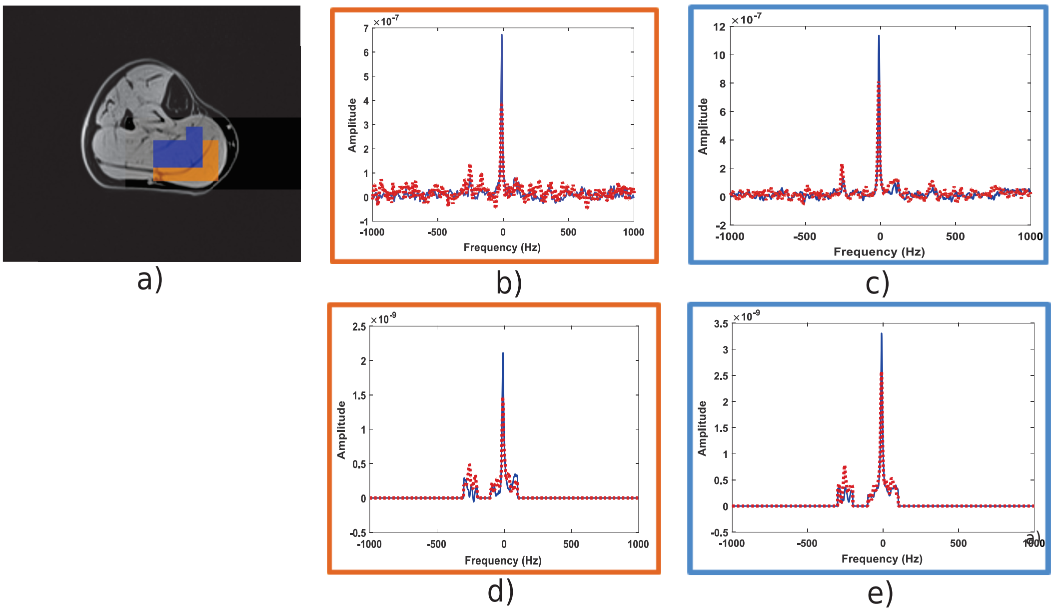

a) b) c) d) e)

Figure 4.22.: ^{31}P spectra at beginning (in blue) and end (in dotted red) of exercise in the conventional case for the gastrocnemius muscle (b) soleus muscle (c) and in the under-sampled case for the gastrocnemius muscle (d) and soleus muscle (e) on the averaged voxels shown in the anatomic image in (a). The soleus muscle corresponds to the highlighted voxels in blue and the gastrocnemius muscle to the highlighted voxels in orange. In a), the anatomic image, and the highlighted pixel were chosen from the zero-flled 16 x 16 CSI grid. As we can see, the spectra in d) and e), which were acquired from under-sampled FID signal, are reconstructed only on the pre-given spectral support (on the user special card). The spectra in d) and e) were reconstructed from an under-sampled FID signal, which is why the spectra are reconstructed only in the *a priori* known spectral support.

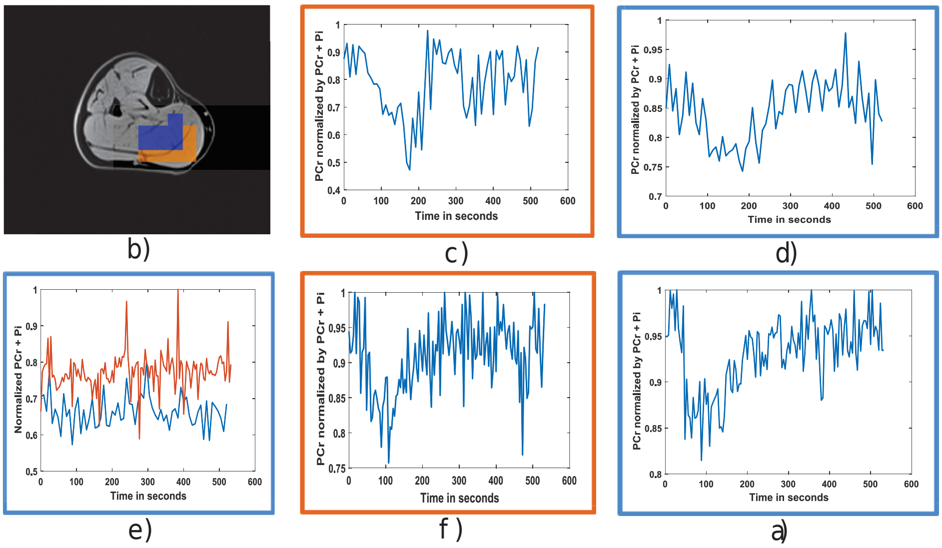

Figure 4.23.: Normalized PCr time evolution in the soleus and gastrocnemius muscles for both acquisition methods (b), c), e), f)). In a), the anatomic image, and the highlighted pixel were chosen from the zero-flled 16 x 16 CSI grid. The blue voxels are in the soleus muscle and the orange voxels are in the gastrocnemius muscle. Normalized PCr evolution time courses in the gastrocnemius are shown in b) for the conventional acquisition and in e) for the under-sampled one. Normalized PCr evolution time courses in the soleus are shown in d) for the conventional acquisition and in f) for the under-sampled one. Sum of PCr and Pi is given in d) for the soleus muscle, in blue for the conventional case and in red for the under-sampled case.

4.3.13 Discussion of $^{31}\mathrm{P}$ experiments

4.3.13.1. Study and discussion otn SNR for $^{31}\mathrm{P}$ experiments

In our experiments, the SNR was calculated and spectra before and after denoising are shown in figure 4.24, for the same pixel and spectra as in figure 4.21, acquired at rest with a T_R of 4 s. In figure 4.25, spectra acquired with a T_R of 2 s for dynamic experiments, for the gastrocnemius muscle (same pixels as in figure 4.22) are shown. T_1 values of phosphorus metabolites are quite long (see table 2.2), thus reducing the T_R from 4 s to 2 s affects the SNR as we can see on the figures.

SNR values, calculated as the ratio of peak (PCr) magnitude amplitude to standard deviation of noise (in decibels, the SNR would be 20 times the decimal loagrithm of this ratio), were for the spectra shown in figure 4.24 with a T_R of 4s are, for PCr, of 23.4dB for the raw spectrum, 28.5dB for the apodized spectrum, 40dB for the apodized spectrum with 10 averages and for Pi, of 10.3 dB for the apodized spectrum, 15,6 dB for the apodized spectrum with 10 averages. The Pi, indeed, cannot be distinguished in the raw individual spectrum.

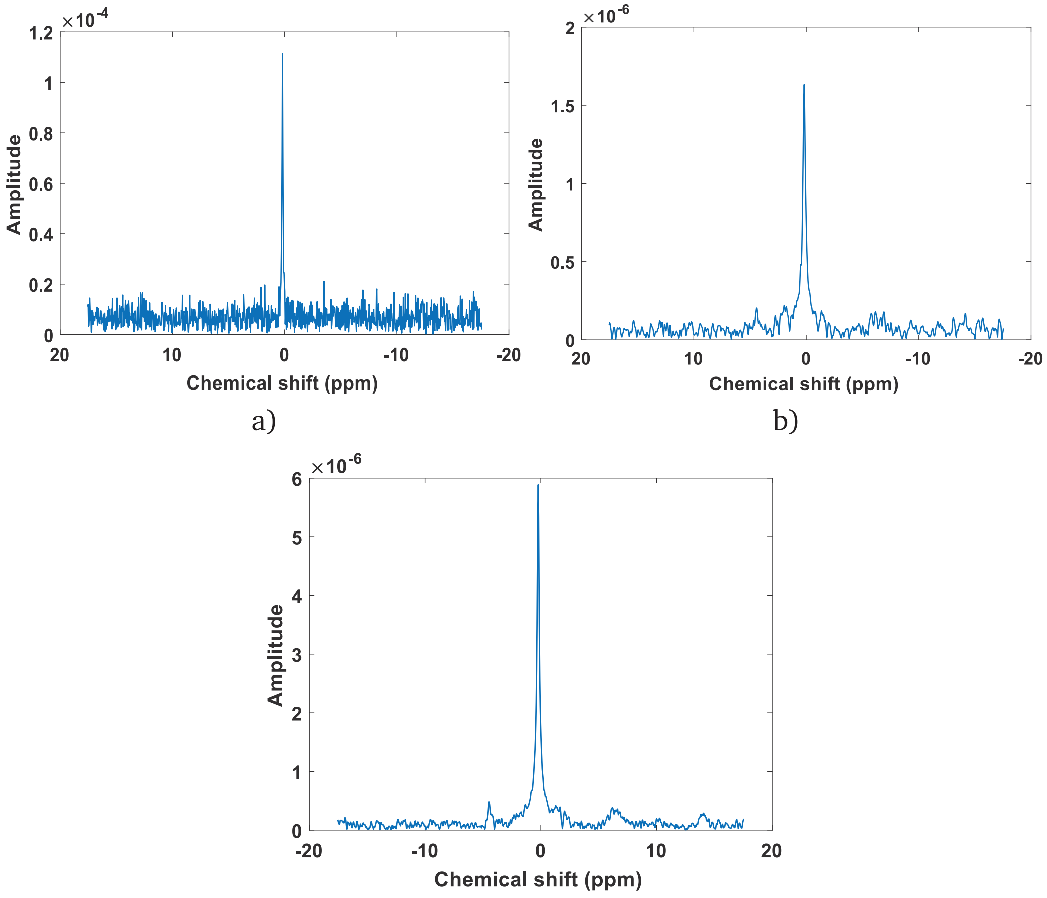

a)

b)

c)

Figure 4.24.: Illustration of a magnitude spectrum acquired at rest with a T_{R} of 4 s (for static experiments). The raw unprocessed magnitude spectrum is shown in a), denoised spectrum in b), and denoised and averaged spectrum in c) (10 accumulations).

SNR values for the spectra (at rest, before exercise) are shown in figure 4.25 are, for PCr, of 20.3 dB for the raw spectrum (averaged pixels in the gastrocnemius muscle), 22.8 dB after denoising, and for Pi, of 5.3 dB after denoising. Indeed, the difficulty in this application is the asssessment of Pi, with a correct SNR, in order to further quantify it.

The chosen support for our under-sampled acquisitions does not contain the alpha and beta ATP resonant frequencies, which is a problem when the LS reconstruction is performed. This choice has been made to reduce the length of the support to its minimum, in order to reach a higher reduction factor for the under-sampling.

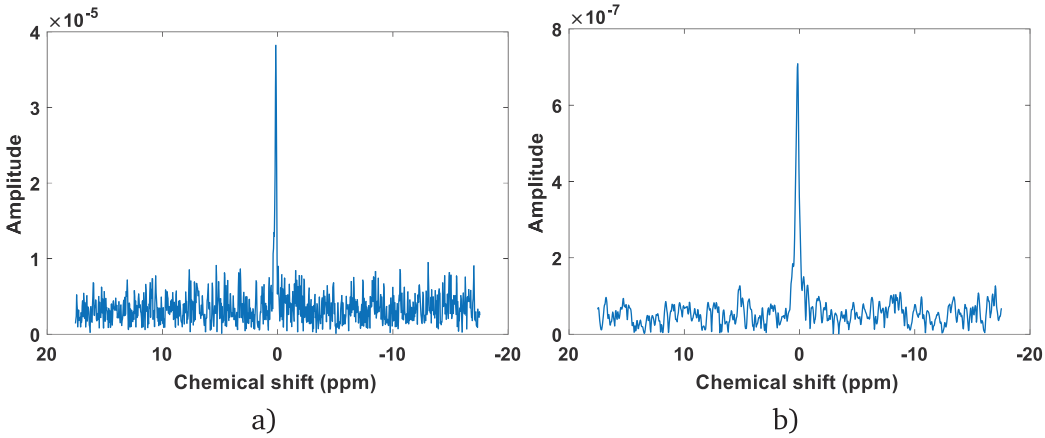

Figure 4.25.: Illustration of a magnitude spectrum acquired with a T_{R} of 2 s for dynamic experiments. The raw unprocessed magnitude spectrum is shown in a), denoised spectrum in b).

However, it affects our spectra reconstruction. The ATP metabolite concentrations is assumed not to change during the exercise, and what we are looking at is PCr and Pi variations to assess PCr constant recovery time, and ensure that the sum of PCr and Pi remains constant. Even if our reconstructed spectra on the chosen support is contaminated by ATP metabolites, the variations of PCr and Pi amplitudes peaks and frequencies should only be due to PCr and Pi concentration variations during the exercise. The use of a selective RF pulse exciting only PCr and Pi could however solve this issue.

Simulations have been done with increasing gaussian noise according to PCr amplitude peak (standard deviation of 0 to 20 % of PCr amplitude). For the simulations, a simulated phosphorus spectrum was generated as in chapter 3, but with different amplitude ratios, to be closer to what we actually have in practice. The amplitude of Pi was set to 10 % of the amplitude of PCr, and ATP amplitudes were set to 9 %. The SNR was calculated from the simulated phorphorus spectra and the SRER has been calculated as in chapter 3 according to the formula

$$\mathrm{SRER} = 20 \times \log \frac{||x||_{L_2}}{||x - x_m||_{L_2}}, \tag{4.16}$$

where x is the original spectrum and x_m is the reconstructed spectrum, with both restricted to the spectral support. A common logarithm with base 10 is used here.

The results are shown in figure 4.26 and show that the reconstruction improves when a simulated signal without ATP is given as an input. In order to assess Pi, the SRER on its support has to be higher than 3-4 dB, which corresponds to a SNR of around -23 dB and a standard deviation of 3 % of the PCr amplitude.
In order to improve the signal reconstruction with the same support, a prior static fully sampled acquisition could be done. Therefore, the knowledge of ATP amplitude and frequency informations we get from this acquisition could be taken into account as an priori knowledge before LS signal reconstruction.

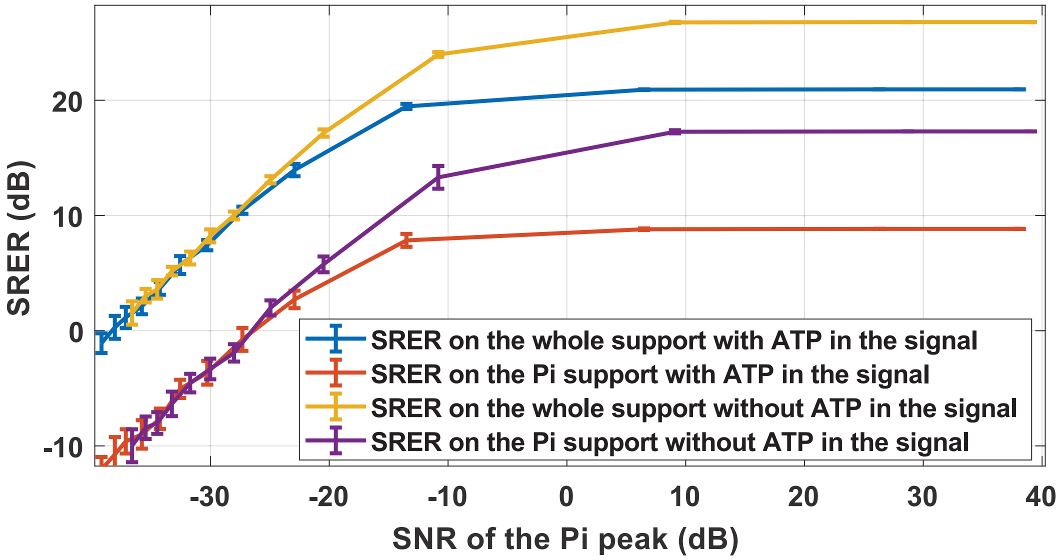

Figure 4.26.: Evolution of the SRER on the whole chosen support with the SNR of Pi.

SNR is the main limitation to the application of our under-sampled method. It is already SNR challenging and complex to process data from a conventional case, and moving to the under-sampled case amplifies those problems. Even if, in the results shown, the phosphorus data could be processed and PCr recovery values were extracted, the SNR could indeed be improved by using, for example, a more sensitive coil, by using a 7 T MR system, or/and using a selective RF pulse for dynamic applications.

4.3.13.2. Conclusion

The novel fast spiral MRSI acquisition strategy has been presented and tested in-vivo on phosphorus experiments. The very first *in vivo* experiments at rest have been done to compare the two methods in terms of SRER. The new proposed acquisition method was tested in order to reach a reduction of the acquisition time by a factor of almost 2 compared to the spiral CSI. We believe we are at the limit of the signal-to-noise ratio for the correct Pi reconstruction. The reported SRER only reflects the quality of the reconstruction of PCr which carries the major part of the signal energy; this metric masks the difficulties in practice of measuring the Pi. Indeed, the approximation given by our support (which does not take into account alpha ATP and beta ATP) is detrimental for the reconstruction of the Pi, in the undersampled case, for this SNR. During the exercise, as soon as the Pi starts to increase, the SNR conditions are more favorable to a correct reconstruction. Dynamic phosphorus experiments have been done for both methods. For dynamic phosphorus applications, we are particularly interested in PCr and Pi evolutions over time. The spectrum support can be considered sparse and the method is of interest (considering that ATP signal amplitude is not high enough to hamper correct reconstruction of PCR and Pi). The SNR is lower with ^{31}P, so the factor of reduction for under-sampling cannot be too large. Results showed that we were able to extract the recovery constant of PCr even in the under-sampled case. In the case of an undersampling, the temporal resolution of the dynamic experiment (time between each full 31P spectra) is lower than in the conventional sampled case, which is interesting for better PCr recovery quantification (if sufficient SNR is available). At 3 T, the SNR is low for ^{31}P applications, and even more if an under-sampling is used. Therefore, in our case, the analysis required complex data and denoising processing. Indeed, the main limitation for the application of the spiral MRSI sequence, and even more for the under-sampled spiral MRSI sequence, is the SNR. Maybe, testing the sequences at 7 T would have more significant results, or using more sensitive coils and selective RF pulses.

4.3.14 Conclusion of the chapter 4

This chapter presents the results and details the implementation of 1) a conventional spiral MRSI sequence and 2) a under-sampled spiral MRSI sequence. The under-sampling (which is also an irregular sampling) that has been implemented, as well as the SBS algorithm, are detailed in the previous chapter. The method implemented here differs from the method proposed in the previous chapter in the way that all the partition have the same under-sampling pattern, and no use of the circular shift theorem nor of the proposed algorithm to optimize the temporal samples to acquire of each partition is done. This implies a simplified reconstruction process where the spatial dimension is reconstructed before reconstructing the spectral dimension, on the contrary to what is done on the proposed method in chapter 3.

Implementing the method in practice raised many problems due to low SNR, especially in the phosphorus case, unwanted peak replication artifacts in the case of a full temporal sampling spiral ^{1}H-MRSI, with less sparse spectra. This is why acquistion parameters had to be properly chosen, given the application, as the spatial resolution, the repetition time, the reduction factor for the under-sampling, the spectral support. However, the sequences were applied successfully and compared in the case of fat-water applications, static and dynamic phosphorus experiments. Futur clinical applications in dynamic ^{31}P MRSI are at the moment challenging and requires a validation of the sequences on reproductible data.

In the next chapter, a clinical protocol is presented, with its challenges and clinical constraints that are to be kept in mind for an inclusion of the developed sequences into the clinical environment.

5

Non localized $^{31}\mathrm{P}$ application in the context of a clinical protocol and perspectives towards the use of the proposed method and implementations in clinical practice

Summary

5.1 Introduction

Parallel to theoretical and sequence developments done in this thesis, a clinical protocol has been developed for mitochondrial capacity assesment via ^{31}P MRS. This clinical protocol has been tested on healthy volunteer before the inclusion on patient in the context of the "SPECTROscopie irm du phosphore 31 dans lâĂŹArtheriopathie Oblierante des Membres Inferieurs" protocol (SPECTROAOMI) (in collaboration with Jill Slade and Anne Tonson from the University of Michigan) detailed in the next section. This clinical application and experimental protocol development was the opportunity to face clinical practical constraints such as patients handling, material installation, timing constraints. This chapter details the clinical protocol SPECTROAOMI, and results we have at the moment on four patients. The final and ideal objective would be to include in the protocol the developed fast MRSI sequence to assess mitochondrial capacity in different muscles. Note that this is not the case in the present study, for which a spatially non localized FID ^{31}P MR spectroscopy sequence with a BISTRO saturation band is currently used. Indeed, this clinical study was launched during the 3rd year of this thesis work, while the method and sequence developments presented in chapters 3 and 4 were not yet finalized.

5.2 SPECTROAOMI clinical protocol

5.2.1 Introduction

Obliterative arterial disease of the lower limbs (AOMI) is defined as partial or total obstruction of one, or more, lower extremity arteries most often of atherosclerotic origin. It is a common pathology whose five-year mortality of a patient with AOMI is about 30%, mainly of cardiovascular origin.

The clinical manifestations are variable: absence of clinical signs, claudication with the effort translating into intense muscular pain when walking, cease when effort is stopped, disorders trophic and decubitus pain in advanced forms. The positive diagnosis is based on clinical examination and measurement of the systolic pressure index (SPI), which is the ratio between systolic pressure at the ankle and brachial systolic pressure. The threshold value for the diagnosis of AOMI is inferior to 0.90. Apart from critical ischemia whose immediate therapeutic objective is the rescue of the limb by a specialized surgical team in a hospital setting, a revascularization is proposed in case of claudication remaining disabling after at least 3 months of well-conducted medical treatment, or more early in case of threatening proximal lesion.

From a physio pathological level, mitochondria have a predominant role in ATP generation necessary for energetic needs of myocytes. It increases drastically during muscle contraction on exertion. This energy production is obviously conditioned by the availability of oxygen. In patients with AOMI, the decrease in blood flow after a significant stenosis has the direct consequence of disrupting oxygen to the distal muscles and thus limits muscle performance. Mitochondrial breath is the only metabolic pathway capable of providing the energy needed to support an effort of several minutes, intermittent claudication in the AOMI was logically attributed to a hemodynamic mechanism of intermittent hypo perfusion of muscles [McD15].

However, more recently, an increasing number of histological or functional studies have suggested episodes of ischemia-reperfusion, namely episodes of muscle ischemia on exercise followed by a return to a muscular perfusion rate sufficient to meet the needs at rest, could be at the origin of a true mitochondriopathy [BH00; Kou+15; Mak+07; Pip+08]. Indeed, several studies on isolated mitochondria showed a significant decrease in the activity of the various complexes of the transport chain electrons in the claudicant muscle relative to the healthy muscle [Pip+08]. This intrinsic alteration - i.e. independent of the O2 - contribution of the mitochondrial function has the direct consequence of increasing the muscle metabolic failure (i.e. decreased muscle oxidative capacity) related to degradation of muscle perfusion and therefore has every reason to contribute to the symptomatology and intolerance to exercise during the evolution of AOMI. In addition, a relationship between the degree of reduction in mitochondrial function measured in vivo and the risk of faster and more severe progression of AOMI at 1 year has been reported in patients with mild intermittent claudication symptoms or moderate [Isb+06], emphasizing the value of a therapeutic intervention aimed at the restoration of mitochondrial function of the muscle in parallel with the traditional management of perfusion defect.

In clinical routine, the possible association with a muscular mitochondriopathy is most often ignored, mainly because of the lack of available investigative method, for the sole benefit of hemodynamic factor that is intended to maintain or, where appropriate, restore by rehabilitation Vascular Control to Prevent Progression to Critical Ischemia or Tissue Necrosis irreversible. The medicinal treatment of a patient carrying an AOMI combines antiplatelet, inhibitor of the conversion enzyme (IEC) and statin.

In vivo, muscle mitochondrial function can be directly assessed if a protocol is performed (paradigm) exercise in magnetic resonance spectroscopy of phosphorus 31 (^{31}P) in MRI [Pag+97]. This functional exploration of mitochondrial respiration allows the analysis of the kinetics of Phosphocreatine (PCr) resynthesis which quantifies the oxidative muscle capacity. The PCr recovery time constant (τ_{PCr}) has been shown to be largely slowed down (up to 3 times) in patients with moderate claudication compared to a control group [Isb+06; Pip+00].

So far, studies in patients with AOMI in ^{31}P spectroscopy have used exercise paradigms developed for physiological studies on volunteers without vascular attack, and are largely dependent on functional hyperemia [Isb+06; Pip+00; Sch+06; Wu+11; Bra+04]. Most used combine dynamic plantar flexion exercises supported until exhaustion or onset pain [Isb+06; Sch+06] or sub-maximal isometric of 90s [Pip+00; Bos+99] for which the dependence of the metabolic recovery to muscle perfusion has been widely demonstrated [Bos+99; McN+15]. But, it is clearly established that the reduction of O2 inputs by a vascular hemodynamic factor alters the recovery [Has+07].

In case of an impairment of peripheral vascular function as in the AOMI and due to deterioration of oxidative capacity measured by the τ_{PCr}, it is therefore difficult to differentiate the part linked to this reduction.

5.2.2 Method

5.2.2.1. Exercise protocol

In order to explore the mitochondrial function suitable for patients with AOMI, we propose to use a new exercise paradigm that was initially developed and validated on volunteers healthy at Michigan State University (MSU) [Sla+06]. The MSU protocol consists of a series of 15 voluntary plantarflexions of 2 seconds separated by a minimum of 30 seconds of rest realized thanks to an MRI-compatible ergometer placed in the MRI. This protocol reliably quantifies τ_{PCr} despite minimal hydrolysis (about 10 %) at the limit of the sensitivity of the measurement. This weak sensitivity is offset by summation of metabolic responses of 10 contraction / relaxation cycles recorded under steady-state metabolic conditions [Sla+06]. This exercise paradigm is indeed causing stress minimal metabolic and does not depend on an increase in O2 intake, and is therefore perfectly adapted to the target population. This protocol which allows in vivo study of muscle mitochondrial function regardless of vascular function was deployed, tested and its reliability confirmed on healthy volunteers on the 3T MRI of North Hospital from Saint-Etienne.

The main objective is to study the mitochondrial function by ^{31}P MR spectroscopy before and after revascularization in patients with AOMI at the ischemic stress stage with exercise paradigm free of vascular factor (MSU protocol). This approach should quantify the relative contribution of the vascular and mitochondrial components to the degradation of muscle function in AOMI. The expected answer is that revascularization by raising the vascular limiting factor should be accompanied by an immediate improvement of the τ_{PCr} in the absence of mitochondriopathy. On the other hand, in the case of mitochondrial disease, the τ_{PCr} should remain altered in early post-revascularization. The experimental design targets a population of patients with AOMI at the stage of exercise ischemia and indication of revascularization. MRI of the pre-revascularization lower extremities will be performed during the hospitalization preceding the realization of the gesture. A second post-revascularization MRI will be performed before the patient.

5.2.2.2. Experimental MR protocol

Figure 5.1.: Installation setup of the patient or volunteer. She/he would lay down supine, her/his foot attached to a pedale ergometer Trispect module. An additional screen not shown here was behind the patient, and that is where instructions were displayed thanks to the e-Primes software.

Each patient was laying done supine on the MR bed of the scanner, the feet attached to the pedal of the tibial spectrometer module, with a surface coil ^{31}P/^{1}H Tx/Rx under its calf muscle. To prevent movement of the leg from the patient, the studied leg was properly attached, with a vacuum pillow filled with polystyrene. For dynamic ^{31}P measurements, isometric plantarflexions of the calf muscle were periodically operated using an MR compatible ergometer (Trispect, Ergospect, Innsbruck, Austria). The patient was equipped with a mirror so that he could see a monitor screen. On this monitor screen, on which instructions were displays using e-Primes software (Psychology Software Tool, USA), regarding when to push or stop thus achieve the best synchronisation as possible with the MR acquisition. MR scans were performed using a non localized, MR-FID sequence with saturation bands described in chapter 4, section 4.2 (BISTRO). A trigger was added in the sequence that sends a optical trigger to the e-Primes box. This was done to prevent the patient to push during the acquisition window.

Prior to the MR protocol, Maximum Voluntary Contractions (MVC) forces were performed. MVC consist in a maximal force output on the pedal by the patient for 1 - 2 s. This has been done 5 times and was therefore averaged to get the mean MVC. The total length of the protocol was about 1 h and 15 min (including installation of patients, instructions, MVC and MR imaging and spectroscopy).

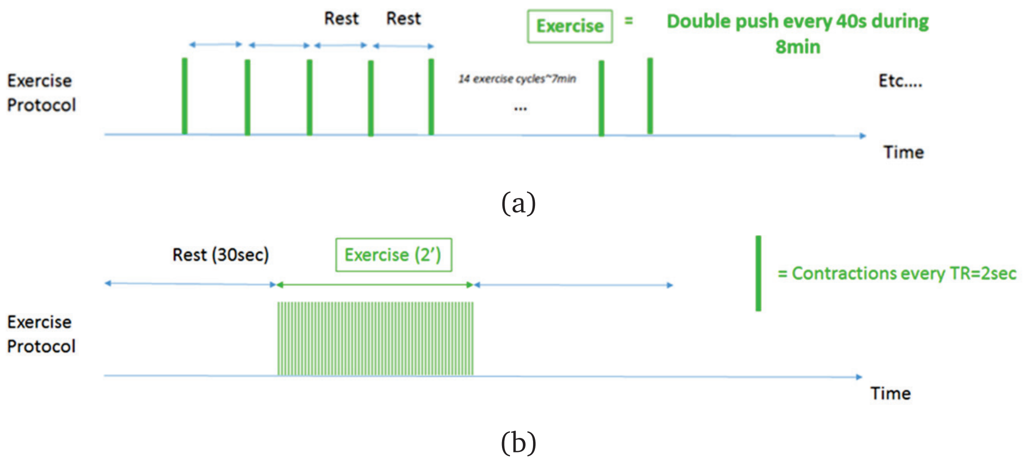

(a)

(b)

Figure 5.2.: Illustration of 2 developed protocol applied in the clinical project SPECTROAOMI. In a), the low rate dynamic protocol and in b) the standard high rate dynamic protocol

Prior to ^{31}P experiments, localization were done with a dixon sequence (Flip angle 9°, T_{R} 4.1 ms, T_{E} 1.4 ms, matrix size 118×192, FOV $169 \times 206\ \mathrm{mm}^2$). Thus, resting ^{31}P acquisitions were done with a 90° flip angle, a T_{R} 30 s, 10 averages, a bandwidth of 2500 Hz, and saturation bands placed on anterior muscles. Additional resting acquisitions were done with the same parameters but a T_{R} of 4 s. Then, 2 dynamic protocols were performed () with a non-localized FID sequences with saturation bands and with the same parameters (T_{R} of 4 s), but with different dynamic resolution times T_{res} (time between two exercises), see figure 5.2:

- a low rate dynamic protocol developed by [Sla+06] consisting in 1 min of rest, a double push every 40s (T_{res} = 40 s) for 8min and a 1 min rest.
- a standard high rate dynamic protocol was also done consisting in 40 s of rest, followed by 1 push every 4 s (T_{res} = 4 s) for 2min and finally a resting period of 6 min.

5.2.2.3. Data processing and analysis

Data was processed using CSIAPO software [LF+10] for phasing, MATLAB (The MathWorks) and the method QUEST (QUantitation based on QUantum ESTimation) [Rat+05; Rat+10] implemented according the "customized version" cQUEST, i.e a version where the user can design, through a parameter file, several parameters constraints and parameters prior knowledges. Data was first phased on CSIAPO and thus a MATLAB routine enabled to quantify PCr, Pi and ATP metabolited on each acquired non-localized spectra using the QUEST method. For the QUEST analysis, 3 initial metabolites files of PCr, Pi and ATP (containing α, γ and β ATP information) were taken into account. Those files were generated from the sum of all acquired spectra in the dynamic experiment. As Pi frequency can change according to the pH, a frequency shift was allowed in the fitting process. An extra-damping was also allowed. In some cases, a Pi "splitting" can be seen on acquired spectra. In that case, 2 Pi metabolites files were generated so that both Pi could be quantified.
Thus, when the fit of all individual spectra was processed, a mono-exponential fit was performed on normalized PCr by the sum of the resting PCr to get the PCr recovery constant time. pH was calculated from the frequency difference between PCr and Pi. It is related to both frequencies as given in equation 4.14.

The pH has been averaged at rest to get the resting pH and just after the exercise for 1 min to get the minimum pH.

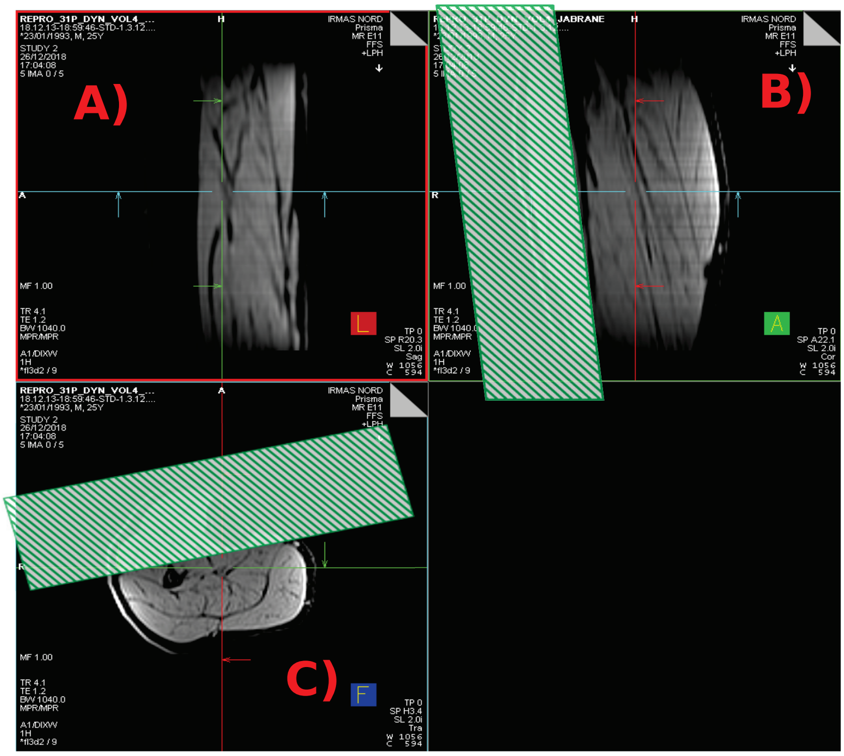

Figure 5.3.: A) Sagittal, B) coronal and C) transverse dixon images of the fifth volunteer. The OVS band was placed on the tibialis anterior muscle as shown in hatching green. The coil was placed under the calf muscle so that the gastrocnemius and the soleus muscles were studied.

5.2.2.4. Reproducibility tests

Before clinical applications and processing data on diseased patients, reproducibility tests of the protocol have been done on 5 healthy volunteers. The clinical protocol developed for SPECTROAOMI was performed, for each volunteer, 2 times. For each session, the volunteer was reinstalled in the machine before the launch of the protocol. The objective was to see how our whole protocol including the installation of the patient, of the surface coil, and the data processing was reproducible or not. Figure 5.3 shows the anatomic images in sagittal, coronal and axial plane for the fifth volunteer. The studied muscles were the gastrocnemius and the soleus muscle, as the coil was placed under the calf. The BISTRO OVS was placed on the tibialis anterior muscle as shown in figure 5.3.

Table 5.5 gives the results of the PCr recovery constant time, pH and PCr depletion for each patient, and for the 2 times.
The results of the quantification done by the developed data processing routing and fitted spectra are shown in figure 5.4. The standard deviation of the τ_{PCr} between

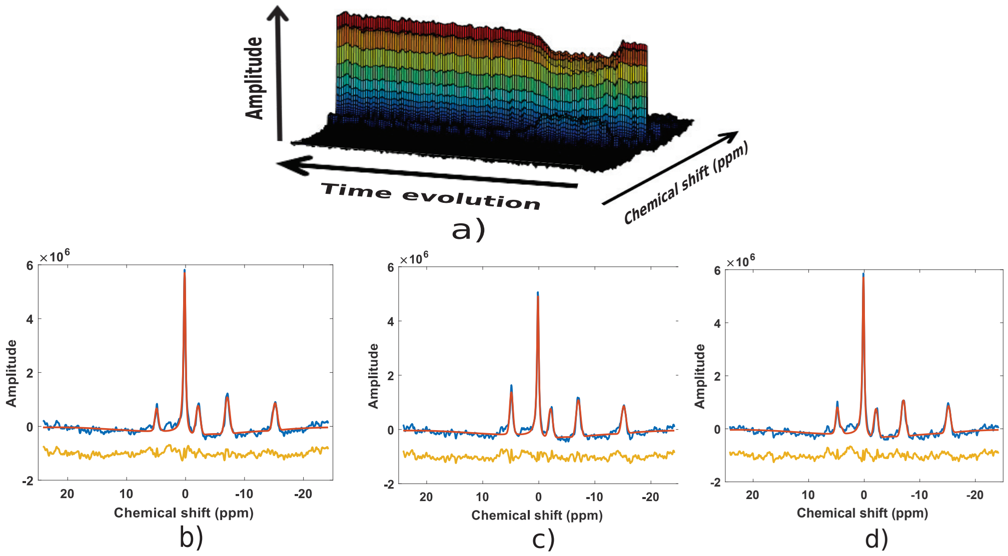

Figure 5.4.: For the fifth volunteer and for the standard high rate dynamic protocol, the first time, the stack plot of raw phased spectra (acquired with a spatially non localized FID sequence with a saturation band placed on the tibialis anterior muscle) is given in a). In b), c) and d), the raw phased spectra in blue, estimated spectra in red and residual spectra in yellow (shifted for illustration) are given during rest, exercise and recovery (during an exercise protocol including 30 s rest, 2 min exercise and 6 min rest).

the first time and the second time for each volunteer is illustrated in figure 5.6. The mean standard deviation of the PCr difference between test and retest scans was 1.09 s, which in percent corresponds to a mean of 5 % deviation. We can see from quantification results that the fitted spectra have good estimations of the amplitude, damping and frequency values of the raw spectra. Frequencies are quite well fitted, but damping and amplitude not as much. Indeed, in figure 5.4, it can be seen that the fitted amplitudes are a little lower than the actual ones. This is actually related to the damped envelope. In our routine, a small extra-damping is authorized without some bounds for the fit to be done According to B_0 inhomogeneities from one experiment to an other, FWHM can change a lot, from a few Hz to around 30 Hz, and the extra damping parameter bound could be reached.

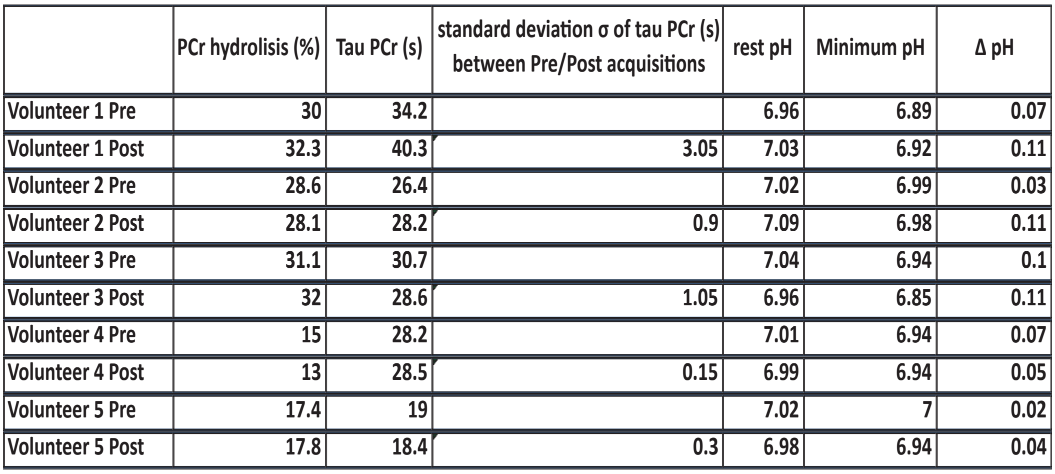

	PCr hydrolisis (%)	Tau PCr (s)	standard deviation σ of tau PCr (s) between Pre/Post acquisitions	rest pH	Minimum pH	Δ pH
Volunteer 1 Pre	30	34.2		6.96	6.89	0.07
Volunteer 1 Post	32.3	40.3	3.05	7.03	6.92	0.11
Volunteer 2 Pre	28.6	26.4		7.02	6.99	0.03
Volunteer 2 Post	28.1	28.2	0.9	7.09	6.98	0.11
Volunteer 3 Pre	31.1	30.7		7.04	6.94	0.1
Volunteer 3 Post	32	28.6	1.05	6.96	6.85	0.11
Volunteer 4 Pre	15	28.2		7.01	6.94	0.07
Volunteer 4 Post	13	28.5	0.15	6.99	6.94	0.05
Volunteer 5 Pre	17.4	19		7.02	7	0.02
Volunteer 5 Post	17.8	18.4	0.3	6.98	6.94	0.04

Figure 5.5.: Table summarizing PCr hydrolisis, PCr recovery constant time and pH change the first time (Pre) and second time (Post) for the four volunteers of the reproducibility tests.

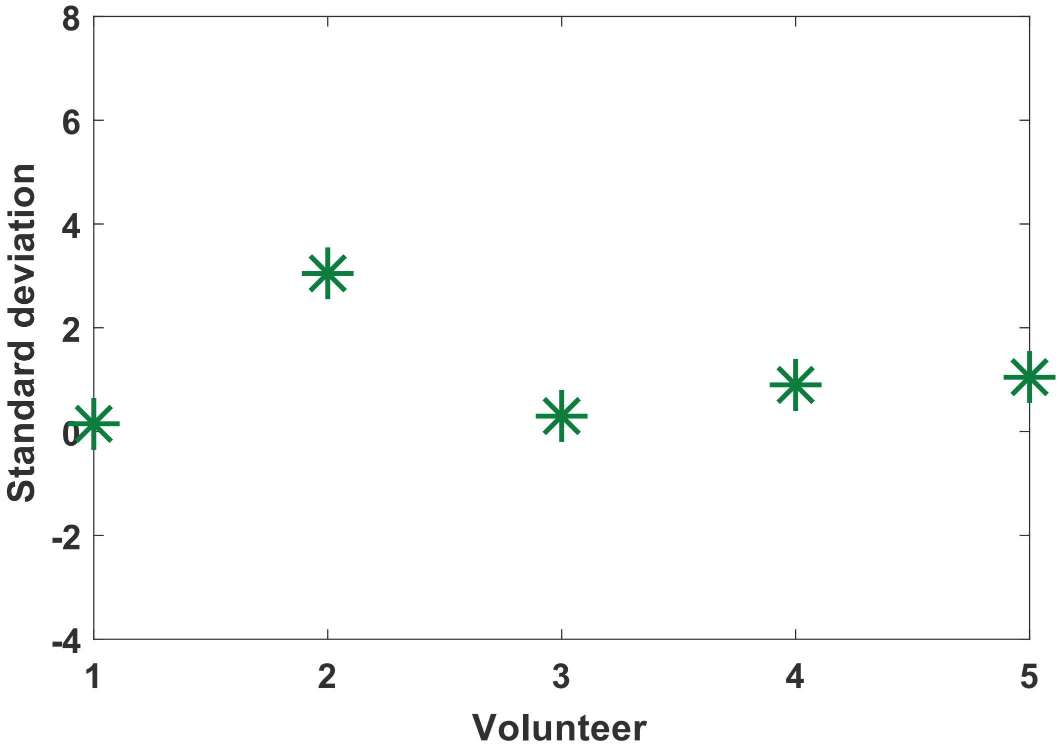

Figure 5.6.: Standard deviation of the τ_{PCr} for each volunteer (from 1 to 5), between the first and second time performing the exercise protocol (40 s rest, 2 min exercise with pushes every 2 s, 6 min rest). The mean standard deviation was 1.09 s.

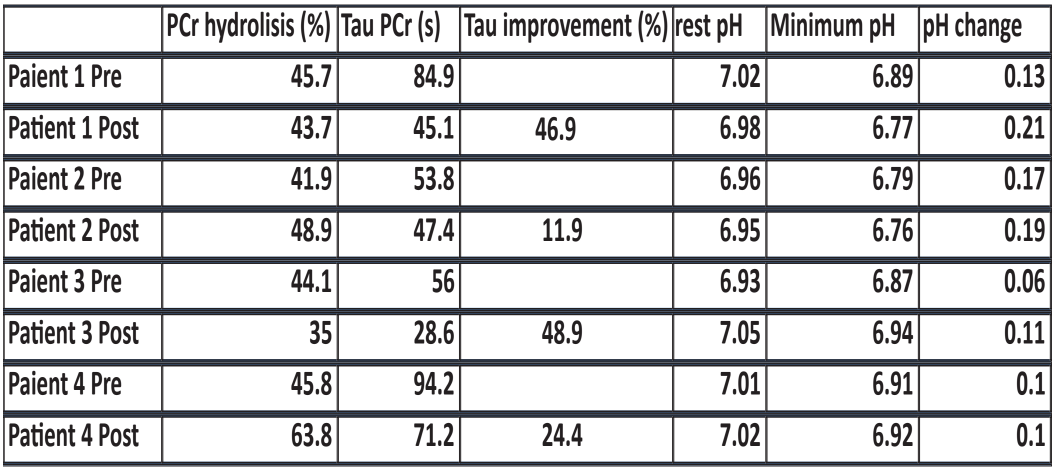

	PCr hydrolisis (%)	Tau PCr (s)	Tau improvement (%)	rest pH	Minimum pH	pH change
Paient 1 Pre	45.7	84.9		7.02	6.89	0.13
Patient 1 Post	43.7	45.1	46.9	6.98	6.77	0.21
Paient 2 Pre	41.9	53.8		6.96	6.79	0.17
Patient 2 Post	48.9	47.4	11.9	6.95	6.76	0.19
Paient 3 Pre	44.1	56		6.93	6.87	0.06
Patient 3 Post	35	28.6	48.9	7.05	6.94	0.11
Paient 4 Pre	45.8	94.2		7.01	6.91	0.1
Patient 4 Post	63.8	71.2	24.4	7.02	6.92	0.1

Figure 5.7.: Table summarizing PCr hydrolisis, PCr recovery constant time and pH change before surgery (Pre) and after surgery (Post) for the four patients of the SPECTROAOMI clinical protocol.

5.2.3 Results

Table 5.7 shows the results of the PCr recovery constant time, pH and PCr hydrolisis for each patient, before and after surgery. We can see, for all patients, an increase of the PCr recovery constant time. The mean τ_{PCr} improvement is about 33 %. A stack plot of raw phased spectra of one patient after surgery is given in figure 5.8. In this figure, we can see the drop of PCr amplitude, which is the main frequency peak, and the increase of the Pi amplitude. The PCr, Pi and ATP amplitudes evolution time courses are shown in figure 5.9. The ATP amplitude value is constant over time and during exercise. The PCr recovery curve and the associated mono-exponential fit are also shown in this figure.

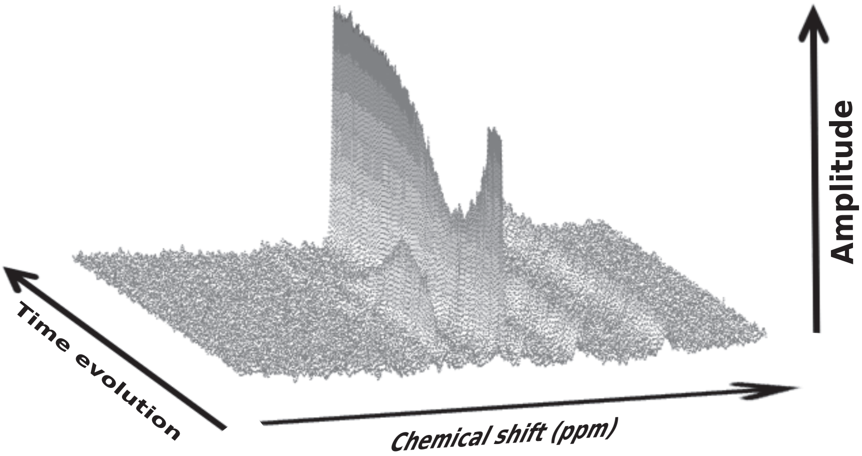

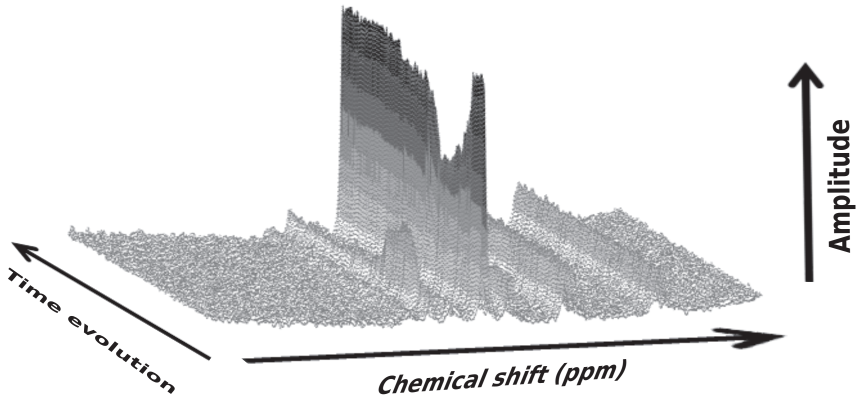

Figure 5.8.: Stack plot of raw acquired spectra (with a spatially non localized FID sequence with a saturation band placed on the tibialis anterior muscle) after phasing and signal apodization for the second patient before (left) and after (right) surgery for an exercise protocol including 30 s rest, 2 min exercise and 6 min rest.

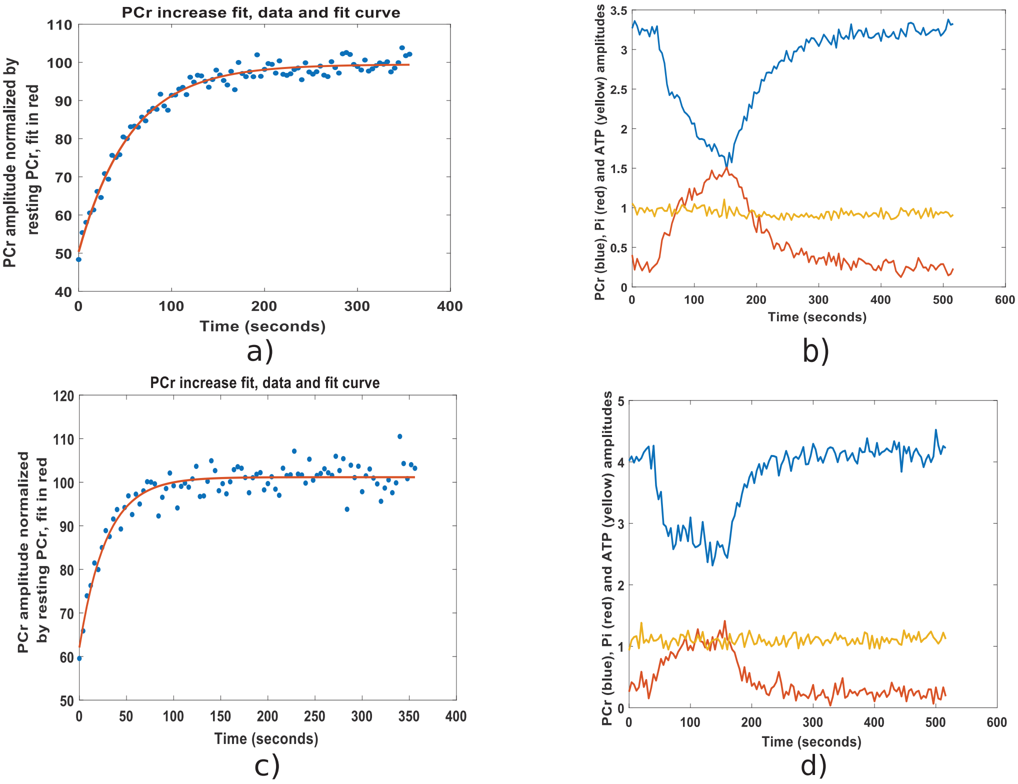

Figure 5.9.: PCr increase curve and corresponding fit a), PCr, Pi and ATP amplitudes evolution over time b) before surgery, and after surgery (c), d)) for the third patient. The exercise protocol included a 30 s rest, 2 min exercise and 6 min rest at the end.

5.2.4 Discussion

So far four patients have been included in the SPECTROAOMI protocol. Results showed an increase in mitochondrial capacity after surgery. The obstruction of the vessels by the AOMI disease and the not well perfused muscle would reduce mitochondrial capacity of AOMI patients. Further inclusion are needed to make strong assumptions that should come in the coming years. Reproducibility tests that were done make our results reliable. Indeed, for patients 1,3 and 4, the PCr recovery constant improvement τ_{PCr} was so distinctly stronger that it cannot be attributed to a problem of data processing or patient installation.

5.3 Conclusion

We have at the moment encouraging results on the four patients of the SPECTROAOMI protocol. This protocol is done on patients with a lower leg artheriopathy, and assess oxidative capacity before and after revascularization. Oxidative capacity is also of interest for other possible clinical applications as muscular fatigue, extreme body thinness (anorectics) or sports. The capacity to access to mitochondrial capacity within individual muscles of the body that is given by the developed spiral MRSI sequence and the novel under-sampled spiral MRSI sequence is thus of interest for clinical practice. The inclusion of one of these sequences into one clinical exercise protocol could give access to recovery constant times of different muscle, as seen in the previous chapter, with the same dynamic temporal resolution (4 s) or twice lower (8 s for spiral MRSI). For the future, the idea is thus to validate the sequence and its performances on several patients, and determine how to include it in clinical protocols.

5.4 Perspectives towards the application of an under-sampled spiral MRSI sequence

This chapter raises clinical difficulties and constraints that exist about patient comfort, acqusition time, reproducibility, signal to noise ratio. For phosphorus clinical applications, the use of a non-localized FID sequence leads to a high SNR (as we take the signal from a big excited volume) and enables a proper quantification of data to access PCr constant recovery time constants or pH for example. We saw in the previous chapter that using Chemical Shift Imaging considerably reduces the SNR, and the acquisition time. Indeed, the proposed under-sampled spiral MRSI sequence allows us to significantly reduce the acquisition time compared to phase encoding CSI and possibly perform dynamic phosphorus MRSI experiments. However, it has been seen that the low SNR prevents its application at the moment. Overcoming this problem would allow, for example in the context of this SPECTROAOMI protocol, to extract PCr recovery constant and pH from different individual muscles, before and after surgery, and see if the same muscles are exercising, at the same intensity, and which one contributes the most to the force output.

General Conclusion

6

In this thesis, a new fast MRSI method has been developed which lead to one publication, and an article currently under revision both studying and describing sampling strategies. The adopted method exploits signal sparsity and *a priori* known support to under-sample signals and combines both a signal under-sampling strategy with a spiral k-space sampling. This method has been implemented in the Siemens IDEA environment and tested on a 3T Prisma MR scanner in ^{1}H and ^{3}1P *in vivo* applications. The context of this PhD relied on energetic metabolism and mitochondrial capacity assessment by the mean of ^{3}1P MRS, and that is why the first aim of this sequence development was to apply it on dynamic ^{3}1P MRSI, but for SNR purposes and sequence validation, it was first tested on proton, and then on static phosphorus MRSI.

The fast acquisition method that has been developed stems from a publication of Gao and Reeves in [GR00] where the *a priori* knowldegde of spatial support was taken into account for the SBS algorithm and the signal under-sampling, and also from previous work proposed by a former PhD student in the laboratory Dany Merhej in [Mer+14] where the *a priori* knowledge of NMR spectra support enabled with sample selection via the SBS algorithm to propose fast 2D spectroscopy acquisition strategy. In this thesis, the challenge was first to find out how this SBS sample selection could benefit an acquisition gain in spiral spectroscopic imaging and then to implement it on the MRI scanner. We were able to obtain in vivo data using the proposed method, but the low SNR at 31P and the remaining artifacts for proton applications do not allow us to conclude that our proposal has been definitively validated. Some improvement could be made to the method: as we saw in chapter 3, the l_2 norm reconstruction is perfect without noise, but amplifies noise in a noisy scenario. Maybe other reconstruction algorithm could be developed and improve the signal reconstruction, with the same acquisition scheme. For example, with l_1 regularization term for signal reconstruction as in the LASSO method. We tried to keep in mind physical constraints that exist in MRI to develop the theory of our method. However, a significant constraint has not sufficiently been taken into account and remains to be considered: the T2* decrease of the signal. Although our simulations took into account the fact that the sinusoidal signal was a damped signal, our sample selection SBS does not assume that our signal is damped and causal. Indeed, the SBS algorithm could be weighted such that it will privilege samples selection at the beginning of the signal, just after the RF excitation, where the signal is of higher intensity. Another study that could be interesting to conduct is the integration in the SBS algorithm of Cramer-Rao bounds (on the parameter of interest) as a criteria to be minimized. Moreover, one could consider to apply the sequential backwards selection algorithm to other types of k-space sampling than spiral, for example radial sampling or other innovative k-space trajectory sampling as in [Laz+19].

As the final goal was to do dynamic phosphorus application, the implemented spiral MRSI and under-sampled spiral MRSI sequences were tested on some volunteers in dynamic but suffer limitation of SNR, and especially in the case of the under-sampled sequence. Even if we were able to extract PCr recovery constant times and phosphorus metabolite maps with a complex data processing, this is a limitation to keep in mind for future application. Maybe the use of a 7T MR scanner would have more significant results with a higher SNR. This under-sampled spiral MRSI sequence is also limited by its spectrum support, which actually in practice is not really sparse and also not really small compared to the full bandwidth length. However, it would be of particular interest for sparser signals than in the phosphorus and proton cases, like in hyperpolarized ^{13}C applications.

The methodological development works of this thesis were done in parallel to the development of the SPECTROAMI protocol (2016-2017), its launch (2018) and the inclusion of four patients (2018-2019). This protocol included patients, software and equipment installations and was thought to be a good way to evaluate clinical constraints for further possible inclusion of our developments into the clinical environment. So far the protocol has encouraged results that show an improvement of oxidative capacity from before to after a revascularization for patients with a lower leg artheriopathy. The inclusion of the developed under-sampled spiral MRSI in this protocol or another clinical protocol could be made to access oxidative capacity within different individual muscles. Of course, the sequence should be totally validated first. An article showing the proof of concept of the method in vivo is intended to be submitted in a near future. Non-cartesian imaging and spectroscopic imaging developments are also particularly interesting for the detection of short T_2 metabolites and the developments realised in the context of this thesis could also be of interest for Ultra Short TE applications such as collagen [Siu+15; Jon+11], or cortical bone [DB13] detection.

The development of new acquisition strategies in MRSI is relevant, indeed the state of the art lacks of high spatially resolved MRSI applications, especially in the muscle, because of its very long acquisition time. Even if the data reconstruction process quickly becomes more complex, the development of acquisition strategies like EPSI or spiral MRSI and their improvement are still relevant to study human metabolism and energetic metabolism without being incommoded by acquisition time.

List of Publications

A

Peer reviewed Journal publication

- J. KARKOURI, H. RATINEY, M. VIALLON, R. PROST, F. MILLIOZ, Time undersampled acquisition for multidimensional sparse signals with application to magnetic resonance spectroscopic imaging, Transaction on Signal Processing, Original version submitted in April 2019, Major revision submitted in August 2019

Proceeding paper

- J. KARKOURI, F. MILLIOZ, M. VIALLON, R. PROST, H. RATINEY, Time samples selection in spiral acquisition for sparse magnetic resonance spectroscopic imaging, Proceedings for International Conference on Image processing, Beijing 2017

International Conferences and proceedings

- J. KARKOURI, F. MILLIOZ, M. VIALLON, R. PROST, H. RATINEY, Irregular spiral acquisition for compressive sensing in MRSI,Proceedings of the International Society for Magnetic Resonance in Medicine, Honolulu 2017
- J. KARKOURI, F. MILLIOZ, M. VIALLON, R. PROST, H. RATINEY, Fast Irregular MRSI spiral acquisition for sparse spectra. Application to 31P MRSI in muscles, Proceedings of the International Society for Magnetic Resonance in Medicine, Paris 2018
- J. KARKOURI, F. MILLIOZ, T. TROALEN, M. VIALLON, R. PROST, H. RATINEY, Accelerated Spiral Chemical shift Imaging for proton density and T2* Fat-Water Quantification, Proceedings International Symposium on Biomedical Imaging, Venice 2019

National Conferences and proceedings

- J. KARKOURI, F. MILLIOZ, M. VIALLON, R. PROST, H. RATINEY, Imagerie spectroscopique et compressed sensing, Bordeaux 2017

- J. KARKOURI, F. MILLIOZ, M. VIALLON, R. PROST, H. RATINEY, Imagerie spectroscopique et compressed sensing, Instituts thématiques multi-organismes, Lyon 2017
- J. KARKOURI, F. MILLIOZ, M. VIALLON, R. PROST, H. RATINEY, Imagerie spectroscopique spirale rapide basée sur un sous-échantillonnage irrégulier temporel : démonstration in vitro, Strasbourg 2019

B

List of Abreviations

AMP - Adenosine Monosphophate
ADP - Adenosine Diphosphate
ATP - Adenosine Triphosphate
AFP - Adiabatic Full Passage
AHP - Adiabatic Half Passage
CK - Creatine Kinase
Cr - Creatine
CS - Compressed sensing
CSI - Chemical Shift Imaging
emf - Electromotive force
EPSI - Echo Planar Spectroscopic Imaging
FAD - Flavin adenine dinucleotide
FID - Free Induction Decay
FFT - Fast Fourier Transform
FLASH - Fast Low Angle shot imaging
FWHM - Full Width at Half Maximum
HMPT - hexa-methyl-phosphorous-triamide
LASER - Localized Adiabatic SElective Refocusing **MRS** - Magnetic Resonance Spectroscopy
MRSI - Magnetic Resonance Spectroscopic Imaging
NAD - Nicotinamide adenine dinucleotide
NMR - Nuclear Magnetic Resonance
NUFFT - Non Uniform Fast Fourier Transform
OVS - Outer Volume Suppression
PCr - Phosphocreatine
PDE - Phosphodiesters
Pi - Inorganic phosphate
PME - Phosphomonoesters
PPA - phenyl-phosphonic acid
PRESS - Point REsolved Spectroscopy
PSF - Point Spread Function
RARE - Rapid Imaging with refocused echoes

RF - RadioFrequency
RIP - Restricted Isometric Property
SAR - Specific Absorption Ratio
SBS - Sequential Backwards Selection
SNR - Signal to Noise Ratio
SPECTROAOMI - SPECTROscopie irm du phosphore 31 dans lâĂŹArtheriopathie Oblierante des Membres Inferieurs
STEAM - STimulated Echo Acquisition Mode
SVS - Single Voxel Spectroscopy
TBP - Time Bandwidth Product
TE - Echo Time
TMS - Tetra-methyl-silane
TR - Repetition Time
VOI - Volume of interest

Bibliography

[Ada+98] Elfar Adalsteinsson, Pablo Irarrazabal, Simon Topp, et al. “Volumetric spectroscopic imaging with spiral-based k-space trajectories”. In: *Magnetic resonance in medicine* 39.6 (1998), pp. 889–898 (cit. on p. 52).

[AB09] Neil Armstrong and Alan R Barker. “Oxygen uptake kinetics in children and adolescents: a review”. In: *Pediatric exercise science* 21.2 (2009), pp. 130–147 (cit. on p. 15).

[Ask+12] Nurten C Askin, Berna Atis, and Esin Ozturk-Isik. “Accelerated phosphorus magnetic resonance spectroscopic imaging using compressed sensing”. In: *2012 Annual International Conference of the IEEE Engineering in Medicine and Biology Society*. IEEE. 2012, pp. 1106–1109 (cit. on p. 57).

[Ber+04] Matt A Bernstein, Kevin F King, and Xiaohong Joe Zhou. *Handbook of MRI pulse sequences*. Elsevier, 2004 (cit. on pp. 20, 34).

[Blo46] Felix Bloch. “Nuclear induction”. In: *Physical review* 70.7-8 (1946), p. 460 (cit. on p. 18).

[Blo+07] Kai Tobias Block, Martin Uecker, and Jens Frahm. “Undersampled radial MRI with multiple coils. Iterative image reconstruction using a total variation constraint”. In: *Magnetic Resonance in Medicine: An Official Journal of the International Society for Magnetic Resonance in Medicine* 57.6 (2007), pp. 1086–1098 (cit. on p. 56).

[BD09] Thomas Blumensath and Mike E Davies. “Iterative hard thresholding for compressed sensing”. In: *Applied and computational harmonic analysis* 27.3 (2009), pp. 265–274 (cit. on p. 55).

[Bod17] Pierre Bodenes. “Study of the application of pulsed electric fields (PEF) on microalgae for the extraction of neutral lipids.” PhD thesis. Université Paris-Saclay, 2017 (cit. on p. 11).

[Boe+97] Chris Boesch, Johannes Slotboom, Hans Hoppeler, and Roland Kreis. “In vivo determination of intra-myocellular lipids in human muscle by means of localized 1H-MR-spectroscopy”. In: *Magnetic resonance in medicine* 37.4 (1997), pp. 484–493 (cit. on p. 52).

[Bog+09] Wolfgang Bogner, Marek Chmelik, Albrecht Schmid, et al. “Assessment of (31)P Relaxation Times in the Human Calf Muscle: A Comparison between 3 T and 7 T In Vivo”. In: *Magnetic resonance in medicine : official journal of the Society of Magnetic Resonance in Medicine / Society of Magnetic Resonance in Medicine* 62 (Sept. 2009), pp. 574–82 (cit. on p. 29).

[Bog+12] Wolfgang Bogner, Stephan Gruber, Siegfried Trattnig, and Marek Chmelik. "High-resolution mapping of human brain metabolites by proton FID-MRSI at 7 T". In: *NMR in biomedicine* 25 (June 2012), pp. 873–82 (cit. on p. 52).

[Bog+14a] Wolfgang Bogner, Borjan Gagoski, Aaron T Hess, et al. "3D GABA imaging with real-time motion correction, shim update and reacquisition of adiabatic spiral MRSI". In: *Neuroimage* 103 (2014), pp. 290–302 (cit. on p. 112).

[Bog+14b] Wolfgang Bogner, Aaron T Hess, Borjan Gagoski, et al. "Real-time motion-and B0-correction for LASER-localized spiral-accelerated 3D-MRSI of the brain at 3 T". In: *Neuroimage* 88 (2014), pp. 22–31 (cit. on p. 112).

[Bos+99] Michael D Boska, JA Nelson, N Sripathi, et al. "31P MRS studies of exercising human muscle at high temporal resolution". In: *Magnetic Resonance in Medicine: An Official Journal of the International Society for Magnetic Resonance in Medicine* 41.6 (1999), pp. 1145–1151 (cit. on p. 134).

[Bot87] Paul A Bottomley. "Spatial localization in NMR spectroscopy in vivo". In: *Annals of the New York Academy of Sciences* 508.1 (1987), pp. 333–348 (cit. on p. 35).

[Bot+84] Paul A Bottomley, Thomas B Foster, and Robert D Darrow. "Depth-resolved surface-coil spectroscopy (DRESS) for in Vivo1H, 31P, and 13C NMR". In: *Journal of Magnetic Resonance (1969)* 59.2 (1984), pp. 338–342 (cit. on p. 87).

[Boy+14] Nikita Boyko, Gulver Karamemis, Viktor Kuzmenko, and Stan Uryasev. "Sparse signal reconstruction: LASSO and cardinality approaches". In: *Dynamics of Information Systems*. Springer, 2014, pp. 77–90 (cit. on pp. 55, 80).

[BH00] Eric P Brass and William R Hiatt. "Acquired skeletal muscle metabolic myopathy in atherosclerotic peripheral arterial disease". In: *Vascular Medicine* 5.1 (2000), pp. 55–59 (cit. on p. 133).

[Bra+04] Eric P Brass, William R Hiatt, and Simon Green. "Skeletal muscle metabolic changes in peripheral arterial disease contribute to exercise intolerance: a point-counterpoint discussion". In: *Vascular medicine* 9.4 (2004), pp. 293–301 (cit. on p. 134).

[Bro+87] H Ralph Brooker, Thomas H Mareci, and Jintong Mao. "Selective Fourier transform localization". In: *Magnetic resonance in medicine* 5.5 (1987), pp. 417–433 (cit. on p. 42).

[Bro+14] Robert W Brown, Y-C Norman Cheng, E Mark Haacke, Michael R Thompson, and Ramesh Venkatesan. *Magnetic resonance imaging: physical principles and sequence design*. John Wiley & Sons, 2014 (cit. on p. 16).

[CT04] Emmanuel Candes and Terence Tao. "Near optimal signal recovery from random projections: Universal encoding strategies?" In: *arXiv preprint math/0410542* (2004) (cit. on p. 54).

[CT05] Emmanuel Candes and Terence Tao. "Decoding by linear programming". In: *arXiv preprint math/0502327* (2005) (cit. on p. 54).

[Can08] Emmanuel J Candes. “The restricted isometry property and its implications for compressed sensing”. In: *Comptes rendus mathematique* 346.9-10 (2008), pp. 589–592 (cit. on p. 54).

[CW08] Emmanuel J. Candès and Michael B. Wakin. “An introduction to compressive sampling”. In: *IEEE signal processing magazine* 25.2 (2008), pp. 21–30 (cit. on p. 61).

[Can+06] Emmanuel J. Candès, Justin Romberg, and Terence Tao. “Robust uncertainty principles: Exact signal reconstruction from highly incomplete frequency information”. In: *IEEE Transactions on information theory* 52.2 (2006), pp. 489–509 (cit. on pp. 53, 60).

[Cha+15] Itthi Chatnuntawech, Borjan Gagoski, Berkin Bilgic, et al. “Accelerated 1H MRSI using randomly undersampled spiral-based k-space trajectories”. In: *Magnetic resonance in medicine* 74.1 (2015), pp. 13–24 (cit. on p. 52).

[CH06] Jie Chen and Xiaoming Huo. “Theoretical results on sparse representations of multiple-measurement vectors”. In: *IEEE Transactions on Signal processing* 54.12 (2006), pp. 4634–4643 (cit. on p. 62).

[Chi+18] Mark Chiew, Wenwen Jiang, Brian Burns, et al. “Density-weighted concentric rings k-space trajectory for 1H magnetic resonance spectroscopic imaging at 7 T”. In: *NMR in biomedicine* 31.1 (2018), e3838 (cit. on pp. 48, 52).

[Con+89] Steven Conolly, Dwight Nishimura, and Albert Macovski. “A selective adiabatic spin-echo pulse”. In: *Journal of Magnetic Resonance (1969)* 83.2 (1989), pp. 324–334 (cit. on p. 25).

[Con+91] Steven Conolly, Gary Glover, Dwight Nishimura, and Albert Macovski. “A reduced power selective adiabatic spin-echo pulse sequence”. In: *Magnetic resonance in medicine* 18.1 (1991), pp. 28–38 (cit. on p. 25).

[Cot+05] Shane F Cotter, Bhaskar D Rao, Kjersti Engan, and Kenneth Kreutz-Delgado. “Sparse solutions to linear inverse problems with multiple measurement vectors”. In: *IEEE Transactions on Signal Processing* 53.7 (2005), pp. 2477–2488 (cit. on pp. 62, 81).

[Cro+02a] Gregory J Crowther, Michael F Carey, William F Kemper, and Kevin E Conley. “Control of glycolysis in contracting skeletal muscle. I. Turning it on”. In: *American Journal of Physiology-Endocrinology And Metabolism* 282.1 (2002), E67–E73 (cit. on p. 12).

[Cro+02b] Gregory J Crowther, William F Kemper, Michael F Carey, and Kevin E Conley. “Control of glycolysis in contracting skeletal muscle. II. Turning it off”. In: *American Journal of Physiology-Endocrinology And Metabolism* 282.1 (2002), E74–E79 (cit. on p. 12).

[DG19] Robin A De Graaf. *In vivo NMR spectroscopy: principles and techniques*. John Wiley & Sons, 2019 (cit. on pp. 22, 31, 33, 38, 40, 62, 72).

[Don06a] David L. Donoho. “Compressed sensing”. In: *IEEE Transactions on information theory* 52.4 (2006), pp. 1289–1306 (cit. on pp. 53, 60).

[Don06b] David L Donoho. “For most large underdetermined systems of linear equations the minimal ðİŞĄ1-norm solution is also the sparsest solution”. In: *Communications on Pure and Applied Mathematics: A Journal Issued by the Courant Institute of Mathematical Sciences* 59.6 (2006), pp. 797–829 (cit. on p. 55).

[DL02] Wolfgang Dreher and Dieter Leibfritz. “Fast proton spectroscopic imaging with high signal-to-noise ratio: spectroscopic RARE”. In: *Magnetic Resonance in Medicine: An Official Journal of the International Society for Magnetic Resonance in Medicine* 47.3 (2002), pp. 523–528 (cit. on p. 46).

[DB13] Jiang Du and Graeme M Bydder. “Qualitative and quantitative ultrashort-TE MRI of cortical bone”. In: *NMR in Biomedicine* 26.5 (2013), pp. 489–506 (cit. on p. 149).

[Dua+08a] Marco F Duarte, Mark A Davenport, Dharmpal Takhar, et al. “Single-pixel imaging via compressive sampling”. In: *IEEE signal processing magazine* 25.2 (2008), pp. 83–91 (cit. on pp. 55, 56).

[Dua+08b] Marco F. Duarte, Mark A. Davenport, Dharmpal Takhar, et al. “Single-pixel imaging via compressive sampling”. In: *IEEE signal processing magazine* 25.2 (2008), pp. 83–91 (cit. on p. 61).

[DM93] Jeff H Duyn and Chrit TW Moonen. “Fast proton spectroscopic imaging of human brain using multiple spin-echoes”. In: *Magnetic resonance in medicine* 30.4 (1993), pp. 409–414 (cit. on p. 47).

[Duy+98] Jeff H Duyn, Yihong Yang, Joseph A Frank, and Jan Willem van der Veen. “Simple correction method for k-space trajectory deviations in MRI”. In: *Journal of Magnetic Resonance* 132.1 (1998), pp. 150–153 (cit. on p. 101).

[Fes] Jeffrey A. Fessler. “Image Reconstruction Toolbox”. In: *https://web.eecs.umich.edu/ fessler/-code* () (cit. on pp. 75, 98).

[FS03] Jeffrey A. Fessler and Bradley P. Sutton. “Nonuniform fast Fourier transforms using min-max interpolation”. In: *IEEE transactions on signal processing* 51.2 (2003), pp. 560–574 (cit. on pp. 48, 75, 98).

[Fie+15] Georg B Fiedler, Martin Meyerspeer, Albrecht I Schmid, et al. “Localized semi-LASER dynamic 31 P magnetic resonance spectroscopy of the soleus during and following exercise at 7 T”. In: *Magnetic Resonance Materials in Physics, Biology and Medicine* 28.5 (2015), pp. 493–501 (cit. on pp. 52, 87).

[Fra+87] Jens Frahm, Klaus-Dietmar Merboldt, and Wolfgang Hänicke. “Localized proton spectroscopy using stimulated echoes”. In: *Journal of Magnetic Resonance (1969)* 72.3 (1987), pp. 502–508 (cit. on p. 35).

[Gam+08] Urs Gamper, Peter Boesiger, and Sebastian Kozerke. “Compressed sensing in dynamic MRI”. In: *Magnetic Resonance in Medicine: An Official Journal of the International Society for Magnetic Resonance in Medicine* 59.2 (2008), pp. 365–373 (cit. on p. 56).

[GR00] Yun Gao and Stanley J. Reeves. “Optimal k-space sampling in MRSI for images with a limited region of support”. In: *IEEE transactions on medical imaging* 19.12 (2000), pp. 1168–1178 (cit. on pp. 57, 61, 147).

[GD01] Michael Garwood and Lance DelaBarre. “The return of the frequency sweep: designing adiabatic pulses for contemporary NMR”. In: *Journal of magnetic resonance* 153.2 (2001), pp. 155–177 (cit. on p. 36).

[Glo99] Gary H Glover. “Simple analytic spiral k-space algorithm”. In: *Magnetic Resonance in Medicine: An Official Journal of the International Society for Magnetic Resonance in Medicine* 42.2 (1999), pp. 412–415 (cit. on pp. 92–94).

[Gor+95] Irina F Gorodnitsky, John S George, and Bhaskar D Rao. “Neuromagnetic source imaging with FOCUSS: a recursive weighted minimum norm algorithm”. In: *Electroencephalography and clinical Neurophysiology* 95.4 (1995), pp. 231–251 (cit. on p. 83).

[Gov+00] Varanavasi Govindaraju, Karl Young, and Andrew A Maudsley. “Proton NMR chemical shifts and coupling constants for brain metabolites”. In: *NMR in Biomedicine* 13.3 (2000), pp. 129–153 (cit. on pp. 31, 62).

[GB14] Michael Grant and Stephen Boyd. “CVX: Matlab software for disciplined convex programming, version 2.1”. In: *http://cvxr.com/cvx/* (2014) (cit. on p. 80).

[Gri+02] Mark A Griswold, Peter M Jakob, Robin M Heidemann, et al. “Generalized autocalibrating partially parallel acquisitions (GRAPPA)”. In: *Magnetic Resonance in Medicine: An Official Journal of the International Society for Magnetic Resonance in Medicine* 47.6 (2002), pp. 1202–1210 (cit. on p. 50).

[Haa+86] Axel Haase, Jens Frahm, Dieter Matthaei, W Hanicke, and K-D Merboldt. “FLASH imaging. Rapid NMR imaging using low flip-angle pulses”. In: *Journal of Magnetic Resonance (1969)* 67.2 (1986), pp. 258–266 (cit. on p. 41).

[Hah50] Erwin L Hahn. “Spin echoes”. In: *Physical review* 80.4 (1950), p. 580 (cit. on p. 33).

[Ham] Mark Hammer. “MRI Physics: Pulse Sequences”. In: *http://xrayphysics.com/sequences.html* () (cit. on p. 48).

[Han+18] Gilbert Hangel, Bernhard Strasser, Michal Považan, et al. “Ultra-high resolution brain metabolite mapping at 7 T by short-TR Hadamard-encoded FID-MRSI”. In: *Neuroimage* 168 (2018), pp. 199–210 (cit. on p. 52).

[Has+07] Luke J Haseler, Alexander Lin, Jan Hoff, and Russell S Richardson. “Oxygen availability and PCr recovery rate in untrained human calf muscle: evidence of metabolic limitation in normoxia”. In: *American Journal of Physiology-Regulatory, Integrative and Comparative Physiology* 293.5 (2007), R2046–R2051 (cit. on p. 134).

[Hat+17] Gokce Hale Hatay, Muhammed Yildirim, and Esin Ozturk-Isik. “Considerations in applying compressed sensing to in vivo phosphorus MR spectroscopic imaging of human brain at 3T”. In: *Medical & biological engineering & computing* 55.8 (2017), pp. 1303–1315 (cit. on p. 57).

[Hen+86] JÃijrgen Hennig, A Nauerth, and H Friedburg. “RARE imaging: A fast imaging method for clinical MR”. In: *Magnetic resonance in medicine : official journal of the Society of Magnetic Resonance in Medicine / Society of Magnetic Resonance in Medicine* 3 (Dec. 1986), pp. 823–33 (cit. on p. 41).

[HS09] Matthew A. Herman and Thomas Strohmer. “High-resolution radar via compressed sensing”. In: *IEEE transactions on signal processing* 57.6 (2009), pp. 2275–2284 (cit. on pp. 55, 61).

[Hu+08] Simon Hu, Michael Lustig, Albert P. Chen, et al. “Compressed sensing for resolution enhancement of hyperpolarized 13C flyback 3D-MRSI”. In: *Journal of magnetic resonance* 192.2 (2008), pp. 258–264 (cit. on p. 62).

[Iot+93] Stefano Iotti, Raffaele Lodi, Chiara Frassineti, Paolo Zaniol, and Bruno Barbiroli. “In vivo assessment of mitochondrial functionality in human gastrocnemius muscle by 31P MRS. The role of pH in the evaluation of phosphocreatine and inorganic phosphate recoveries from exercise”. In: *NMR in biomedicine* 6.4 (1993), pp. 248–253 (cit. on p. 11).

[Isb+06] David C Isbell, Stuart S Berr, Alicia Y Toledano, et al. “Delayed calf muscle phosphocreatine recovery after exercise identifies peripheral arterial disease”. In: *Journal of the American College of Cardiology* 47.11 (2006), pp. 2289–2295 (cit. on pp. 133, 134).

[Jac+91] John I Jackson, Craig H Meyer, Dwight G Nishimura, and Albert Macovski. “Selection of a convolution function for Fourier inversion using gridding (computerised tomography application)”. In: *IEEE transactions on medical imaging* 10.3 (1991), pp. 473–478 (cit. on p. 98).

[Jin+16] Kyong Hwan Jin, Dongwook Lee, and Jong Chul Ye. “A general framework for compressed sensing and parallel MRI using annihilating filter based low-rank Hankel matrix”. In: *IEEE Transactions on Computational Imaging* 2.4 (2016), pp. 480–495 (cit. on p. 56).

[JP09] Kenneth O Johnson and James G Pipe. “Convolution kernel design and efficient algorithm for sampling density correction”. In: *Magnetic Resonance in Medicine: An Official Journal of the International Society for Magnetic Resonance in Medicine* 61.2 (2009), pp. 439–447 (cit. on p. 98).

[Jon+11] Sanne de Jong, Jaco J Zwanenburg, Fredy Visser, et al. “Direct detection of myocardial fibrosis by MRI”. In: *Journal of Molecular and Cellular Cardiology* 51.6 (2011), pp. 974–979 (cit. on p. 148).

[Kai+07] Chris A Kaiser, Monty Krieger, Harvey Lodish, and Arnold Berk. *Molecular cell biology*. WH Freeman, 2007 (cit. on p. 10).

[Kam+10] Thomas Kampf, Alexander Fischer, Thomas Basse-LÃijsebrink, et al. “Application of compressed sensing to in vivo 3D F-19 CSI”. In: *Journal of magnetic resonance (San Diego, Calif. : 1997)* 207 (Sept. 2010), pp. 262–73 (cit. on p. 57).

[Kar+17] Jabrane Karkouri, Fabien Millioz, Magalie Viallon, Rémy Prost, and Hélène Ratiney. “Time samples selection in spiral acquisition for sparse magnetic resonance spectroscopic imaging”. In: *Image Processing (ICIP), 2017 IEEE International Conference on*. IEEE. 2017, pp. 4128–4131 (cit. on pp. 61, 66, 74, 75, 86, 97).

[Kem+14] Graham Kemp, Raja Elina Raja Ahmad, Klaas Nicolay, and Jeanine Prompers. “Quantification of skeletal muscle mitochondrial function by 31P magnetic resonance spectroscopy techniques: A quantitative review”. In: *Acta physiologica (Oxford, England)* 213 (Apr. 2014) (cit. on p. 11).

[Kem+93] Graham J. Kemp, David J. Taylor, Jeffrey F. Dunn, Simon P. Frostick, and Georges K. Radda. “Cellular energetics of dystrophic muscle”. In: *Journal of the neurological sciences* 116.2 (1993), pp. 201–206 (cit. on p. 15).

[Kem+94] Graham J. Kemp, Campbell H Thompson, P. R. Barnes, and George K. Radda. “Comparisons of ATP turnover in human muscle during ischemic and aerobic exercise using 31P magnetic resonance spectroscopy.” In: *Magnetic resonance in medicine* 31 3 (1994), pp. 248–58 (cit. on p. 15).

[Kim+03] Dong-hyun Kim, Elfar Adalsteinsson, and Daniel M Spielman. “Simple analytic variable density spiral design”. In: *Magnetic Resonance in Medicine: An Official Journal of the International Society for Magnetic Resonance in Medicine* 50.1 (2003), pp. 214–219 (cit. on p. 92).

[Kno+12] Florian Knoll, Christian Clason, Kristian Bredies, Martin Uecker, and Rudolf Stollberger. “Parallel imaging with nonlinear reconstruction using variational penalties”. In: *Magnetic resonance in medicine* 67.1 (2012), pp. 34–41 (cit. on p. 56).

[Koc+06] Kevin M Koch, Peter B Brown, Douglas L Rothman, and Robin A de Graaf. “Sample-specific diamagnetic and paramagnetic passive shimming”. In: *Journal of magnetic resonance* 182.1 (2006), pp. 66–74 (cit. on p. 29).

[Kou+15] Panagiotis Koutakis, Sara A Myers, Kim Cluff, et al. “Abnormal myofiber morphology and limb dysfunction in claudication”. In: *journal of surgical research* 196.1 (2015), pp. 172–179 (cit. on p. 133).

[Kra+17] Felix Krahmer, Christian Kruschel, and Michael Sandbichler. “Total variation minimization in compressed sensing”. In: *Compressed Sensing and its Applications*. Springer, 2017, pp. 333–358 (cit. on p. 55).

[Lar+11] Peder EZ Larson, Simon Hu, Michael Lustig, et al. “Fast dynamic 3D MR spectroscopic imaging with compressed sensing and multiband excitation pulses for hyperpolarized 13C studies”. In: *Magnetic resonance in medicine* 65.3 (2011), pp. 610–619 (cit. on p. 57).

[Laz+19] Carole Lazarus, Pierre Weiss, Nicolas Chauffert, et al. “SPARKLING: variable-density k-space filling curves for accelerated T2*-weighted MRI”. In: *Magnetic resonance in medicine* 81.6 (2019), pp. 3643–3661 (cit. on p. 148).

[LF+10] Yann Le Fur, François Nicoli, Maxime Guye, et al. “Grid-free interactive and automated data processing for MR chemical shift imaging data”. In: *Magnetic Resonance Materials in Physics, Biology and Medicine* 23.1 (2010), pp. 23–30 (cit. on p. 138).

[Lia+12] Dong Liang, Edward VR DiBella, Rong-Rong Chen, and Leslie Ying. “k-t ISD: dynamic cardiac MR imaging using compressed sensing with iterative support detection”. In: *Magnetic resonance in medicine* 68.1 (2012), pp. 41–53 (cit. on p. 56).

[Lin+11] Sajan Goud Lingala, Yue Hu, Edward DiBella, and Mathews Jacob. “Accelerated dynamic MRI exploiting sparsity and low-rank structure: kt SLR”. In: *IEEE transactions on medical imaging* 30.5 (2011), pp. 1042–1054 (cit. on p. 56).

[LK15] Alfredo L Lopez Kolkovsky. “1H and 31P NMR Spectroscopy for the study of brain metabolism at Ultra High Magnetic Field from Rodents to Men”. PhD thesis. Paris 11, 2015 (cit. on pp. 21, 43).

[Luo+01] Yili Luo, Robin A. Graaf, Lance DelaBarre, Alberto TannÃžs, and Michael Garwood. “BISTRO: An outerâĂŘvolume suppression method that tolerates RF field inhomogeneity”. In: *Magnetic Resonance in Medicine* 45 (June 2001), pp. 1095 –1102 (cit. on p. 87).

[Lus+06] Michael Lustig, Juan M Santos, David L Donoho, and John M Pauly. “kt SPARSE: High frame rate dynamic MRI exploiting spatio-temporal sparsity”. In: *Proceedings of the 13th annual meeting of ISMRM, Seattle*. Vol. 2420. 2006 (cit. on p. 57).

[Lus+08] Michael Lustig, David L. Donoho, Juan M. Santos, and John M. Pauly. “Compressed sensing MRI”. In: *IEEE signal processing magazine* 25.2 (2008), pp. 72–82 (cit. on pp. 48, 56, 60).

[Ma+17] Chao Ma, Bryan Clifford, Yuchi Liu, et al. “High-resolution dynamic 31P-MRSI using a low-rank tensor model”. In: *Magnetic resonance in medicine* 78.2 (2017), pp. 419–428 (cit. on p. 52).

[Mag+15] Mahon L Maguire, Sairam Geethanath, Craig A Lygate, Vikram D Kodibagkar, and Jürgen E Schneider. “Compressed sensing to accelerate magnetic resonance spectroscopic imaging: evaluation and application to 23 Na-imaging of mouse hearts”. In: *Journal of Cardiovascular Magnetic Resonance* 17.1 (2015), p. 45 (cit. on p. 57).

[Mak+07] Konstantinos I Makris, Aikaterini A Nella, Zhen Zhu, et al. “Mitochondriopathy of peripheral arterial disease”. In: *Vascular* 15.6 (2007), pp. 336–343 (cit. on p. 133).

[Mal+05] Wasim Q Malik, Hammad A Khan, David J Edwards, and Christopher J Stevens. “A gridding algorithm for efficient density compensation of arbitrarily sampled Fourier-domain data”. In: (2005), pp. 125–128 (cit. on p. 99).

[Man77] Peter Mansfield. “Multi-planar image formation using NMR spin echoes”. In: *Journal of Physics C: Solid State Physics* 10.3 (1977), p. L55 (cit. on p. 41).

[Mar+11] Marcio Marim, Elsa Angelini, Jean-Christophe Olivo-Marin, and Michael Atlan. “Off-axis compressed holographic microscopy in low-light conditions”. In: *Optics letters* 36.1 (2011), pp. 79–81 (cit. on p. 55).

[Mau+94] Andrew A Maudsley, GB Matson, JW Hugg, and MW Weiner. “Reduced phase encoding in spectroscopic imaging”. In: *Magnetic resonance in medicine* 31.6 (1994), pp. 645–651 (cit. on pp. 47, 48).

[May+16] Martin Mayer, Gabor Hannak, and Norbert Goertz. “Exploiting joint sparsity in compressed sensing-based RFID”. In: *EURASIP Journal on Embedded Systems* 2016.1 (2016), p. 8 (cit. on p. 81).

[McD15] Mary McGrae McDermott. “Lower extremity manifestations of peripheral artery disease: the pathophysiologic and functional implications of leg ischemia”. In: *Circulation research* 116.9 (2015), pp. 1540–1550 (cit. on p. 133).

[McN+15] Chris J McNeil, Matti D Allen, Eric Olympico, J Kevin Shoemaker, and Charles L Rice. “Blood flow and muscle oxygenation during low, moderate, and maximal sustained isometric contractions”. In: *American Journal of Physiology-Regulatory, Integrative and Comparative Physiology* 309.5 (2015), R475–R481 (cit. on p. 134).

[Méd09] Jacques Médart. *Manuel pratique de nutrition: l’alimentation préventive et curative*. De Boeck Supérieur, 2009 (cit. on pp. 8, 10).

[Mer+14] Dany Merhej, Hélène Ratiney, Chaouki Diab, et al. “Fast multidimensional NMR spectroscopy for sparse spectra”. In: *NMR in Biomedicine* 27.6 (2014), pp. 640–655 (cit. on pp. 60, 61, 72, 82, 147).

[MW06] RONALD A Meyer and ROBERT W Wiseman. “The metabolic systems: control of ATP synthesis in skeletal muscle”. In: *Advanced Exercise Physiology, CM Tipton (ed.). ACSM s Lippincott Williams & Wilkins, Philadelphia* (2006), pp. 370–384 (cit. on pp. 12–14).

[Mey+03] Martin Meyerspeer, Martin Kršŝák, and Ewald Moser. “Relaxation times of 31P-metabolites in human calf muscle at 3 T”. In: *Magnetic Resonance in Medicine: An Official Journal of the International Society for Magnetic Resonance in Medicine* 49.4 (2003), pp. 620–625 (cit. on p. 29).

[Mey+11] Martin Meyerspeer, Tom Scheenen, Albrecht Ingo Schmid, et al. “Semi-LASER localized dynamic 31P magnetic resonance spectroscopy in exercising muscle at ultra-high magnetic field”. In: *Magnetic resonance in medicine* 65.5 (2011), pp. 1207–1215 (cit. on p. 15).

[Nab+10] Christine Nabuurs, Bertolt Huijbregts, Bé Wieringa, Cees W Hilbers, and Arend Heerschap. “31P saturation transfer spectroscopy predicts differential intracellular macromolecular association of ATP and ADP in skeletal muscle”. In: *Journal of Biological Chemistry* 285.51 (2010), pp. 39588–39596 (cit. on p. 15).

[Nie+18] Fabian Niess, Georg B Fiedler, Albrecht I Schmid, et al. “Dynamic multivoxel-localized 31P MRS during plantar flexion exercise with variable knee angle”. In: *NMR in Biomedicine* 31.6 (2018), e3905 (cit. on p. 52).

[Ord+86] Roger J Ordidge, Alan Connelly, and Joost AB Lohman. “Image-selected in vivo spectroscopy (ISIS). A new technique for spatially selective NMR spectroscopy”. In: *Journal of Magnetic Resonance (1969)* 66.2 (1986), pp. 283–294 (cit. on p. 87).

[Ord+96] Roger J Ordidge, Marzena Wylezinska, James W Hugg, Edward Butterworth, and Florence Franconi. “Frequency offset corrected inversion (FOCI) pulses for use in localized spectroscopy”. In: *Magnetic resonance in medicine* 36.4 (1996), pp. 562–566 (cit. on p. 39).

[Pag+97] Anthony Paganini, Jeanne Foley, and Ronald Meyer. “Linear dependence of muscle phosphocreatine kinetics on oxidative capacity”. In: *The American journal of physiology* 272 (Feb. 1997), pp. C501–10 (cit. on p. 133).

[Par+13a] Prodromos Parasoglou, Ding Xia, Gregory Chang, and Ravinder R Regatte. “3D-mapping of phosphocreatine concentration in the human calf muscle at 7 T: comparison to 3 T”. In: *Magnetic resonance in medicine* 70.6 (2013), pp. 1619–1625 (cit. on pp. 15, 52).

[Par+13b] Prodromos Parasoglou, Ding Xia, Gregory Chang, and Ravinder R Regatte. “Dynamic three-dimensional imaging of phosphocreatine recovery kinetics in the human lower leg muscles at 3T and 7T: a preliminary study”. In: *NMR in Biomedicine* 26.3 (2013), pp. 348–356 (cit. on pp. 15, 52).

[Par+13c] Prodromos Parasoglou, Ding Xia, and Ravinder R Regatte. “Spectrally selective 3D TSE imaging of phosphocreatine in the human calf muscle at 3 T”. In: *Magnetic resonance in medicine* 69.3 (2013), pp. 812–817 (cit. on p. 52).

[Par+13d] Prodromos Parasoglou, Ding Xia, Gregory Chang, Antonio Convit, and Ravinder R Regatte. “Three-dimensional mapping of the creatine kinase enzyme reaction rate in muscles of the lower leg”. In: *NMR in Biomedicine* 26.9 (2013), pp. 1142–1151 (cit. on p. 15).

[Phi+97] James W Phillips, Richard M Leahy, and John C Mosher. “MEG-based imaging of focal neuronal current sources”. In: *IEEE Transactions on Medical Imaging* 16.3 (1997), pp. 338–348 (cit. on p. 83).

[Pip+00] Iraklis I Pipinos, Alexander D Shepard, Petros V Anagnostopoulos, Asterios Katsamouris, and Michael D Boska. “Phosphorus 31 nuclear magnetic resonance spectroscopy suggests a mitochondrial defect in claudicating skeletal muscle”. In: *Journal of vascular surgery* 31.5 (2000), pp. 944–952 (cit. on p. 134).

[Pip+08] Iraklis I Pipinos, Andrew R Judge, Joshua T Selsby, et al. “The myopathy of peripheral arterial occlusive disease: part 1. Functional and histomorphological changes and evidence for mitochondrial dysfunction”. In: *Vascular and endovascular surgery* 41.6 (2008), pp. 481–489 (cit. on p. 133).

[Poh+97] R Pohmann, M Von Kienlin, and A Haase. “Theoretical evaluation and comparison of fast chemical shift imaging methods”. In: *Journal of Magnetic Resonance* 129.2 (1997), pp. 145–160 (cit. on p. 45).

[PT94] Steven L Ponder and Donald B Twieg. “A novel sampling method for 31P spectroscopic imaging with improved sensitivity, resolution, and sidelobe suppression”. In: *Journal of Magnetic Resonance, Series B* 104.1 (1994), pp. 85–88 (cit. on p. 47).

[Pos+13] Stefan Posse, Ricardo Otazo, Stephen R. Dager, and Jeffry Alger. “MR spectroscopic imaging: principles and recent advances.” In: *Journal of magnetic resonance imaging : JMRI* 37.6 (June 2013), pp. 1301–1325 (cit. on pp. 47, 62, 73).

[Pru+99] Klaas P Pruessmann, Markus Weiger, Markus B Scheidegger, and Peter Boesiger. “SENSE: sensitivity encoding for fast MRI”. In: *Magnetic resonance in medicine* 42.5 (1999), pp. 952–962 (cit. on p. 50).

[Pur+46] Edward M Purcell, Henry C. Torrey, and Robert V Pound. “Resonance absorption by nuclear magnetic moments in a solid”. In: *Physical review* 69.1-2 (1946), p. 37 (cit. on p. 18).

[Jen] “Quasi-linear relationship between Gibbs free energy of ATP hydrolysis and power output in human forearm muscle”. In: *The American journal of physiology* 268 (July 1995), pp. C1474–84 (cit. on p. 15).

[Rat+05] Hélène Ratiney, M Sdika, Y Coenradie, et al. “Time-Domain Semi-Parametric Estimation Based on a Metabolite Basis Set”. In: *NMR in biomedicine* 18 (Feb. 2005), pp. 1–13 (cit. on pp. 62, 138).

[Rat+10] Helene Ratiney, Mark J Albers, Herald Rabeson, and John Kurhanewicz. “Semi-parametric time-domain quantification of HR-MAS data from prostate tissue”. In: *NMR in biomedicine* 23.10 (2010), pp. 1146–1157 (cit. on p. 138).

[RB10] Saiprasad Ravishankar and Yoram Bresler. “MR image reconstruction from highly undersampled k-space data by dictionary learning”. In: *IEEE transactions on medical imaging* 30.5 (2010), pp. 1028–1041 (cit. on p. 56).

[RH95a] Stanley J. Reeves and Larry P. Heck. “Selection of observations in signal reconstruction”. In: *IEEE Transactions on Signal Processing* 43.3 (1995), pp. 788–791 (cit. on p. 60).

[RH95b] Stanley J. Reeves and Larry P. Heck. “Selection of observations in signal reconstruction”. In: *IEEE Transactions on Signal Processing* 43.3 (1995), pp. 788–791 (cit. on pp. 63, 64).

[RZ99] Stanley J Reeves and Zhao Zhe. “Sequential algorithms for observation selection”. In: *IEEE Transactions on Signal Processing* 47.1 (1999), pp. 123–132 (cit. on p. 72).

[Riv+10] Yair Rivenson, Adrian Stern, and Bahram Javidi. “Compressive fresnel holography”. In: *Journal of Display Technology* 6.10 (2010), pp. 506–509 (cit. on p. 55).

[SD+19] Alejandro Santos-Díaz, Diana Harasym, and Michael D Noseworthy. “Dynamic 31P spectroscopic imaging of skeletal muscles combining flyback echo-planar spectroscopic imaging and compressed sensing”. In: *Magnetic resonance in medicine* 81.6 (2019), pp. 3453–3461 (cit. on pp. 52, 57).

[Sar+01] Gordon E Sarty, Raoqiong Bennett, and Robert W Cox. “Direct reconstruction of non-Cartesian k-space data using a nonuniform fast Fourier transform”. In: *Magnetic Resonance in Medicine: An Official Journal of the International Society for Magnetic Resonance in Medicine* 45.5 (2001), pp. 908–915 (cit. on pp. 48, 98).

[Sch+12] Albrecht I Schmid, Vera B Schrauwen-Hinderling, Martin Andreas, et al. “Comparison of measuring energy metabolism by different 31P-magnetic resonance spectroscopy techniques in resting, ischemic, and exercising muscle”. In: *Magnetic resonance in medicine* 67.4 (2012), pp. 898–905 (cit. on p. 15).

[Sch+06] Michael FH Schocke, Regina Esterhammer, Stephanie Ostermann, et al. “High-energy phosphate metabolism during calf ergometry in patients with isolated aorto-iliac artery stenoses”. In: *Investigative radiology* 41.12 (2006), pp. 874–882 (cit. on p. 134).

[Sha34] Claude E. Shannon. “Communication in the presence of noise”. In: *Proc. Inst. Radio Eng* 371 (1934) (cit. on p. 53).

[SG93] Dikoma C Shungu and Jerry D Glickson. “Sensitivity and localization enhancement in multinuclear in vivo NMR spectroscopy by outer volume presaturation”. In: *Magnetic resonance in medicine* 30.6 (1993), pp. 661–671 (cit. on p. 34).

[Siu+15] Adrienne G Siu, Andrew Ramadeen, Xudong Hu, et al. “Characterization of the ultrashort-TE (UTE) MR collagen signal”. In: *NMR in Biomedicine* 28.10 (2015), pp. 1236–1244 (cit. on p. 148).

[Sla+06] Jill M Slade, Theodore F Towse, Mark C DeLano, Robert W Wiseman, and Ronald A Meyer. “A gated 31P NMR method for the estimation of phosphocreatine recovery time and contractile ATP cost in human muscle”. In: *NMR in Biomedicine: An International Journal Devoted to the Development and Application of Magnetic Resonance In vivo* 19.5 (2006), pp. 573–580 (cit. on pp. 134, 137).

[Sud+13] Prasad Sudhakar, Laurent Jacques, Xavier Dubois, Philippe Antoine, and Luc Joannes. “Compressive schlieren deflectometry”. In: *2013 IEEE International Conference on Acoustics, Speech and Signal Processing*. IEEE. 2013, pp. 5999–6003 (cit. on p. 55).

[Sud+15] Prasad Sudhakar, Laurent Jacques, Xavier Dubois, Philippe Antoine, and Luc Joannes. “Compressive imaging and characterization of sparse light deflection maps”. In: *SIAM Journal on Imaging Sciences* 8.3 (2015), pp. 1824–1856 (cit. on p. 55).

[Tac09] Mohamed Tachrount. “Spectroscopie proton du cerveau humain à 3T: Imagerie spectroscopique volumétrique spirale à TE court”. PhD thesis. Université Joseph-Fourier-Grenoble I, 2009 (cit. on p. 18).

[TM09] Hao Tan and Craig H Meyer. “Estimation of k-space trajectories in spiral MRI”. In: *Magnetic Resonance in Medicine: An Official Journal of the International Society for Magnetic Resonance in Medicine* 61.6 (2009), pp. 1396–1404 (cit. on p. 101).

[TG+96] Alberto Tann, Michael Garwood, et al. “Improved performance of frequency-swept pulses using offset-independent adiabaticity”. In: *Journal of Magnetic Resonance-Series A* 120.1 (1996), pp. 133–137 (cit. on p. 25).

[TG97] Alberto Tannús and Michael Garwood. “Adiabatic pulses”. In: *NMR in Biomedicine: An International Journal Devoted to the Development and Application of Magnetic Resonance In Vivo* 10.8 (1997), pp. 423–434 (cit. on pp. 24, 25).

[Tao05] Terence Tao. “An uncertainty principle for cyclic groups of prime order”. In: *Mathematical Research Letters* 12.1 (2005), pp. 121–127 (cit. on p. 63).

[Tho+95] CAMPBELL H Thompson, GRAHAM J Kemp, ALISON L Sanderson, and GEORGE K Radda. “Skeletal muscle mitochondrial function studied by kinetic analysis of postexercise phosphocreatine resynthesis”. In: *Journal of Applied Physiology* 78.6 (1995), pp. 2131–2139 (cit. on p. 15).

[TG07] Joel A. Tropp and Anna C. Gilbert. “Signal recovery from random measurements via orthogonal matching pursuit”. In: *IEEE Transactions on information theory* 53.12 (2007), pp. 4655–4666 (cit. on p. 61).

[Val+14] Ladislav Valkovič, Marek Chmelík, Ivica Just Kukurová, et al. “Depth-resolved surface coil MRS (DRESS)-localized dynamic 31P-MRS of the exercising human gastrocnemius muscle at 7 T”. In: *NMR in Biomedicine* 27.11 (2014), pp. 1346–1352 (cit. on p. 87).

[Val+16] Ladislav Valkovič, Marek Chmelík, Martin Meyerspeer, et al. “Dynamic 31P–MRSI using spiral spectroscopic imaging can map mitochondrial capacity in muscles of the human calf during plantar flexion exercise at 7 T”. In: *NMR in Biomedicine* 29.12 (2016), pp. 1825–1834 (cit. on p. 52).

[Val+17] Ladislav Valkovič, Marek Chmelík, and Martin Krššák. “In-vivo31P-MRS of skeletal muscle and liver: A way for non-invasive assessment of their metabolism”. In: *Analytical biochemistry* 529 (2017), pp. 193–215 (cit. on p. 52).

[VL10] Namrata Vaswani and Wei Lu. “Modified-CS: Modifying compressive sensing for problems with partially known support”. In: *IEEE Transactions on Signal Processing* 58.9 (2010), pp. 4595–4607 (cit. on p. 81).

[Ver+04] Peter Vermathen, Roland Kreis, and Chris Boesch. “Distribution of intramyocellular lipids in human calf muscles as determined by MR spectroscopic imaging”. In: *Magnetic Resonance in Medicine: An Official Journal of the International Society for Magnetic Resonance in Medicine* 51.2 (2004), pp. 253–262 (cit. on p. 52).

[Ver+12] Peter Vermathen, Pierre Saillen, Andreas Boss, Monica Zehnder, and Chris Boesch. “Skeletal muscle 1H MRSI before and after prolonged exercise. I. Muscle specific depletion of intramyocellular lipids”. In: *Magnetic resonance in medicine* 68.5 (2012), pp. 1357–1367 (cit. on p. 52).

[Vor08] Georges Voronoi. “Nouvelles applications des paramètres continus à la théorie des formes quadratiques. Deuxième mémoire. Recherches sur les parallélloèdres primitifs.” In: *Journal für die reine und angewandte Mathematik* 134 (1908), pp. 198–287 (cit. on p. 99).

[Wan+12] Jian Wang, Seokbeop Kwon, and Byonghyo Shim. “Generalized orthogonal matching pursuit”. In: *IEEE Transactions on signal processing* 60.12 (2012), pp. 6202–6216 (cit. on pp. 55, 61).

[Wei12] Kilian Weiss. “Magnetic resonance imaging of cardiac metabolism”. PhD thesis. ETH Zurich, 2012 (cit. on p. 47).

[WL16] Lyle Wiemerslage and Daewoo Lee. “Quantification of mitochondrial morphology in neurites of dopaminergic neurons using multiple parameters”. In: *Journal of neuroscience methods* 262 (2016), pp. 56–65 (cit. on p. 10).

[Wie+12] Florian Wiesinger, Eliane Weidl, Marion I Menzel, et al. “IDEAL spiral CSI for dynamic metabolic MR imaging of hyperpolarized [1-13C] pyruvate”. In: *Magnetic resonance in medicine* 68.1 (2012), pp. 8–16 (cit. on p. 57).

[WV14] Thakshila Wimalajeewa and Pramod K Varshney. “OMP based joint sparsity pattern recovery under communication constraints”. In: *IEEE Transactions on Signal Processing* 62.19 (2014), pp. 5059–5072 (cit. on p. 81).

[Wu+11] Jim S Wu, Catherine Buettner, Howard Smithline, Long H Ngo, and Robert L Greenman. “Evaluation of skeletal muscle during calf exercise by 31-phosphorus magnetic resonance spectroscopy in patients on statin medications”. In: *Muscle & nerve* 43.1 (2011), pp. 76–81 (cit. on p. 134).

[Yip86] Elizabeth L. Yip. “A note on the stability of solving a rank-p modification of a linear system by the Sherman–Morrison–Woodbury formula”. In: *SIAM Journal on Scientific and Statistical Computing* 7.2 (1986), pp. 507–513 (cit. on p. 64).

[Zah+12] Benjamin Zahneisen, Thimo Hugger, Kuan J Lee, et al. “Single shot concentric shells trajectories for ultra fast fMRI”. In: *Magnetic resonance in medicine* 68.2 (2012), pp. 484–494 (cit. on p. 56).

[Zha+98] Yantian Zhang, Hoby P Hetherington, Ernest M Stokely, Graeme F Mason, and Donald B Twieg. “A novel k-space trajectory measurement technique”. In: *Magnetic resonance in medicine* 39.6 (1998), pp. 999–1004 (cit. on p. 101).

[Zhu+03] Xiao-Ping Zhu, An-Tao Du, Geon-Ho Jahng, et al. “Magnetic resonance spectroscopic imaging reconstruction with deformable shape-intensity models”. In: *Magnetic Resonance in Medicine: An Official Journal of the International Society for Magnetic Resonance in Medicine* 50.3 (2003), pp. 474–482 (cit. on p. 118).

[ZS12] Justin Ziniel and Philip Schniter. “Efficient high-dimensional inference in the multiple measurement vector problem”. In: *IEEE Transactions on Signal Processing* 61.2 (2012), pp. 340–354 (cit. on p. 81).

[Åđa09] ÃŰmer Åđayli. “ACCURACY IMPROVEMENTS OF NIRS AND INVESTIGATION OF MUSCLE OXIDATIVE METABOLISM”. PhD thesis. Jan. 2009 (cit. on p. 10).

C

Annexes

C.1 Annexe 1

TIME SAMPLES SELECTION IN SPIRAL ACQUISITION FOR SPARSE MAGNETIC RESONANCE SPECTROSCOPIC IMAGING

Jabrane Karkouri^{1,2} *- Fabien Millioz*^{1} *- Magalie Viallon*^{1} *- Rémy Prost*^{1} *- Hélène Ratiney*^{1}

[1]Université de Lyon, INSA Lyon, Université Claude Bernard Lyon 1, UJM-Saint Etienne
CNRS, Inserm, CREATIS UMR 5220, U1206, F69621 LYON, France
[2] Siemens Healthineers, 93210 Saint-Denis, France

ABSTRACT

Magnetic resonance spectroscopic imaging (MRSI) has multiple interests in clinical practice, and especially for brain disease diagnosis. However, it faces quite long acquisition time in practice which limits their use in a clinical environment. Fast MRI acquisitions can help to reduce this acquisition time and intensify their clinical use. In this work, a new fast Magnetic Resonance Spectroscopic image acquisition method is introduced and evaluated based on a k-t space spiral sampling. The time-domain subsampling, below the Shannon-Nyquist rate, is allowed on the hypothesis of a sparse spectrum with an a priori known support. Then the nonzero components of the spectrum of each voxel are recovered using an over-determined least square problem. When data are noise-free the recovered spectrum is exact. In the real-world noisy scenario the error in the recovered spectrum highly depends on the acquired samples. We reduce this error to an acceptable level by selecting irregularly the samples using the Sequential Backward Selection algorithm. A realistic simulated irregular spiral acquisition proves the feasibility of the proposed approach.

Index Terms— Magnetic resonance spectroscopic imaging, spiral spectroscopic imaging, k-space, compressed sensing, under-sampling

1. INTRODUCTION

Nuclear Magnetic Resonance Spectroscopy is an *in vivo* technique that can provide information about metabolite concentration in the human body. Magnetic Resonance Spectroscopic Imaging (MRSI) [1] is a non-invasive imaging technique that gives spatial distribution of metabolite signals in a specific region, these metabolites signals themselves being characterized by their resonance frequencies. MRSI has indeed various clinical applications in different organs such as the brain, the liver, breast and muscles. Its drawbacks are due to its long acquisition time, low spatial resolution, difficulty to reach an acceptable Signal to Noise Ratio (SNR) and due to its sensitivity to spatial magnetic field inhomogeneity. Nowadays, fast MRSI techniques based on simultaneous spatial (k-space) and spectral (t-space) encoding already exist [1]. These particular sampling techniques can reduce the total acquisition time compared to the conventional phase-phase encoding. Compressed sensing (CS) is another way to reduce the number of samples acquired below the Shannon-Nyquist criterion. The sparsity of the signal is mandatory for the signal reconstruction using CS. In the case of Magnetic Resonance Imaging (MRI), applying CS can then significantly reduce the acquisition time. Some work has been done in order to apply CS in MRI[2] and MRSI[3].

In [4] a fast multidimensional MRS is proposed for sparse spectra. It relies on prior knowledge of the spectrum support to recover a multidimensionnal spectrum using undersampled NMR acquisition. We propose to extend this method to magnetic resonance spectroscopic imaging. Due to the separability of the 3D discrete Fourier transform- two dimension in the k-domain (kx, ky, i.e the spatial frequency domain), one dimension in the time domain, which is called the Free Induction Decay (FID) signal, the problem is reduced to independent one dimensional problems for each (kx, ky). In this work, we chose a spiral encoding scheme because it uses oscillating, continuous gradient which is an efficient way to encode the k-t space.

The challenge is that all (kx, ky) points should be acquired at the same time t. Reaching both the desirable spatial and temporal resolution within one excitation is usually impractical. As the result, multiple excitations are usually invoked which increases the acquisition time. In our method, the nonzero components of the spectrum will be recovered using an over-determined least square problem. The result is exact when data are noise-free. In the noisy scenario the error in the recovered spectrum highly depends on the acquired samples. We both reduce this error to an acceptable level and approach the simultaneous time acquisition of the (kx,ky) FID by selecting irregularly the samples using the Sequential Backward Selection (SBS)algorithm [5] in spiral-based k-space trajectories acquisitions [6]. We will show that, by this way, the total number of excitations can be reduced and thus total scan time. Note that our proposal differs from [7] in the sense that, here, it is the a priori known spectral support which is used

978-1-5090-2175-8/17/$31.00 ©2017 IEEE

to reduce the scan time and not the spatial support. Spatial and spectral information are acquired simultaneously in spiral acquisition while in [7] conventional phase-phase k-space encoding was used.
The paper is organized as follows: section 2 presents the proposed approach. Section 3 shows some results and a discussion follows. Finally a conclusion is given.

2. METHOD

2.1. Estimation of the spectrum support

In the particular case of *in vivo* MR spectroscopy, the spectrum support S is known. The chemical shifts (i.e resonating frequencies) of the different chemical compounds and metabolites are a priori known.In addition, measured B0 field inhomogeneity map to account for the peak linewidth (i.e the damping factor in the time domain) could be used to complete the support estimation. Note that the linewidth reduces the spectrum sparsity. An experimental approch could be also used to estimate the spectrum support. The support could be deduced from the spectrum acquired on the full volume of interest.

2.2. Spectrum reconstruction by Least-Square

Problem statement:

- given the sampled time domain FID signal y related to a kx-ky point in the discrete k space
- find its non-zero spectrum samples in its a priori known support S.

The FID signal y is a vector of size n related to its spectrum, also of size n, by:

$$y = Fx \tag{1}$$

Where F is the unitary discrete Fourier matrix of size $n \times n$. We denote x_s the restriction of x to its m non-zeros values (its support S). Then, we can restrict the Fourier matrix F to F_s of size $n \times m$, then (1) can be rewritten:

$$y = F_s x_s \tag{2}$$

The columns of F_s correspond to the non-zero samples of the spectrum. Acquiring $p > m$ with $p < n$ FID samples results in an over-determined equation system:

$$y_p = Ax_s \tag{3}$$

Where A is a $p \times m$ matrix obtain by selecting from F_s the rows which correspond to the p-acquired elements from y. Then we solve this system by Least-Square (LS):

$$x_s = (A^*A)^{-1}A^*y_p \tag{4}$$

Where * denotes conjugate and transpose. The matrix is full-rank [[8], from Lemma 1.3 (proof for n prime)] and the recovery of x_s is exact. It has been recognized in [[9]-Theorem 1] that *"in the absence of any other information, one could easily argue that no method would exhibit a fundamentally better performance"*. When data are noisy (hypothesis of a zero mean noise identically distributed with variance σ^2) it results an error with mean square error given by [4]:

$$E||x - x_s||^2 = \sigma^2 tr[(A^*A)^{-1}] \tag{5}$$

Clearly as F is unitary the lower error is obtained for $p = n = m$, subsampling the FID signal results in noise magnification. The trace in (5) increases monotically as rows are removed.[5] proposes to minimize this trace by selecting the sample in y (the FID signal) by an algorithm known as *Sequential Backward Selection* (SBS), it results an irregular sampling. The SBS algorithm sequentially eliminates one row at a time from the m candidates until p rows remain. At each step the resulting inverse matrix is computed at a low cost from the Sherman-Morrison formula. Note that the indexes of the samples to be retained are computed once and for all before the acquisition. Finally, using the SBS algorithm, we under-sample the time dimension and reconstruct the spectrum.

2.3. k-t space spiral sampling

After the radio-frequency pulse excitation, possibly localizing the Volume of Interest (VOI), the spiral encoding sequence for MRSI uses successive time varying gradients during the acquisition time period. These gradient waveforms trace successive spirals in the kx-ky space starting usually from its center. One time sample is acquired at each spiral (kx-ky space). A trade-off needs to be found between the duration of the spiral, the spatial resolution and the resulting spectral bandwidth.

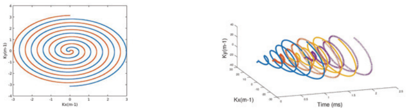

(a) (b)

Fig. 1. a) spatial interleaving ($N_{spat} = 2$), and b) temporal interleaving ($N_{time} = 4$)

In order to reduce the duration time of a spiral, a method consists in sampling the k-space with multiple acquisitions and interleaved spirals instead of one (Figure 1a). If one spiral duration is larger than the required temporal resolution to reconstruct the spectroscopic bandwidth, temporal interleaves are necessary to acquire each time sample. This technique consists in applying at each pulse Repetition Time (TR) (each excitation) successive spirals for the acquisition with a delay proportional to the temporal resolution (Figure 1b)

The following additional notation will be used:

- N_{spat} the number of spatial interleavings
- Δt_{cs} the time sample interval required for the wanted temporal resolution according to Nyquist sampling.

- T_s the duration of a spiral
- T_{sig} is the acquisition window length time
- N_{time} the number of temporal interleaving
- N_{ex} is the number of excitations needed in order to sample all the temporal and spatial points in the k-space. $N_{ex} = N_{spat} \times N_{time}$
- $n = T_{sig}/\Delta t_{cs}$ is the total number of time samples in the conventional spiral acquisition approach (see (1)).
- p, the number of time samples, irregularly spaced and defined by the SBS algorithm (see (3))

In conventional spiral MRSI acquisition, the total acquisition time is $T = N_{ex} \times TR$. We aim to demonstrate the possibility to reduce the total acquisition time, in the spiral MRSI case, by using the irregular sampling scheme given by SBS and a subsequent LS reconstruction.

2.4. Implementation Method

Two sampling strategies were implemented and compared: A) the so-called *Conventional spiral sampling Approach* B) the SBS-based irregular sampling for spiral trajectories. For both approaches, successive conventional Archimedean spirals were used. Once the k-t space was obtained, a gridding algorithm was used to resample the data onto a cartesian grid before computing the discrete Fourier transform [10].

A) Conventional spiral MRSI: time domain uniformly sampled
In the conventional sampling the full k-space is uniformly sampled at each time sample with a number N_{spat} spirals. With a number N_{time} of temporal interleaving, all the desired temporal points are sampled. The number of temporel necessary interleaving is $N_{time} = T_s/\Delta t_{cs}$. Then the total acquisition time is: $T = N_{ex} \times TR = N_{spat} \times N_{time} \times TR$

B) SBS based time domain irregular sampling for spiral trajectories

Preliminary

The FID signal is both complex and causal. Following [11] we construct a symmetrized signal by time reversal and complex conjugate of the FID that improves the sparsity of the resulting signal because its Fourier transform is real.

Problem Statement:

- given a subsampling factor p/n , a spiral duration T_s and the spirals gradient constrained by the technology (3T MR system in our simulations)
- find the minimum number $N_{exsbs} < N_{ex}$ of excitations.

Proposed solution: With SBS the number of spatial interleaving N_{spat} does not change from the conventional method. The number of temporal interleaving is reduced, and the number of excitation is reduced to a number N_{exsbs} depending on the length of a spiral T_s, see the pseudo-code below for finding N_{exsbs}. The gain $G = N_{ex}/N_{exsbs}$, which is directly related to the reduction of the acquisition time, can be deduced.

Pseudo code for finding N_{exsbs}

Input and variables: p previouly calculated SBS irregular positions are stored in the vector P, recall that $p < n$, and the acquired sample number p_t at the current discrete time index t are stored in the vector P_t. The index t_{prev} is used to select two time samples ensuring a spacing greater than the spiral length.

Initialisation:

$P_t = [], \ p_t = 0, \ Nexsbs = 0$

Procedure:

```
while $p_t < p$ do
  $N_{exsbs} = N_{exsbs} + 1$
  $t_{prev} = -T_s/\Delta t_{cs}$
  for $t = 0$ to $T_{sig}/\Delta t_{cs}$ do
    if $t \in P$ & $(t - t_{prev}) > T_s/\Delta t_{cs}$ then
      $t_{prev} = t, p_t = p_t + 1, \{P_t\}_{p_t} = t$
    end if
  end for
end while
```

2.5. MR Spectroscopy signal simulations

Both approaches were tested on ^{31}P MRSI data, showing sparse spectral feature and derived from real in vivo data as shown Fig. 2. A three compartment phantom (Fig. 3) was used with different metabolite ratio in each compartment. The FOV was of 25 cm, the image matrix size was 64×64. For the conventional approach A, a spiral length time of 1ms, 256 spirals per excitation, a number N_{time} of temporal interleaving of 4 so that there is a total of 1024 temporal points with a temporal resolution of 0.25 ms were used. For the approach B using SBS, we chose a reduction factor of 4, which means that we will sample 4 times less temporal points than Shannon-Nyquist. Here, we retain $p = 256$ points from $n = 1024$. The two approaches will be compared using the Signal Reconstruction to Error Ratio (SRER):

$$SRER = 20log \frac{||originalspectrum||_{L_2}}{||originalspectrum - reconstructedspectrum||_{L_2}}$$

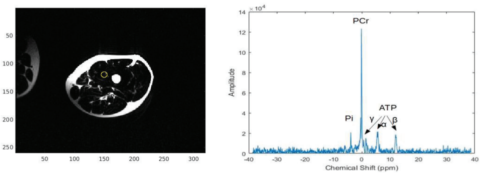

(a) (c)

Fig. 2. *In vivo* anatomic and ^{31}P spectrum (from the highlighted voxel) acquired on the quadriceps of a man at 3T. The three metabolites Phosphocreatine (PCr), Adenosine Triphosphate (ATP) and Phosphate Inorganic (PI) are indicated and show to constitute a sparse spectrum

3. RESULTS

Spiral length in Ts/Δtcs	64	32	16	8	4
Gain G	3.6	3.2	2.7	2.7	2

Table 1. Excitation gain vs the spiral length for $n/p = 4$

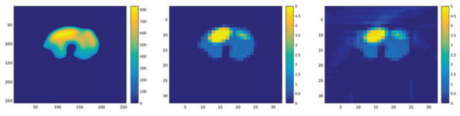
(a) (b) (c)

Fig. 3. For t=0, a) Acquired *in vivo* ^{31}P image at 3T b) Phantom (based on *in vivo* image) ; c) Reconstructed image with a gridding algorithm

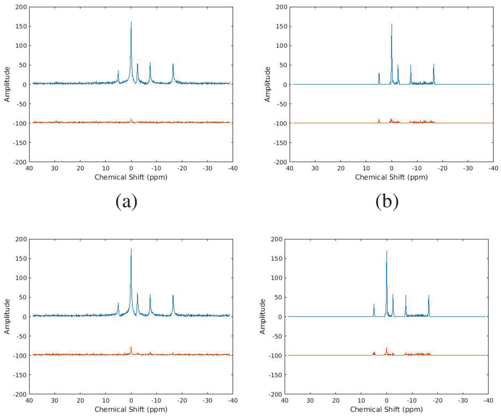

(a) (b) (c) (d)

Fig. 4. Magnitude of the reconstructed spectrum (σ noise 10% PCr) of a voxel in the left ellipse of the image (fig.3) (a) for the method A , (b) for the proposed approach B. A voxel in the right ellipse (c) for A, (d) for B. The reconstruction error magnitude (shifted by -100) is given on the bottom.)

Table 1 gives the gain G with the length of the spiral. Fig. 3 illustrates the MRSI phantom data used in this study and Fig. 4 the reconstructed spectra in 2 different regions. The SRER are respectively 25.8 dB and 24.9 dB without noise for method A and B, for the pixel in the center and 23.6 dB and 19.8dB for method A and B with noise (averaged with 20 noise realisations, σ = 10% PCr). These results show that, additionnaly to being able to reconstruct the original image, we are able with our method to reconstruct the spectroscopic signal without significantly decreasing the SRER.

4. CONCLUSION

We have proposed a novel way to reduce the scan time by a technique based on LS reconstruction and the SBS algorithm acting for undersampling the temporal direction in MRSI spiral-based acquisition. We have evaluated the relevance of such approach by implementing this acquisition strategy on an MR scanner where the spiral acquision is simulated. The results prove the feasability of the proposed approach.

5. ACKNOWLEDGEMENTS

This work was partly supported by the LABEX PRIMES (ANR-11-LABX-0063), program "Investissements d'Avenir" (ANR-11-IDEX-0007) and Siemens Healthineers.

6. REFERENCES

[1] S. Posse, R. Otazo, S.R. Dager, and J. Alger, "MR spectroscopic imaging: principles and recent advances.," *Journal of magnetic resonance imaging : JMRI*, vol. 37, no. 6, pp. 1301–25, 2013.

[2] M. Lustig and D.L. Donoho, "Compressed sensing MRI," *IEEE Signal Processing Magazine*, vol. 25, no. 2, pp. 72–82, 2008.

[3] S. Hu, M. Lustig, A. Balakrishnan, P.E. Larson, R. Bok, J. Kurhanewicz, S.J. Nelson, A. Goga, J.M. Pauly, and D.B. Vigneron, "3D compressed sensing for highly accelerated hyperpolarized 13C MRSI with *in vivo* applications to transgenic mouse models of cancer," *Magn. Reson. Med.*, vol. 63, no. 2, pp. 312–21, 2010.

[4] D. Merhej, H. Ratiney, C. Diab, M. Khalil, M. Sdika, and R. Prost, "Fast multidimensional NMR spectroscopy for sparse spectra," *NMR Biomed*, vol. 27, no. 6, pp. 640–55, 2014.

[5] S.J. Reeves and L.P. Heck, "Selection of observations in signal reconstruction," *IEEE Trans. Signal Proc.*, vol. 43, pp. 788–791, 1995.

[6] E. Adalsteinsson, P. Irarrazabal, S. Topp, C. Meyer, A. Macovski, and D.M. Spielman, "Volumetric spectroscopic imaging with spiral-based k-space trajectories.," *Magn. Reson. Med.*, vol. 39, no. 6, pp. 889–898, 1998.

[7] Y. Gao and S. Reeves, "Optimal k-space sampling in MRSI for images with a limited region of support," *IEEE Trans. Med. Imaging*, vol. 19, pp. 1168–1178, 2000.

[8] T. Tao, "An uncertainty principle for cyclic groups of prime order," *Mathematical Research Letters*, vol. 12, no. 1, pp. 121–127, 2005.

[9] E.J. Candès, J.K Romberg, and T. Tao, "Stable signal recovery from incomplete and inaccurate measurements," *Communications on Pure and Applied Mathematics*, vol. 59, no. 8, pp. 1207–1223, 2006.

[10] J. Fessler, "Image reconstruction toolbox," *https://web.eecs.umich.edu/ fessler/code*.

[11] M. Mayzel, K. Kazimierczuk, Orekhov, and V. Yu., "The causality principle in the reconstruction of sparse NMR spectra," *Chem. Commun.*, vol. 50, pp. 8947–8950, 2014.

List of Figures

List of Tables